

University of Lille, ENSAIT & GEMTEX

Graduate School MADIS-631

Ph.D. Thesis

To obtain the grade of:

Doctor from the University of Lille

Specializing in

Computer Science and Automation

By

Timea Banfalvi

Unsupervised Classification of 3D Morphologies of Human Legs for the Implementation of Adaptive Morphotypes and Medical Compression Stockings

Thesis defended on 9 December 2025 before the jury composed of:

Imed KACEM	Prof.	University of Lorraine	Reviewer
Émilie POISSON CAILLAULT	Prof.	University of Littoral Côte d'Opale	Reviewer
Cédric HEUCHENNE	Prof.	University of Liège	Examiner
Pascal BRUNIAUX	Prof.	University of Lille	Supervisor
Kim Phuc TRAN	Assoc. Prof.	University of Lille	Supervisor
Guillaume TARTARE	Assoc. Prof.	University of Lille	Co-Supervisor
Cyril CHAIGNEAU	Engineer	Sigvaris France	Invited member

Word count: 49,219

Number of Pages: 219

Université de Lille, ENSAIT & GEMTEX

Ecole Doctorale MADIS-631

Thèse de Doctorat

pour obtenir le grade de:

Docteur de l'Université de Lille

dans la spécialité

Informatique, Automatique

par

Timea Banfalvi

Classification Non-Supervisée de Morphologies 3D de Jambes Humaines pour la Mise en Œuvre de Morphotypes Adaptatifs et de Bas Médicaux de Compression

Thèse soutenue le 9 décembre 2025 devant le jury composé de :

Imed KACEM	Professeur	Université de Lorraine	Rapporteur
Émilie POISSON CAILLAULT	Professeure	Université du Littoral Côte d'Opale	Rapporteuse
Cédric HEUCHENNE	Professeur	Université de Liège	Examinateur
Pascal BRUNIAUX	Professeur	Université de Lille	Directeur de Thèse
Kim Phuc TRAN	Maître de Conférences	Université de Lille	Directeur de Thèse
Guillaume TARTARE	Maître de Conférences	Université de Lille	Co-Encadrant
Cyril CHAIGNEAU	Ingénieur	Sigvaris France	Invité

Nombre de mots: 49,219

Nombre de pages: 219

Abstract

The role of Medical Compression stockings (MCS) is to meet explicit medical requirements while also responding to the implicit expectations of patients. To contribute to compression therapy, a combination of knowledge about the functions of MCSs must be considered, including therapeutic imperatives, patient involvement in the treatment, and a meticulous process of reflection, design, and product optimization. This thesis is part of an I-Demo project (SYMPHONIES project), which aims to digitize the entire process of creating MCSs concerning the therapeutic effects, which could be evaluated by simulating the venous system from the digital twin of the leg. This digitization requires, first and foremost, knowing the morphology of the patient's leg, its size, and the spatial distribution of pressure provided by the MCS that will surround the leg. A digital MCS creation process must then be set up, which requires three representation models:

- Leg model, defined through the development of adaptive leg morphotypes;
- Ease model, integrating comfort and fit by controlling product ease on the leg model;
- MCS model, a 3D surface used to design the product, providing an initial pressure distribution via material-specific post-treatment, and supporting the mechanical model of MCS (linked to a second thesis in this project).

As of today, the legs are not classified in sizes according to their 'typical morphology specifications'; they are only referred to as theoretical conical shapes (with specifications on ankle, calf, and thigh circumferences as well as floor to knee height and floor to crotch height). There is therefore a difference between the theoretical modeling of a lower limb and the real anatomical shape of the leg, where each cross-section has its specific shape corresponding to the physiognomy of each individual. It is necessary to analyze the morphology of the leg in a large population of individuals to improve the knowledge of the shape/dimensions of patients. Thereby, this study starts with the classification of the 3D shapes of the leg. The objective of this work is to define an exhaustive methodology to obtain morphological classes characterizing the 3D shapes of the leg and to extract the most significant morphotypes for each class. A database has been filled by the 3D shapes of the scanned legs of the population under consideration. An unsupervised classification technique was employed to conduct a global geometric analysis of the 3D shape of the leg, clustering the population into morphological groups. To enhance the quality of the data partitioning, an anomaly detection model was employed to identify and remove outliers and anomalous subjects. At the end of the classification, the leg morphotypes of each morphological class were extracted from the database to obtain a realistic representation of the shape of the leg. A recommendation system, along with a corresponding sizing system, has been proposed, and it serves as the base for the parametrization of the adaptive morphotypes. These morphotypes have been developed taking into account volumetric and height changes of the new subject, following the size recommendation. These adaptive leg morphotypes will be the morphological and dimensional interface between the digital twin (thesis 3 associated with this project) and the MCS. Although the complete digital creation process of the MCS relies on three interconnected models (leg, ease,

and MCS), this thesis focuses on the development of the leg model and its adaptive morphotypes. It also introduces a morphology-specific leg sizing system and an associated recommendation tool. The ease model, designed to integrate notions of comfort, fit, and mechanical properties, remains an open challenge to be addressed in the continuation of the SYMPHONIES project. This work thus establishes a critical foundation for future integration of the digital MCS, enabling an optimized design process for therapeutic compression.

Keywords: Unsupervised classification, Normalization, and 3D shape descriptor, Human morphology, Size system, Anthropometry, Parametric model

Résumé

(*French*)

Le rôle des Bas Médicaux de Compression (BMC) est de répondre à des exigences médicales explicites et d'autre part aux attentes implicites des patient(e)s. Pour contribuer au traitement par la compression, chaque fonction que procurent les BMC résulte à la fois de la connaissance des impératifs thérapeutiques, de l'implication des patient(e)s dans le traitement et d'un processus méticuleux de réflexion, de conception et d'optimisation des produits. Cette thèse entre dans le cadre d'un projet I-Démo (projet Symphonies) qui a pour objectif la numérisation de l'ensemble du processus de création des BMC en relation avec les effets thérapeutiques qui peuvent être évalués par la simulation du système veineux à l'aide du jumeau numérique de la jambe. Cette numérisation nécessite en priorité de connaître la morphologie de la jambe du patient et son dimensionnement, de connaître la répartition spatiale de pression apportée par le BMC qui entourera la jambe. Un processus numérique de création de BMC doit alors être mis en place qui requiert trois modèles de représentation disposés en cascade:

- Le modèle de la jambe qui se concrétise par le développement de morphotypes adaptatifs;
- Le modèle d'aisance qui peut intégrer les notions de confort et de bien aller en contrôlant l'aisance du produit sur le modèle de la jambe;

- le modèle de BMC représenté par une surface 3D nécessaire au développement du produit, à l'obtention d'une première représentation de la répartition de pressions par un post-traitement spécifique en lien avec la matière, au développement du modèle mécanique du BMC (thèse 2 associée à ce projet).

À ce jour, les jambes ne sont pas classées en tailles selon leurs spécifications morphologiques; elles sont uniquement assimilées à des formes coniques théoriques (avec des spécifications sur les circonférences de la cheville, du mollet et de la cuisse, ainsi que sur la hauteur du sol au genou et la hauteur du sol à l'entrejambe). Il existe donc une différence entre la modélisation théorique d'un membre inférieur et la forme anatomique réelle de la jambe, où chaque coupe horizontale a sa propre forme correspondant à la physionomie de chaque individu. Il est nécessaire d'analyser la morphologie de la jambe sur une large population d'individus afin d'améliorer la connaissance de la forme/des dimensions des patients. Ainsi, cette étude commence par la classification des formes 3D de la jambe. L'objectif de ce travail est de définir une méthodologie exhaustive pour obtenir des classes morphologiques caractérisant les formes 3D de la jambe et d'extraire les morphotypes les plus significatifs pour chaque classe. Une base de données aété alimenter par les formes 3D des jambes scannées de la population considérée. Différentes techniques de classification non supervisées ont été utilisées pour analyser la géométrie de la forme 3D de la jambe globalement, ceci en regroupant la population en groupes morphologiques. Afin d'améliorer la qualité du partitionnement des données, un modèle de détection des anomalies a été utilisé pour supprimer les valeurs aberrantes et les sujets atypiques.

À la fin de la classification, les morphotypes de jambe de chaque classe morphologique ont été extraits de la base de données afin d'obtenir une représentation réaliste de la forme de la jambe. Un outil de recommandation, associé à un système de dimensionnement, a été proposé et sert de base à la paramétrisation des morphotypes adaptatifs. La méthodologie de conception des morphotypes adaptatifs a été développée dans un outil d'aide à la décision de type CAO, pour tenir compte des changements de volume et de hauteur d'un nouveau patient. Ces morphotypes ont été développés en tenant compte des changements de volume et de hauteur du nouveau sujet, conformément à la recommandation de taille. Ces morphotypes de jambe adaptatifs constitueront l'interface morphologique et dimensionnelle entre le jumeau numérique (thèse 3 associée à ce projet) et le BMC. Bien que le processus complet de création numérique du BMC repose sur trois modèles interconnectés (jambe, aisance, et BMC), cette thèse s'est concentrée essentiellement sur le développement du modèle de la jambe et de ses morphotypes adaptatifs, tout en proposant un système de dimensionnement des jambes spécifique à la morphologie ainsi qu'un outil de recommandation associé. Le modèle d'aisance, destiné à intégrer les notions de confort, d'ajustement et de propriétés mécaniques, demeure une question ouverte à approfondir dans le cadre de la suite du projet Symphonies. Le présent travail constitue ainsi une base essentielle pour l'integration future du BMC numérique, permettant d'optimiser le processus de conception des dispositifs de compression thérapeutique

.

Mots clés: Classification non-supervisée, Normalisation et descripteur de forme 3D, Morphologie humaine, Système de tailles, Anthropométrie, Modèle paramétrique

Declaration of Authorship

I, **Timea BANFALVI**, declare that this thesis titled, "Unsupervised classification of 3D morphologies of human legs for the implementation of adaptive leg morphotypes and Medical Compression Stockings" and the work presented in it are my own. I confirm that:

- This work was done wholly or mainly while in candidature for a research degree at the University of Lille.
- Where any part of this thesis has previously been submitted for a degree or any other qualification at this University or any other institution, this has been clearly stated.
- Where I have quoted from the work of others, the source is always given. Except for such quotations, this thesis is entirely my work.
- Where the thesis is based on work done by me jointly with others, I have clarified exactly what others did and what I have contributed myself.

Signed:

_____

Date:

_____

Acknowledgements

The completion of this thesis has been a long journey, and I would not have been able to accomplish it without the guidance, support, and encouragement of many people. It is with great gratitude that I acknowledge their contributions here.

First and foremost, I would like to express my deepest gratitude to Professor Pascal Bruniaux, my thesis director, for his invaluable guidance and support throughout this journey. You have been my mentor since before I began my research and have continued to be so, challenging me to grow both as a researcher and as a person. Thank you for believing and trusting in me. You have been an inspiration to me.

I am also very grateful to Professor Kim Phuc Tran, co-director of this work, whose expertise and constructive feedback helped refine the ideas and methodology of this research. Your perspective has enriched this project in important ways.

Special thanks go to my co-supervisor, Guillaume Tartare, whose mentorship and friendship have meant a great deal to me. Your advice and encouragement made an enormous difference, and I am grateful for your professional guidance.

I gratefully acknowledge the support of BPI France, whose financial assistance made this research possible. I would also like to thank Cyril Chaigneau at Sigvaris for your collaboration, practical insights, and enthusiasm, which have been valuable in ensuring the relevance of this work. Thanks should also go to Antoine Durand for his expertise in software development, which enabled this project to move beyond theory into practical application. I'd like to acknowledge Dac Hieu Nguyen and Kim Duc Tran for their invaluable

contributions to this work. Their expertise in data science and their assistance in preparing publications significantly strengthened both the practical and scholarly aspects of this thesis.

Finally, I extend heartfelt thanks to my parents, husband, and friends for their patience and encouragement, and to the memory of François Dassonville, whose friendship and early support I deeply miss.

Dissemination

The work presented in this thesis has been disseminated in the following journal publications and conference papers, presented in reverse chronological order:

- T. Banfalvi, D. H. Nguyen, K. D. Tran, G. Tartare, P. Bruniaux, X. Zeng, and K. P. Tran, 'Anomaly Detection in Morphologies of Human Legs for the Implementation of Adaptive Leg Morphotypes and Medical Compression Stockings', 3rd ISSAT International Conference on Data Science in Business, Finance and Industry - Da Nang, Vietnam, January 6-8, 2024.

- T. Banfalvi, K. D. Tran, G. Tartare, P. Bruniaux, and K. P. Tran, 'Unsupervised classification of 3D morphologies of human legs for the implementation of adaptive leg morphotypes and Medical Compression Stockings: A survey and perspective', 10th EAI International Conference on IoT Technologies for HealthCare, Dong A University, Danang, Vietnam, 22-24 Oct 2024.

- T. Banfalvi, D. H. Nguyen, K. D. Tran, G. Tartare, and P. Bruniaux, 'Deep Convolutional K-Means of 3D morphologies of human legs for the implementation of adaptive leg morphotypes and Medical Compression Stockings', 10th EAI International Conference on IoT Technologies for HealthCare, Dong A University, Danang, Vietnam, 22-24 Oct 2024.

- T. Banfalvi, K-P. Tran, P. Bruniaux, G.Tartare, 'Deep unsupervised classification of human leg shapes applicable in the design of medical compression stockings'. Poster presented at the 'Journée régionale des Doctorants en Sciences de la Mer et Automatique', Boulogne-sur-Mer, Juillet 2024.

- T. Banfalvi, P. Bruniaux, G.Tartare, F. Dassonville, 'Unsupervised Classification of 3D morphologies of human legs for the implementation of adaptive leg morphotypes and medical compression stockings'. Poster presented at the 31^{st} GEMTEX day, Roubaix, France, Nov. 2023.

- T. Banfalvi, P. Bruniaux, G. Tartare, and F. Dassonville, 'Unsupervised classification of 3D morphologies of human legs applicable in the use of medical compression stocking design', in Proceedings of the 18th 'Ergonomie et Informatique Avancée' Conference, Bidart, France: ACM, pp. 1–8. doi: 10.1145/3624323.3624327, Oct. 2023.

- T. Banfalvi, P. Bruniaux, G.Tartare, F. Dassonville, 'Unsupervised classification of 3D morphologies of human legs for the implementation of adaptive leg morphotypes and Medical Compression Stockings'. Poster presented at the 9^{th} 'Journée régionale des Doctorants en Automatique', Roubaix, June 2023

- T. Banfalvi, I-P. Miguélez, P. Bruniaux, D. Soulat, X. Legrand, A-R. Labanieh, G. Tartare, « État de l'art sur le développement d'une solution de modélisation de la conception d'un Bas Médical de Compression (BMC)'. Poster presented at the 30^{th} GEMTEX day, Roubaix, France, Nov. 2022.

Contents

Abstract **iii**

Declaration of Authorship **xi**

Acknowledgements **xiii**

Dissemination **xv**

1 Introduction **1**

1.1 The Symphonies project 4

1.2 Problem statement 6

1.3 Research outline 8

1.4 Publications 11

2 Background and Literature Review **13**

2.1 Introduction to Compression therapy 13

2.1.1 Chronic Venous Insufficiency 14

2.1.2 Lymphoedema 16

2.1.3 Overview of Medical Compression Stockings 18

2.1.4 Sizing and design of Medical Compression Stockings . 19

2.1.5 Causes for poor fit and non-compliance 20

2.1.6 Comfort and fit optimizations 21

2.2 Leg morphology and anthropometry 23

2.2.1 Previous research on human leg morphology's variability 23

2.2.2 The impact of leg morphology on the fit and effectiveness of compression garments 27
2.3 3D shape analysis and classification 29
2.3.1 Data management and processing of 3D scans 30
2.3.2 3D shape normalization 32
2.3.3 Geometric learning approaches applied to 3D scans . . 34
2.3.4 3D shape classification 39
2.3.5 Principal Component analysis (PCA) 40
2.3.6 Unsupervised Classification methods 41
K-means clustering 42
DB SCAN clustering 43
Spectral Clustering 44
Cluster quality evaluation 46
2.3.7 Deep clustering 48
2.4 Contributions 53

3 Exploration of Lower Limb Morphological Classes Using Classical Unsupervised Techniques Across Multiple Shape Descriptors 55
3.1 Introduction 55
3.2 Background and Literature Review 57
3.3 Definition and extraction of morphological shape descriptors . 58
3.3.1 Data acquisition and post-processing 58
3.3.2 Morphological shape descriptors 62
1D shape descriptor 62
2D shape descriptor 63
3D shape descriptor 68
3.3.3 Shape correspondence 75
3.4 Unsupervised learning from morphological data 80

3.4.1 Principal Component Analysis 80
3.4.2 Unsupervised classification of multidimensional shape descriptors 83
Spectral Clustering 85
Clustering quality and algorithm initiation 85
Ensemble learning 87
3.5 Results 88
3.5.1 1D data classification 88
3.5.2 2D data classification 91
3.5.3 3D data classification 93
3.6 Conclusions 98

4 Deep Learning Architecture for Clustering and Anomaly Detection in Morphological Data 101

4.1 Introduction 101
4.2 Methodology 102
4.2.1 Post-processing of 3D mesh surface 102
Fully Convolutional Mesh Autoencoder 103
Deep Support Vector Data Description 106
4.2.2 MeshDeepSVDD: Anomaly Detection in 3D Meshes via Fully Convolutional Mesh Autoencoder and Deep SVDD 107
Mesh representation learning with FCMA model . . . 107
4.2.3 Anomaly Detection with Deep SVDD 108
4.3 Results 110
4.3.1 Mesh Reconstruction with FCMA model 110
4.4 Conclusions 117

5 Proposition of a new sizing system for the design of MCS 119

5.1 Introduction 119

5.2 Background and literature review 121
5.3 Methodology 122
5.3.1 Identification of circumferential evolution patterns . . 125
5.3.2 Creation of sizing tables 128
5.3.3 Creation of recommendation system 129
5.4 Results 133
5.5 Conclusions 139

6 Creation of adaptive morphotypes 141
6.1 Introduction 141
6.2 Background and literature review 142
6.3 Methodology 145
6.3.1 Visible Human Project and bone center identification . 145
6.3.2 Length adjustment 148
6.3.3 Volume and size adjustment 150
6.3.4 Circumferential evolution adjustment 153
6.3.5 Surface creation 154
6.4 Results 155
6.5 Conclusions 164

7 Conclusions 167
7.1 Overview of main findings 168
7.2 Limitations 174
7.3 Future research perspectives 176

A 181

B 183

C 201

D **211**

D.1 Outliers detected by MeshDeepSVDD 211

E **217**

F **219**

F.1 Geometrical separation of the 3 morphological groups defined by the 3D shape descriptor 219

F.2 Gender separation 220

F.3 Body mass index (BMI) separation 221

F.4 Sigvaris sizing separation 223

G **227**

G.1 Geometric comparison between original and adapted form of the legs 227

References **229**

Chapter 1

Introduction

Compression therapy is a widely used treatment for chronic venous diseases that involves applying pressure to improve blood flow and reduce swelling and it is an indispensable treatment option [1] in the management of patients who suffer from diseases like Chronic Venous Insufficiency, a chronic and progressive disease of the leg veins [2], or Lymphoedema, which manifests by an abnormal collection of lymphatic fluid [3]. Both of these diseases are more common in women [3], [2], [4]. Compression stockings are widely used long-term treatment options for both of these diseases [5], [4], [6], as wearing them can improve blood circulation and reduce symptoms, but there are still a large number of patients non-compliant [5] that can hinder the treatment outcome. The most common practice is the use of graduated compression stockings, which apply the highest pressure at the ankle and gradually decrease it towards the thigh. They are classified based on the pressure they exert at the ankle [5]. As they have to be worn for a prolonged time, and it is recommended that they should be worn daily, in a way, they act as a second skin. The key feature of compression garments is the fit, because they have to adapt to the underlying morphology of the wearer at the same time it has to provide a predicted effect [7]. Poorly fitted compression stockings could cause serious harm to the wearer that could lead to pressure necrosis,

impaired arterial flow, or even amputation [5]. The underlying anatomy of the limb can passively influence the applied pressure in each zone, resulting in varying pressure [8], especially in the case of the traditional homogeneous compression stockings, as these stockings are designed in a way that they consider the limb cross-section as perfectly circular. With traditional compression stockings, pressure damage can be developed by the shape of the patient itself [9], [8], in case the product is not well fitted. Both chronic diseases have shape-related deformation present in the severe stages [10], [11]. Custom-made compression garments are the most accurate therapeutic products that support the external healing process [12]. By using 3D body scanners instead of manual measurements and by the development of a reliable compression knitted fabric assessment method, it is possible to calculate the correct product dimensions that apply the intended pressure gradient to the leg. Medical compression stockings can be fully personalized to the individual's measurements, but this method is rarely used in an industrial setting because of manufacturing constraints, and obvious costs. Despite these disadvantages, development of personalized compression therapy has been already suggested in multiple studies [13], some of which have used parametric models of the lower leg [14] to propose custom fit sizing systems, others reevaluated the leg shape to create better, more effective sizing systems that account for higher variations in shape [15]. Most often, the design of compression products relies on sizing tables to create off the shelf products. In ready-to-wear and made-to-measure apparel production, one of the driving forces is the definition of fit [16], [17]. Ready-to-wear sizes are derived from anthropometric surveys conducted by governments and research institutions to build an anthropometric profile, represented with sample subjects of a specific population [18]. The issue with current sizing systems is that standard sizes should be matched to individual body measurements, and to find an

optimal size, the dimensions of the client should be very close to standard values [19]. Body types that are far from being average are still undeserved and difficult to dress, even with made-to-measure protocols [16]. The mathematical definition of the body-to-garment relationship is a challenging task as bodies are different in size and shape, which can change with ethnicity, sex, weight gain, and aging. Understanding the link between a 3D garment and a 2D pattern is of high importance, and for this, it is also necessary to understand body morphology. Yet, we still define garments with traditional 2D block-patterns, that might be adapted to different circumference ratios and body proportions externally [16], [19], but keeping the internal shaping the same through grading, making no difference between a small size and an extra-large size, which assumes that the garment will drape the same way on a smaller curve as on a larger curve while these in reality are different body shapes. It is also common to derive certain measurements, with proportional rules from principal measurements [19], which deepens the gap between body types. Following these rules, it is only possible to create patterns from an average body, with high symmetry, standard proportions, and posture. For this reason, it is very important to understand 3D scanning technology and how the data is being processed, as it is the only way to go from an impersonalized sizing approach to a personalized clothing design [20], also representing a closer step to apparel sustainability [16] and mass customization. Data collection with 3D body scans will benefit manufacturers in redefining their sizing systems and garment patterns to better suit various body types. 3D-driven pattern making on 3D acquired demographic data can result in multiple benefits: inclusion for body types that fall out of statistical norms, improve comfort at wearing through smart design, increase customer satisfaction, therefore less returns, and less industrial waste while increasing client fidelity [16], [21].

1.1 The Symphonies project

France 2030 is an investment plan for the future, launched on October 12, 2021, that allocates €54 billion to catch up on France's industrial lag by massively investing in innovative technologies and supporting ecological transition [22]. The 10 key objectives are regrouped in three main pillars: better production, better living, and better understanding, focusing on modernizing industry, improving quality of life through innovation in health and food, and enhancing scientific and technological knowledge. The General Secretariat for Investment leads this plan on behalf of the Prime Minister of France, and it is implemented by the Ecological Transition Agency (ADEME), the National Research Agency (ANR), Bpifrance, and the Caisse des Dépôts [23]. The i-Démo initiative is a call for projects under the France 2030 investment plan, managed by Bpifrance, and it aims to support large-scale, structuring research, development, and innovation projects that contribute to the development of industrial and service companies in promising markets. To enhance France's industrial competitiveness, this program encourages the collaboration among businesses, research organisations and other stakeholders [24].

The Symphonies project is a winner of a call for projects under the i-Démo program, launched as part of France 2030 recovery plan [25]. This project aims to develop a digital solution to improve the care of patients with lymphoedema, which is a chronic and irreversible disease – a dysfunction of the lymphatic system, causing swelling of the limbs - affecting over 250 000 people just in France. The developed digital tools will not only be useful for the patients and healthcare professionals to follow up on the development of the disease, but also for the industrial partners, who will be able to use these tools

for better and more inclusive product design, and by this revolutionizing the medical textile market.

The leader of the project is **Sigvaris Group France**, which is specialised in the design, manufacture, and sale of medical compression products to treat a wide range of medical needs [26]. Sigvaris is collaborating with five other partners, each of whom has a specific task to complete to make the Symphonies project succeed. These five partners are the following:

- Ecole Nationale Supérieure des Arts et Industries Textiles (GEMTEX)
- Ecole Nationale de Mines Saint Etienne (SAINBIOSE)
- Institut National des Sciences Appliquées (INSA Lyon)
- Institut Français des Textiles et de l'Habillement (IFTH)
- Healabs

The first task in the symphonies project is the **development of a modeling solution for the design of a Medical Compression Stocking (MCS)**, which involves the development of a product design software tailored to individual body morphologies, integrating a digital twin of the lower limb with a simulation tool that models the mechanical behavior of compression fabrics. This software is intended to predict how the compression garment will physiologically impact the body, particularly in terms of pressure applied to the venous and lymphatic systems. The influence of different textile materials, each with unique mechanical properties, will be analyzed. A key objective is to evaluate the relationship between the applied external pressure and the resulting decrease in internal pressure within these vascular networks. This task is being jointly carried out by the Sigvaris Group France, Ecole Nationale Supérieure des Arts et Industries Textiles (GEMTEX Laboratory), and Ecole Nationale de Mines Saint-Etienne (SAINBIOSE Laboratory).

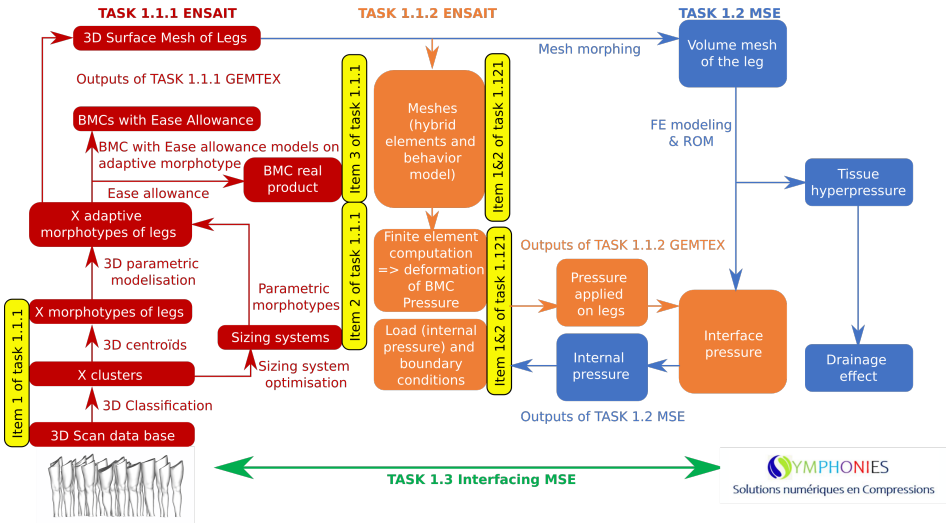


FIGURE 1.1: Workflow of Task 1 in the Symphonies project: Development of a modeling solution for the design of a Medical Compression Stocking (MCS)

Figure 1.1 presents the workflow of the development of a modeling solution for the design of MCSs, divided into three major sub-tasks between the GEMTEX and SAINBIOSE laboratories. GEMTEX is currently involved in two of these sub-tasks, which are carried out in parallel, and these are the following:

- **Sub-task 1.1.1: Analysis of the morphology of MCS wearers and creation of a design model**
- **Sub-task 1.1.2: Development of a MCS mechanical simulation model**

1.2 Problem statement

Despite the rapid development of 3D body scanning technologies in recent years, which has made digital anthropometry a fast and accurate task, there is still a lack of robust and explainable AI methods that can accurately partition real-life anatomic data into distinct clusters without the need for existing labels. 3D shapes that are obtained from digital anthropometry in their row

form have a complex and irregular character that makes 3D shape analysis a real challenge. Moreover, these types of data are often subject to outliers, which can skew analysis and compromise results. When we focus on the shape and size variations of the human leg, we need to capture the subtle shape variations rather than broad categorical differences; therefore, we need a 3D shape descriptor that can capture intra-class variability, preserving overall topology in a compact form and well-suited for comparative study. While there have been studies conducted to analyse the shape of 3D body scans, using Principal Component Analysis (PCA) [27], [28] or Deep Neural Networks (CNN) [29], [30] to extract most relevant variations and features from 3D anthropometric data and further partition with unsupervised methods, the explainability of the obtained results still stays limited as the variations cannot be meaningfully interpreted. Additionally, PCA is proven to be sensitive to pose variations. These quantitative shape differences might describe variance and subtle geometric differences, but often lack biological interpretability or act as black boxes, limiting clinical trust and adaptation.
Dealing with anatomic data, especially with geometries that present soft tissue alterations that characterize Lymphoedema and CVI, raises the question of outliers, which could interfere with the correct identification of morphological clusters, especially if the available data is scarce. The emergence of deep learning, like convolutional neural networks, has changed feature extraction from medical data, allowing us to understand more complex structures. Recent studies have explored novel techniques that enhance anomaly detection by focusing on global structures rather than pixel-level details [31], local consistency [32], and uncertainty modelling [33] to improve classification performance which holds a prospective solution in case of human legs, where anomalies can be subtle and require models that consider global shape when it comes to anomaly detection.

Although previous studies have explored body type classification with various shape descriptors, little attention has been given to the anatomical classification of the lower limb with the purpose of improving compression therapy with the development of parametric leg models. Both leg classification regarding shape and size, and the development of adaptive parametric leg models are crucial to allow manufacturers to design compression solutions that adapt to the user's underlying leg morphology and apply the intended pressure gradient, necessary for healing and long-term management of chronic conditions. It has been pointed out in multiple studies that the fit of the compression products is highly influencing the exerted pressure on the leg [34], [35], [36], yet current sizing tables, used in the industry, fail to include certain leg shapes and sizes, leaving a high percentage of patients with products that slip, wrinkle and cause discomfort, which directly influences their compliance with treatment. Moreover, some sources also state that compression garments should take into consideration the interface pressure across the limb and not only in the three key anthropometric levels (ankle, calf, thigh), and that assessing the pressure applied by the garment should involve a real human limb shape to have validity [37].

1.3 Research outline

The role of MCSs (Medical Compression Stockings) is to meet explicit medical requirements. Additionally, it must respond to the implicit expectations of patients as well. To contribute to compression therapy, each function that MCSs provide results from a combination of knowledge of the therapeutic imperatives, patient involvement in the treatment, and a meticulous process of reflection, design, and product optimization. This thesis is part of the i-Démo project (Symphonies project), which aims to digitize the entire process

of creating MCSs concerning their therapeutic effects, which can be evaluated by simulating the venous system using the digital twin of the leg. This digitization requires, first and foremost, knowing the morphology of the patient's leg, its size, and additionally, the spatial distribution of pressure provided by the MCS that will surround the leg. A digital MCS creation process must then be set up, which requires fulfilling the following research objectives:

RO1 Integrate morphological classification with biomechanical and fabric data to optimize sizing and fitting of MCSs.

RO2 Design anomaly detection and clustering frameworks to identify abnormal leg shapes relevant to medical compression therapy.

RO3 Develop and evaluate unsupervised and deep learning models to classify 3D leg morphologies and extract representative morphotypes.

To meet these objectives, the following research questions should be answered:

RQ1 How can AI techniques detect abnormal leg morphologies relevant to MCS treatment?

RQ2 What are the most effective combinations of unsupervised clustering and deep learning methods for classifying 3D leg morphologies and supporting adaptive design rules for MCSs?

RQ3 How can morphological data be used to create a comprehensive system for automated sizing and fitting of MCSs, based on leg shape, pressure mapping, and fabric properties?

Chapter 2 provides a comprehensive overview of existing research on compression therapy that concentrated and tried to decode the shape of the leg as a major influencing factor of the interface pressure, highlighting the

problems related to the leg shape of the patients and pressure correspondence that exist in the state-of-practice. As most literature that we have reviewed suggested that the industry should focus more on the real leg shape of patients when they are designing compression products, one of the major research gap that we have identified was that most of studies focused on the circumferential variability at major anatomical levels either as 1D data or 2D cross section, and especially in case of the latter, the studied population only extends to a few subjects. One of the main objectives of this thesis was to identify what could describe the leg morphology of a larger population, which goes beyond 1D anthropometric data, and at the same time, it is also repeatable and discriminative enough to define clusters. Accordingly, this research focuses on the comprehension of a larger scale 3D scanned data at an anatomical level, including, in the state of the art, the study of the surface soft tissue and bony landmarks of the lower limb to identify the key focus zones that could create a 3D shape descriptor contributing to the explanation of the results. To answer our first research question and explore what the most effective classic and modern unsupervised clustering methods are for 3D leg morphology classification, we first developed a taxonomy of the literature to categorize current approaches and a benchmark comparison of selected methods.

The results related to the identification of various shape descriptors and morphological groups through classic machine learning techniques are presented in Chapter 3. A novel unsupervised anomaly detection model (Mesh Deep SVDD) that integrates the Fully Convolutional Mesh Autoencoder (FCMA) with Deep SVDD for a 3D mesh processing framework tailored to our 3D leg morphology dataset is presented in Chapter 4, where we highlight the advantages and disadvantages of such an approach. Since in our database we have subjects who suffer from chronic conditions, it was necessary to preview the

modalities through which an AI can detect outliers or abnormal leg structures relevant to medical compression treatment, which answers our second research question. As a result, we also present an interpretable anomaly detection system applicable to 3D morphological mesh data obtained from 3D body scanners usable in a clinical setting.

Chapter 5 outlines the methodology employed to create a new sizing logic and recommendation tool for the adaptive parametric leg morphotypes, with a reflection on how 2D anthropometric data could be interpreted as growth rules to create a more inclusive and more effective product sizing.

Chapter 6 presents an automated solution for a 3D medical compression stocking model that is derived from a negative ease model built on a decreasing gradient pressure logic towards the thigh and the integration of textile mechanical properties, obtained in a collaborative project. These two chapters give an answer to how 3D morphological data could be used to create a comprehensive system for automated sizing and fitting of MCS based on leg shape, pressure mapping, and fabric properties.

Chapter 7 summarizes the answers to the presented research questions, highlighting the main findings and reflecting on their significance concerning the initial research objectives. It highlights the key contributions of the work and acknowledges the limitations encountered during the study. In addition, it highlights the potential directions for future research.

1.4 Publications

The work presented in this thesis has been disseminated in the following conference papers, presented in reverse chronological order.

- T. Banfalvi, D. H. Nguyen, K. D. Tran, G. Tartare, P. Bruniaux, X. Zeng, and K. P. Tran, 'Anomaly Detection in Morphologies of Human Legs for

the Implementation of Adaptive Leg Morphotypes and Medical Compression Stockings', 3rd ISSAT International Conference on Data Science in Business, Finance and Industry - Da Nang, Vietnam., 6-8 January, 2025.

- T. Banfalvi, K. D. Tran, G. Tartare, P. Bruniaux, and K. P. Tran, 'Unsupervised classification of 3D morphologies of human legs for the implementation of adaptive leg morphotypes and Medical Compression Stockings: A survey and perspective', 10th EAI International Conference on IoT Technologies for HealthCare, Dong A University, Danang, Vietnam, 22-24 Oct, 2024.

- T. Banfalvi, D. H. Nguyen, K. D. Tran, G. Tartare, and P. Bruniaux, 'Deep Convolutional K-Means of 3D morphologies of human legs for the implementation of adaptive leg morphotypes and Medical Compression Stockings', 10th EAI International Conference on IoT Technologies for HealthCare, Dong A University, Danang, Vietnam, 22-24 Oct, 2024.

- T. Banfalvi, P. Bruniaux, G. Tartare, and F. Dassonville, 'Unsupervised classification of 3D morphologies of human legs applicable in the use of medical compression stocking design', in Proceedings of the 18th 'Ergonomie et Informatique Avancée' Conference, Bidart, France: ACM, Oct. 2023, pp. 1–8. doi: 10.1145/3624323.3624327.

Chapter 2

Background and Literature Review

In this chapter, we explore the state-of-the-art related to problems arising from the poor fit of Compression products, how the shape of the leg can influence the pressure applied to the lower limb, and how these problems are already being managed. This we present in Section 2.1. In Section 2.2, we explore the anatomical study of the human leg, highlighting the research that has already described morphological changes in the human leg. Next, we explore the existing classic and modern unsupervised and deep learning methods used for data partitioning, paying special attention to the existing anomaly detection solutions.

2.1 Introduction to Compression therapy

Compression therapy is a widely used treatment for chronic venous diseases that involves applying pressure to improve blood flow and reduce swelling, and it is an indispensable treatment option [1] in the management of patients who suffer from diseases like Chronic Venous Insufficiency or Lymphoedema. To improve venous return and reduce oedema, compression systems, especially compression hosiery, aim to provide graduated compression to the lower limb [38]. To achieve this graduate compression, the highest pressure should be applied at the ankle, which gradually decreases towards

the knee. Eagle [9] explains that graduate compression can be achieved by applying a bandage with uniform tension to a leg with a normal proportionality. Eagle also pointed out that in many cases, patients do not have a regular leg shape, and it might even be disproportionate, which can result in varying pressure at any given point. The incorrect level of pressure can lead to pressure damage; therefore, it is of great interest to make a correspondence between leg shape, size, and product design. Moffat [39] precisely states that achieving precise and consistent pressure is a difficult task, as on diverse limb shapes, pressure can vary significantly. The underlying anatomy can passively generate uneven pressure in and can also result in uncomfortable wearing perception [8].

2.1.1 Chronic Venous Insufficiency

Reich-Schupke [2] defines Chronic Venous Insufficiency (CVI) as “a chronic, progressive disease of the leg veins caused by primary alterations in the vein wall and/or vein valves, or secondary alterations after thrombosis, accompanied by visible veins in the leg, venous reflux and venous hypertention, as well as microcirculation disorders and trophic alterations in the lower leg and foot.” He also states that women are more frequently affected than men. Nicolaides [40] describes that venous hypertension, which is a result of "structural or functional abnormalities of the vein," causes the symptoms that can characterize chronic venous insufficiency. According to Wegen-Franken [41], CVI is a more severe form of chronic venous disease (CVD), which, in terms of clinical classification, according to CEAP [11], is associated with C4 to C6. The medical management of venous hypertension is compression therapy with therapeutic graduated-compression stockings [42]. As Motykie et al. [42] describe, the calf-muscle pump, which contracts around veins and

forces the blood to move, acts as a safeguard against the development of venous hypertension. The paper also mentions that the direction of blood flow is determined by the valves inside the vein. The combination of the pumping motion of the calf muscle and the directing nature of the valves makes the blood circulate in an upward motion. The above-mentioned hypertension appears as a result of valve failure. CVI can significantly alter the soft tissue morphology of the suffering patient as the symptoms of this disease include visible veins as well as possible "irreversible damage to the skin, fatty tissue, connecting tissue and musculature" as Reich-Schupke described in [2]. According to Motykie et al. [42], CVI considerably reduces the quality of life of patients, because the pain and discomfort associated with the disease can lead to a loss of mobility, reduction in work capacity, and also has an impact on their social life.

Classification of chronic venous insufficiency Porter et al. [11] created a classification system in 1994, abbreviated as CEAP, in which they defined a way to group legs presenting signs of chronic venous disease according to "Clinical signs (C), Ethiology (or cause) (E), Anatomic distribution (A) and Pathophysiology (P)". For the **clinical classification**, they assign the leg to one of the following seven classes:

- **Class 0** - No visible or palpable signs of venous disease
- **Class 1** - Telangiectases, reticular veins, malleolar flare
- **Class 2** - Varicose veins
- **Class 3** - Edema without skin changes
- **Class 4** - Skin changes, such as pigmentation, venous eczema, lipodermatosclerosis
- **Class 5** - Skin changes with healed ulceration
- **Class 6** - Skin changes with active ulceration

The assigned class will be abbreviated as $C_{0\text{-}6}$. In addition to this classification, they also characterize the leg as asymptomatic or symptomatic, adding to this abbreviation the letter A or S, like the following: $C_{0\text{-}6,\,A}$ or $C_{0\text{-}6,\,S}$. The **Etiologic classification** refers to the categorization of venous dysfunction as congenital, abbreviated as E_C and refers to the disorder that is present from birth, with symphtoms appearing later in life; primary, described as a venous dysfunction with an unknown cause, abbreviated as E_P or secondary, which appears as a result of an acquired condition, abbreviated as E_S. The **anatomic classification** describes the venous disease as "superficial (A_S), deep (A_D), perforating (A_P)" or as a combination of these. The **pathophysiologic classification** refers to whether the clinical signs of the disease are caused by venous reflux (P_R), obstruction (P_O), or both.

2.1.2 Lymphoedema

Primary Lymphoedema is a chronic and incurable disease that, according to Macdonald et al. [3], manifests "by an abnormal collection of lymphatic fluid as a result of an anatomical alteration to the lymphatic system" and it occurs most often in the legs. It can occur at three stages of life: at birth, at adolescence, or above the age of 35, and it is more likely in women than in men, the ratio being 87% to 13% [3]. Secondary Lymphoedema can be associated with chronic wound, chronic venous disease, radiation, infection, or trauma, along with other exogenous causes [3], [4]. Secondary lymphoedema often occurs as a result of cancer treatment, such as Breast cancer and certain types of Gynecological cancers, making the male-to-female appearance ratio 1:9 [4], proving that this chronic disease is more likely in women. As Macdonald et al. [3] put it, "Lymphoedema is a high-protein edema, which is the result of damage or absence of the normal lymphatic system". Both primary and

secondary lymphoedema are irreversible and progressive, and they have a terrible effect on the quality of life of patients [4]. Kitayama [4] highlights the importance of improving the outcome of treatment in future studies, as lymphoedema is "intractable and few cases are completely cured". There are 4 stages of Lymphoedema, and they are the following [10]:

- **Stage 0** - normal leg with abnormal lymphatic transport
- **Stage 1** - early oedema, improvable by limb elevation
- **Stage 2** - pitting oedema, not improved by limb elevation
- **Stage 3** - fibroadipose deposition and skin changes

Depending on the increase of the extremity's volume, lymphoedema can be characterised as mild(< 20% volume increase), moderate(20-40% volume increase), or severe(> 40% volume increase) as described by Goss et al. [10]. They also describe that the difficulty in taking manual measurements to determine the volume of the lymphoedema is caused by multiple factors: the volume has to be calculated, it is difficult to accuratelly determine the reference points for future assesments and it is also problematic to manage the tightness at which the tape measure is handled by the examiner as the circumference could vary significantly at different tightness.

Treatment of lymphoedema For the treatment of lymphoedema, just as in the case of chronic venous insufficiency, the staple treatment is with the help of compression stockings and bandages. Additionally, in case of lymphoedema, practitioners also use exercise therapy with compression, manual lymphatic drainage, and skin care in combination [4].

2.1.3 Overview of Medical Compression Stockings

Compression stockings are widely used as long-term treatment options for Chronic venous insufficiency and lymphoedema [5], [4], [6]. Wearing compression stockings can improve blood circulation and reduce symptoms of the disease, but there are still a large number of patients who are non-compliant [5] that can hinder the treatment outcome. In case of CVI, graduated compression stockings are used, which apply the highest pressure at the ankle, gradually decreasing it towards the thigh, and they are classified based on the pressure that they exert at the ankle [5]. Two main units of measure are used in expressing the compression level of medical compression stockings. One is millimeters of mercury (mmHg), which, as the author of [43] explains, comes from the mechanics of compression stockings that are designed to compress the soft tissue and blood vessels of the leg, thereby reducing their volume and changing the blood pressure. This mechanism is also mentioned in [6]. As blood pressure in medicine is expressed in mmHg, this unit was adapted to compression stockings as well. The second unit of measure is Pascals (Pa), which is more commonly used in technical sciences.
In case of lymphoedema, as Kankariya [6] has described, "the increased pressure in the veins stimulates pumping of the lymphatic system and encourages re-absorption of lymphatic fluid", encouraging more reabsorption and less leaking of fluid.
Three factors influence the pressure applied by the stocking [5]:

- stiffness and elasticity of the material that the stocking is made of
- the size and shape of the leg
- activity of the wearer (lying, sitting, or in active movement)

There are four different classes of compression hosiery recognized in the French standard, and they are characterized by the sub-bandage pressure

that they exert at the ankle [5]:

- **Class 1** - 10-15 mmHg
- **Class 2** - 15-20 mmHg
- **Class 3** - 20-36 mmHg
- **Class 4** - > 36 mmHg

Size selection To select the correct size of the product, first of all, the measurements have to be taken correctly. For this, it is recommended that patients should be measured in the morning and without the presence of oedema [44]. In case of lymphoedema and atypical-shaped legs, the author of [44] recommends custom-made compression hosiery, and particularly, it is mentioned that in case of lymphoedema, flat-bed knit is required.

2.1.4 Sizing and design of Medical Compression Stockings

Medical compression stockings have to be worn for a prolonged time, and it is recommended that they should be worn on a daily basis; in a way, they act as a second skin. The key feature of compression garments is the fit, because it has to adapt to the underlying morphology of the wearer. At the same time, it has to provide a predicted effect [7]. Nørregaard et al. [45] mention in their paper that the ready-to-wear compression stockings are not adapted to the morphological changes that venous leg ulcer creates in patients who are suffering from the more severe form of CVI, and suggest a reevaluation of sizing systems that are more adapted to this morphology. Lozo et al. [43] stated in their paper that "the elongation of the knitted fabric on a specific leg part depends on the amount of elongation force, but also the length of the yarns knitted into a course. They also have found in their analysis that in the

case of the high compression pantyhose, they have not found a "mathematical correlation between the elongation and the compression of the knitted fabric". This conclusion was drawn from the pressure analysis, where they have tested the same compression stocking on two different-sized wooden legs. The elongation of the larger leg has occurred, but it did not significantly change the applied compression on the leg. After this discovery, they were meditating on the leg size that this compression stocking was intended for. The authors highlighted basic parameters that are important for the correct construction of compression stockings, from which the following are considered important in our case:

- the choice of a machine of certain construction, fineness, and needle bed diameter
- the knitting technologist should be provided with the sketch of the leg shape containing both leg lengths and circumferences
- in modern production, the method of personalizing the product could be applied

2.1.5 Causes for poor fit and non-compliance

Palfreyman et al. [5] emphasize that a poorly fitted compression stocking could cause serious harm to the wearer that could lead to pressure necrosis, impaired arterial flow, or even amputation. As Liu et al. [8] described, the underlying anatomy of the limb can passively influence the applied pressure in each zone, resulting in varying pressure, especially in the case of the traditional homogeneous compression stockings, as these stockings are designed in a way that they consider the limb cross-section as perfectly circular. This uneven pressure can result in discomfort while wearing, which directly results in non-compliance. In [38], they describe that in the case of areas with

bone prominences and zones with a smaller radius, the pressure is higher than in muscular areas at the same level, where the radius of the curve is larger. This cross-sectional variation and the pressure relationship are illustrated in Figure 2.1. The same phenomenon is described in papers [9], [8], stating that pressure damage can be developed by the shape of the patient itself.

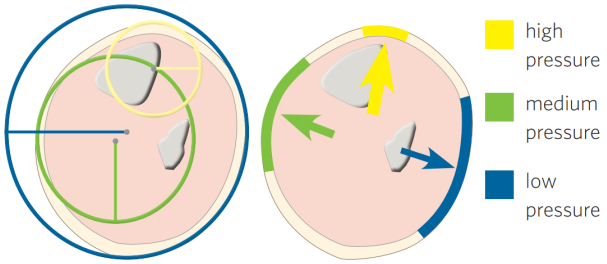


FIGURE 2.1: Cross sections through the lower right leg showing how different pressures may be generated according to the radius of curvature of the leg as described in [38]

2.1.6 Comfort and fit optimizations

According to Kowalski et al. [12], custom-made compression garments are the most accurate therapeutic products that support the external healing process. One of the important factors in the modeling and designing of compression products that this paper mentions is the accuracy of the body measurements, which can be enhanced by the use of 3D body scanners as a replacement for the less reliable manual measurements. The second factor is the development of a reliable compression knitted fabric assessment method that could provide information related to the required pressure value. In their paper, they propose an algorithm that could be used in the design of compression products, allowing the determination of correct product dimensions that would exert the correct graded value of unit pressure along the body part.

In the previous Section 2.1.5, we presented the discomfort and pressure incoherence caused by the irregular cross-sections of the lower limb, an issue for which Liu et al. [8] proposed a 3D knitted hybrid compression stocking that has a heterogeneous structure differentiating the elastic modulus of the knitted fabric, in function of the underlying anatomy, using lower elastic modulus in front of the muscle (calf) and higher elastic modulus in front of the bone (tibia). This construction has the advantage of reducing peak pressure at bony prominences and augmenting the contraction of the calf muscle.

Granberry et al. [46] studied the geometric variability of the lower leg to propose a novel sizing system for active compression garments, which require high body shape and size fidelity. For this, they have conducted 3D anthropometrical studies to define body variability and statistically divide size groups based on body measurements. They have highlighted that achieving a precise fit is very challenging because of the lack of correlation between leg measurements, and they have also suggested that, within all leg circumferences, the ankle measurement is a key dimension to organize the population into distinct groups, because this area of the body is less susceptible to gaining weight or developing muscle mass. Their research highlighted that, in general, men have larger lower leg circumferences than women, and they suggest that they should have larger compression garments. It has also been pointed out that women have a wider knee size range than men and that the ankle and calf size of men has a larger variability due to larger muscle mass. Figure 2.2 depicts the shape variability of male and female subjects in three anthropometric zones: ankle, calf, and knee.

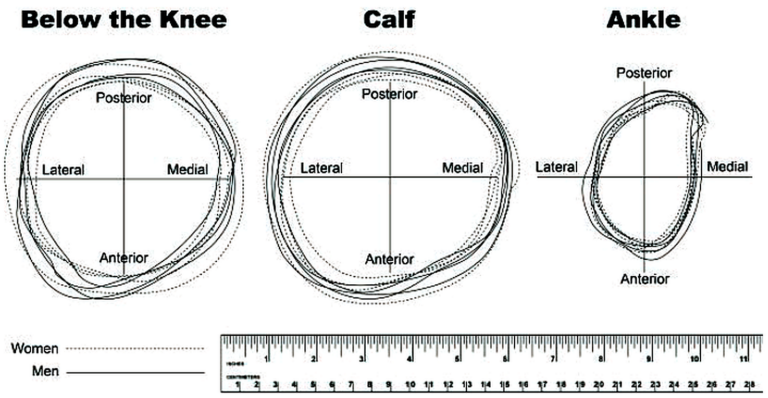


FIGURE 2.2: Superposed cross sections of the knee, calf, and ankle for average male and female subjects from different size quartiles, depicting the shape variability and irregularity of these areas as described in [46]

2.2 Leg morphology and anthropometry

This section discusses anatomic and anthropometric discoveries related to the lower limb, also highlighting some of the surface landmarks that could be used in the development of shape descriptors and the extraction of anthropometric data.

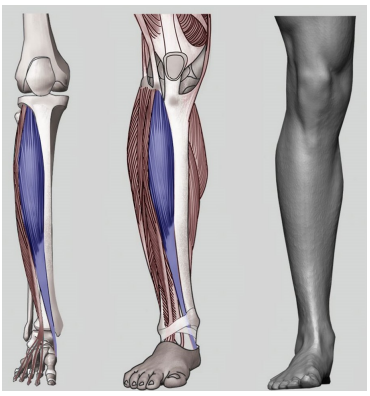
2.2.1 Previous research on human leg morphology's variability

Body size and shape are two factors that vary considerably among the human population [47]. Height and weight are absolute measures of body size, and body mass index is a relative index reflecting body shape, as the author of [47] states. The author of [48] defines sexual dimorphism as " a systematic difference in size and shape between female and male members of the same species." While compared to animals, humans show less sexual dimorphism, men and women still have numerous differences. The term sexual dimorphism is commonly used for secondary sex characteristics, which are unrelated to reproduction, such as height, weight, or body shape.

Morphological variability of the leg bones In human anatomy, the relationship between the proximal and distal limb segments is called intra-limb proportion. In case of the lower limb, we call it the crural ratio (tibia length/femur length) [49]. Holliday et al. [49] suggest that in the recent human population, the distal lower limb segment (tibia length) is more variable than the proximal segment (femur length), and this variation is more likely in the case of men than in the case of women. In his study, he also suggests that the best assumption should be that both proximal and distal limb segments have an equal intrinsic variance. To measure the relative variation of the limb segments, Holliday in [50] calculated the coefficient of variance with the following formula: CV = standard deviation/mean*100. In the same paper [50], the author also shows evidence that in the case of the lower limb, the relative variation of the tibia is much higher than that of the femur. The study uses combined sex samples as there is little sexual dimorphism in the crural index, deduced from the split results that have not significantly changed when male and female samples were separated.

Morphological variability of the leg muscles Quoting the words of Pośnik et al. [51], « muscles and their tendons are not considered the most variable structures in humans".

Muscles of the lower leg: In the anterior compartment of the lower leg, we find the tibialis anterior muscle. The tibialis anterior, visible on Figure 2.3a, is a "long, narrow fusiform-shaped muscle located in the anterior compartment of the leg" [52]. The gastrocnemius is a large superficial muscle [53] located in the posterior compartment of the leg, visible on Figure 2.3c.



(A) Anterior view of the lower leg, highlighting the tibialis anterior muscle.Adapted from [52].



(B) Anterior view of the lower leg, highlighting the Extensor Digitorum Longus muscle. Adapted from [54].



(C) Posterior view of the lower leg, highlighting the gastrocnemius muscle. Adapted from [53].

FIGURE 2.3: Muscles of leg

Morphological variability of the adipose tissue Humans show significant average sex differences in body composition [55]. Mansour et al. [56] explain that "Adult women have significantly higher fat mass values and relatively lower lean mass compared to men". Nikitovic [48] and Wells [55] state that "The ratio of lean to fat is much greater in males than females". According to the findings in [57], "Males had more bone and skeletal muscle and less fat than did females for both lower and upper extremities." Wells in [55] also noted that the fat and lean deposition is directed towards different body locations between the two sexes. This phenomenon can contribute significantly to the differences in shape, the author calling it shape dimorphism. Sexual

dimorphism related to shape can also be influenced by age; the findings in [55] show that both men and women by the age of 70 – 80 lose their early adult shape. The same paper states that obesity and low body mass index can both decrease shape dimorphism. Nindl et al. [58] demonstrated that "Men have more of their muscle mass in their arms and women have more of their fat mass in their legs", this phenomenon being the main reason for gender differences in body composition.

Surface anatomy of the leg Surface landmarks of the human body fall into two categories: soft surface forms and hard surface forms. Within the soft surface forms we can name, the superficial muscles, tendons, ligaments, and fatty tissues, and within the hard surface forms we can identify bone prominences that can be seen on the surface of the body [59]. The bones of the lower limb are the femur, tibia, fibula, and patella. Certain parts of these bones can be seen or palpated on the surface of the leg, and these are the following:

- Greater Trochanter
- Lateral Condyle of Femur
- Medial Condyle of Femur
- Patella
- Tibial Tuberosity
- Head of Fibula
- Lateral Malleolus
- Medial Malleolus

2.2.2 The impact of leg morphology on the fit and effectiveness of compression garments

The shape of the leg has important implications in relation to pressure and garment design [34]. The pressure exerted is affected by the properties of the underlying tissue and relative proportions of these at any particular cross-section [34]. The fit of a compression garment is crucial in order to ensure the correct interface pressure that is going to be applied to the body part. As Teyeme et al. [35] points out, insufficient pressure will limit the efficacy of the compression garment; on the other hand, too high compression can lead to discomfort and serious damage to health. It has been emphasized in this study that both "The mechanical properties of the fabric and the curvature radius of the respective body part" should be considered in the construction of compression garments. We may as well put the question of why the design of these products is still stuck with the conventional conical construction, considering the leg as a perfectly symmetrical cylinder, when in real life, the shape of the lower limb varies greatly. According to the authors of [35], over the non-uniform human body shapes, the compression garment with a specific tension exerts and distributes pressure unevenly; therefore," the extent of pressure depends on the garment fit and construction and the size and shape of the body part."

Lawrence et al. [36] throughout their experiments have proved that the compression of the lower limb below the knee contributes most of the increase of velocity of blood in the femoral vein. This conclusion was drawn from the observation that after applying 18-14 mmHg of pressure to the below-knee region, the deep venous velocity significantly increased, but when applying the same amount of pressure to the entire leg length, the velocity did not increase. Another interesting finding of this study was that none of

the pressure ranges can cause blood flow impairment in the muscles. On the other hand, high external pressure (> 30 mmHg) applied to the leg can cause a decrease in muscle blood flow. The overall conclusion is that graduate external compression (20 mmHg at ankle – 10 mmHg at thigh) can increase the deep venous velocity, and very high pressure (reaching 30 mmHg at calf) can lead to subcutaneous tissue flow impairment and can reduce deep vein velocity.

The study of Williams et al. [37] evaluated the effects of wearing undersized, oversized, and the recommended-sized compression leggings and tights, designed for athletes, in different body postures. One of the remarks that they have made was that in the standing position, the pressure is significantly higher than in the seated position. Their analysis has also revealed that the pressure profile measured across different landmarks on the leg is "neither graduated nor progressive". By measuring the interface pressure in the soft tissue part of the landmarks, they have noted that the pressure is higher in the calf region and it varies significantly in different landmarks. The study suggests that compression garments should take into consideration the interface pressure across the limb. The solution for this should perhaps be a new sizing system that takes into consideration the shape and size evolution of the leg across its length. They also mentioned that assessing the pressure applied by the garment should involve a real human limb shape to have validity, as this method would take into account the body composition and the posture, which are both important factors.

2.3 3D shape analysis and classification

One of the fundamental problems in geometric processing is 3D shape analysis, which is used for finding the intrinsic or extrinsic correspondence between 3D shapes [60]. The complex and irregular character of 3D data represents the main challenge in 3D shape analysis [61], because unlike 2D data, 3D shapes don't have a regular grid structure, and they can be represented in multiple ways (point cloud, polygonal mesh, voxel, grid) [62]. As Ahmed et al. [63] describe, shape descriptors are simplified representations of the 3D objects that contain geometric and topological characteristics of their shape and make the processing easier, at the same time allowing comparability among different 3D shapes. Intrinsic shape descriptors can capture the variability of the surface geometry, and they remain unchanged under isometric deformations, regardless of the 3D embedding of the object [60]. On the other hand, when the representation is not invariant to deformations, it means that the data is being treated as a Euclidean structure; therefore, it is extrinsic [60].

Intrinsic shape descriptor The intrinsic properties of a 3D shape are linked to the surface and stay constant when isometric deformations occur to the object.

Extrinsic shape descriptor The extrinsic properties of a 3D object are highly dependent on the placement and orientation of the object in Euclidean space and will be affected when rigid transformations occur.

The increasing use of 3D anthropometry and the availability of high-precision 3D scanners make it possible to use 3D shape analysis in the context of classifying human body shapes. 3D scanners collect the precise geometry of the human body in the form of point clouds that can be converted into

polygonal meshes. Today's 3D scanner technology has evolved to the point that this transformation is done automatically, meaning that the previously required post-treatment processing that involved artifacts like noise, outliers, holes, or ghost-geometry (armpits and crotch in case of human body) [64], is not a requirement anymore. Additionally, body segmentation and landmark identification have also been added to the automatic/ semi-automatic functions, making data collection a straightforward task. The collected data is a valuable asset in 3D geometric analysis, but it can be considered as a rather complex and irregular structure, due to the large number of vertices that are not sampled consistently throughout the database, and both point clouds and meshes can take part in both Euclidean and non-Euclidean domains [63].

2.3.1 Data management and processing of 3D scans

The rise of 3D body scanning technology allows anthropometric data generation in a productive way due to the tools designed in the past 30 years, related to scan processing and data management, anthropometric sections. In comparison to traditional anthropometry, digital anthropometry has multiple advantages, the first of which is the large number of different data types that one can gather: 3D landmarks, 3D meshes, digital anthropometric measurements, and sections. Aggregated data refers to large databases of 3D body scans that are mainly used in scientific experimental studies with the purpose of describing the size and shape variability of a given population.

Data processing and post-treatment Alemany et al. [65] review the five steps of processing 3D body scans, which are the following:

- **Calculation of the aligned point cloud**: 3D scanners have multiple sensors that can capture the body from different angles, creating an individual point cloud for each sensor. As the author describes, these point clouds are aligned together to represent the body. In this form, the 3D scan still has artifacts: noise data, missing information, and overlapping points, and these artifacts can impact the final 3D body scan.
- **Generation of the 3D body mesh**: As described in the paper, the best form of data to collect metrics is a mesh; therefore, it is important to transform the point cloud from the previous step into a mesh surface. The author emphasizes that in the case of refinement (hole filling, smoothing, removal of noise data, etc.), the accuracy of the real geometry can decline; therefore, he recommends storing both point cloud and mesh forms of data.
- **Calculation of landmarks**: Landmarks refer to anatomical features and bony prominences that should be located on the body. One way of identifying these features is to use physical landmarks placed on the body beforehand, which would create an artifact on the mesh, thus making them easily identifiable. The advancement of AI and the availability of large anthropometric surveys(with available landmarks and correctly standardized) made it possible to automatically calculate the position of anthropometric landmarks on a new 3D body scan.
- **Calculation of body measurements**: Knowing the position of body landmarks makes it possible to automatically extract anthropometric measurements such as heights, circumferences, widths and depths, angles, and they are based on multiple metrics (Euclidean distance, convex hull, etc.)
- **Creation of a watertight 3D body model** According to the author, shape registration is a crucial step in shape analysis of the body, which means

that for this purpose, it is recommended to have a watertight mesh that is artifact-free and has an invariant topology (point-to-point correspondence)

2.3.2 3D shape normalization

In the context of human body shape analysis, especially in the case of limbs, one factor that we need to take into consideration is that the height of subjects is variable, while the shape change is moderate; therefore, to be able to extract shape descriptors comparably, we need to apply scaling to the segmented body part. Hamad et al. [66] used a minimal bounding sphere in their classification algorithm, where the goal was to extract a 3D shape descriptor that would classify woman torsos in morphological groups. They used this method to preserve the proportionality of the human body, which can change with the height of the subject.

Minimal Bounding Sphere The minimal bounding sphere is the smallest sphere that can enclose a set of points in a 3D space [67]. In 3D model processing, finding and normalizing the size of the radius of a minimal bounding sphere can improve stability of the model against scaling [67]. This is important in the case of both intrinsic and extrinsic shape descriptors. Figure 2.4 presents the normalization approach with the minimal bounding sphere, implemented by Hamad et al. [68], who used the algorithm of Gärtner [69]

Another method that could be used to calculate the minimal bounding sphere is the algorithm of Welzl [70]. This method is implemented by Semechko [71] in a Matlab function, allowing to compute the exact minimum bounding sphere of a 3D point cloud or a triangular surface mesh (Figure 2.5).

Mathematically, the minimum bounding sphere is defined as the unique sphere

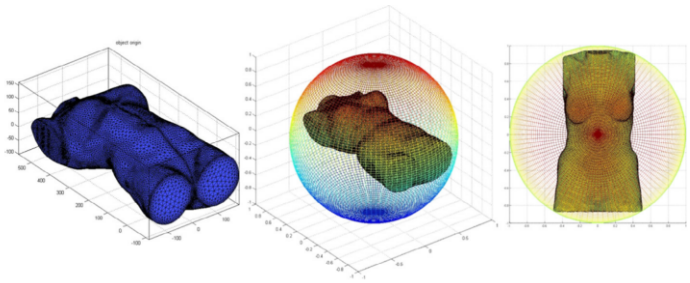


FIGURE 2.4: 3D data normalization with the minimal bounding sphere as presented by Hamad et al. [68]

of smallest radius R that encloses all given points $x_i \in \mathbb{R}^3$:

$$\|x_i - C\| \leq R, \quad \forall i,$$

where $C \in \mathbb{R}^3$ is the center of the sphere. The algorithm fits a sphere to 2–4 boundary points by solving systems of linear equations derived from this geometric constraint.

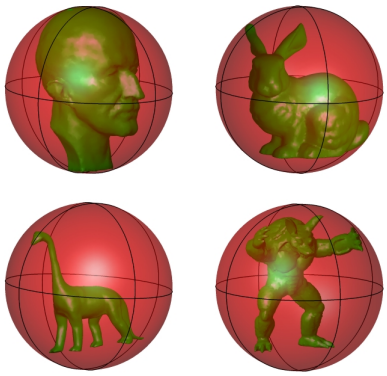


FIGURE 2.5: Exact minimal bounding sphere of Weltz implemented by Semechko [71]

Iterative Closest Point algorithm (ICP) rigid shape registration To determine differences between 3D objects and to achieve optimal alignment is a

requirement. This process is called global registration. One of the most popular registration methods is called ICP (iterative closest point), which computes the rigid transformation (rotation and translation) between two point sets by determining the optimal translation and rotation to minimize the sum of squared errors [72].

2.3.3 Geometric learning approaches applied to 3D scans

Geometric learning approaches for various 3D shape representations have been developed significantly since 2015. New deep network architectures have been introduced to process and regenerate 3D shapes for geometric learning [73]. In computer vision, 3D data is a resource that contains valuable information about the geometry of an object [63]. There are two main categories of 3D data representation: Euclidean-structured 3D data, which has an underlying grid structure allowing global parametrization, and non-Euclidean 3D data, characterized by an irregular structure, making deep learning a challenging task. According to Ahmed et al. [63], in the Euclidean representation category, enter the descriptors, projections, RGB-D, volumetric, and multi-view, and in the non-Euclidean category, enter the point clouds, grids, and meshes. They illustrate the different types of 3D data representations in Figure 2.6.

As previously mentioned, 3D shapes are available in many forms, and these shapes can be studied with both classic and modern learning approaches. Many of the recently available studies present geometric deep learning methods on large, labeled data. As our topic of interest is geometric learning for unsupervised classification (without labels), in this subsection, we will present the classic and modern methods that are usable for feature extraction that aims to represent the 3D objects in a compact and discriminative way.

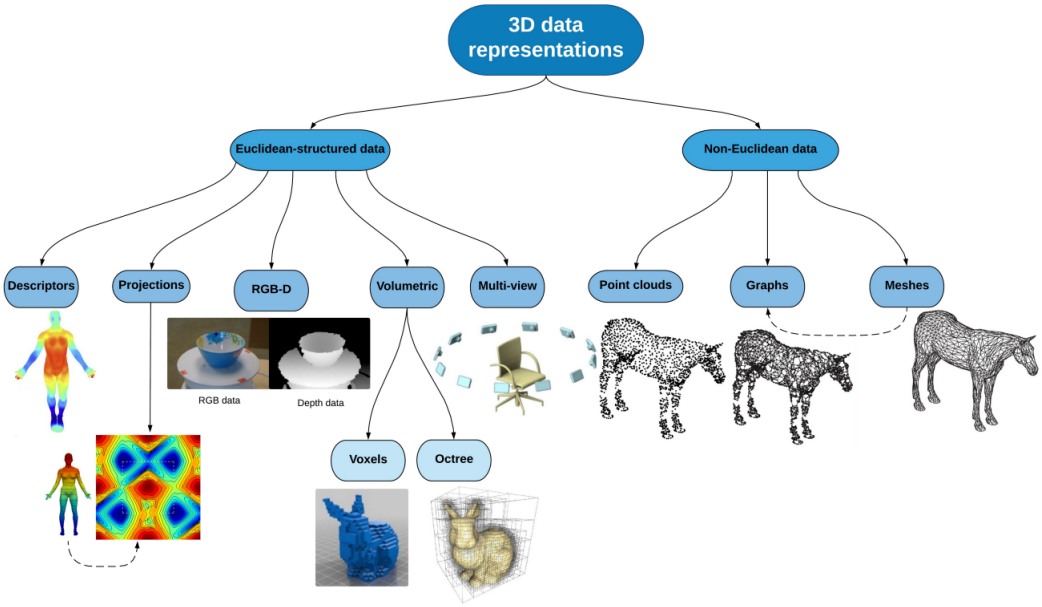


FIGURE 2.6: 3D data representation as described by Ahmed et al. [63], presenting the Euclidean and Non-Euclidean domain of data representation

Manifold learning is a dimensionality reduction technique, and it has two approaches: linear and non-linear [74]. Within the linear methods, we can mention Principal Component Analysis (PCA) and multidimensional scaling (MDS), which are two common statistical methods. For nonlinear multivariate data we can use methods like Isomap [75], local linear embedding [76], Laplacian eigenmaps [77], diffusion maps [78]. According to Izenman [74], nonlinear manifold learning creates "a low-dimensional representation of an unknown nonlinear manifold that is embedded in the high-dimensional space". In the low-dimensional embedding, the similar data points are closer to each other, and the definition of similarity between these points is defined differently for all the mentioned methods: Isomap uses geodesic distance, LLE

uses local reconstruction, diffusion connectivity is used in the case of diffusion maps, and the Laplacian graph is used in the case of Laplacian eigenmaps. These lower-dimensional characteristics can be introduced in clustering algorithms to assign each data point to a group. It is important to mention that all the non-linear manifold learning techniques are intrinsic shape descriptors because they learn the underlying geometry of data, independent of their embedding; meanwhile, PCA and MDS are extrinsic, because they have to be embedded in the Euclidean space, therefore, they are sensitive to global position, rotation, and scale.

Shape descriptors A 3D shape descriptor is a feature representation that encodes the geometric and spatial information of a 3D shape [79]. A good shape descriptor has to have high discriminative properties to be applicable in clustering algorithms that aim to group similar 3D objects. A global shape descriptor can encode information about the entire object geometry, and can be computed directly from the input [80], and local shape descriptors can describe information about points, faces, or different segments of the 3D shape, or as Bibissi et al. [79] defined, they encode the proximity of a point into a feature vector. Rostami et al. [80] pointed out that global shape descriptors are mainly used in shape recognition, classification, and shape retrieval, while the local descriptors were used for segmentation, labeling, point-to-point correspondence, and shape matching. They also mentioned that global descriptors can be extracted from all types of input data and can be implemented in a larger variety of learning methods.

Point cloud-based methods Point clouds are spatial representations of 3D objects that approximate their geometry in an unstructured way [81]. Although point clouds do not contain surface information about the 3D object,

they still represent the most widely used 3D data form in reconstruction and classification tasks due to their relatively easy acquisition. PointNet [82] is the first architecture that directly processes point clouds and extracts features for classification tasks by learning spatial encoding of each point and aggregating individual point features to a global point cloud signature. Qi et al. [83] state that it is important to also know the local structure of points, which PointNet does not exploit; therefore, they have updated the algorithm so that it would process points "Hierarchically sampled in a metric space" and introduce PointNet++. According to Su et al. [30], PointNet is not designed to observe local information; it cannot describe detailed structural information. They also state that the two mentioned models cannot easily describe local regions in 3D point clouds. The authors of [30] propose a deep learning framework for disentangling body type and pose information from 3D point clouds by learning interpretable latent representations of the data in an autoencoder structure, proving that the derived latent features are able to describe body type. Armstrong et al. [29] propose an unsupervised approach to partition the latent space features of 3D point clouds obtained from a VAE structure and disentangle body type and pose just as in [30]. They describe the intrinsic shape (geometric shape) of point clouds with the Laplace-Beltrami operator and provide a shape descriptor that is invariant to pose changes. Their algorithm can identify the shape of individuals in different poses, without the need for labelled data.

Polygonal mesh-based methods Polygonal meshes are a collection of vertices, edges, and faces used to define the shape and contour of a 3D object [84]. Compared to point clouds and graphs, meshes contain information about the object's surface; therefore, using meshes as an input in the deep learning algorithm could preserve more information about the shape of the

3D object. As [85] stated, meshes can also encode connectivity information, thus forming a more comprehensive representation of the underlying surface. Among the deep learning methods that use meshes as input, we can mention the method proposed by Gao et al. [62], who proposed a Graph Convolutional Neural Network method, in which they introduced a feature tensor containing the face adjacency indexes (3 for each face), the XYZ coordinates of the center point of each face and the vectors from the center point to each of the three vertices of a triangle face. They tested their algorithm on ModelNet40 [86], which is a clean collection of 3D CAD models for 662 object categories specifically prepared for deep learning. With their method, they have achieved a 91% classification accuracy and obtained shape descriptors with rich features. Another method that uses meshes as input proposes an algorithm called MeshNet [61] that takes the features of each face, similar to the previous work (Center, Corner, Neighbor index), adds to the list the normal of each face, and creates a list of features, introduced as an input in a Mesh convolution neural network. They also tested their algorithm on ModelNet40 and achieved 91.9% of classification accuracy. Their descriptor contains both spatial and structural features of each face, and the algorithm's ability to process faces individually solves the complexity of mesh-based non-Euclidean data. The third method we reviewed is MeshCNN [85], a Convolutional Neural Network specifically designed for meshes. It is known that CNN structures work very successfully on 2D images, where the pixels are in an ordered grid structure. The issue of mesh irregularity has been resolved by Hancock et al. [85], on which previously CNNs were not applicable, by treating the edges as pixels, for which they have designed a convolution and pooling operator. In their work, they mention that pooling downsamples the number of features in the network by eliminating less informative features. Compared to the other two methods mentioned [62], [61], this algorithm takes

input edge features instead of face features, namely the two edge-length ratios, the dihedral angle, and the two inner angles for each face. The method could reach 98.6% classification accuracy on the SHREC 30 dataset. The final deep learning method is called SubdivNet [87], which takes as input closed 2-manifold triangle meshes with subdivision sequence connectivity, extracts a 13-dimensional vector (7-d shape descriptor: the face area, the three interior angles of the triangle, and the inner products of the face normal with the three vertex normals; 6-d pose descriptor: position of the face center and the face normal). They have designed a mesh convolution operator that can support variable kernel size, dilation, and stride, just as in the image domain, as well as a mesh pooling and upsampling operator. This is important because the preserved feature vectors can be introduced in successful 2D CNN algorithms such as ResNet50 [88] or Deeplab [89]. The advantage of both MeshCNN and SubdivNet is that they work with relative features, making them invariant to rotation, translation, and uniform scaling [85]. The above-presented deep learning algorithms are mainly supervision-based, meaning their database has labels assigned to the objects in question.

2.3.4 3D shape classification

Li et al. [15] have analysed the shape and size of the female torso to classify the upper body in different categories. As they have described, this classification is necessary to improve the design and fit of clothing products. They have taken anthropometric measurements from a large-scale anthropometric survey, to which they have applied Principal component analysis to identify the most important size-related variables. They have also used 3D body scans of the same subjects and performed 3D Principal component analysis, from which they could also point out that the height, similarly to the 1D

PCA, is the highest influential component throughout the data and that it should be neglected in geometric shape analysis. In their findings, they have shown proof of the existence of 9 shape categories that are mainly influenced by two shape-related and one size-related factor. As a part of their methodology, they have computed a mean 3D shape for each of the categories. In the presented paper, they did not take the body height as an anthropometrical variable in their study, as this variable is shown to be influential for sizing; therefore, it is only relevant for defining product sizing and not for shape analysis. They also proved that the lower rank chosen Principal Components are related to the true shape difference. They have also concluded that geometric morphometry has a weak correlation to traditional anthropometric measurements and that it would be useful to relate the achieved body classification to these measurements.

2.3.5 Principal Component analysis (PCA)

When a 3D scan is finished (processed), the resulting surface is a triangulated mesh that has point-to-point correspondence [90]. Still, it has a very dense vertex representation, above 10000 points, which means that comparing and aligning two scans in the Euclidean space would be computationally expensive and shape analysis cannot be directly applied [28], therefore many 3D surface anthropometrical studies [28], [90]–[96] applied Principal Component Analysis (PCA) to reduce the dimensionality and complexity of the data and to extract dominant components of shape. The author of [28] mentioned that one of the biggest challenges in "Applying PCA to 3D anthropometric data is to bring all the models in correspondence to each other"; the importance of aligning the 3D body scans before performing a PCA is also mentioned in [90]. Corresponding to each other means that every 3D shape has

to have the same number of points, and every point in one shape has to have a matching point in another shape. In [28], they achieved this correspondence by transforming the 3D mesh to a voxel-based volumetric representation with fixed dimensions, calculating the distance between the voxel and its nearest point on the body surface, and comparing these distances between the 3D body models. In [90], to align the body scans, they have performed a Generalized Procrustes Analysis (GPA), which consists of the creation of a mean shape to which all scans are aligned iteratively until they converge. The authors of [92] have shown evidence that by segmenting the body parts and performing PCA on them separately, the variation becomes higher than in the case of the full body. For example, they performed a PCA on the leg and the first principal component described the variation of the leg's height, the next four principal components described the straightness of the leg, the pose along the left-right direction, the bending extent, and the scale of the leg.

2.3.6 Unsupervised Classification methods

Clustering analysis is an unsupervised learning method [97] that partitions the data without the existence of labels [98], and it aims to discover latent knowledge of the data [99]. The existing clustering algorithms fall into different categories: partitioning, density-based, hierarchical, graph-based [99]. These algorithms aim to group data with similar characteristics [98] and to achieve higher intra-cluster and lower inter-cluster similarities. These data are usually multidimensional, and they are classified based on a predefined similarity criterion [97]. It can also be a goal to project the multidimensional data in a lower space in 2D or 3D with the purpose of visualization of the clusters [100].

K-means clustering

The K-means clustering is a widely used and acknowledged clustering algorithm [98], [101], that falls into the partitioning category [97]. The objective of this clustering method is to partition the given dataset into k distinct groups, k being defined by the user. Each cluster is represented by a mean value, also known as the centroid [99]. It clusters data into groups with equal variance by minimizing inertia or within-cluster sum-of-squares [100]. Each data point is assigned to the closest centroid, using the Euclidean distance most of the time as a similarity metric [102]. It is considered an efficient and easily implementable algorithm with low computational complexity [98]. One of the limitations of the K-means algorithm is that it needs the number of clusters to be defined by the user, which is a difficult task, especially with large datasets and it also tends to be sensitive to defining the cluster centers, because the initial centers are often randomly assigned [98], causing a large number of iterations and often a convergence to a local minima [99], instead of global minima. It is designed to handle convex-shaped, compact, and well-separated data [99], and for this reason, it does not handle well overlapping clusters [98]. It is also known to be influenced by outliers [99]. To improve the performance of the K-means algorithm, Fahim et al. [99] suggested using DBSCAN clustering, which could be a preprocessing step for K-means, as this algorithm does not require the initial definition of the cluster numbers, finding the center of groups with very high density. Ghazal et al. [102] state that the distance metrics used to calculate data similarities play an essential role in the improvement of the algorithm. They suggest that, besides the often-used Euclidean distance, the user could experiment with the Manhattan distance and Minkowski distance.

DB SCAN clustering

The Density-Based Spatial Clustering of Applications with Noise (DBSCAN), just as its name says, is a density-based clustering technique, and it is a widely popular algorithm [103]. It is based on the idea that a cluster is a region in a data-space with a very high density of data, separated by a sparser region [104]. This algorithm can identify arbitrarily shaped clusters (unlike K-means or hierarchical clustering [104]), and it can identify noise data as well [105]. One of the key advantages of DBSCAN is that there is no need to pre-define the number of clusters; the number of clusters is based on the density structure of the data and other parameters of the algorithm [106]. The two main parameters that DBSCAN relies on are the **Epsilon (ϵ)**, which defines the maximum radius of a neighborhood around a point [106] and **MinPts**, which defines the minimum number of data points that need to be identified in order to form a cluster. Bushra et al. [104] and Al-Batah et al. [103] state that a distance less than or equal to ϵ is considered a neighborhood. It is therefore crucial to correctly determine the value of ϵ, because if it is too large, then it would merge multiple clusters, and on the contrary, if it is too small, it would identify too many data points as outliers [103]. According to Bushra et al. [104], one of the limitations of the DBSCAN algorithm is handling high-dimensional complex data, especially when the data is sparse, referring to this problem as "curse of dimensionality". Singh et al. [106] highlight that in case the clusters are of varying density, the algorithm has a hard time finding the correct clusters, as it works best when the clusters are equally dense.

Spectral Clustering

Spectral clustering is a graph theory-based method for partitioning data, especially effective for non-convex structures [107]. It has become one of the most popular clustering algorithms because it outperforms traditional clustering algorithms, such as K-means [108].

Each data point is represented as a vertex in the graph, and the weight of each connecting edge represents the similarity between the points [107]. As Ding et al. [107] describe, the objective of spectral clustering is to divide the graph into sub-graphs in a way that the within-subgroup connections should be maximized and the between-subgroup connections should be minimized, and that the group of points within each sub-graph constitutes a cluster. The process of implementing spectral clustering involves several key steps, and these key steps are described in the studies of von Luxburg [109] [110]:

- Construction of the similarity graph where each data point is represented as a node in a graph, and the edges between nodes represent the similarity between the corresponding data points.
- Computation of the Laplacian matrix, which is a matrix that captures the relationship between the nodes in the graph
- Computation of the eigenvectors and eigenvalues of the Laplacian matrix.
- Selection of a subset of the eigenvectors corresponding to the smallest eigenvalues, which are called "spectral components".
- Application of a clustering algorithm, such as K-means, to the data points based on their spectral components.

Construction of the similarity graph One important step before implementing the spectral clustering algorithm is to compute the similarity graph.

According to Benkaouz et al. [111], a K-nearest neighbors algorithm provides each data point with its k most similar data points, defined by a similarity metric, building a KNN graph where each node is connected with a weighted edge to its k most similar nodes. Von Luxburg [109] states that the main goal of the similarity graph is to construct a model of the local neighborhood relationships between the data points. Spectral clustering can be sensitive to changes in the similarity graph and to the choice of its parameters. Initializing the parameters of the similarity matrix is a great challenge and there has not been yet identified a sure method, that would give the best results without any trial.

Choice of Laplacian matrix The second step of spectral clustering is the computation of the Laplacian matrix, using as input the weighted adjacency matrix. There have been many discussions on the topic of choosing an unnormalized or a normalized Laplacian matrix to compute the eigen components in the papers of [112], and [113], who presented algorithms for normalized spectral clustering and [109], who provides a tutorial for the two previous methods and also presents the concept of unnormalized spectral clustering. Von Luxburg, in [110], concluded that the normalized clustering algorithm should be a preferred method in practical applications. She also mentions in [109] that the Random Walk Laplacian matrix has more advantages when it comes to defining clusters.

The basic idea behind spectral clustering is to use the eigenvectors of the graph Laplacian matrix to embed the data points into a lower-dimensional space, where they can be clustered using a standard clustering algorithm, such as K-means.

Cluster quality evaluation

Spectral clustering is sensitive to initiation, meaning that there are several elements in the algorithm that need to be decided before obtaining a final data partition. It involves the computation of the similarity matrix and the Laplacian matrix, which also involves the calculation of the eigenvalues and eigenvectors, and finally, the application of a K-means clustering algorithm on a spectral embedding. The number of neighbors used to determine the connectivity of the similarity graph and the number of clusters that create homogeneous groups are hard to determine and represent a difficult choice, as scientists have not yet found a logical interaction between the two [109]. To find the correct parameters, performance evaluation metrics could be used to determine the clustering quality at specific values of neighbors and clusters. One way to evaluate the performance of spectral clustering is to use cluster validity indices, which are quantitative measures used to assess cluster compactness, separation, or cluster stability. Many existing methods could be applied to spectral clustering to determine the optimal number of clusters.

According to Rousseeuw [114], the Silhouette is a graphical representation of the predicted clusters by a classification algorithm, based on the comparison of the tightness and separation of each cluster. In his paper, he proves that this partitioning technique is able to show which object lies well within their cluster and which ones are between clusters. He also mentions that the average silhouette score could be used to select an accurate number of clusters. Rousseeuw points out that to construct the silhouettes, two things are needed: the partition, determined by the clustering algorithm, and the collection of all proximities between objects (ex, in the Euclidean space).

Another promising cluster separation measure was proposed by David L. Davies and Donald W. Bouldin [115] who used an index to evaluate the

quality of clustering results. This clustering solution is based on the within-cluster similarity and between-cluster dissimilarity, computed by calculating the ratio of the sum of distances between each cluster's centroid and the closest cluster's centroid, to the average distance between each point in a cluster and its centroid. As stated by these two researchers, the minimization of this parameter could indicate the natural partition of the data sets. The index ranges from 0 to infinity, where 0 signifies a perfect partition of data, and the higher this number gets, the worse the clustering results are.

The third method that we have reviewed with the purpose of determining the optimal number of clusters is based on the Cluster Quality Index (CQI) introduced by T. Calinski and J. Harabasz [116]. The CQI is calculated as a ratio of the between-cluster variance to the within-cluster variance, and the optimal number of clusters is given at the maximum value of the CQI within a range of k

The study of von Luxburg [109] presents the eigen gap heuristic tool, which is specifically designed to determine the number of clusters in spectral clustering. The idea behind the eigen gap is to plot the smallest eigenvalues defined by the Laplacian matrix and look for the point where there is a significant gap between adjacent eigenvalues.

The Elbow method is an evaluation method that is used to detect the optimal number of clusters, based on the observation that increasing the number of clusters reduces the sum of within-cluster variance of each cluster, as explained in [117]. The optimal number of clusters is chosen at the elbow point (the turning point on the curve), as increasing the number of clusters beyond this point does not improve the clustering results.

Ensemble feature learning Classic ensemble learning methods directly use the labels obtained from different clustering of the same data to obtain a more

robust classification, but this way they neglect the intrinsic data structures that, for example, a Laplacian matrix could exploit. Li et al. [118] have introduced a new ensemble learning method that is applicable in the case of Spectral clustering. The key idea behind ELSC is the implicit combination of the Laplacian graphs obtained from base spectral clustering algorithms. The input in this algorithm, therefore, will be the n Laplacian matrices that will be summed to form a consensus Laplacian matrix from which a final consensus embedding could be calculated and used as input for K-means.

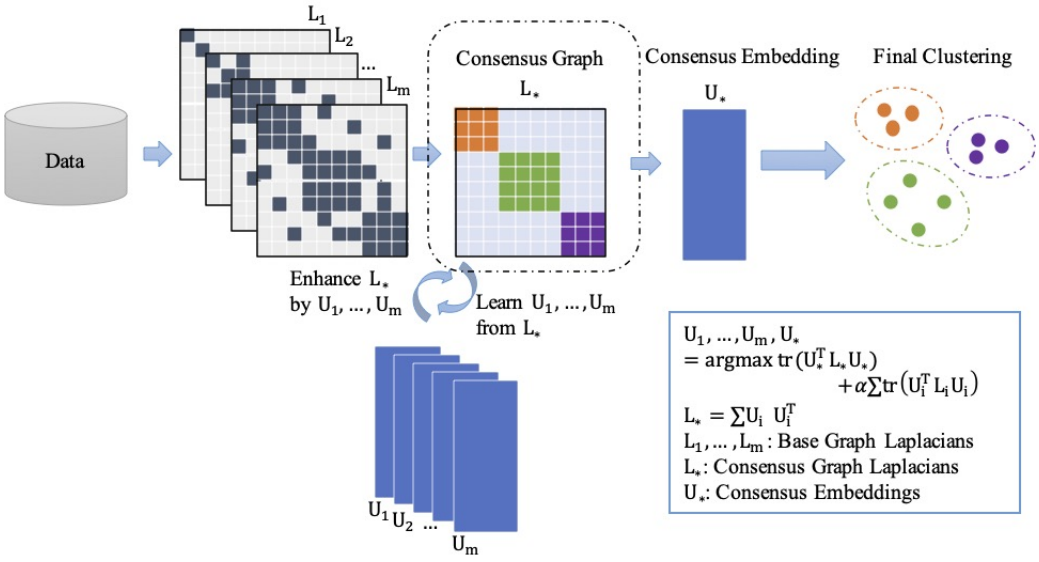


FIGURE 2.7: Ensamble learning for spectral clustering[118]

2.3.7 Deep clustering

Deep clustering is a type of unsupervised learning method that leverages deep neural networks to group data in distinct clusters without the need for ground truth labels, often transforming higher-dimensional data into a low-dimensional representation or feature space [119]. Wei et al. [120] defined deep clustering as an enhancement of traditional clustering analysis, through which one can acquire a high-level feature representation of data by

autonomously learning a feature representation, capturing data structures more effectively.

Deep Neural Network-based clustering Deep Neural Networks are fundamental neural network models that typically comprise an input layer, a hidden layer, and an output layer, and they can take various forms, like Fully connected Neural Networks, Convolutional neural networks, Deep Belief Networks, or Residual Networks [120].

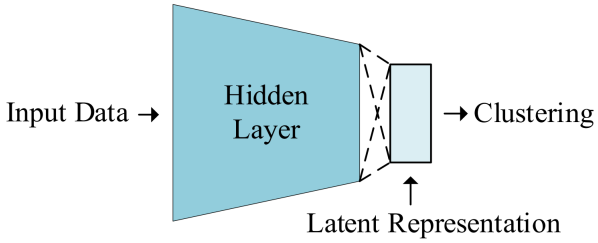


FIGURE 2.8: General framework of DNN-based clustering as presented by Wei et al. [120]

Autoencoder based clustering An Autoencoder architecture comprises an encoder layer, an embedding layer or bottleneck space, and a decoder layer, and it works by mapping the input layer into a latent space, a lower-dimensional form of the data, and by reconstructing the extracted features into the original data form [120].

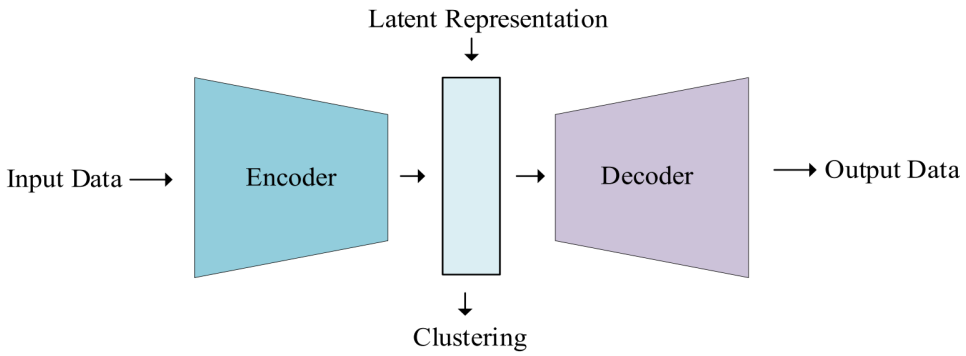


FIGURE 2.9: General framework of AE-based clustering as presented by Wei et al. [120]

Explainable AI In medical diagnosis and process optimization, the explainability and transparency of deep neural networks are crucial [121]. The author of this study specifies that the output of such a network can not be explained in any way. In [122], it is stated that the complexity of neural networks prevents users from finding a reasonable explanation for a prediction. The concept of explainable artificial intelligence was first introduced in 2015 by DARPA [123], and the goal of this project was to create new learning techniques that allow users to understand and trust AI systems. The user of such models needs to understand the logic that the AI system follows to give a prediction. The notion of black-box arises in the context of artificial intelligence because, as users, we can observe the input that goes into the algorithm of a neural network, and we can also observe the output, called a prediction, but whatever happens between these two layers is unknown to both the end user and the developer. Explainable AI in the context of Convolutional Neural Networks has already been introduced, but this concept is still not widely adopted. There are two main categories of XAI methods used in CNNs: one that interprets the decision of the CNN and the other that interprets the architecture of such an algorithm [124]. In the first case, the XAI highlights those parts of the input that led to the decision; in the second case, the XAI analyzes the behavior of the network layers.

Anomaly detection Anomaly detection is a critical part of machine learning which focuses on the detection of data samples that are unusual or abnormal [125] and it is a widely applied method in different scientific sectors such as industrial process monitoring [125], [126], [127], failure prevention [128], fraud detection [129], [130], medical diagnosis on image data [131], security screening [132], network intrusion detection [133], detection of unusual device activity in IoT [134], [135]. Anomaly detection encompasses a wide

range of methods from classical machine learning techniques to modern, deep learning based methods. From the classical methods used for anomaly detection, we can enlist the Support Vector Data Description (SVDD) and One-Class Support Vector Machines (OCSVM), which use a hypersphere or hyperplane, or decision boundary to enclose a dataset, identifying as anomalous all the samples that fall out of this range. These are methods that are most used in anomaly detection [135], but they require a significant memory usage and are computationally expensive when the datasets are large and complex [126]. Accurate models with complex decision boundaries that need large sets of real data often fall short due to memory usage. Isolation Forest (IF) is another classical, very popular approach to anomaly detection, based on which anomalies are considered as a few data points with distinct features that are easy to isolate. They can fail in detecting hard anomalies in data that are high-dimensional and non-linearly separable, which is an issue that contributes to false anomaly assignment [130]. Researchers have proposed various improvements to these classical anomaly detection methods. Zhang et al. [125] proposed an improved version of SVDD by integrating a deep feature extraction, preserving the structure of the data (Deep Structure Preservation SVDD). For an effective feature extraction, they enhanced the optimization process by simultaneously considering both the hypersphere volume minimization and the network reconstruction error minimization. Their experimental results show a better anomaly detection performance compared to other deep SVDD approaches.

Pang et al [127] proposed a hybrid algorithm that incorporates vector quantization in a one-class support vector machine (VQ-OCSVM), which extracts the normal data distribution and maps it in a higher-dimensional feature space, where the OCSVM builds the classifier. With this method, they

can avoid the kernel parameter selection problem present in the classical version. In the case of complex data distribution, their method has a better generalization capacity due to the integration of generative and discriminative learning. Yang et al. [134] improved the abilities of OCSVM by combining it with Nyström and Gaussian mixture models that speed up prediction time, conserving the detection accuracy. Qiao et al. [135] improved the quarter-sphere-based OCSVM and combined it with a Deep Belief Network (DBN-IQSSVM) to process high-dimensional sensing data in an unsupervised manner and detect anomalies. Instead of training OCSVM traditionally, they introduce the idea of finding a Boundary Support Vector (BSV) during training, which makes their process computationally efficient and achieves higher accuracy than DBN-SOCSVM.

Xu et al [130] propose a deep Isolation Forest model that integrates causally initialized neural networks that can map the original data in a new random representation form, enabling a versatile data partition with more effective isolation of anomalies, outperforming state-of-the-art methods.

Zhang et al. [126] proposed a Memory augmented Adversal Autoencoder with a CNN-Transformer (CTMAANet), using the advantage of the last two for a richer feature extraction, maintaining intermediate features by suppressing the generalization, and defining anomalies with both the reconstructed image and its feature space. Their method outperformed the already existing CNN-based adversarial machine learning models.

Anomaly detection for 3D data For fine-grain geometry discrimination, 3D anomaly detection is crucial [136]. One of the challenges in this field is the lack of real-world 3D anomalous data, which hinders the development of 3D AD models [137]. There are only a few methods that leverage the potential of

3D information in anomaly detection, even though 3D understanding is fundamental to computer vision [138]. In the field of unsupervised anomaly detection, there are two main approaches: reconstruction-based methods and representation-based methods. The reconstruction-based methods aim to learn the underlying patterns and distribution of normal data, without the presence of anomalies. In the case of Autoencoder-based methods, which try to reconstruct the input object, the models learn the normal patterns, and when the object presents anomalies, the model will struggle to reconstruct it, leading to a higher reconstruction error [139]. IMRNet [136], proposed by Li et al., is a novel 3D point-cloud anomaly detection method with a Geometry-aware Point-cloud Sample module able to extract anomaly points. EasyNet [140] is an encoder-decoder architecture developed for 3D depth map reconstruction. Representation-based methods extract latent representations from 3D meshes using the encoder layer of an autoencoder architecture. A common technique is to build a memory bank that stores the latent features extracted from normal 3D mesh surfaces. Horowitz et al. [138] investigated the role of 3D information in anomaly detection and segmentation, identifying the rotation invariance as a key feature for a successful outcome. They proposed Back to the Feature (BTF), a method that combines classical, handcrafted, rotation-invariant 3D features (FPFH) with deep, color-based features (PatchCore) and achieved a ROCAUC of 99.3%, outperforming previous state of the art.

2.4 Contributions

Motivated by the limitations of the existing MCS sizing systems found in the state-of-the-art, which detail the lack of integration of shape-specific details in the design of Compression Stockings, this thesis proposes new approaches

to improve shape and size classification of human legs, thereby enhancing product design for the industry of MCS. The key contributions of this work are as follows:

1. A novel unsupervised anomaly detection framework (MeshDeepSVDD), that integrates the Fully Convolutional Mesh Autoencoder (FCMA) with DeepSVDD for 3D mesh processing, outperforming the current state-of-the-art 3D anomaly detection models in the MulSen-AD dataset.

2. An anatomy-specific intrinsic 3D shape descriptor database and a topologically invariant leg mesh database, which are simplified and non-complex representations of the human leg, overcoming the complex nature of 3D data, usable for deep learning tasks.

3. A new framework for product design that answers the limitations of current product sizing methods, proposing a sizing logic for different leg categories, based on which a recommendation tool could direct the user to adapt a parametric leg to the optimal size and shape, unlocking the possibility of 3D compression stocking design with a graduated pressure configuration, adapted to 3D morphology of the patient.

Chapter 3

Exploration of Lower Limb Morphological Classes Using Classical Unsupervised Techniques Across Multiple Shape Descriptors

3.1 Introduction

The structure of the human body has been studied since the ancient times, body types have been first introduced by the Greek Hippocrates around 400 B.C., Leonardo da Vinci created anatomical sketches of the human body in the renaissance period, contributing to the anatomical knowledge, Andreas Vesalius (16th century) is considered as the scientist who raised anatomy from "facts and fiction to an exact science" [141]. Both of the latter contributed to the profound understanding of human anatomy, including the outer silhouette. Sheldon et al. [142] classified the human form into three morphotypes: mesomorph, endomorph, and ectomorph. Anthropometry has always been the tool of scientists to quantify the shape and size of the body. To replace manual measurement tools such as tapes and calipers, with

which taking measurements took a longer time and less precision, 3D scanners have been introduced, which can take hundreds of anthropometric measures in seconds, with a higher precision than ever. Since then, 3D surface anthropometry has become the most common methodology to study the geometry and morphology of external human body tissues [143].

3D scanning technology has revolutionized anthropometric studies [144], because it allows, on the first hand, the automatic and immediate collection of predefined body measurements in a precise and effective way, reducing the possibility of human error and maintaining repeatability. On the other hand, it also allows for the collection of the 3D geometry of the human body in a way that the shape could be studied thoroughly. The technology of 3D scanning has evolved to a point where the post-processing operations, taking up a great amount of time, have been reduced and automated [64], removing the need for noise treatment and mesh cleanup; therefore, collecting 3D body models became a straightforward task. Nevertheless, these technologies allow the automatic collection of a large variety of data types [65] such as 3D models, 3D body landmarks, and anthropometric sections that can easily contribute to the geometric learning of morphological descriptors.

In this chapter, we are going to present the work related to our first research objective, which concentrates on the development and evaluation of existing unsupervised learning models with the purpose of extracting significant morphological groups. We present hereby 3 types of shape descriptors; one developed from simple anthropometric measurements of the lower limb, that the state-of-the-art entitles as 1D data or 1D shape descriptor; one developed from a volumetric 2D representation of circumferential measurements and their corresponding heights and finally a more complex 3D shape descriptor, that evokes certain anatomical concepts and landmarks of the lower limb, all used to identify rules in certain morphological groups and help us explain

why certain geometries go in specific clusters. The results in this chapter help us understand the variability of the human leg and highlight the need for the development of a more inclusive sizing system for compression products.

3.2 Background and Literature Review

A broadly adapted solution for 3D surface analysis is PCA, which is a type of linear manifold learning method considered to be an extrinsic shape descriptor, as for the correct comparison of 3D shapes, they have to be embedded in the Euclidean space to avoid position, rotation, and scale sensitivity [74]. Ben et al. [28] mentioned that one of the biggest challenges in "Applying PCA to 3D anthropometric data is to bring all the models in correspondence to each other"; the importance of aligning the 3D body scans before performing a PCA is also mentioned in [90]. Corresponding to each other means that every 3D shape has to have the same number of points, and every point in one shape has to have a matching point in another shape. Numerous 3D surface anthropometrical studies [28], [90]–[96] applied this method to reduce the dimensionality and complexity of the data and to extract dominant components of shape. This statistical technique is used to simplify data without losing the most important variational information and to find patterns or structure in a given dataset. By identifying the dominant variables in each principal component, we can tell how much each variable influences the total variation in the lower-dimensional space. For instance, Azouz et al. [145] in their 3D male body shape analysis have identified that weight is the first and most varying component, accounting for 33.86% of the total variations, while the posture is the second most variable factor, representing 15.11% of the total variations. This analysis made it possible to cluster their data into three groups, which they have compared to Sheldon's mesomorph, ectomorph,

and endomorph body shapes, but in a more quantitative manner. Xi et al. [92] proved that body segmentation followed by PCA can give more reliable results, and described that in the case of the leg, the first and most variable component was the leg height, followed by the straightness of the leg, pose along left and right directions, bending extent, and the scale of the leg. Another study that used PCA for female torso classification was conducted by Li et al. [27] also basing their analysis on the first five principal components. Hamad et al. [68] used 3D shape descriptors in the form of geodesic distances between anthropometric landmarks on the female torso and identified 3 main body morphologies through a two-level clustering procedure, where they have combined the power of Self Organizing Maps and K-means. An interesting classification approach was presented by Liu et al. [146], who used 3 shape describing parameters according to which the shape of the leg of a Chinese population can be categorized into three lower leg shapes and two upper thigh shapes.

3.3 Definition and extraction of morphological shape descriptors

The main objective of this chapter is to evaluate the lower limb from an anthropometric point of view. In this study, we have conducted two 3D anthropometric measurement campaigns with two different 3D body scanners.

3.3.1 Data acquisition and post-processing

First measurement campaign The first measurement campaign was conducted with the Size Stream SS20, a 3D body scanner that uses infrared

depth sensors, with a non-radiant technology as the emitted infrared is low-intensity. The precision of this scanner is +/- 5mm circumferential accuracy. Data has been collected in conformity with the General Data Protection Regulation [147]. In this first measurement campaign, we have collected 127 3D body scans of 85 women and 49 men, aged between 18 and 65. One of the disadvantages of this scanner was that, although it allowed automatic measurement of 240 body measurements, it did not allow either the extraction of anthropometric points (as the precision does not allow the detection of physical markers) or the measurement of multiple leg heights and circumferences. As in this study, we wanted to precisely measure multiple leg circumferences, as it has been described in multiple scientific sources for Lymphoedema assessment, we needed to develop a method that allowed us to collect 17 circumferential measurements on the length of the leg in CAD software. We defined the length of the leg as the distance between the lateral malleolus and the crotch point. As both of these points are relatively easy to detect with an approaching flat 3D surface, we could ensure the reliability and accuracy of our method. Figure 3.1 shows the 17 circumferential measurements and the corresponding segment height, calculated by dividing the length of the leg into 16 equal segments.

Second measurement campaign A second measurement campaign has been conducted in our research facility during which we have collected 3D human scans of 131 subjects, 74 of which are women (precisely 64 under 30 and 10 above the age of 30) and 57 men (50 under 30 and 7 above the age of 30). The position of the body is in a standard anthropometric standing position. The subjects have been asked to place 3D stickers on 10 anthropometric bony landmarks on their left legs. They have been instructed to palpate the bone

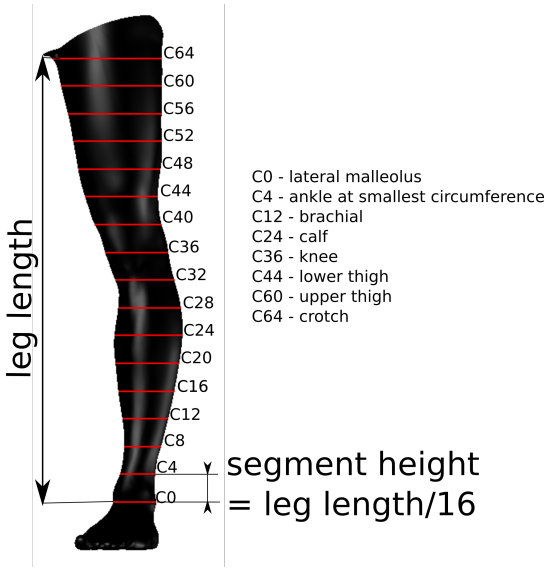


FIGURE 3.1: Circumference collection protocol, developed in CAD system. The segment height is equal to 1/16 of the leg length.

prominences of the following anthropometric landmarks, which are also illustrated in Figure 3.2.: Ilium, Anterior Superior Iliac Spine (ASIS), Great Trochanter, Popliteal Fossa (fat pad), Lateral Epicondyle, Patella (kneecap), Medial Epicondyle, Tibial Tuberosity, Lateral Malleolus (outer ankle bone), Medial Malleolus (inner ankle bone). This operation was necessary as the body scanner (VITUSbodyscan®) with a precision of +/- 1mm can detect the 3D stickers placed on the landmarks, therefore facilitating the data collection.

Using the 10 anthropometric landmarks, we were able to automatically collect the 17 circumferential measurements along the leg length, we could determine a variation of the Q-angle (angle measured between the planes determined by the ASIS – Patella and Patella – Tibial Tuberosity) and the angle recurvatum (angle measured between the planes determined by the Great Trochanter – Lateral Epicondyle and Lateral Epicondyle – Lateral Malleolus. These two angles are not measured in the same way as clinically determined (with a standing position where the legs are straight), as in our case, the legs

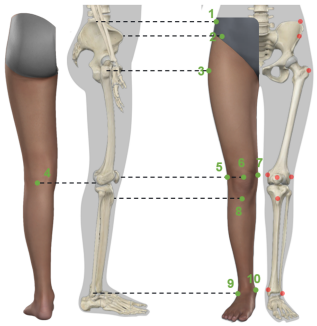
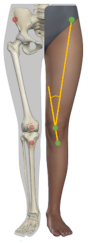


FIGURE 3.2: Anthropometric soft tissue landmarks on the leg: 1) Ilium, 2) ASIS, 3) Great Trochanter, 4) Popliteal Fossa, 5) Lateral Epicondyle, 6) Patella, 7) Medial Epicondyle, 8) Tibial Tuberosity, 9) Lateral Malleolus, 10) Medial Malleolus



(A) Q-angle measured between the plane described by the ASIS and Patella and the plane described by the Patella and Tibial Tuberosity



(B) Recurvatum angle between the plane by the Great Trochanter and Lateral Epicondyle and the plane by the Lateral Epicondyle and Lateral Malleolus

FIGURE 3.3: Lower Limb angles

are slightly spread, which results in a slightly different angle in comparison to a straight-legged posture. The Q angle, visible in Figure 3.3a, was taken into consideration because it can provide shape-related information, for example, detecting conditions such as bowed leg or knocked knee [146], [148]. The recurvatum angle is visible in Figure 3.3b, and it is considered for the same reason as the Q-angle.

Even if the clinical methods of measuring these two angles differ from our method, it can be viewed as reliable, as all subjects have been instructed to stand in the same position, placing the landmarks on their legs with high attention, and the measurements have been taken precisely by the software.

Other measurements the software took were the length of the femur, determined by the distance between the Great Trochanter and the Lateral Epicondyle, and the length of the tibia, determined by the distance between the Tibial Tuberosity and the medial malleolus. These two measurements provide us with proportion-related information. As the software is capable of automatically determining the position of the crotch, gluteal fold, and calf, we were able to take into consideration these anthropometric landmarks as well. In addition, we have programmed the software to detect the extreme points of each circumference in X+/- and Z+/- directions. We took the XYZ Cartesian coordinates of all the above-mentioned points and used them in future analysis.

3.3.2 Morphological shape descriptors

Shape descriptors are simplified representations of the 3D objects that contain geometric and topological characteristics of their shape and make the processing easier, at the same time allowing comparability among different 3D shapes [63]. A good shape descriptor has to have high discriminative properties to be applicable in clustering algorithms that aim to group similar 3D objects. In the following section, we will present 3 types of shape descriptors.

1D shape descriptor

Generally, in sizing studies, a classic way of defining shape is through Principal Component Analysis, which is applied to anthropometric measurements taken by either manual measurements or, more recently, by 3D body scanners. PCA can identify the most variable components within the database, and usually it is accompanied by a clustering analysis that identifies size

groups where the population of each cluster is showing high inter- and low intra-cluster similarities.

2D shape descriptor

The dataset is composed of 258 2D curves describing the volumetric growth of the lower limb at equal distances taken from the ankle until the crotch, representing the circumferential evolution of the leg through the 15 measurements between C4 and C60 illustrated in Figure3.1. A single curve is represented as:

$$\{(x_1, y_1), (x_2, y_2), \ldots, (x_{16}, y_{16})\}$$

where $x_i \in \mathbb{R}$ and $y_i \in \mathbb{R}$ denote the coordinates of the i^{th} point along the curve, and $i = 1, \ldots, 15$. The full dataset can be expressed as two matrices:

- $\mathbf{X} \in \mathbf{R}^{N \times 15}$: each row containing the x coordinates (equidistant heights in mm) for one curve.
- $\mathbf{Y} \in \mathbf{R}^{N \times 15}$: each row containing the corresponding y coordinates (circumferences in mm) for the same curve.

Where N is the total number of curves, here 258.

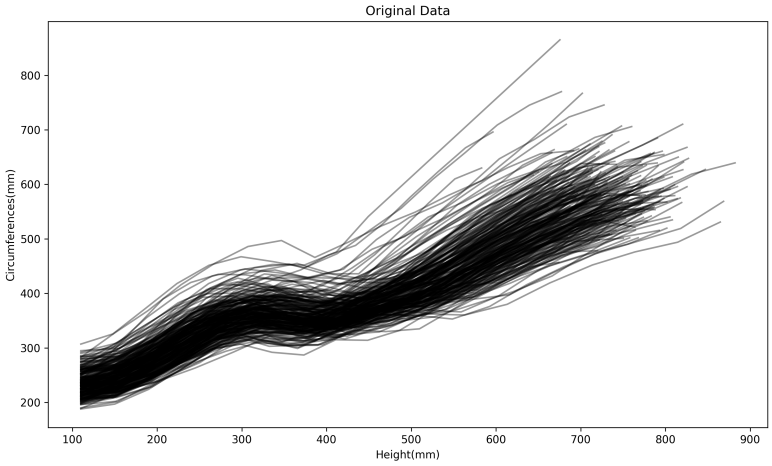


FIGURE 3.4: Visualisation of the 2D shape descriptor database in the original form, representing the curve evolutions of 258 subjects from C4 (ankle at the smallest girth and C60 (upper thigh

As can be visualized in Figure 3.4, the subjects in our database have different leg heights, which makes it difficult to compare them statistically. In order to render all the legs to the same height, it was necessary to normalize these curves to a mean height value, which in our case is target leg length = 701.25 mm. To normalize the curve database, we have applied a row-wise uniform scaling transformation to the above-described descriptors, using a fixed reference point. Given the input matrices $\mathbf{X}, \mathbf{Y} \in \mathbf{R}^{N\times 15}$ and a vector of scale factors, the transformation is defined as:

$$x' = x_f + (x - x_f) \cdot s, \quad y' = y_f + (y - y_f) \cdot s \tag{3.1}$$

Where:

- $(x_f, y_f) = (0, 0)$ is the fixed reference point in the origin,
- (x, y) are the original coordinates of a point on the curve
- s is the row specific scaling factor calculated with equation (3.2)

- (x', y') are the scaled coordinates

$$s = \frac{\text{target leg length}}{\text{original leg length}} \tag{3.2}$$

This transformation corresponds to a **uniform scaling centered at a fixed point** at the origin of the coordinate system, in this case, but the fixed point could be set at the ankle as well, a case which will be presented in Chapter 5. This approach is similar to the typical matrix-based scaling generally used in computer graphics, presented in [149], where they describe the following 3 operations that need to be performed in case of a fixed-point scaling:

- Translate the fixed point to the origin (T1)
- Scale the 2D object with respect to the origin (S)
- Translate the fixed point to its original position (T2)

This way, the transformation matrix will be given by the following equation:

$$M = T_2 \cdot S \cdot T_1$$

In matrix form, this will look like:

$$M = \begin{bmatrix} 1 & 0 & x_f \\ 0 & 1 & y_f \\ 0 & 0 & 1 \end{bmatrix} \cdot \begin{bmatrix} s & 0 & 0 \\ 0 & s & 0 \\ 0 & 0 & 1 \end{bmatrix} \cdot \begin{bmatrix} 1 & 0 & -x_f \\ 0 & 1 & -y_f \\ 0 & 0 & 1 \end{bmatrix}$$

Multiplying these matrices will give us the transformation matrix:

$$M = \begin{bmatrix} s & 0 & (1-s)x_f \\ 0 & s & (1-s)y_f \\ 0 & 0 & 1 \end{bmatrix}$$

The next step is to apply this transformation matrix to a point, we get:

$$\begin{bmatrix} x' \\ y' \\ 1 \end{bmatrix} = \begin{bmatrix} s & 0 & (1-s)x_f \\ 0 & s & (1-s)y_f \\ 0 & 0 & 1 \end{bmatrix} \cdot \begin{bmatrix} x \\ y \\ 1 \end{bmatrix}$$

Which simplifies to:

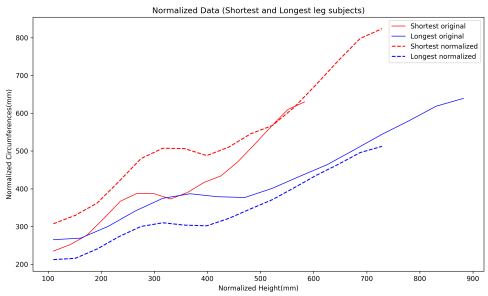
$$x' = sx + (1-s)x_f, \quad y' = sy + (1-s)y_f$$

Giving our applied formula:

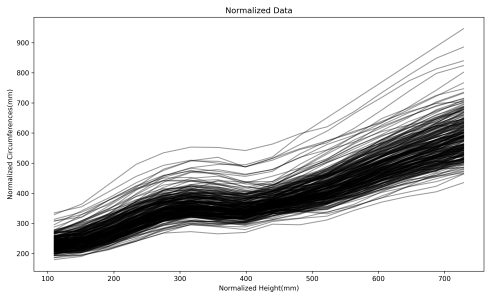
$$x' = x_f + (x - x_f) \cdot s, \quad y' = y_f + (y - y_f) \cdot s$$

This fixed point transformation is particularly important in the development of the adaptive morphotype, presented in Chapter 6.

Figure 3.5a illustrates the above-described transformation in the case of the shortest and longest leg in the database. As it could be observed, normalizing a shorter leg to an average length will increase the circumferential values, contrary to the longer leg's circumferences, which will become smaller, while maintaining proportionality and shape. The resulting normalized 2D descriptors can be visualised in Figure 3.5.



(A) Example of the shortest and longest leg circumference evolution before and after normalization



(B) Visualisation of the normalized 2D shape descriptor database with an average leg length of 701.25 mm.

FIGURE 3.5: Lower Limb angles

In the case of the 2D shape descriptor, we are interested in finding groups of legs that have similar circumferential evolution along the leg. To do that, we are opting to minimize the distances between these curves in a way that we wouldn't change the shape of the curve. For this, we have chosen an approach that superposes the first point (C4) of all the curves, translating it to 0 so that the rest of the values follow with the same transformation. For this we represent our data as a matrix $A \in \mathbf{R}^{2\times 15}$, where each row corresponds to a pair (x_i, y_i). To align each row such that the first component x_i is translated to a fixed target value $t \in \mathbf{R}$, we define the translation operation:

$$T(A)_{i,j} = A_{i,j} - A_{i,0} + t, \quad \text{for } i \in \{0, \ldots, 14\},\ j \in \{0, 1\}$$

Here, $A_{i,0}$ denotes the first component x_i of the i-th pair. The result is a new matrix $A' = T(A)$, where each row is translated such that its first entry equals the target value t, while preserving the relative offset between components:

$$A'_i = (t, y_i - x_t + t)$$

This affine transformation is a type of data alignment that preserves the internal structure of the curves by applying a shift to the data [150]. For the entire dataset, this transformation can be seen in Figure 3.6.

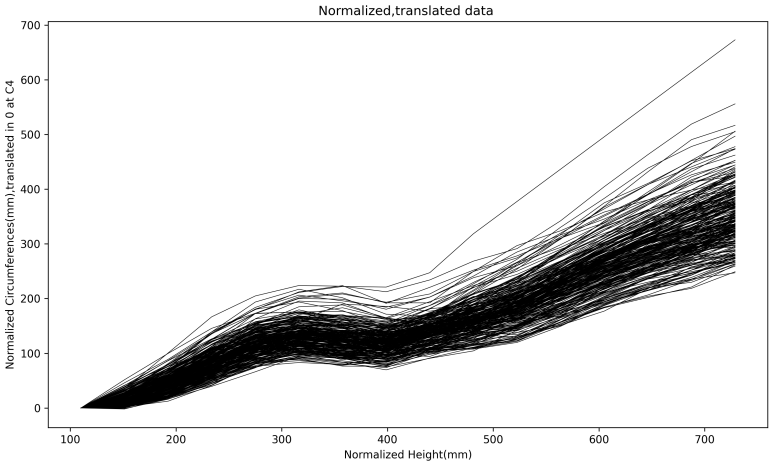
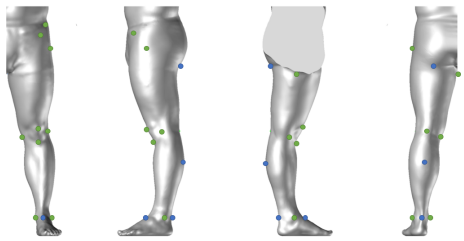


FIGURE 3.6: Visualisation of the 2D shape descriptor database translated in 0 at the ankle while preserving the relative offset of the curve

3D shape descriptor

Our challenge was to find a way to capture the shape differences of the leg using more than circumferential measurements. Our idea was to take longitudinal projections in different areas of the leg instead of cross sections. One of the challenges in doing so was to create a projectable polygon frame in a CAD software called DesignConcept 3D from Lectra, in which we can import one-by-one each scan, as well as the XYZ coordinates of the anthropometric points collected from Anthroscan®, and the frame would automatically adapt to the properties of the currently studied leg. In this section, the above-mentioned projection frame will be described, and the obtention of the output data from this software will be discussed. Figure 3.7a illustrates the 16 anthropometric points recovered from Anthroscan. The position of these points is manipulated with an Excel file that is linked to the predefined parameters of the Cartesian points in DC3D, meaning that if the subject changes, the position of the points changes as well. Figure 3.7b illustrates the extreme points on the 15 cross sections (17- crotch and ankle) in X+/- and



(A) Anthropometric landmarks exported from Antroscan® imported in Design-Concept® 3D



(B) Extreme points in X+/- and Z+/- direction on the 15 circumferences connected by a spline

FIGURE 3.7: Transfer of the Anthroscan landmarks in a CAD software

Z+/- direction. This figure also illustrates that if we connect longitudinally these points on the four sides of the leg, we can visualize a wavy display of the respective lines.

We wanted to achieve a level of linearity when we connected these points. Therefore, we chose four anthropometric points on each side of the leg and connected each adjacent point with a straight line. The goal was to align the extreme points that fall between two adjacent landmarks in Figure 3.8 following the rule of linear interpolation between two known points. We import the x, y, or z coordinates of the original extreme point (depending on which side of the leg the point is situated), then we calculate the third coordinate with the help of equation 3.3 (Figure 3.9). The resulting points, connected by a spline, can be seen in Figure 3.10a. Figure 3.10b illustrates the original spline (black) and the new spline (green).

$$x = x_1 + \frac{(y - y_1)}{(y_2 - y_1)} \times (x_2 - x_1) \tag{3.3}$$

The role of the new point configuration was to take the silhouette of the leg from 4 sides in a controlled way, considering as many anthropometric points as possible. The inner and outer silhouettes can also be compared to side seams on form-fitted pants. These silhouettes also represent the alignment

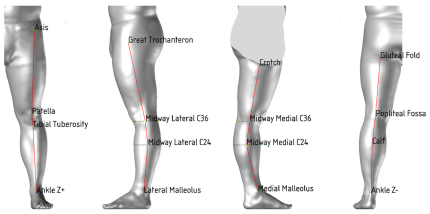


FIGURE 3.8: Chosen landmarks used as the "known points" in the linear interpolation equation 3.3

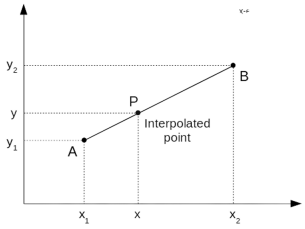
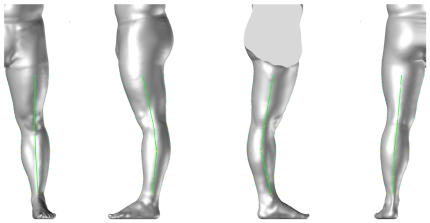


FIGURE 3.9: Linear interpolation between two known points, A, representing a landmark in Figure 3.8 and B, representing the adjacent pair of A; P is the extreme point that falls between A and B; each extreme point has two known coordinates, and the third is calculated using a formula

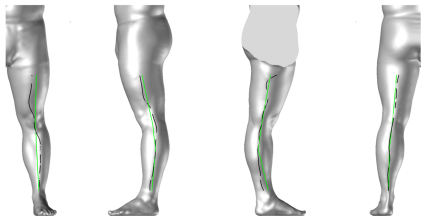
of the leg and the Q-angle, which is a comparative factor between individual legs.

This realignment operation was important from the point of view of comparability because if we leave the extreme point in its original state, this gives an uncontrolled spline for every subject, as the leg soft tissue is unique in every subject's case, making the original spline unusable.

After having the optimal position of the above-mentioned points, we continued by creating a framework on these points; in this way, if all our frame is connected to parametrized points, once the parameters change, the frame changes with them. The idea was to get the leg silhouettes from as many sides as possible. To create this frame, we chose 5 levels on the leg. 1st level is at the ankle, 2nd level is at level C12 (approximate bronchial level), 3rd level is a combination between level C24 (approximate calf level) and the Tibial



(A) New position of extreme points and the corresponding spline that connects them; in this state, the position of the points is not necessarily on the surface of the leg, as they have been shifted in X and Z directions

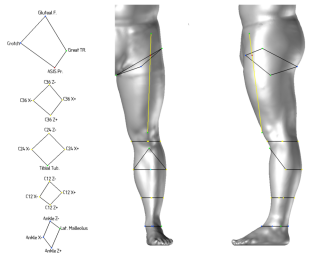


(B) Comparison between the original state of the extreme points and the new position of points that are not extreme points anymore but are positioned in a controlled way, same for every subject

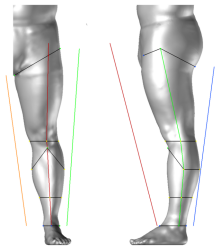
FIGURE 3.10: Result of the point interpolation method

Tuberosity, the 4th is at level C36 (approximate knee level) and the 5th is also a combination between the crotch, ASIS projection (Figure 3.11a: yellow line between ASIS and Patella, the red point on yellow line representing the intersection point of the plane between the crotch and Trochanter and the yellow line. This red point is projected on the surface of the leg. Great Trochanter and the Gluteal Fold. We connected the corresponding four points at each level, which can also be visualised in Figure 3.11a. With 3D transformations, we translated the points on the outside of the leg surface to stay on a line connecting the barycentre of the corresponding level and the translated point. This way, we have created contours connecting the translated points that will be projected on the surface of the leg. The first set of projection contours that create the silhouette of the leg on the four sides (left, front, right, back) can be visualized in Figure 3.11b and the resulting projected lines in Figure 3.11c These four projection contours are automatically adapting to the subject in study, once the XYZ coordinates are imported, meaning no further manual manipulation is needed.

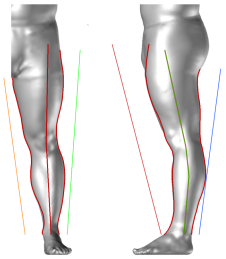
A second set of projection contours has been created to get the projection of



(A) The five levels on the leg serving as a basis for the projection frame; ASIS projection method



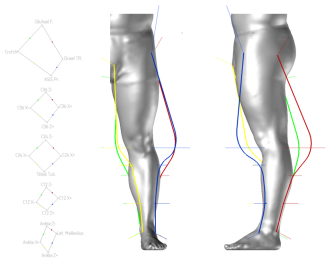
(B) Projection lines that give the silhouette from each side of the leg (left, front, right, back)



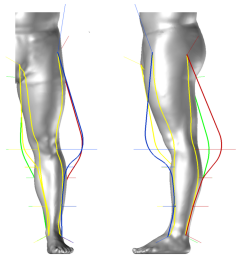
(C) Projected lines on the surface of the leg obtained with the help of the projection lines

FIGURE 3.11: Creation process of the first set of projection lines

the leg midway between the 4 side silhouettes. We repeated the same transformation of midway points visible on the right of Figure 3.12a to the outside of the leg and created projection contours in the form of a 3D spline. We have created a plane between levels C36 and C24 on each projection contour, representing the projection plane and serving as the director of projection. Because we are dealing with a 3D spline that is not placed in the same plane at every level (the ankle, bronchial, and crotch are not in the same plane as the knee and calf), the projection of these points would not fall in the correct place. To remediate this problem, we have introduced sliding points at the level of the crotch, bronchial, and ankle, which will approach the projection contour to the surface of the leg, thus assuring the correct position of projection. Because the knee and calf levels are always projected correctly (as they are in the same plane as the projection plane), we have receded the contour from the leg surface, so we can ensure that the contour stays outside of the

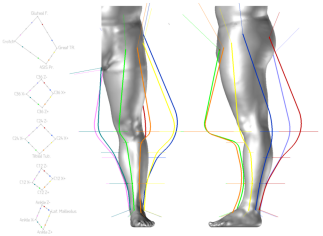


(A) Midway points between the silhouettes that are translated out of the leg

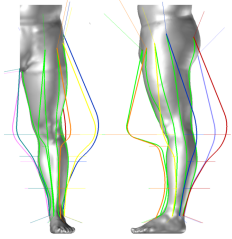


(B) Projection frame and projected contours midway between the silhouettes.

FIGURE 3.12: Creation process of the second set of projection lines



(A) Points between the silhouette points and mid-points creating the third set of projection frame



(B) Third set of projected lines, that, along with the others, divide the leg into 16 non-equal segments

FIGURE 3.13: Creation process of the third set of projected lines

leg surface at all levels. For the reason of the sliding points, before projecting the contours on the leg's surface, a manual operation of approaching these points had to be introduced.

Similarly, to the midway contours, we have created a third set of projection contours, this time targeting the mid portion between a red projection line (silhouette, Fig.13), adjacent to a yellow projection line (midway, Figure 3.12b). The process is identical to the midway projection contours, and the shape of the third set of points and projection contours can be visualized in Figure 3.13a. The resulting projected lines in Figure 3.13b divide the leg's circumference into 16 non-equal segments, and this characteristic of the projection is perfectly repeatable on any leg shape.

We limited the projected lines to three steps to define the leg portion that will serve as input in the classification algorithm (Figure 3.14). The first step is

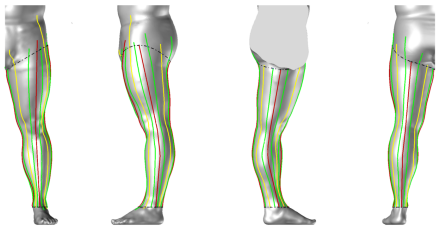


FIGURE 3.14: Limitation of the projected lines with planes and points

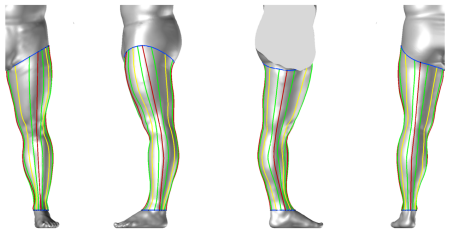


FIGURE 3.15: Creation process of the third set of projection lines

a limitation of the upper frontal barrier, which happens with the help of a plane defined between the crotch point and the greater trochanter; all lines falling between these two landmarks have been limited with this plane. The second step comprises the limitation of the lower leg barrier, which also happened with the help of a horizontal plane defined at the level of the Lateral Malleolus. At this step, all of the projection lines are limited. The third step is a limitation of the upper back-barrier, which happens with the help of sliding points placed on the projection lines to contour the shape of the buttocks. This zone is highly variable, with the highest difference between men and women; therefore, finding the position of these sliding points is a manual operation. When all lines have been limited, a contour spline has been interpolated through each endpoint, at both the upper and lower ends of the leg. The interpolation frame can be visualized in Figure 3.15.

It has to be noted that we have chosen to use this specific contouring of the upper barrier of the leg instead of simply cutting the leg with a horizontal plane at the crotch level because the lowest point of the glutes sometimes falls under the level of the crotch, especially in case of women, therefore we judged that this way the shape will also contain information about this particular area, conserving the shape more precisely.

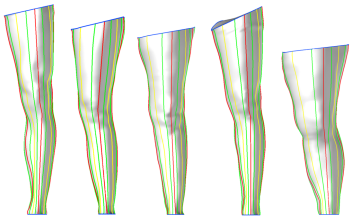


FIGURE 3.16: Projected lines on different shapes of legs.

These two files have been further modified in software called WeCov3r Studio [151], where we could extract the XYZ Cartesian coordinates of the polygons. In the case of the 16 projection lines, we extracted 50 equally distant points on each polygon. Figure 3.16 is an example of five different leg shapes with 16 projected lines that could be considered a simplified representation of the leg's shape.

3.3.3 Shape correspondence

3D Normalisation Goodall et al. [152] define the shape of a geometrical figure as the attributes that remain unchanged under certain transformations like translations, rotations, and uniform scaling. 3D normalization using Minimal Bounding Sphere (MBS) in combination with other and rigid transformations is a well-established approach in shape analysis and geometric morphometrics. The minimal bounding sphere is the smallest sphere that can enclose a set of points in a 3D space [67]. Multiple 3D anthropometric studies used the MBS to solve the scale differences of human bodies with varying heights [68], [66], and it is wildly used method in computer graphics as well [71]. Normalizing the size of the radius of a minimal bounding sphere can improve stability of the model against scaling [67], and it is important in the case of both intrinsic and extrinsic shape descriptors. Another requirement to determine differences between 3D objects is finding an optimal alignment.

Procrustes analysis is a rigid shape analysis that is used to find "the best fit between two or more landmarked shapes" [153]. The Iterative closest point is a global registration method, which computes the rigid transformation (rotation and translation) between two non-uniform point sets by determining the optimal translation and rotation to minimize the sum of squared errors [72].

On our 3D shape descriptor set, we first applied scaling with the Minimal bounding sphere. The xyz coordinates of the 3D shape descriptor are collected and processed as follows:

Point Cloud Data Processing Let a 3D point cloud $\mathcal{P} \subset \mathbb{R}^3$ be defined as:

$$\mathcal{P} = \{\mathbf{p}_i = (x_i, y_i, z_i) \in \mathbb{R}^3 \mid i = 1, \ldots, N\}$$

where N is the number of points in the cloud. The point cloud is read from an `.xyz` file and stored in matrix form:

$$\mathbf{P} = \begin{bmatrix} x_1 & y_1 & z_1 \\ x_2 & y_2 & z_2 \\ \vdots & \vdots & \vdots \\ x_N & y_N & z_N \end{bmatrix} \in \mathbb{R}^{N \times 3}$$

Computing the Farthest Points To constrain the bounding sphere, we identify the pair of points $(\mathbf{p}_i, \mathbf{p}_j)$ with the maximum Euclidean distance:

$$(\mathbf{p}_a, \mathbf{p}_b) = \arg \max_{i,j \in \{1,\ldots,N\}, i<j} \left\| \mathbf{p}_i - \mathbf{p}_j \right\|_2$$

Sphere Through Two Points Given the farthest points $\mathbf{p}_a$ and $\mathbf{p}_b$, the center $\mathbf{c}_0$ and radius r_0 of the sphere passing through them are computed as:

$$\mathbf{c}_0 = \frac{\mathbf{p}_a + \mathbf{p}_b}{2}, \quad r_0 = \frac{1}{2} \|\mathbf{p}_a - \mathbf{p}_b\|_2$$

Minimizing the Bounding Sphere To compute the minimum bounding sphere, we adopt an approach inspired by **Welzl's algorithm** [70], which is a recursive randomized method for determining the smallest enclosing ball of a point set in $\mathbb{R}^d$. However, in this study, we modify the classical approach to incorporate an explicit constraint: the resulting sphere must pass through the two farthest points in the point cloud.

Let the farthest points be $\mathbf{p}_a$ and $\mathbf{p}_b$, and let the initial guess for the center and radius be:

$$\mathbf{c}_0 = \frac{\mathbf{p}_a + \mathbf{p}_b}{2}, \quad r_0 = \frac{1}{2} \|\mathbf{p}_a - \mathbf{p}_b\|_2$$

To enforce the constraint while optimizing the bounding sphere, we formulate a loss function that penalizes points lying outside the sphere:

$$\min_{\mathbf{c}\in\mathbb{R}^3, r\geq 0} \sum_{i=1}^{N} \left[\max\left(0, \|\mathbf{p}_i - \mathbf{c}\|_2 - r\right)\right]^2$$

This constrained optimization problem is solved using the L-BFGS-B algorithm from the `scipy.optimize` module, which is suitable for bounded smooth optimization.

Scaling the Point Cloud To normalize the geometry, each point is scaled such that the enclosing sphere becomes a unit sphere centered at the origin:

$$\mathbf{p}'_i = \frac{\mathbf{p}_i - \mathbf{c}}{r}, \quad \forall i = 1, \ldots, N$$

Let the scaled point cloud be:

$$\mathcal{P}' = \{\mathbf{p}'_i \in \mathbb{R}^3 \mid i = 1, \ldots, N\}$$

so that

$$\|\mathbf{p}'_i\|_2 \leq 1$$



(A) Frontal view (B) Side view

FIGURE 3.17: Superposed minimal bounding spheres of the tallest (blue) and shortest (green) subject in the database



(A) Frontal view (B) Side view

FIGURE 3.18: Superposed minimal bounding spheres of the tallest (blue) and shortest (green) subject in the database after scaling the radius to 1

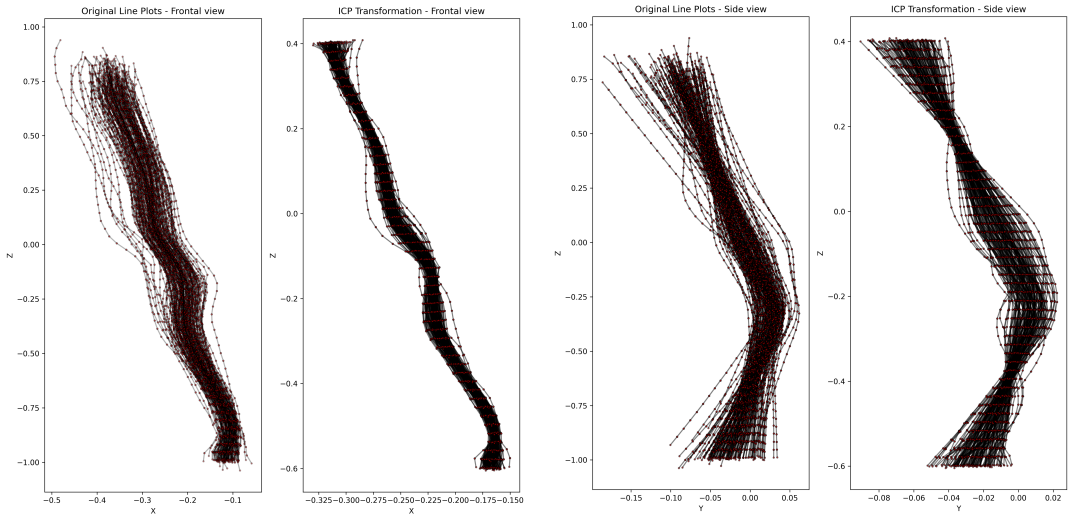
The ICP implementation from Open3D [154] was used to perform point cloud registration. The three states of 3D data are presented in Figure 3.19.



(A) 3D dataset raw state (B) 3D dataset after MBS (C) 3D dataset after ICP

FIGURE 3.19: 3D normalisation stages of the 3D shape descriptor dataset

The same ICP registration has been performed along with a uniform scaling on the individual 16 projection lines that we used in our classification algorithm. We illustrated this rigid 3D transformation in Figure 3.20, which presents the projection line, corresponding to the medial contour of the leg, passing through the crotch point, the medial epicondyle, mid calf, and medial malleolus. Figure 3.20a presents the curve in the frontal view (X-Z plane) and Figure 3.20b from the side view (Y-Z plane), illustrating the database before and after the ICP transformation.



(A) Frontal view (B) Side view

FIGURE 3.20: Projection line, corresponding to the medial contour of the leg, passing through the crotch point, the medial epicondyle, mid calf, and medial malleolus, illustrating the database before and after the ICP transformation and scaling



FIGURE 3.21: Visualization of the 16 projection lines of the entire dataset after the ICP transformation

The achieved 3D shape descriptors conserve the shape information even through multiple rigid transformations. Figure 3.21 illustrates the 16 projection lines of the entire dataset of 131 individuals.

3.4 Unsupervised learning from morphological data

3.4.1 Principal Component Analysis

To study the variance importance in our 1D dataset, we have used PCA. First of all, we wanted to identify the redundant data in our leg circumference set. To do so, we have run the algorithm on the 15 circumferential data, computed the correlation values between variables, as well as the cumulative explained variance of the first three principal components. According to Li et al. [15], the correlation coefficients between variables and principal component scores reveal how the variation of each feature correlates to the variation of each principal component. Figure 3.22 shows the Pearson correlation coefficients between all pairs of features in the form of a square matrix, where the values can range between -1 (perfect negative correlation) and +1

(perfect positive correlation), and the values close to 0 indicate no linear relationship. This correlation coefficient offers insight into the strength of the linear relationship between two variables [155]. Visualization of the hierarchical relationship was performed using the Seaborn Python library [156] clustermap function, which reordered the rows and columns, grouping together similar features. On this figure, first of all, we can observe three main feature groups: thigh, mid-leg, and lower leg features. We can see that the circumferential measurement of the thigh (C44 - CCr) is a highly correlated feature, ranging between 0.86-0.99, meaning that they grow and shrink together. The mid-leg features (C24 - C36) are closely related to each other, but we can also observe that they are closer in variance to the thigh features than to the lower-leg features (C4 - C20).

TABLE 3.1: Individual explained variance

	PC1 (%)	**PC2 (%)**	**PC3 (%)**
Full dataset with 16 circumferences	89.3	5.7	1.7
Reduced dataset with 6 circumferences	88.2	6.8	2.2

TABLE 3.2: Cumulative explained variance

	PC1 + PC2 (%)	**PC1 + PC2 + PC3 (%)**
Full dataset with 16 circumferences	95	96.7
Reduced dataset with 7 circumferences	95	97.2

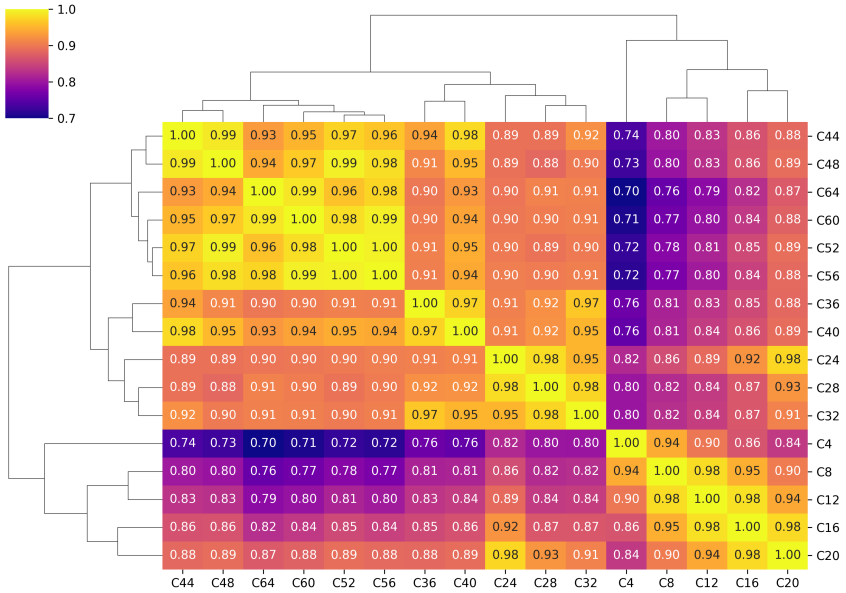
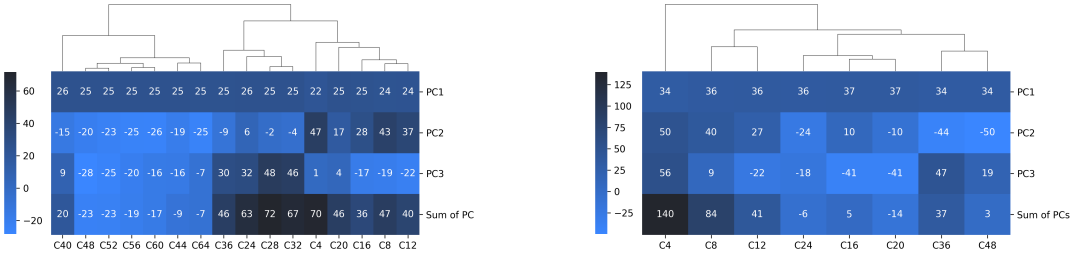


FIGURE 3.22: Correlation coefficients between variables arranged in a Clustermap to reveal the redundant data

Figure 3.23a shows the contribution of features to the first 3 principal components using the same cluster-based visualization. The pattern of the 3 regional linear links is observable in this case as well. We made the same observation about the first PC as Jolliffe [157], which was the overall size growth described by this PC. In case of the second principal component, we can highlight the variational contribution of lower-leg features, and in case of the third principal component, the same contribution could be described, but with the mid-leg features. Table 3.1 describes that most of the variation is described by the first PC (overall size growth), 89.3%, the second principal component (lower-leg features), 5.7%, and the third PC (mid-leg features), 1.7% of the total variations. From this information, we deduced that in order to keep the overall size variation, we should preserve at least 1 feature from the three zones. We could also deduce that the lower-leg features contribute more to the total variations than the mid-leg region features. To reduce the number of features and to also exclude the redundant data, we have selected

the variables that have the highest sum of contributions (visible in Figure 3.23a, 4th row). We took into consideration the hierarchical cluster groups and the specific zones in which the features are. The final set of circumferential variables is C4, C8, C12, C16, C20, C24, C36, C48, which corresponds to most of the lower leg area from ankle to calf, and the knee and mid thigh circumferences.



(A) Full circumferential database (B) Reduced circumferential database

FIGURE 3.23: Variational contributions of the first three PC, before and after the variable reduction

3.4.2 Unsupervised classification of multidimensional shape descriptors

Spectral clustering is a graph theory-based method for partitioning data, especially effective for non-convex structures [107]. It has become one of the most popular clustering algorithms, because it outperforms the traditional clustering algorithms such as K-Means [108].

Distance computation and Graph Construction To obtain the morphological groups, we applied the Spectral Clustering algorithm to group similar leg shapes using our 3 multidimensional shape descriptors. One important step before implementing the spectral clustering algorithm is to compute the similarity graph. According to Benkaouz et al. [111], a K-nearest neighbors

algorithm provides each data point with its k most similar data points, defined by a similarity metric, building a KNN graph where each node is connected with a weighted edge to its k most similar nodes. Von Luxburg [109] states that the main goal of the similarity graph is to construct a model of the local neighborhood relationships between the data points. In our application, we chose the K-nearest neighbor graph using the scikit-learn library [100]. As we have three different data dimensions, we needed to adopt different distance calculations. In the case of the 1D descriptor that contains the three PC as the main variables, we have computed a weighted adjacency matrix, using the Euclidean distance metric to determine the similarity between the variables. In case of the 2D and 3D curves, where we are dealing with XY and XYZ coordinates sampled across multiple instances (15 points for the 2D and 50 points for the 3D), we needed to compute the pairwise Euclidean distance matrix across all samples. This results in a 2D and 3D array $\mathbf{D} \in \mathbf{R}^{n_{\text{samples}} \times n_{\text{samples}} \times n_{\text{samples}}}$ containing the x, y and z coordinates of the 2D and 3D curves.

$$\mathbf{D}_{ij}^{(k)} = \sqrt{(X_{ik} - X_{jk})^2 + (Y_{ik} - Y_{jk})^2 + (Z_{ik} - Z_{jk})^2} \tag{3.4}$$

To obtain a single scalar dissimilarity value between each pair of samples, the distance matrix is summarized across all landmarks using a statistical aggregation method (mean). The resulting 2D matrix $\mathbf{S} \in \mathbf{R}^{n_{\text{samples}} \times n_{\text{samples}}}$ is defined as:

$$\mathbf{S}_{ij} = \frac{1}{n_{\text{points}}} \sum_{k=1}^{n_{\text{points}}} \mathbf{D}_{ij}^{(k)} \tag{3.5}$$

This summarized distance matrix is then used as an input to construct a graph-based representation of the data. We compute a weighted adjacency matrix $\mathbf{W} \in \mathbf{R}^{n_{\text{samples}} \times n_{\text{samples}}}$ using the k-nearest neighbors (k-NN) approach,

and the resulting adjacency matrix was symmetrized. We then weight the edges of the graph using the corresponding entries from **S**. This graph structure captures the geometric similarity between the curves and serves as a basis for spectral clustering.

Spectral Clustering

The first step of spectral clustering is the computation of the Laplacian matrix, using as input the weighted adjacency matrix. There have been many discussions on the topic of choosing an unnormalized or normalized Laplacian matrix to compute the eigen components in [158], [112], who presented algorithms for normalized spectral clustering and, who provides a tutorial for the two previous methods and [109] also presents the concept of unnormalized spectral clustering. Von Luxburg, in [110], concluded that the normalized clustering algorithm should be a preferred method in practical applications. She also mentions in [109] that the Random Walk Laplacian matrix has more advantages when it comes to defining clusters. For this reason, we computed the normalized random walk Laplacian matrix and extracted the first k (k in this case is the number of neighbors) eigenvectors corresponding to the first smallest eigenvalues. To extract the final partition of our data, we have to apply a clustering algorithm like K-means on the sorted eigenvectors of the Laplacian matrix.

Clustering quality and algorithm initiation

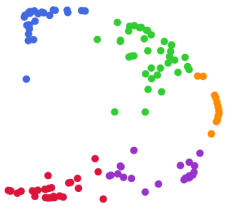
Two initial parameters need to be defined in our approach of spectral clustering: the number of neighbors that we use to build our graph and the number of clusters that gives the best data partitioning. To determine the optimal number of n, which is necessary to build the similarity graph, we constructed

a systematic search over a predefined range. for each value $n \in \{1, 2 \dots 10\}$ a graph was constructed. For each of these graphs, clustering was performed for values of $k \in \{1, 2 \dots 20\}$ and for each k the following clustering quality indexes have been computed: modularity (Q) [159], average silhouette score [114], Davies-Bouldin index [115], Calinski-Harabasz score [116], the best score has been retained for each of these indexes for the current n. This process has been repeated for all values of n, and we compared the best scores and selected the one that consistently yielded superior performance across multiple indices.

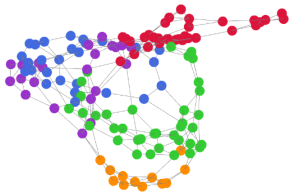
TABLE 3.3: Clustering Evaluation Metrics and Optimal k and n Values

Silhouette	k	DBI	k	CHI	k	Modularity	k	n
0.71	5	0.45	5	22489.38	3	0.72	8	3
0.63	4	0.49	17	10794.51	4	0.74	9	4
0.62	5	0.53	10	6749.81	3	0.67	11	5
0.59	15	0.55	16	5765.91	3	0.68	6	6
0.54	16	0.61	17	4096.89	3	0.64	8	7
0.52	9	0.69	11	4725.9	3	0.63	5	8
0.49	9	0.75	9	4927.24	3	0.60	7	9
0.43	19	0.79	19	3572.18	3	0.58	6	10

Table 3.3 shows an example of clustering evaluation metrics for a 3D projection line. The best results came back for $n = 3$ in the case of three evaluation metrics (Silhouette = 0.71, DBI = 0.45, CHI = 22489.4) and $n = 4$ in the case of Modularity = 0.74. As discussed, the chosen k had to be proposed by more than one quality index, and most usually the silhouette score and the DBI, which we found the most reliable, were the deciding indices. Therefore, in the presented example, k was chosen to be 5 for n = 3.



(A) Spectral embedding of data with n=3, k=5

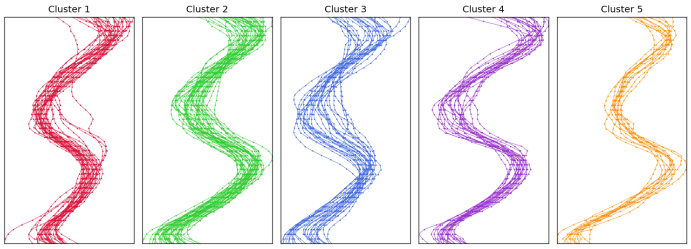


(B) Similarity graph of data with n=3, k=5

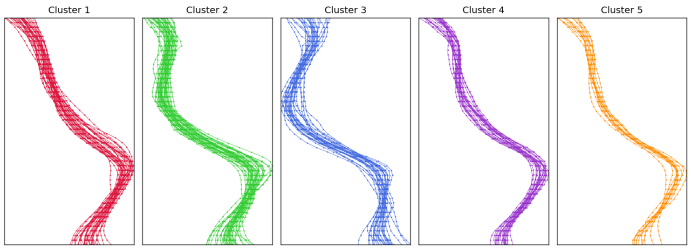
FIGURE 3.24: Visualisation of clusters



(A)



(B) Frontal view (X-Z plane)



(C) Side view (Z-Y plane)

FIGURE 3.25: 3D shape descriptors of the 10^{th} projection corresponding to the lateral silhouette of the leg. Visualisation of the 5 clusters identified for the 10^{th} projection line

Ensemble learning

Classic ensemble learning methods directly use the labels obtained from different clustering of the same data to obtain a more robust classification, but this way they neglect the intrinsic data structures, which, for example, a Laplacian matrix could exploit. Li et al. [118] have introduced a new ensemble learning method that is applicable in the case of Spectral clustering. The

key idea behind ELSC is the implicit combination of the Laplacian graphs obtained from base spectral clustering algorithms. The input in this algorithm, therefore, will be the n Laplacian matrices that will be summed to form a consensus Laplacian matrix from which a final consensus embedding could be calculated and used as input for K-means. Building on this idea, we have performed 16 base spectral clustering for each of the 16 leg projections, and retained the Laplacian matrices that gave the best partitioning. The consensus Laplacian matrix L^* is computed as the sum of the 16 base Laplacians:

$$L^* = \sum_{i=1}^{16} L_{(i)}$$

The rest of the algorithm is maintained the same way as for the base classifications.

3.5 Results

In this chapter, we have presented the methodology that we have used to partition our extended database (258 subjects) with the help of the 1D and 2D shape descriptors and the reduced database (131 subjects) with the help of the 3D shape descriptor. In this chapter, we will present the obtained results derived from the classification of the three shape descriptors, and we will provide a characterisation of the identified morphological groups.

3.5.1 1D data classification

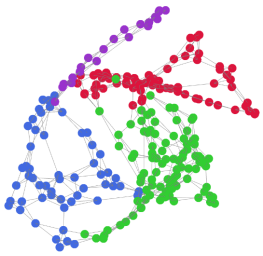
To learn morphological distribution among our 258 subjects, we have employed PCA on the normalized values of 15 circumferential measurements. As a first step, we have reduced the number of variables from 15 to 8 to remove redundancy and only keep the features that contain at least 97.2 %

($PC_1 + PC_2 + PC_3$) of the total variations. These features are entitled C4 (ankle at it's smallest girth), C8, C12, C16 and C20 (equidistant circumferences between ankle and calf), C24 (calf), C36 (knee) and C48 (mid-thigh). The PCA pointed out that the values of the lower leg have a higher variation than the upper leg. The 3 retained PCs were then introduced in our spectral clustering algorithm to obtain a final partition. As previously explained in Subsubsection 3.4.2, to decide on the number of neighbors and clusters, we have used multiple quality metrics and applied a systematic search for ranges of n and k. The results are shown in Table 3.4, which highlights the highest Silhouette score for n = 4 and the lowest DBI for n = 4. The suggested cluster number is 4 in both cases; therefore, the algorithm has been initialized with these parameters. Figure 3.26a represents the similarity graph built with the

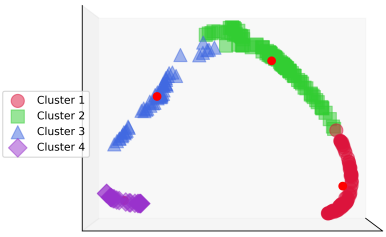
Silhouette	k	**DBI**	k	**CHI**	k	**Modularity**	k	n
0.64	4	0.50	18	84913.94	3	0.81	12	3
0.66	**4**	**0.47**	**4**	51851.45	3	0.75	7	**4**
0.60	5	0.54	5	26237.14	3	0.76	9	5
0.56	6	0.62	6	24153.95	3	0.73	9	6
0.55	12	0.59	12	20145.73	3	0.73	8	7
0.51	14	0.67	16	18163.47	3	0.70	8	8
0.52	12	0.66	16	13827.70	3	0.70	8	9

TABLE 3.4: Clustering metrics for the classification of 1D data

4 nearest neighbors of each data point, where the edges reflect the similarity. From this structure, the Laplacian graph captured the connection between each data point, notably how strongly they are connected. To represent this information in a lower-dimensional space, the three lowest eigenvectors of the Laplacian matrix were chosen and plotted in 3D. This spectral embedding is visible in Figure 3.24a, where we can also visualize the centroids of each cluster.



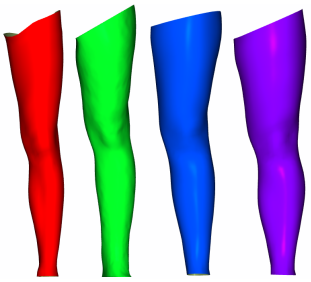
(A) Similarity graph of data with n=4, k=4



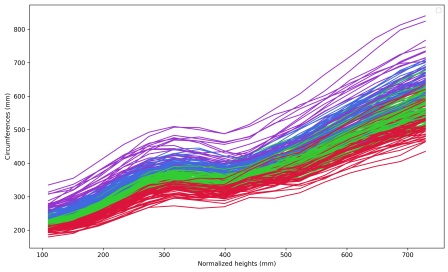
(B) Spectral embedding of data with n=4, k=4

FIGURE 3.26: Visualization of clusters

After this step, we have identified the cluster centroids, marked as red dots in Figure 3.24a, and retraced them to the nearest data point, which will represent the morphotype of each cluster. These morphotypes can be seen in Figure 3.27a, where the same observation is made: a gradual increase in size between the morphotypes.



(A) 4 morphotypes of the 1D shape classification



(B) Cluster visualisation of the 1D classification with the help of the evolution curves (2D SD)

FIGURE 3.27: Visualisation of clusters

Figure 3.27b is used to observe the 4 clusters identified by the 1D data classification in the form of circumferential evolution. One additional remark that we can make in this case is that, clearly, variable C4, C8, C12, which have been proven to be the most influential variables in the dataset (3.23b), are perfectly separated into 4 size groups, and as we go up on the leg, the separation becomes more interfered with between the groups.

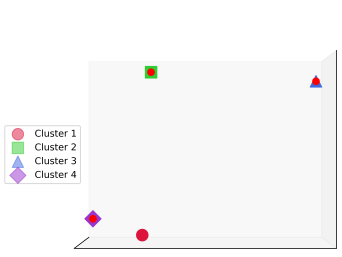
3.5.2 2D data classification

As presented in Paragraph 3.3.2, we consider the form of data obtained by affine translation of the normalized circumferential evolutions as the 2D shape descriptor, also seen in Figure 3.6. From the resulting quality metrics, we can

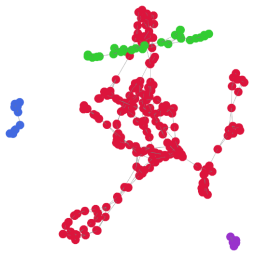
Silhouette	k	**DBI**	k	**CHI**	k	**Modularity**	k	n
1.00	4	0.00	4	8.28×10^{30}	4	0.3	4	3
0.74	10	0.28	8	80465.29	3	0.85	14	4
0.73	11	0.33	15	25949.61	5	0.83	12	5
0.67	19	0.40	14	21499.21	3	0.81	11	6
0.70	13	0.37	13	19217.36	3	081	9	7
0.68	10	0.45	18	15867.33	3	0.81	10	8
0.69	13	0.42	14	15787.70	3	0.79	10	9
0.68	13	0.44	14	13249.09	3	0.77	9	10

TABLE 3.5: Clustering metrics for the classification of 2D shape descriptors

obtain a similarity graph for n = 3 that can partition the data into 4 "perfect" clusters, according to the Silhouette scores and DBI, which both give perfect repartition values. In reality, when we observe both the similarity graph and spectral embedding in Figure 3.28b and 3.28a, we can see that indeed there is a visible separation of groups that produced no interconnections between the clusters. On the other hand, group 1 (red) is too large and by itself could be treated as a separate similarity graph due to the 208 data points that got assigned here.



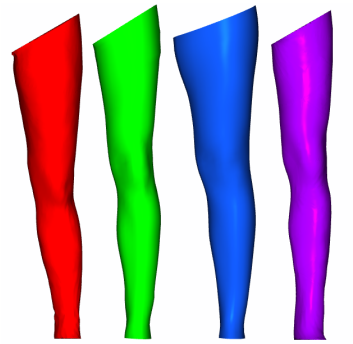
(A) Spectral embedding of data with n=3, k=4



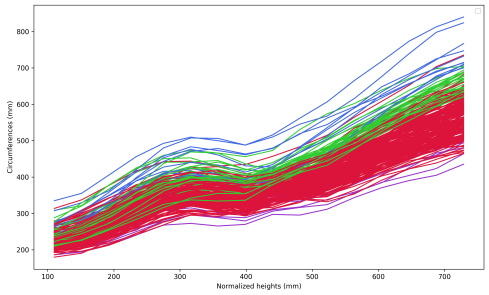
(B) Similarity graph of data with n=3, k=4

FIGURE 3.28: Visualisation of clusters

We identified the morphotypes (Figure 3.29a of each group the same way as in the case of the 1D data and visualized the clusters projected on the circumferential evolutions (Figure 3.29b. From these observations, we can conclude that Cluster 1 could be alone having multiple hidden evolutions; therefore, Morphotype 1 is not necessarily a representative shape for its population. On the other hand, Clusters 2, 3, and 4 are more uniformly similar to their own population; for this reason, the corresponding morphotypes describe each group better, respectively. We can also observe in Figure 3.29b that this classification is more shape-related than size-related, as the population of Cluster 2 is distributed among multiple sizes.



(A) 4 morphotypes of the 2D shape classification



(B) Cluster visualisation of the 2D SD classification

FIGURE 3.29: Visualisation of clusters

Figure 3.30 represents the 4 clusters visualized through the three stages of data representation: in original form, in normalized form, and in shifted form (ankle in 0). The superposition of the last three clusters can be visualized very clearly on the third form of data.

In terms of the population of Cluster 2, we have observed that it is a group of mixed genders with both male and female representatives. A second observation was that all these subjects have an average leg length ranging between 644 and 756 mm. In terms of ankle size, we have taken the values from a

Sigvaris sizing table and tried to see where our subjects are placed. The population of Cluster 2 ranges between ankle sizes S to XL.

Cluster 3 is mainly represented by female subjects of higher BMI; there is a single male representative in this group. It is also important to mention that this group has short legs ranging between 527 - 644 mm, and similarly to Cluster 2, the ankle size can range between S and XXL.

Cluster 4 is entirely represented by male subjects with lower BMI and a longer leg length, ranging between 756 - 876 mm. The gender, ankle size, and BMI-related data can be observed in Appendix A.

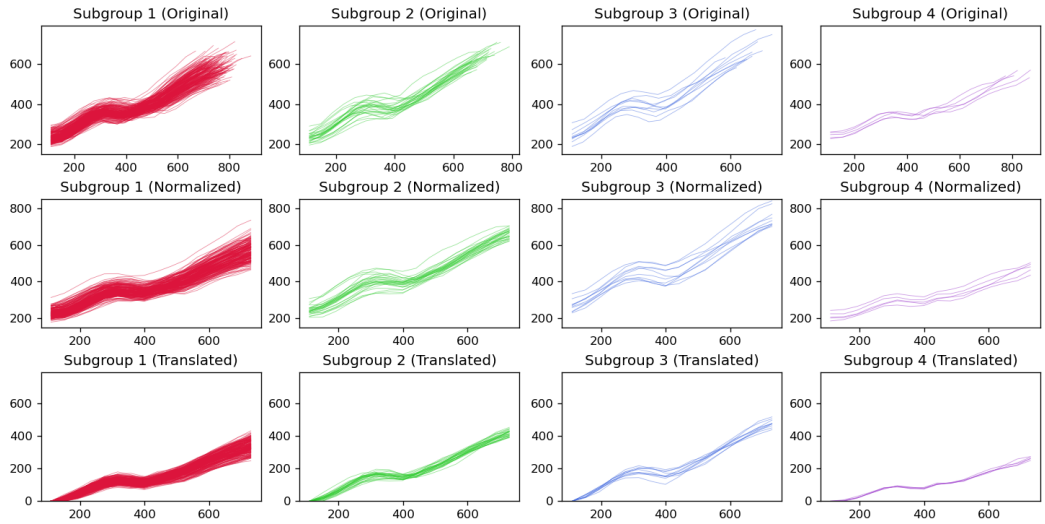


FIGURE 3.30: Visualization of the data sorted in clusters defined by the 2D SD, in three different forms: original, normalized, and normalized translated to 0

3.5.3 3D data classification

As discussed in Subsubsection 3.4.2, the final results of the 3D shape descriptor classification are computed with the help of a consensus Laplacian matrix, which was obtained from 16 base spectral clustering of the 16 projection lines, respectively. The quality metrics that defined the number of neighbors giving the best result for each base classification and allowing the extraction

of 16 Laplacian matrices are presented in Appendix B along with the possible shapes that are hidden in each Laplacian. The resulting eigen space of a 3 neighborhood graph was partitioned with the help of the same quality metrics (Figure 3.31), which both suggested k = 3 and k = 5. We chose k = 3 for the final partition because in an industrial setting, the lower number of morphological groups could be better handled than a higher number, and as both options have similar metrics, we took the lower value.

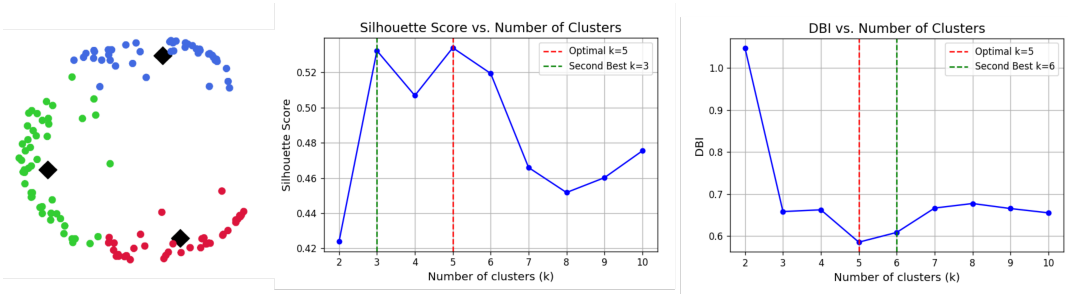
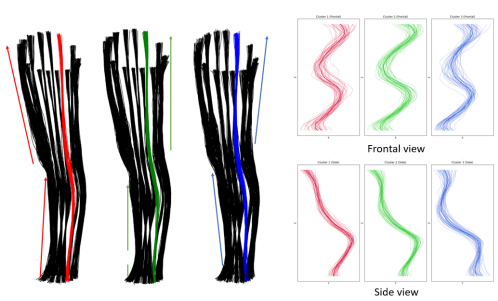
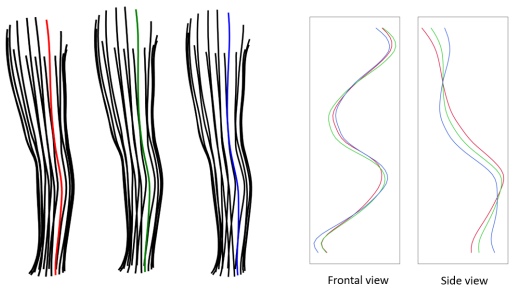


FIGURE 3.31: Spectral embedding of the smallest eigenvectors derived from the consensus Laplacian matrix of the 16 projection lines with n = 3 and k = 3 as suggested by the Average Silhouette score and Davies-Bouldin indexes

Figure 3.32a shows the 131 3D shape descriptors divided into the 3 morphological groups, highlighting the lateral silhouette of the leg that shows the success of the algorithm in identifying similar shapes as the base algorithm. A full list of the 16 projection lines divided into three groups can be visualized in Appendix C.



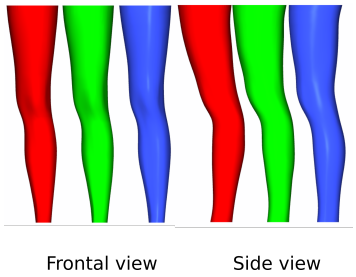
(A) Database of 3D shape descriptors divided into three morphological groups, highlighting the lateral silhouette of the leg, plotted in a frontal and side view



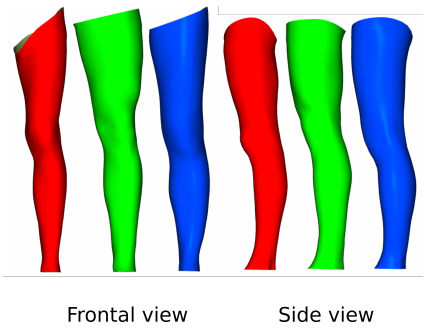
(B) Three mean shapes, computed from the three clusters, highlighting the lateral silhouette in a frontal and side view in a superposed position

FIGURE 3.32: Visualisation of the 3D geometry of the three morphological groups and corresponding mean shapes

By averaging the individual sets of projections for each identified morphological group, we can compute a mean shape, visible in Figure 3.32b. By superposing each individual averaged curve, we can observe the differences between the morphological groups. As the example shows, in the case of the lateral silhouette of the mean shapes, the key difference can be observed on the side view, and it is highly related to the bone alignment or posture of the morphological groups. Slight differences can also be observed on the frontal view of the lateral silhouette, but they are not as pronounced as on the side.



(A) Reconstructed mean shapes of the three morphological groups, visualized from a frontal and side view



(B) Morphotypes of the three morphological groups, represented by the closest subject to the centroid

FIGURE 3.33: Visualization of clusters

This method also allows us to reconstruct a surface mesh using the 16 averaged curves and obtain a general representation of each morphological group. Figure 3.33a shows the three reconstructed mean shapes from both frontal and side views. As can be observed, the overall alignment of the legs is the key geometric difference that has been identified between the groups. If we compare the computed mean shapes with the closest subjects to the centroid of each group, Visible in Figure 3.33b, we can observe the same bone alignment that was mentioned before.

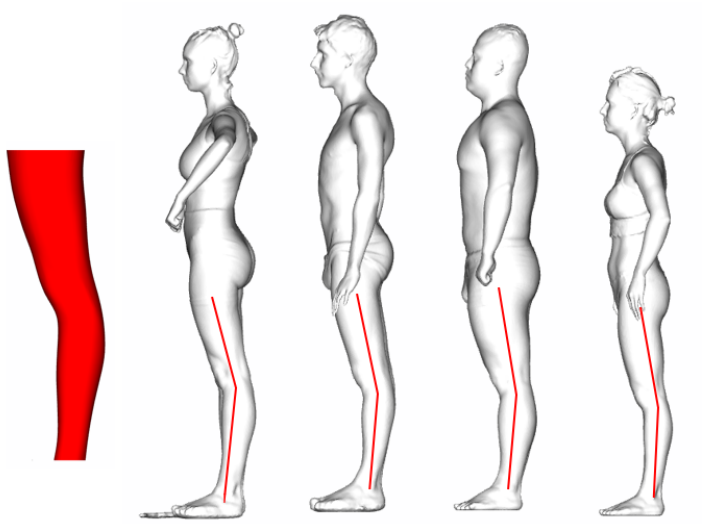


FIGURE 3.34: Example population of Cluster 1, showing a hyperextension of the knee

Figure 3.34 shows 4 examples of subjects, representative of Cluster 1, all of which show a hyperextension of the knee, otherwise known as genu recurvatum [160], which is clinically described as a malposition between the femur and tibia, and it is considered a postural fault.

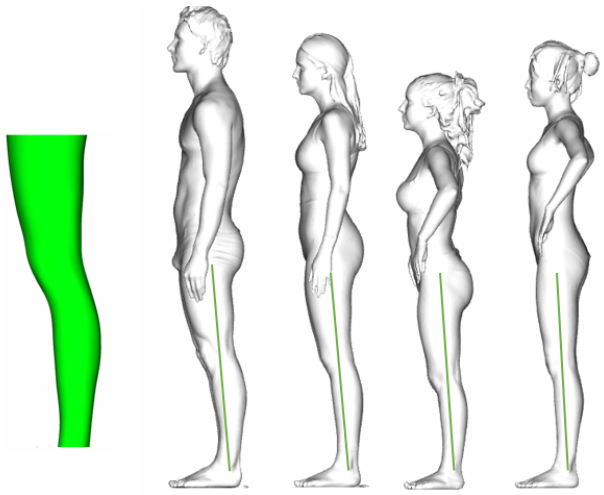


FIGURE 3.35: Example population of Cluster 2, showing a normal alignment of the leg

Figure 3.35 shows 4 examples of subjects, representative of Cluster 3, with a normal alignment of the leg.

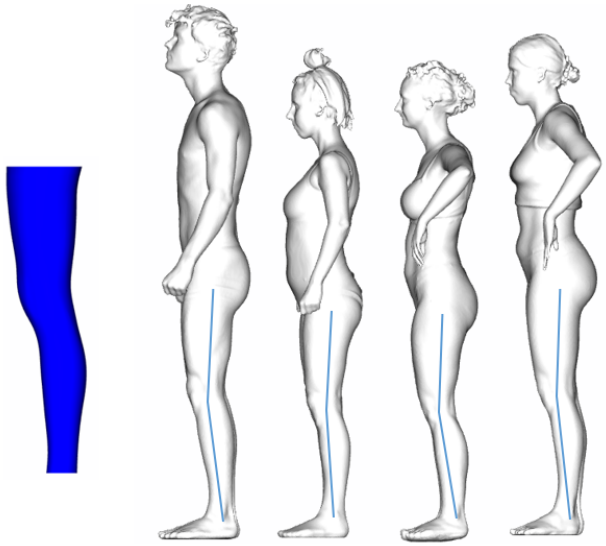
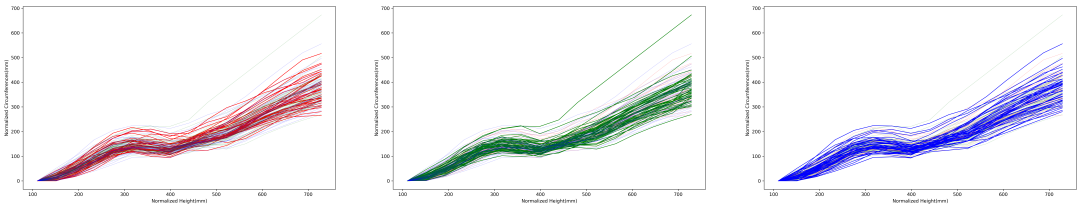


FIGURE 3.36: Example population of Cluster 3, with a flexed knee configuration

Figure 3.36 shows 4 examples of subjects, representative of Cluster 3, with a flexed knee posture or otherwise known as genu flexum [161], which is

developed when a person is bearing their weight on their knee flexes to a greater degree than normal when standing.

Figure 3.37 reveals the three morphological groups found by the 3D shape descriptors. We can observe that the posture of the leg does not influence the circumferential growth of the soft tissue, as none of the morphological groups follow a specific growth pattern; they are not distinct from each other in any particular way.



(A) Circumferential curves of the morphological group 1

(B) Circumferential curves of the morphological group 2

(C) Circumferential curves of the morphological group 3

FIGURE 3.37: The three morphological groups and the corresponding circumferential curves in a normalized, shifted position

3.6 Conclusions

This chapter aimed to identify morphological groups of the lower limb with classic unsupervised learning methods, using multidimensional shape descriptors. For this, we have established two databases: an extended version that contains anthropometric data from 258 human legs, and one that contains 131 high-quality 3D scans and the corresponding 10 anatomic landmarks. The first database was used to extract morphological patterns with 1D and 2D shape descriptors; the second database was used to extract a set of 3D shape descriptors.

The 1D shape descriptor, which uses the 3 first principal components of 8 variables (C4, C8, C12, C16, C20, C24, C36, C48) can differentiate size related

differences between individuals and group them, in the same time it did not make any shape related difference or highlight any shape pattern in the data, which makes us conclude that the 1D shape descriptor is not enough by its own to classify leg shapes in distinct groups.

The 2D shape descriptor could identify 3 well-separated circumferential evolutions, which describe different populations. For instance Cluster 2 contains subject with an average leg length (644 - 756 mm) from various ankle size ranges (S - XL) and mixed gender, Cluster 3 is representing short legged subjects (527 - 644 mm), with the majority being female (96% female, only 1 male subject) with ankle sizes ranging from S to XXL with higher BMI, and Cluster 4 is regrouping long legged (756 - 876 mm) exclusively male subjects of ankle size M and L and lower BMI. These results make us conclude that the same circumferential evolution can be observed in multiple ankle ranges and that, for a correct sizing system, perhaps identifying distinct circumferential evolutions could be the direction to take. We also concluded that Cluster 1, as it was identified by the algorithm, does not realistically represent a single evolution type, and this aspect has to be reviewed in Chapter 5 dedicated to the sizing systems.

With the help of the 3D shape descriptor, we were able to identify 3 geometrical differences among our subjects in study that we consider to be strongly related to the posture of the subjects, that can be considered either normal as shown by the population of Cluster 2, or manifesting genu recurvatum and genu flexum, which are postural faults and present in the population of Cluster 1 and Cluster 3 respectively. These three morphological groups can be easily identified by viewing the subject in the sagittal plane. It has also been noted that the three morphological groups that we have discovered by the 3D shape descriptor are not linked to any specific circumferential growth pattern; therefore, there is a need to find a rule that can help us parametrize

the volumetric growth of the morphotypes.

Chapter 4

Deep Learning Architecture for Clustering and Anomaly Detection in Morphological Data

4.1 Introduction

3D data is a valuable resource that can be used to describe the geometry of a 3D object [63]. Deep learning-based methods have gone through significant advancement, especially in the field of geometric learning from non-Euclidean 3D data, like point clouds, grids, and meshes [73], which still represent unique challenges in this field. Point clouds are the most widely spread data form, used in reconstruction and classification tasks, despite the fact that they do not contain surface information of the object. This is due to the fast and easy data acquisition, made possible by the latest 3D scanning technologies. Point clouds are simple structures that are easier to learn [73], and they describe the spatial representation of a 3D object in an unstructured way [63]. Similar to point clouds, meshes are also considered complex

structures easily acquirable, but they offer topological information, in addition to spatial embedding. However, these types of data often contain outliers, which can bias the analysis, leading to result misinterpretation. The fast development of deep learning models, especially Convolutional Neural Networks, has drastically changed both classification and outlier detection, as the feature extraction process has been built into their structure, making it easier to understand these complex structures. In this Chapter, we propose a novel approach that integrates Deep Convolutional K-means with the Elliptic Envelope algorithm to learn latent features for classification tasks, identify subjects that present anomalies in their legs, and identify outliers within the dataset.

4.2 Methodology

4.2.1 Post-processing of 3D mesh surface

Many sources have extensively explained the difficulty around the complex structure of non-Euclidean 3D data, that it is hard to use the full potential of CNN structures directly on this data [87] and that there is a need for feature descriptors that have high discriminative value and can capture the structures that are important for classification [162]. As Mostapha et al. [163] describe, this complexity comes from the lack of a grid structure on a non-Euclidean surface. To overcome this irregular structure that scanned meshes represent, instead of using the raw segmented mesh, we have generated a triangulated surface mesh by automatically sweeping the 16 projection lines, presented in Chapter 3. This process ensures the identical topology between our dataset of 3D legs. For the creation of the new mesh, each projection

line had to be resampled with exactly 50 points. To enhance the created surface, we introduced in the original set of 16 curves an additional set of interlacing curves. These new curves are generated by sampling intermediate points along temporary orthogonal curves constructed through the existing ones. This technique produces a quadrilateral strip mesh between consecutive curves and converts each quad into two triangles, alternating the diagonal split to improve mesh regularity. In total, we will now have 32 curves of exactly 50 points, so 1568 quadrilaterals will be created and split into 3136 triangles, with a total of 1600 nodes, making the surface smoother, as depicted in Figure 4.1. The mesh creation methodology is briefly introduced here for the dataset context; a complete mathematical formulation will be provided in a forthcoming publication.

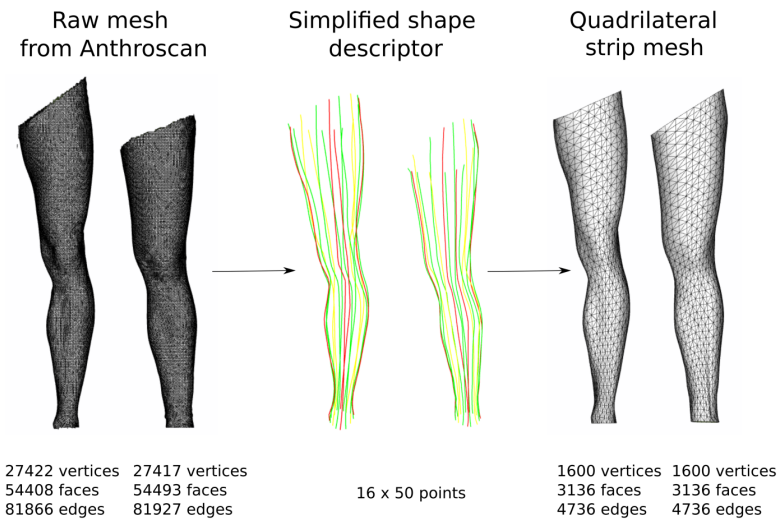


FIGURE 4.1: Construction of a quadrilateral strip mesh surface to assure identical topology between meshes

Fully Convolutional Mesh Autoencoder

Zhou et al. [164] pointed out that one of the main challenges regarding deep learning from meshes is their irregular sampling and connections, in which

the vertices are unevenly distributed, having different connectivity and direction. For this reason, applying the standard CNN kernels, which are used on regular grid data, is not possible. To overcome the template-specific nature and inability to capture fine-grained deformations of previous methods used on mesh data, they proposed a Fully Convolutional Mesh Autoencoder (FCMA), which can be applied on arbitrary mesh data that do not follow a fixed structure and can be triangular mesh, polygonal mesh, or tetrahedral mesh with irregular vertex distribution. This method leverages a novel approach of convolution and (un)pooling operators applicable to irregular mesh data by integrating an innovative spatially varying convolution kernel(vcConv), where each vertex samples convolution weights from a globally shared Weight Basis using vertex-specific locally varying coefficients (vc), significantly reducing the number of parameters, making it more effective. The convolution operation is formulated as follows:

$$y_i = \sum_{x_{i,j} \in \mathcal{N}(i)} W_{i,j}^T x_{i,j} + b \tag{4.1}$$

with vertex-specific convolution weights defined by:

$$W_{i,j} = \sum_{k=1}^{M} \alpha_{i,j,k} \mathcal{B}_k \tag{4.2}$$

where $\mathcal{B}_k$ is the shared Weight Basis, and $\alpha_{i,j,k}$ are the learned variant coefficients (vc).

In accordance with the conventional CNN architectures, the authors introduce pooling and unpooling layers (vdPool and vdUnpool), where vertex features are aggregated based on learned density weights (called "variant densities" or "vd"), effectively managing the irregularity of vertex distributions during mesh down-sampling and up-sampling. This pooling operation is mathematically described as:

$$M\mathbf{y}_i = \sum_{j \in \mathcal{N}(i)} \rho'_{i,j} \mathbf{x}_{i,j}, \quad \rho'_{i,j} = \frac{|\rho_{i,j}|}{\sum_{j=1}^{E_i} |\rho_{i,j}|} \tag{4.3}$$

where $\rho_{i,j} \in \mathbb{R}$ and $\rho'_{i,j}$ are respectively the training parameter and the density value.

The FCMA architecture can be viewed in Figure 4.2, which illustrates the encoder-decoder structure through a down-sampling block and an up-sampling block. Experiments on diverse datasets, including D-FAUST human body meshes [165], high-resolution mesh models, and non-manifold geometries, demonstrated that the FCMA approach achieves state-of-the-art reconstruction accuracy. Comparative ablation studies further validate the advantages of vcConv and vdPool layers, illustrating significant improvements in accuracy, memory usage, and parameter efficiency over traditional and recent mesh convolution methods.

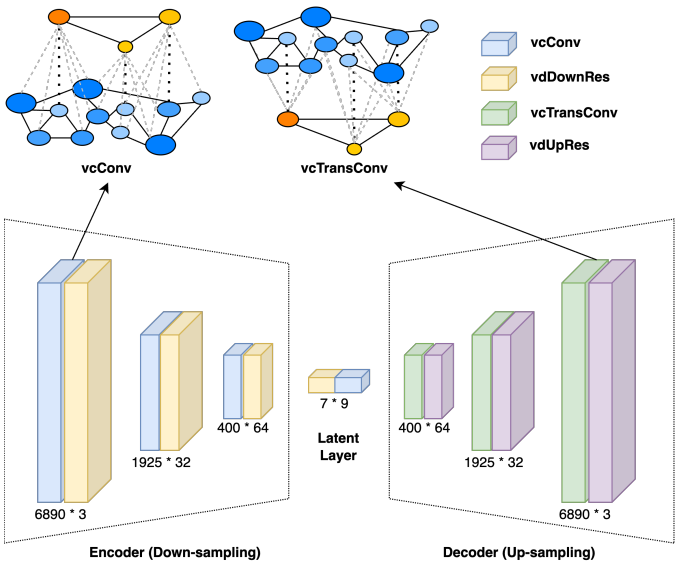


FIGURE 4.2: The architecture of Fully Convolutional Mesh Autoencoder

Deep Support Vector Data Description

Traditional anomaly detection methods like SVDD and One-class SVM, that rely on kernel mapping, learn features independently from input samples and apply anomaly detection afterwards. Being shallow learning models, they do not deal well with high-dimensional data, because of computational complexity [166]. Deep Support Vector Data Description (Deep SVDD) overcomes these weaknesses by integrating in the model simultaneously representation learning and anomaly detection, directly optimizing the model for detecting anomalies. Deep SVDD is a fully deep one-class classification method that can support high-dimensional data and is specifically designed for unsupervised anomaly detection.

Let $\phi(x; W) : \mathbb{R}^d \to \mathbb{R}^p$ denote the mapping learned by a neural network parameterized by weights W, which transforms the input data $x \in \mathbb{R}^d$ into a latent representation. The goal is to find a center $\mathbf{c} \in \mathbb{R}^p$ where most normal data points are inside a hypersphere. The soft-boundary Deep SVDD objective is defined as:

$$\min_{R,W} \; R^2 + \frac{1}{\nu n} \sum_{i=1}^{n} \max\left\{0, \|\phi(x_i; W) - \mathbf{c}\|^2 - R^2\right\} + \frac{\lambda}{2} \sum_{\ell=1}^{L} \|W^\ell\|_F^2, \tag{4.4}$$

where $\nu \in (0, 1]$ controls the fraction of permissible outliers, $\lambda > 0$ is the regularization coefficient, and $\|\cdot\|_F$ denotes the Frobenius norm. The term $\max\{\cdot, 0\}$ is a soft constraint allowing some samples to be outside the hypersphere.

For scenarios where all training data are normal, the One-Class Deep SVDD formulation eliminates the radius term and penalizes the average distance to the center:

$$\min_{W} \frac{1}{n} \sum_{i=1}^{n} \|\phi(x_i; W) - \mathbf{c}\|^2 + \frac{\lambda}{2} \sum_{\ell=1}^{L} \|W^{\ell}\|_F^2. \tag{4.5}$$

The anomaly score $s(x)$ for a test sample x is given by the squared Euclidean distance from the center in the latent space:

$$s(x) = \|\phi(x; W^*) - c\|^2, \tag{4.6}$$

where W^* denotes the learned network parameters. In the soft-boundary case, this score is compared against the learned radius R to determine if the sample is normal or abnormal. A data point becomes abnormal when its score is greater than a predefined threshold. Therefore, the One-Class Deep SVDD implies the prior definition of a threshold.

4.2.2 MeshDeepSVDD: Anomaly Detection in 3D Meshes via Fully Convolutional Mesh Autoencoder and Deep SVDD

In this subsection, we introduce the MeshDeepSVDD method in detail, which is structured in two main phases: training of the Fully Convolutional Mesh Autoencoder model and the anomaly detection with Deep SVDD on Latent Mesh Representations, also illustrated in Figure 4.3.

Mesh representation learning with FCMA model

The key role of the first phase in the MeshDeepSVDD is to leverage the fully convolutional structure of the FCMA model to generate highly accurate reconstructed meshes and to learn their spatially localized latent representations that preserve the geometry of the original mesh in a lower-dimensional space. The extracted features have a crucial role in the next phase, which detects the anomalous data.

Let $V = \{\mathbf{v}_i \in \mathbb{R}^3\}_{i=1}^{N}$ denote the vertex set of a 3D mesh in the training dataset. The FCMA architecture consists of an encoder $f_{\text{enc}}(\cdot; W_{\text{enc}}^0)$ and a decoder $f_{\text{dec}}(\cdot; W_{\text{dec}}^0)$, where W_{enc}^0 and W_{dec}^0 are respectively the initial weights of networks.

The reconstructed mesh $\hat{V}$ is obtained by passing V through the encoder-decoder pipeline:

$$\hat{V} = f_{\text{dec}}(f_{\text{enc}}(V; W_{\text{enc}}^0); W_{\text{dec}}^0) \tag{4.7}$$

To train the FCMA model, we minimize the reconstruction error between the input and the output mesh:

$$\mathcal{L}_{\text{rec}} = \frac{1}{N} \sum_{i=1}^{N} \|\mathbf{v}_i - \hat{\mathbf{v}}_i\|^2 \tag{4.8}$$

Optimizing $\mathcal{L}_{\text{rec}}$ yields the trained encoder and decoder weights W_{enc} and W_{dec}, respectively.

4.2.3 Anomaly Detection with Deep SVDD

A common approach to anomaly detection in autoencoder-based frameworks is to calculate the reconstruction error, where anomalies will be reconstructed poorly compared to normal samples. However, relying solely on reconstruction error has critical limitations, especially in complex, high-dimensional, or spatially structured data like 3D meshes. Deep SVDD is an alternative approach. This method trains the encoder of the neural network to map all normal data into a minimum-volume hypersphere. Therefore, in this phase, we discarded the decoder of FCMA and used only the encoder to generate the latent features. The latent representation $\mathbf{z}$ of mesh V is given by:

$$\mathbf{z}_i = f_{\text{enc}}(V_i; W_{\text{enc}}) \tag{4.9}$$

With Deep SVDD, we initialize the fixed center $\mathbf{c}$ of the hypersphere to match the dimensionality of $\mathbf{z}$. In this case, the value of $\mathbf{c}$ is the mean of latent presentations.

$$\mathbf{c} = \frac{1}{n} \sum_{i=1}^{n} f_{\text{enc}}(V_i; W_{\text{enc}}) \tag{4.10}$$

Deep SVDD minimizes the squared Euclidean distance between the latent features and the hypersphere center:

$$\mathcal{L}_{\text{DSVDD}} = \frac{1}{n} \sum_{i=1}^{n} \| f_{\text{enc}}(V_i; W_{\text{enc}}) - \mathbf{c} \|^2 \tag{4.11}$$

The goal of optimization is to simultaneously learn network parameters W_{enc} and minimize the volume of a data-enclosing hypersphere. This optimization is performed with respect to W_{enc}, resulting in updated encoder weights $W^{\star}_{\text{enc}}$. The objective encourages the encoder to map normal meshes tightly around $\mathbf{c}$ while allowing anomalous meshes to deviate away.

For a test mesh V_t, the anomaly score is computed by measuring the squared distance between its latent representation and the center $\mathbf{c}$:

$$s(V_t) = \| f_{\text{enc}}(V_t; W^{\star}_{\text{enc}}) - \mathbf{c} \|^2 \tag{4.12}$$

To determine whether the test mesh is normal or anomalous, we must predefine a threshold θ. A test sample is classified as anomalous if it exceeds a predefined threshold ($s(V_t) > \theta$).

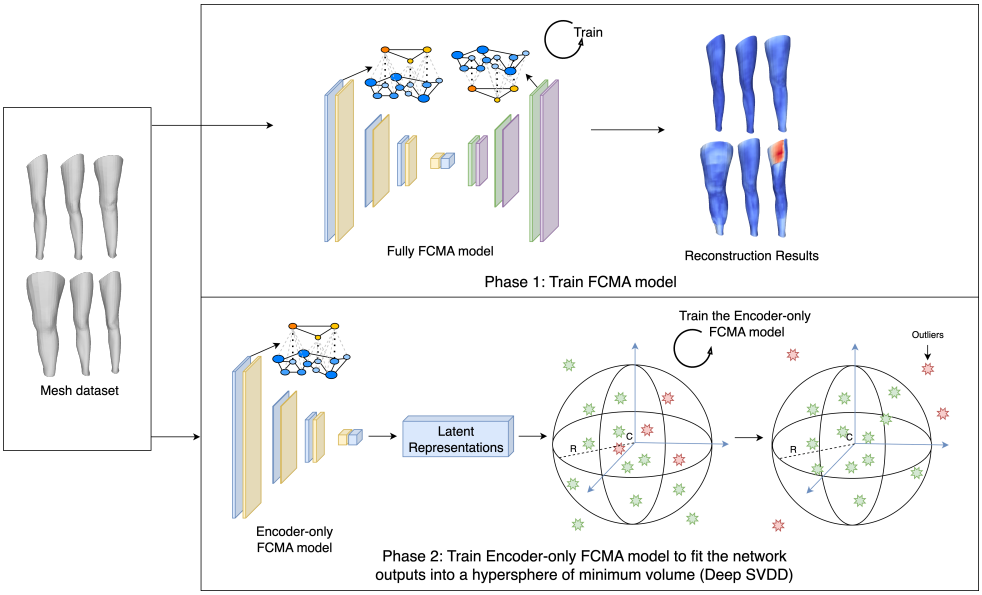


FIGURE 4.3: Overview of the MeshDeepSVDD for Mesh-Based Anomaly Detection

4.3 Results

4.3.1 Mesh Reconstruction with FCMA model

The main goal of the FCMA model is to compress a high-resolution mesh in a compact latent representation in the encoder phase, and then to reconstruct the original mesh from this compact representation in the decoding phase. For this, we configured the FCMA model with 4 vdPool layers for the encoder and 4 vdUnpool layers for the decoder. The encoder progressively reduces the original mesh from 1600 vertices with 3 channels per vertex down to a latent representation consisting of 104 vertices with 7 channels per vertex. The model was trained for 300 epochs using the Adam optimizer with a learning rate of 0.0001. It achieved a mean squared geometric reconstruction error (MSE) of 0.0116, computed as the average Euclidean distances between the predicted and ground-truth vertex positions across the reconstructed meshes. The reconstruction results are illustrated in Figure 4.4.

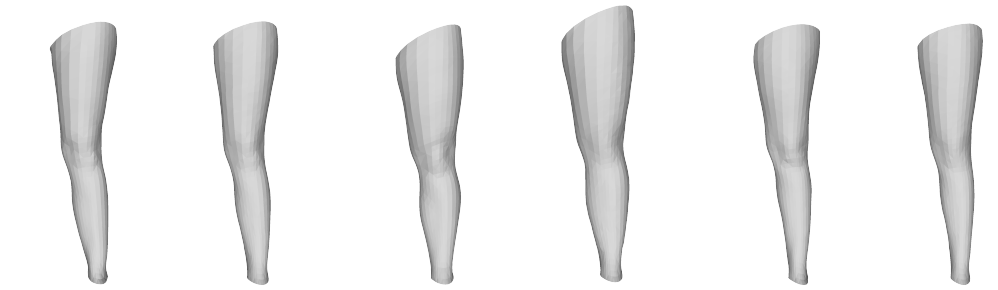


FIGURE 4.4: The reconstruction mesh results

Evaluation on public dataset To evaluate the accuracy of MeshDeepSVDD, we experimented on the MulSen-AD dataset [167], which is the first high-resolution, multi-sensor anomaly detection dataset, specifically designed for object-level anomaly detection for industrial quality inspection. We tested on 3 categories: Capsule, Nut, and Piggy. Due to our target focus on detecting abnormal shapes, the dataset includes point clouds of normal meshes and abnormal meshes manifesting in various forms, such as breaks, cracks, foreign bodies, and deformation. The train and test dataset is described in Table 4.1 and Figure 4.5. The meshes have been resampled to have 5000 vertices each, to ensure consistency.

Category	**Train Set**	**Test Set**	
	#Normal	#Normal	#Abnormal
Capsule	64	10	25
Nut	118	10	17
Piggy	110	10	12

TABLE 4.1: Train and test dataset of MulSen-AD

We compared the anomaly detection performance of our method against the state-of-the-art methods, which are the following:

- Support vector data description (SVDD) with Radial Basis Function Kernel (`nu` value is 0.99)

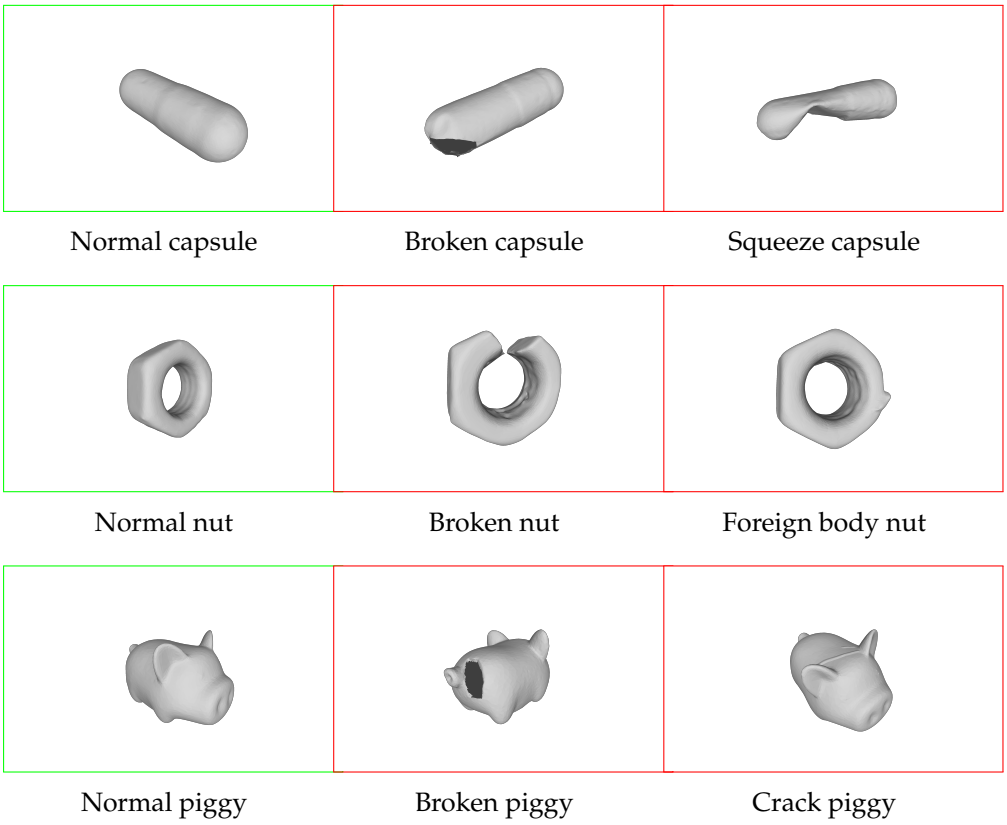


FIGURE 4.5: Illustration of normal and abnormal samples from the Capsule, Nut, and Piggy datasets.

- Kernel density estimation (KDE), using a Gaussian kernel with a bandwidth of 0.5
- Isolation Forest (IF) configured with a contamination rate of 0.5

Method	Capsule	Nut	Piggy	Mean
BTF Raw	60.4	51.2	49.2	53.6
BTF FPFH	83.6	65.3	55.0	67.9
M3DM PointMAE	88.8	81.8	48.3	73.0
M3DM PointBert	92.8	**90.6**	57.5	80.3
PatchCore FPFH	**100.0**	87.7	60.8	82.8
PatchCore FPFH+Raw	55.8	42.5	53.3	50.5
PatchCore PointMAE	85.6	75.3	46.7	69.2
Reg3DAD	93.6	70.0	48.3	70.6
FCMA + SVDD	95.0	50.0	60.0	68.3
FCMA + IF	85.0	55.0	55.0	65.0
FCMA + KDE	96.5	78.0	80.8	85.1
MeshDeepSVDD (Ours)	98.8	88.24	**89.2**	**92.1**

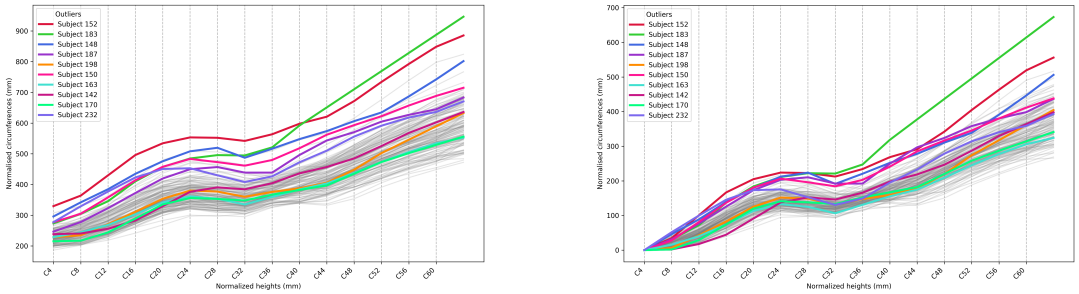
TABLE 4.2: AUC-ROC (%) performance comparison across datasets

In terms of AUC-ROC (Area Under the Receiver Operating Characteristic curve), MeshDeepSVDD achieved excellent scores for the three datasets and significantly outperformed the other methods. The results are presented in Table 4.2, where we can observe that our method has achieved 0 988, 0.920, and 0.892 for Capsule, Nut, and Piggy, respectively. On the other hand, the three tested methods achieved lower performance, two of which (IF and SVDD) had a score of 0.5, having no discriminatory ability between normal and abnormal data.

Visualization and interpretation of outlier features

As the developed MeshDeepSVDD method has shown promising results on the public datasets, we can be confident of its ability to distinguish between anomalous data and normal data. In the case of the human leg dataset, we

analyzed the top ten anomalous samples identified by the highest reconstruction error. For visualization, we have chosen three methods to see the features that make these subjects distinct from the other. First of all we wanted to compare the volumetric differences of the identified outliers with the overall population, this is what Figure 4.6a illustrates, and then we also wanted to visualize if hypothetically all of the subjects would have the same ankle, how would the rest of the circumferences evolute, which is illustrated in Figure 3.5. These two figures revealed that the algorithm has chosen the legs that are larger in terms of volume than the average. The lower leg of these subjects (152, 183, 148, 187, 232) follows a similar evolution between C4 and C20. Subjects 198, 163, and 170 are very similar in volume as well as in circumferential evolution; therefore, in the case of these subjects, Figure 4.6 did not reveal many anomalies. On the other hand, Subject 142 has shown a completely different evolution, having a large arch shape in the lower leg region and a linear, "more padded" upper leg region, which suggests lower muscle development in the lower leg, very different from the average shape.



(A) Normalized volumetric plots of the 131 legs, highlighting the ten anomalous subjects

(B) Ankles translated in 0, illustrating the evolution differences of the circumferences along the leg

FIGURE 4.6: 2D comparison of the 10 anomalous data within the 131 dataset

For a second visualization method, we made a call to the 16 3D projections that circle the leg in a medial - frontal - lateral and anterior direction and describe the intrinsic shape of the longitudinal soft tissues of each leg in the

same area. We chose to plot opposing sides of these projections in 2D (z coordinates with either x or y coordinates), illustrated in Figure 4.7, where the 1^{st} subplot represents the frontal silhouette (medial and lateral sides) and the 5^{th} subplot represents the sagittal silhouette (anterior and posterior sides). These subplots and the individual plots in Appendix D can reveal exactly the outlier features of all 10 subjects. The highest reconstruction error subjects can be considered as outliers (Subject 152, 183, 148, and 187) because they are larger in size and go in the obese category. Subject 183 has a relatively thin ankle in comparison to the large thigh and also presents a "knocked knee" deformation, which is related to how the leg bones are aligned. This feature can also be seen in the case of Subject 163, but this subject also has a high hyperextension of the knee, which makes her an outlier. Subject 148 has a distinct soft tissue structure in the lower leg, having a prominent bump below the knee. Similarly, Subject 232 has a different lower leg region, but the main difference is the thicker ankle and the lower position of the calf muscle when we compare her to the overall population. Subject 150 has a very unique fat deposit, which makes its shape outstanding. The lateral side of the leg is straight, while the medial side is bulging, especially in the calf region. Subject 142, as explained above with the volumetric data, shows this feature in the geometry as well, having a disproportionate soft tissue development in the lower part of the leg in comparison to the upper part of the leg. Projections 1,2,7, and 8 in Figure D.8 show the medial side of the leg, and beneath the calf, we can observe a decline in soft tissue development. For Subject 198, the lateral contour of the calf muscle is raised in a higher position in comparison to others, and this can be seen on Projections 9, 10, and 15 of Figure D.5. Another outstanding feature is the bulging popliteal fossa in the posterior contour, behind the knee (Projections 12, 13, and 14).

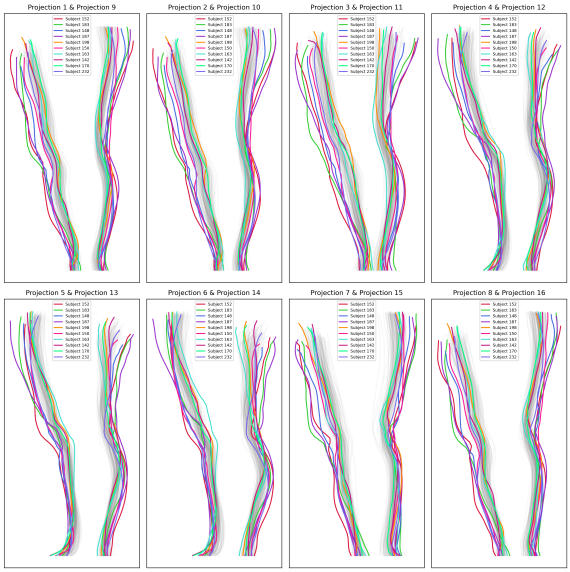


FIGURE 4.7: 16 projection of the top ten anomalous data compared to the overall population of the leg dataset

Figure 4.8 sums up the above-described zones in the top ten anomalous data.

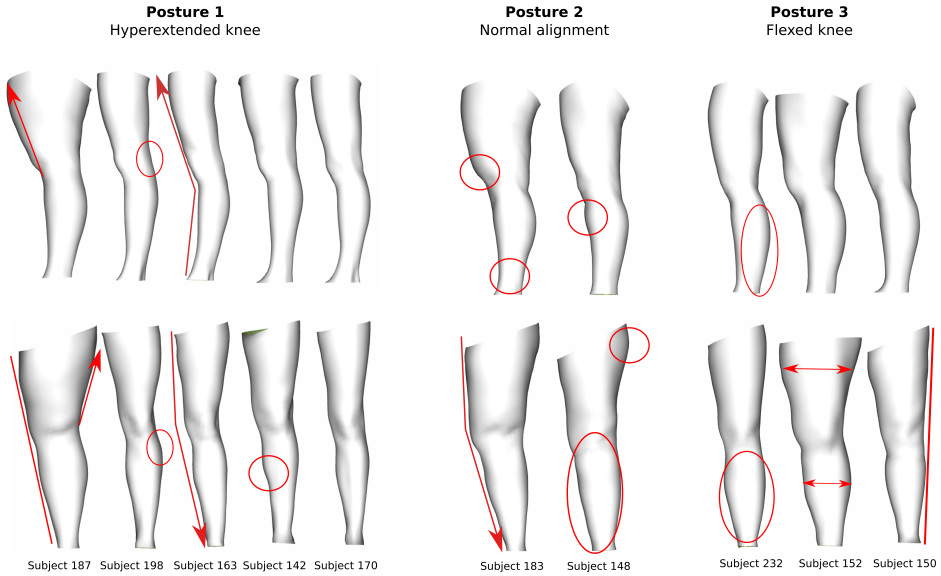


FIGURE 4.8: Top 10 outlier subjects from the leg dataset, highlighting the geometric anomalies

4.4 Conclusions

In this Chapter, we have investigated two novel anomaly detection methods to improve the quality of the data partitioning and remove outliers. We studied the power of a novel anomaly detection method, called MeshDeepSVDD, which has been integrated in a Fully Convolutional Mesh Autoencoder structure, and has been tested on three object categories(nut, piggy, and capsule) of the MultiSen-AD public dataset, successfully identifying the anomalous data with a mean score of 0.92 AUC-ROC. This result outperformed the traditional Support Vector Data Descriptors(SVDD), Kernel density estimation(KDE), and Isolation Forest(IF) methods, which performed significantly lower, not being able to distinguish anomalous data from normal data. Applying this method to the human leg database has successfully identified the top ten anomalous legs in the database of 131 subjects. These subjects have been identified as outliers for the following reasons: oversized or obese legs, knock-kneed or hyperextension of the knee, large and oddly shaped lower leg, especially in the case of two subjects with primary Lymphoedema, disproportionality between upper and lower soft tissue development, unique leg shape, and characteristics. The identification of such anomalies can significantly improve the outcome of data clustering and can even be used to detect chronic diseases like Lymphoedema.

Despite the algorithm's success in detecting anomalies, there are many possibilities for future research to be undertaken. In future works, we will address the "black-box" issue, which is currently the main limitation of the proposed method. This means that the lack of transparency in identifying anomalies and clustering the data into distinct groups has to be enhanced for better interpretability.

Chapter 5

Proposition of a new sizing system for the design of MCS

5.1 Introduction

Medical Compression Stockings, when donned on the leg, take up their shape like a second skin and apply pressure; therefore, the accurate dose of compression imposed by this product, critical for medical treatment of Chronic Venous Insufficiency (CVI), is highly dependent on the shape and size of the lower limb. Depending on the type or severity of this disease, this contact pressure needs to be controlled in an effective way. The pressure exerted is affected by the properties of the underlying tissue and relative proportions of these at any particular cross-section [34]. The fit of a compression garment is crucial in order to ensure the correct interface pressure that is going to be applied to the body part. Over the non-uniform human body shapes, the compression garment with a specific tension exerts and distributes pressure unevenly; therefore," the extent of pressure depends on the garment fit and construction and the size and shape of the body part [35]. An insufficient pressure will limit the efficacy of the compression garment; on the other hand, too high compression can lead to discomfort and serious damage to health

[35]. The shape of the leg has important implications in relation to pressure and garment design/use because it is affected by the properties of the underlying tissue and relative proportions of these at any particular cross-section [34]. For unusual leg sizes, shapes, or deformities, a standard 'off-the-shelf' stocking is unlikely to fit the patient. In these cases, MCS should be customised to the individual limb measurements [168]. Another very important reason to take into consideration the morphology of the human lower limb and, by it, reevaluating the sizing systems of MCSs is because of the high non-compliance of these compression products in the treatment of venous deficiency and lymphoedema. Many studies have been conducted to discover the reasons for non-compliance in wearing MCSs [169], [170], [38], and according to them, poor compliance is due to pain, discomfort, difficulty donning stockings, tightness, feeling hot, perceived ineffectiveness, skin irritation, cost, and lack of cosmetic appeal. Moreover, health practitioners are facing a great difficulty to prescribe off the shelf products for patients suffering from leg ulcers, pointing out that with the three-point measuring method (instep, ankle, calf), MCS only fits 53.5% of patients, and with the seven-point measure, this number reduces to 4.7 %, which is indeed a great challenge and difficulty for the healing process [171].

Compression therapy only benefits patients who remain compliant; therefore, industrials need to put much effort into the reevaluation and optimization of the manufacturing process and product design to enhance comfort, donning ease, pressure configuration, and size accuracy. To respond to these requirements, we will propose in this Chapter a new sizing system that is more adapted to the overall evolution of the leg circumferences, and we also propose a decision tree-based size recommendation tool that could be beneficial for both medical professionals to prescribe the correct product, but also for the industrial collaborators to design their products.

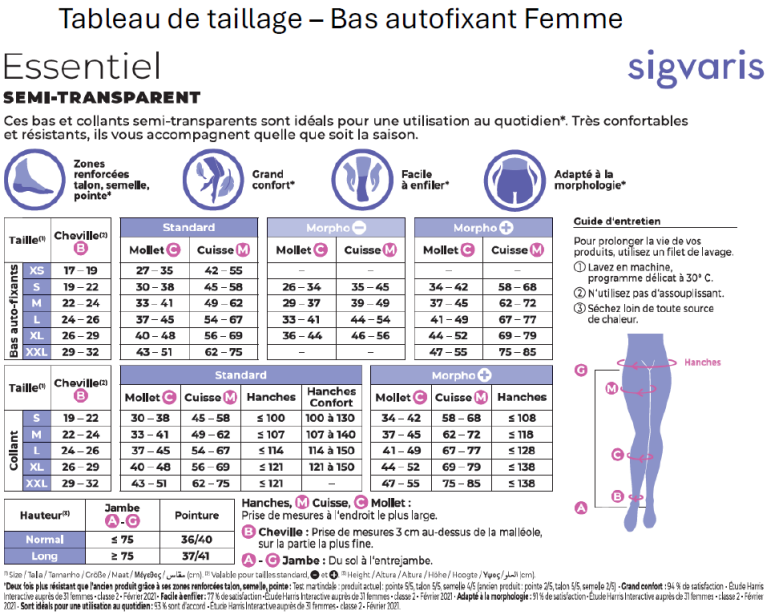
5.2 Background and literature review

Granberry et al. [46] studied the geometric variability of the lower leg to propose a novel sizing system for active compression garments, which require high body shape and size fidelity. For this, they have conducted 3D anthropometrical studies to define body variability and statistically divide size groups based on body measurements. They have highlighted that achieving a precise fit is very challenging because of the lack of correlation between leg measurements, and they have also suggested that, within all leg circumferences, the ankle measurement is a key dimension to organize the population into distinct groups, because this area of the body is less susceptible to gaining weight or developing muscle mass. A second very interesting sizing system reevaluation study was conducted by Liu et al. [146], who studied the shape and size of the lower limb in order to provide a better fit and proper pressure distribution of compression garments. To improve the fit of knee-high and thigh-high compression products, the classification of the lower limb was divided into two parts: above the knee and below the knee. They pointed out that several individuals might have the same calf circumference and have different thigh shapes. The sizing method used in their study is called the multiple percentile method, which is a body-shape focusing sizing system including numerical values for minimum, average, maximum, and various percentiles. The resulting sizing system corresponds to three shape classes. They defined 7 key anthropometric points to measure and implemented 7 size increments from sizes I to VII. They also specified different size orientations for individuals with larger or smaller thighs. According to Kowalski et al. [12], custom-made compression garments are the most accurate therapeutic products that support the external healing process. One of the important factors in the modeling and designing of compression

products that this paper mentions is the accuracy of the body measurements, which can be enhanced by the use of 3D body scanners as a replacement for the less reliable manual measurements. Jindal et al. [172], pointed out that commercialized MCS brands, designed and manufactured in Europe should adapt their product sizing to the morphology of the target country, where they sell the product, the study proved that within the three available MCS brands in India, none of them were truly correct for the morphology of Indian population, causing problems of donning and slippage of the product.

5.3 Methodology

To create the logic of the new sizing table, it was necessary to first identify to which size each subject belongs in the current sizing table of Sigvaris. For this, we have used the sizing table provided by Sigvaris for a stocking model, visible in Figure 5.1.


Tableau de taillage – Bas autofixant Femme

Essentiel

sigvaris

SEMI-TRANSPARENT

Ces bas et collants semi-transparents sont idéals pour une utilisation au quotidien*. Très confortables et résistants, ils vous accompagnent quelle que soit la saison.

Zones renforcées talon, semelle, pointe* | Grand confort* | Facile à enfiler* | Adapté à la morphologie*

	Taille[1]	Cheville[2] (B)	Standard Mollet (C)	Standard Cuisse (M)	Morpho Mollet (C)	Morpho Cuisse (M)	Morpho Mollet (C)	Morpho Cuisse (M)
Bas auto-fixants	XS	17 – 19	27 – 35	42 – 55	–	–	–	–
	S	19 – 22	30 – 38	45 – 58	26 – 34	35 – 45	34 – 42	58 – 68
	M	22 – 24	33 – 41	49 – 62	29 – 37	39 – 49	37 – 45	62 – 72
	L	24 – 26	37 – 45	54 – 67	33 – 41	44 – 54	41 – 49	67 – 77
	XL	26 – 29	40 – 48	56 – 69	36 – 44	46 – 56	44 – 52	69 – 79
	XXL	29 – 32	43 – 51	62 – 75	–	–	47 – 55	75 – 85

	Taille[1]	Cheville[2] (B)	Standard Mollet (C)	Standard Cuisse (M)	Standard Hanches	Standard Hanches Confort	Morpho Mollet (C)	Morpho Cuisse (M)	Morpho Hanches
Collant	S	19 – 22	30 – 38	45 – 58	≤ 100	100 à 130	34 – 42	58 – 68	≤ 108
	M	22 – 24	33 – 41	49 – 62	≤ 107	107 à 140	37 – 45	62 – 72	≤ 118
	L	24 – 26	37 – 45	54 – 67	≤ 114	114 à 150	41 – 49	67 – 77	≤ 128
	XL	26 – 29	40 – 48	56 – 69	≤ 121	121 à 150	44 – 52	69 – 79	≤ 138
	XXL	29 – 32	43 – 51	62 – 75	≤ 121	–	47 – 55	75 – 85	≤ 138

Hauteur[3]	Jambe (A)-(C)	Pointure
Normal	≤ 75	36/40
Long	≥ 75	37/41

Hanches, (M) Cuisse, (C) Mollet : Prise de mesures à l'endroit le plus large.
(B) Cheville : Prise de mesures 3 cm au-dessus de la malléole, sur la partie la plus fine.
(A) - (C) Jambe : Du sol à l'entrejambe.

Guide d'entretien

Pour prolonger la vie de vos produits, utilisez un filet de lavage.
① Lavez en machine, programme délicat à 30° C.
② N'utilisez pas d'assouplissant.
③ Séchez loin de toute source de chaleur.

Hanches

[1] Size / Talla / Tamanho / Cỡ Số / Maat / Μέγεθος / مقاس (cm) [2] Valable pour tailles standard, (B) et (A) [3] Height / Altura / Altura / Höhe / Hoogte / Yüksekلارتفاع (cm)

*Deux fois plus résistant que l'ancien produit grâce à ses zones renforcées talon, semelle, pointe : Test martindale : produit actuel : pointe 5/5, talon 5/5, semelle 4/5 (ancien produit : pointe 2/5, talon 5/5, semelle 3/5) - Grand confort : 94 % de satisfaction - Étude Harris Interactive auprès de 31 femmes - classe 2 - Février 2021 - Facile à enfiler : 77 % de satisfaction - Étude Harris Interactive auprès de 31 femmes - classe 2 - Février 2021 - Adapté à la morphologie : 91 % de satisfaction - Étude Harris Interactive auprès de 31 femmes - classe 2 - Février 2021 - Sont idéals pour une utilisation au quotidien : 93 % sont d'accord - Étude Harris Interactive auprès de 31 femmes - classe 2 - Février 2021.

FIGURE 5.1: Sizing table of Sigvaris stocking model

Currently, Sigvaris has a sizing chart for three morphologies. In their terms, they call these morphologies "Standard", for average measurements, "Morpho minus", for smaller calf and thigh measures, and "Morpho plus" for larger sizes that do not fit the standard proportions. For the "Standard" sizing chart, they have 6 sizes (XS, S, M, L, XL, XXL) available, for the "Morpho minus" 4 sizes (XS, S, M, L), and for the "Morpho plus" 5 sizes (S, M, L, XL, XXL). In addition to this, each size is available in two lengths, which gives a total of 30 sizes for a stocking model.

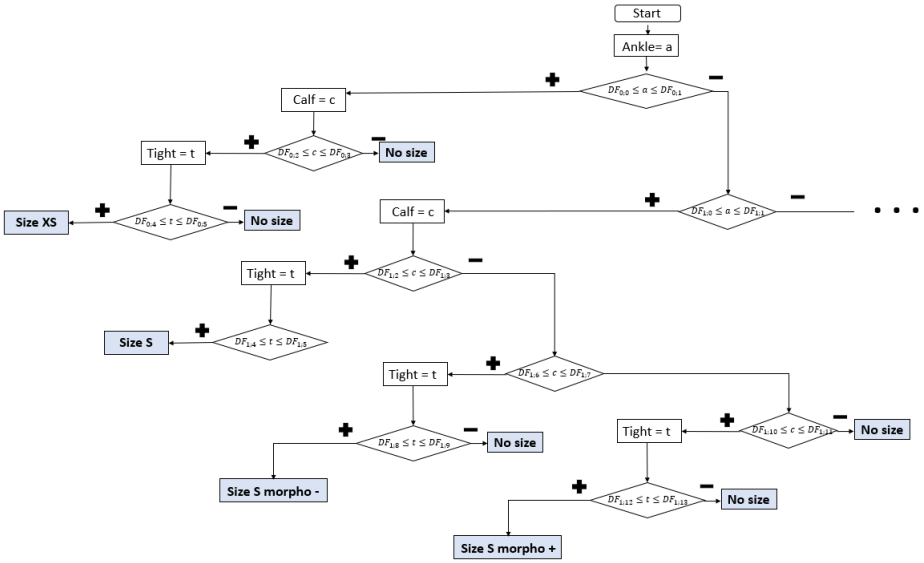


FIGURE 5.2: Size assignment for current Sigvaris Medical compression stockings with the help of a decision tree

To identify to which measure a new patient belongs, three circumferential measurements are taken at the smallest girth of the ankle, at the calf, and at the largest girth of the upper thigh. Based on this knowledge, we have built up a logic of sizing assignment with the help of a decision tree, illustrated in Figure 5.2, that first identifies to which range of ankle measurement the subject belongs to, then it starts to search for the calf range then the thigh range and finally it assigns the correct size, in case it is available. Based on this

evaluation, Table 5.1 shows the size distribution of our 258 subjects, where we can also notice that 55 subjects, making up 21.3% of the total population, could not be assigned a proper size.

Size	Total	Male %	Female %
XS	2	50	50
S	67	28.36	71.64
M	72	36.1	63.9
M+	2	100	-
L-	11	54.55	45.45
L	31	38.7	61.3
XL-	6	50	50
XL	10	60	40
XL	1	-	100
XXL	1	-	100
No size matching	55	43.6	56.4

TABLE 5.1: Percentage distribution by size and gender

In Figure 5.3, we can visualize the size distribution of our database with the help of the circumferential curves, where we can observe that even though the algorithm has identified for 78.7% a matching size, the progressive evolution of the circumferential values does not entirely match. We can take as an example size XS with the two subjects, male and female, the lower leg perfectly superposes, but starting from the knee region, they are very different. Similar differences can be visualized in other size groups as well.

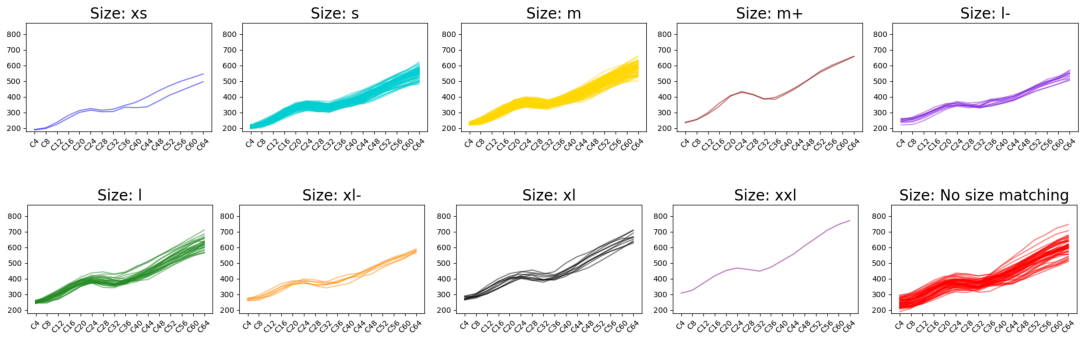


FIGURE 5.3: Sizing distribution visualized with the circumferential evolution curves (heights not considered)

5.3.1 Identification of circumferential evolution patterns

Building on the idea that we have developed in Chapter 3, where we have attempted to classify the 2D shape descriptors in 4 distinct groups, 3 of which have proven to identify similar circumferential evolution patterns, in this Chapter, we will further analyze the evolution curves to find all the distinct patterns that are contained in our database.

In the state of the art, we have already reviewed the work of Liu et al. [146], who have evoked the logic of classifying the leg into two parts: above the knee and below the knee. For this, they have used two parameters: the cosine value of the angle described by the calf and the two adjacent points on a similar curve as what we are presenting, and a gradient value of the upper thigh, which can be lower or higher. In our case we evoked the variables identified by the PCA, which were the C4, C8, C12, C16, C20, C24 (describing the lower leg below the calf) and the C36 and C48 (describing the knee and mid thigh variation), and we performed the 2D classification algorithm described in Chapter 3 on these two segments separately to better distinguish the evolution patterns in our data.

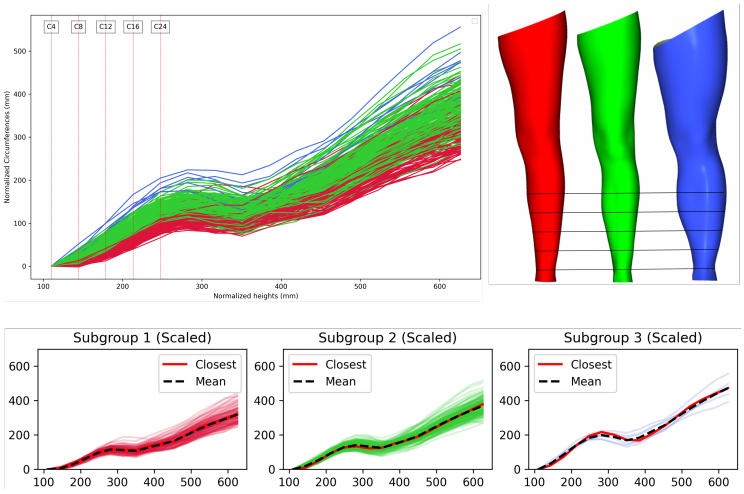


FIGURE 5.4: Three ankle groups

As Figure 5.4 illustrates, the algorithm has found 3 lower leg evolutions that separate well and each describes a different development of the lower leg soft tissue, one having a less developed muscle mass, one that is more like an average, and one that is likely to have more subcutaneous fat present in that area. In terms of the upper leg development in the two designated areas (knee and mid-thigh), the algorithm highlighted 8 evolution groups, which are illustrated in Figure 5.5. In case of the lower thigh circumference value groups like 2,4,5, and 7, we can observe a sort of "break point" in C48, and in case of higher values like group 1 and 3, we notice a convex curving in C60.

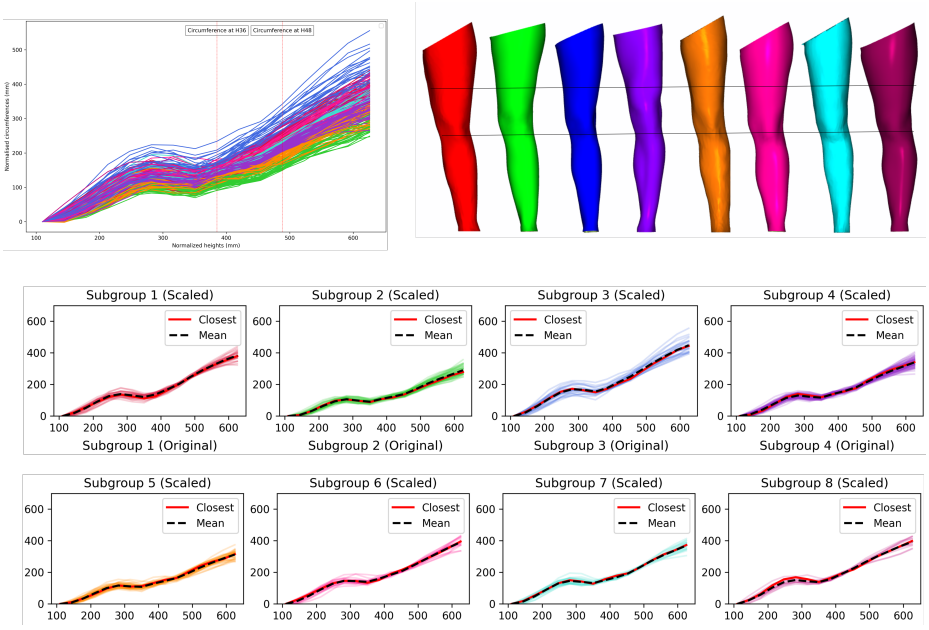


FIGURE 5.5: Eight thigh groups

If we combine these two results, it would give us 18 combinations: 8 groups for the 1^{st} type of ankle, 8 groups for the 2^{nd} type of ankle, and 2 groups for the 3^{rd} type of ankle. These new groups are visible in Figure 5.6, and they have a higher intergroup superposition than in our previous attempts.

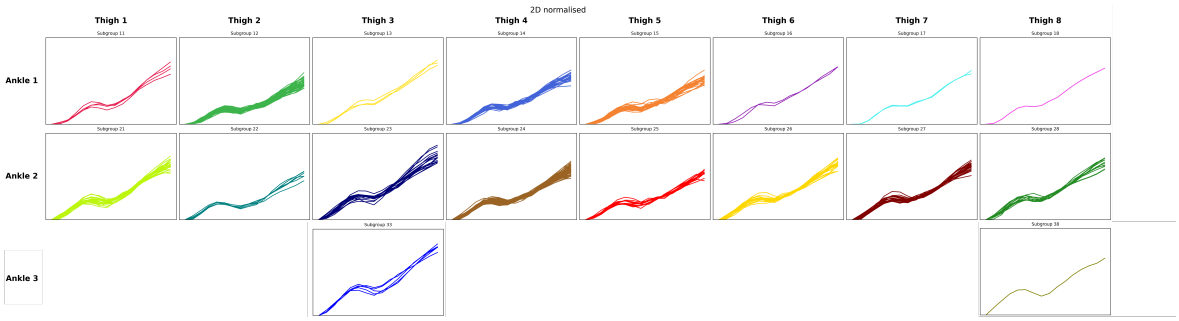
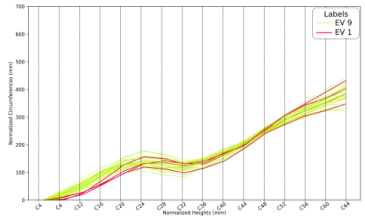
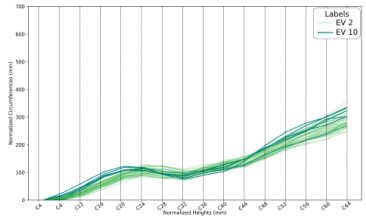


FIGURE 5.6: 18 groups identified as unique patterns

To illustrate the differences between our groups, we took two examples of two subgroups with similar thigh region and different lower leg region and superposed them in Figure 5.7a (higher thigh values) and Figure 5.7b (lower thigh values). We can observe that indeed the subgroups significantly differ in the lower leg region. Highlighting these differences and including them in the sizing logic and overall design of compression products is particularly important as Compression stockings apply the highest pressure at the ankle, gradually decreasing it towards the thigh; therefore, such a difference that we have illustrated could have a high impact on the pressure when it is considered. The impact of different lower leg evolutions compared in the case of the eight thigh evolutions is illustrated in Appendix D.



(A) Comparison of similar upper leg evolution (1^{st} class) with different ankle evolutions (ankle 1 and ankle 2)



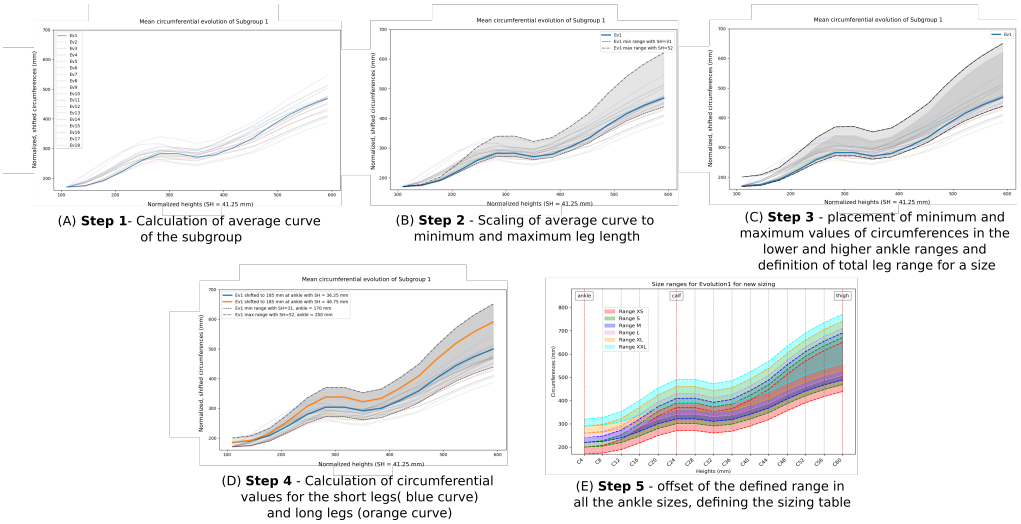
(B) Comparison of similar upper leg evolution (2^{nd} class) with different ankle evolutions (ankle 1 and ankle 2)

FIGURE 5.7: Visualization of similar thigh region and different lower leg region

5.3.2 Creation of sizing tables

To create a sizing table for each of the identified subgroups, we created a process composed of five steps:

- **Step 1:** Computation of the mean evolution curve of each subgroup (Figure 5.8a.).
- **Step 2:** Scaling of the mean evolution curve to reach the minimum (527 mm) and maximum (884 mm) leg length values, with the equation 3.1 presented in Chapter 3 (Figure 5.8b.).
- **Step 3:** Based on the ankle ranges defined by Sigvaris, we shift the minimum mean values (scaled to 527mm) on the lower ankle boundaries (ex. for size XS, this would be 170 mm) and the maximum mean values (scaled to 884 mm) to the higher ankle boundaries (ex. for size XS, this would be 200 mm). We define the area contained between these two boundaries as the range for a specific size (Figure 5.8c.).
- **Step 4:** Calculation of circumferential values for short legs (616 mm) as well as for long legs (795 mm) (Figure 5.8d.). These two curves will be the directing circumferential values for the calculation of the compression stocking size, which should be available in two lengths.
- **Step 5:** Offsetting the defined leg range to all the available sizes (XS, S, M, L, XL, XXL). (Figure 5.8e.).



(A) **Step 1**- Calculation of average curve of the subgroup

(B) **Step 2** - Scaling of average curve to minimum and maximum leg length

(C) **Step 3** - placement of minimum and maximum values of circumferences in the lower and higher ankle ranges and definition of total leg range for a size

(D) **Step 4** - Calculation of circumferential values for the short legs(blue curve) and long legs (orange curve)

(E) **Step 5** - offset of the defined range in all the ankle sizes, defining the sizing table

FIGURE 5.8: Five steps of creating a sizing table for the identified circumferential evolutions

5.3.3 Creation of recommendation system

To facilitate the choice of size in case of a new subject, we have developed a second application that can decide the size of compression stockings needed through multiple steps: a decision tree

Custom-made rule-based decision tree classifier Objective: Decide in which range of the 18 sizing tables the new subject belongs to. Decision trees are one of the most popular machine learning methods that are used to guide a decision process [173]. The defined decision tree classifies the input data based on a multidimensional condition matching system. First, it receives values from the user corresponding to the circumferential values $C_4, C_8, C_{12}, C_{16}, \ldots, C_{60}$ and the value of the leg length, which are retrieved from a user interface. The rules based on which the decision is made are stored in a single table, which contains the minimum and maximum values of each variable throughout 18 sizing tables and the decisions that need to be taken when a condition is met.

In other words, if all the introduced values can be found in a specific sizing table range, the tree will return the size and the name of the sizing table.

$$\begin{bmatrix} C4_{\text{min XS}} & C4_{\text{max XS}} & C8_{i\text{ min XS}} & C8_{i\text{ max XS}} & C12_{i\text{ min XS}} & C12_{i\text{ max XS}} & \dots & C60_{i\text{ min XS}} & C60_{i\text{ max XS}} & R_iXS \\ C4_{\text{min S}} & C4_{\text{max S}} & C8_{i\text{ min S}} & C8_{i\text{ max S}} & C12_{i\text{ min S}} & C12_{i\text{ max S}} & \dots & C60_{i\text{ min S}} & C60_{i\text{ max S}} & R_iS \\ C4_{\text{min M}} & C4_{\text{max M}} & C8_{i\text{ min M}} & C8_{i\text{ max M}} & C12_{i\text{ min M}} & C12_{i\text{ max M}} & \dots & C60_{i\text{ min M}} & C60_{i\text{ max M}} & R_iM \\ C4_{\text{min L}} & C4_{\text{max L}} & C8_{i\text{ min L}} & C8_{i\text{ max L}} & C12_{i\text{ min L}} & C12_{i\text{ max L}} & \dots & C60_{i\text{ min L}} & C60_{i\text{ max L}} & R_iL \\ C4_{\text{min XL}} & C4_{\text{max XL}} & C8_{i\text{ min XL}} & C8_{i\text{ max XL}} & C12_{i\text{ min XL}} & C12_{i\text{ max XL}} & \dots & C60_{i\text{ min XL}} & C60_{i\text{ max XL}} & R_iXL \\ C4_{\text{min XXL}} & C4_{\text{max XXL}} & C8_{i\text{ min XXL}} & C8_{i\text{ max XXL}} & C12_{i\text{ min XXL}} & C12_{i\text{ max XXL}} & \dots & C60_{i\text{ min XXL}} & C60_{i\text{ max XXL}} & R_iXXL \end{bmatrix}$$

$$\text{for } i = 1, \dots, 18$$

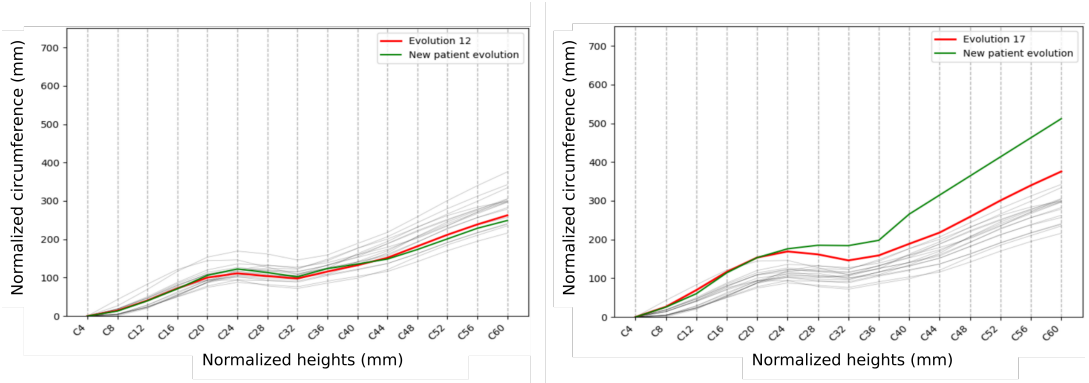
The data gets filtered first by the value of C4, the algorithm checks if the values are in the row of XS (170-200 mm), S (200-220 mm), M (220 - 240 mm), L (240-260 mm), XL (260-290 mm) or XXL (290-320 mm). This step determines in which row the algorithm should continue to search for the rest of the values. For each of the remaining variables from C8 to C60, the function checks whether the input lies within a series of successive column-based intervals in the filtered row(e.g., columns 2-3, 30-31, ..., 504-505 for C8):

$$\begin{bmatrix} C4_{1\text{ min XS}} & C4_{1\text{ max XS}} & C8_{1\text{ min XS}} & C8_{1\text{ max XS}} & \dots & C8_{2\text{ min XS}} & C8_{2\text{ max XS}} & \dots & C8_{18\text{ min XS}} & C8_{18\text{ max XS}} \\ 0 & 1 & 2 & 3 & \dots & 30 & 31 & \dots & 504 & 505 \end{bmatrix}$$

If a condition is met, the corresponding case number is added to a list. After evaluating all inputs, the function computes the intersection of all lists, which represents all the cases where a sizing table was assigned for all C8 - C60. We then map each correct case with a specific column in the sizing table. For example, if the list chose size XS and subgroup 5, it will return the value in row 0, column 510. In case a subject was found in multiple sizing tables, the function will return all the possible options.

Pattern recognition Objective: Compare the new subject's circumferential evolution to the existing 18 circumferential means (ground truth for each

cluster) defined by the unsupervised classification, and find the matching cluster. To achieve this objective, the input data, taken from the new subject, was normalized with equation 3.1 and brought to the same condition as the mean evolution to ensure comparability in the Euclidean space. The reason behind this comparison was to select the curve that is the closest in the Euclidean space to our new instance, which will allow us to select the correct sizing table, and it would mean that the volumetric growth of the new subject follows a similar circumferential growth as one of the defined clusters. To measure the similarity of the new instance with the existing ground truths, the same distance matrix has been computed as what has been used in the construction of the similarity graph for the spectral clustering algorithm. A wrong match can be identified in the case where the algorithm would send back as the most similar curve the name that is not present in the available ranges defined in the previous step. In that case, it would mean that the distance in a specific point on the curve is too large and does not fit the predefined sizing ranges. This case is illustrated perfectly in Figure 5.9b., where the algorithm named Evolution 17 is the closest ground truth evolution curve for subject 212, who has been removed from the database, being identified as anomalous geometry in Chapter 4. These subjects did not fit any sizing table range; therefore, being identified as part of the 17^{th} subgroup is false. This also justifies the need to use both sizing table range identification and pattern recognition as part of the final and more refined size assignment.

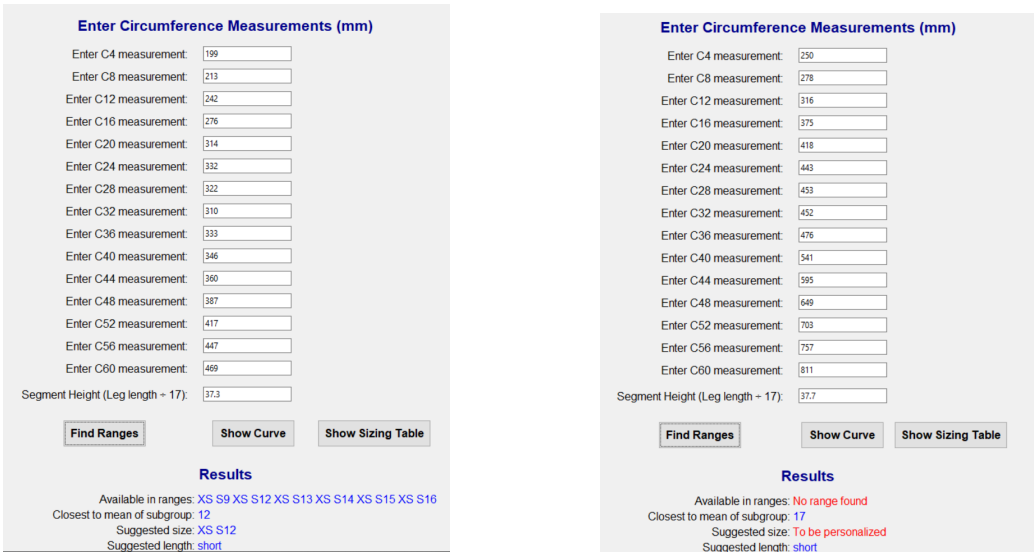


(A) Ground truth assignment for subject 185, where the recommended evolution is very close to the real leg evolution

(B) Ground truth assignment for subject 212, considered as outlier, where the recommended evolution is very close to the real leg evolution

FIGURE 5.9: Visualization of a correct and wrong ground truth assignment

Final size proposal Objective: Compare the results of the two previous steps to correctly identify the real size of the new patient. This objective is fulfilled by a simple verification of the available range list obtained at the first step by the decision tree: if the evolution number obtained by the curve comparison can be found in the proposed list, then the algorithm will return a single element from the mentioned list, which suggests the correct size. Going back to the example of the two subjects evaluated with the curve comparison, the final results for both subjects would be given as Figure 5.10a and Figure 5.10b illustrates: the first subject would be assigned a short XS product designed for Evolution 12 and the second subject wouldn't have a matching size, directing them towards a personalized product. As this example points out, the algorithm will assign either a short or a long stocking, which is a simple decision taken based on the leg length entered in the interface. Given two thresholds for each length, this is rather a simple task to program. Research shows that height dimensions vary less within a population; therefore, it is commonly divided into a lower number of intervals [144]. The thresholds for the short and long products are derived from the current database.



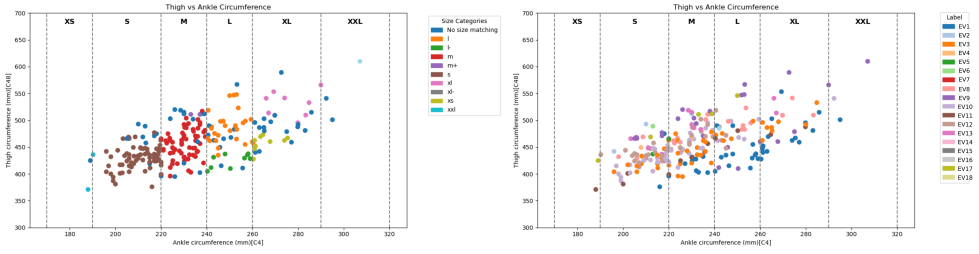
(A) Correct assignment of size

(B) Suggestion of personalization

FIGURE 5.10: Two case scenarios as the outcome of the user interface

5.4 Results

In this section, we are going to present the results related to the found Circumferential evolution groups, highlighting a comparison between the morphological groups found in Chapter 3 and the above-described size groups and the Sigvaris sizing.



(A) Data distribution of Ankle size (C4) and Upper Thigh size (C60) by Sigvaris sizing

(B) Data distribution of Ankle size (C4) and Upper Thigh size (C60) by Evolution type

FIGURE 5.11: 2D scatter plots showing the data distribution of ankle size and upper thigh size, colored by the current Sigvaris sizing and the identified 15 Circumferential evolutions (groups with only 1 subject removed)

In Figure 5.11, we have illustrated the distribution of our dataset based on the ankle size at C4 and upper thigh size at C60. Figure 5.11a. shows this distribution colored by the sizes of Sigvaris, with the gray points marking subjects without a proper fit. Based on this analysis, we can see that the sizing lacks linear logic: subjects with similar ankle sizes can have a significant difference in thigh size. On the other hand, when we observe Figure 5.11b., where we have colored the same distribution according to the identified evolutions, we can see that our system has correctly identified pattern in the data, showing a tendency of growth in a diagonal direction, meaning that as the ankle size grows, the thigh size grows grows as well, and this is true to all the values along the leg length. Figure 5.12 illustrates the linear regression analysis that has been performed on the group of Evolution 13, using the scikit-learn Python library [100]. Within this highlighted group, ankle circumference was strongly predictive of thigh circumference (slope = 1.4, R^2 = 0.90). The high coefficient of determination suggests a powerful linear association, with ankle circumference explaining 90% of the variance in thigh circumference; therefore, the ankle size is an excellent predictor of thigh size for this group, which we can use for the parametrization of the adaptive model

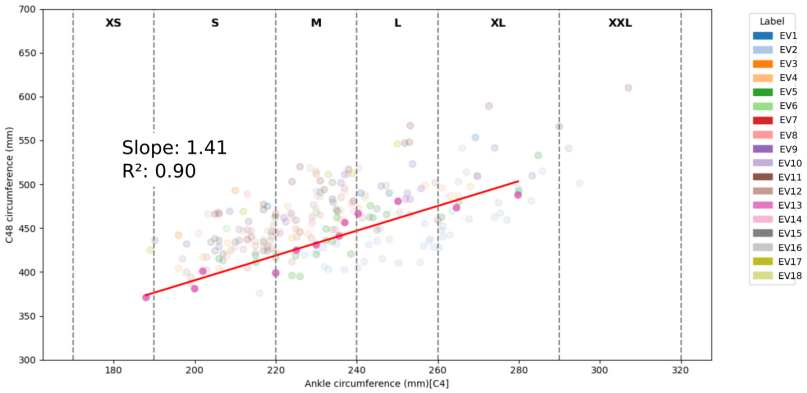


FIGURE 5.12: Simple regression line fit on the cluster of the 13^{th} evolution

Figure 5.13 shows the 13^{th} evolution group in the three states of data transformation, separated by the Sigvaris sizes. On subplot a., the available sizes appear offset along the leg, the evolution remaining very similar, which is a good indicator of the above-described linearity. On subplot c., where the evolution lines are superposed at C4, they are also very close in value at C48. On this same figure, it can also be observed that the subjects of this group are included in a very minimal range; the shape of the different sizes changes: the segment between C32 and C44 has a sharp peak in C36 for XS, which gets smaller by the increase in size, until it disappears for size L. This shows that there is a tendency for shape change between sizes.

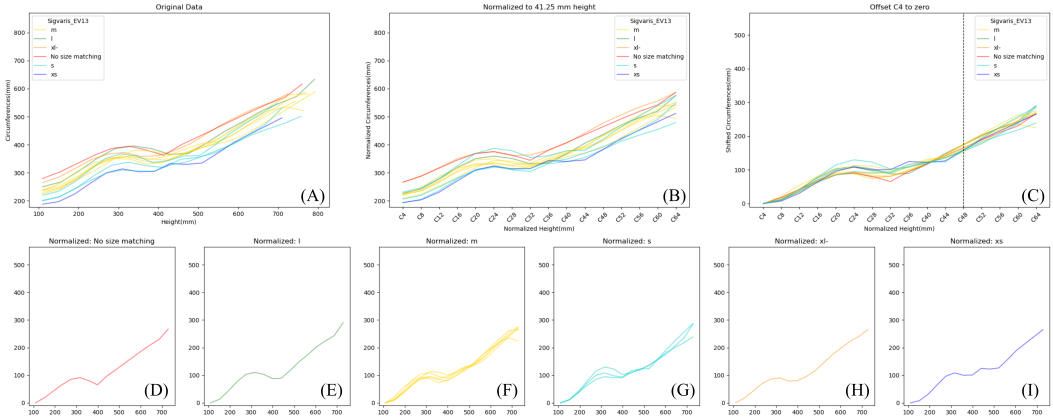


FIGURE 5.13: Evolution 13, illustrated in the three data forms, separated by Sigvaris size

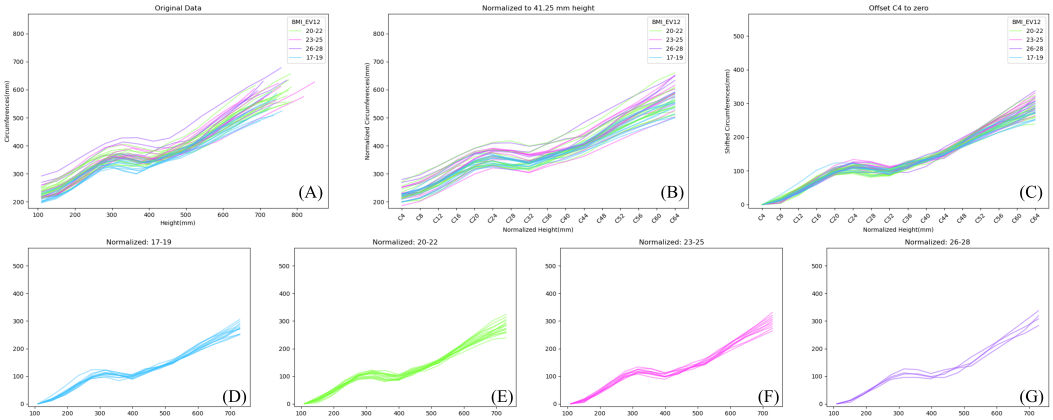


FIGURE 5.14: Evolution 12, illustrated in the three data forms, separated by Body Mass Index (BMI), with no difference in shape between BMI's

Figure 5.14 is an example of evolution (EV12), which demonstrates how the body mass index does not influence the shape of the group's individuals, while Figure 5.15 shows an example (EV4), where subjects with lower BMI (17-19), have a different shape that subjects with a higher BMI (23-28). This proves that BMI is not a good indicator of shape, because it is not consistent throughout the database, and this question needs to be further studied.

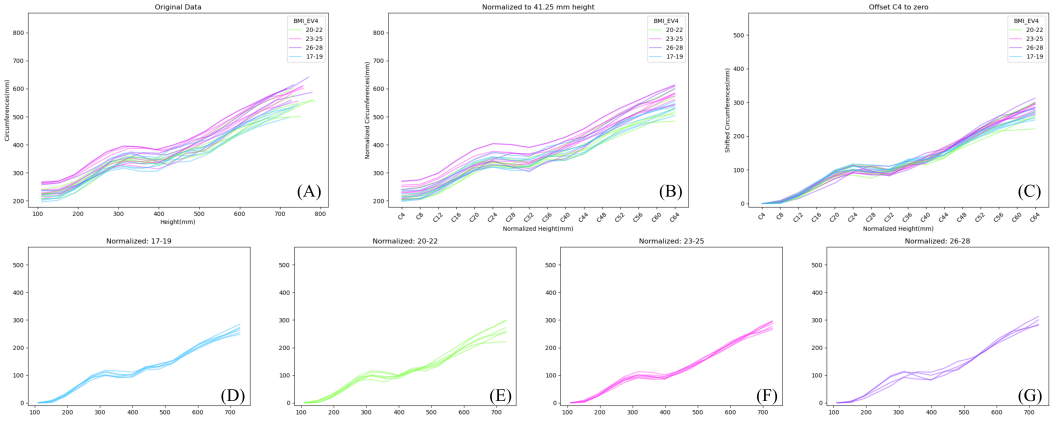


FIGURE 5.15: Evolution 4, illustrated in the three data forms, separated by Body Mass Index (BMI), with shape difference between BMIs

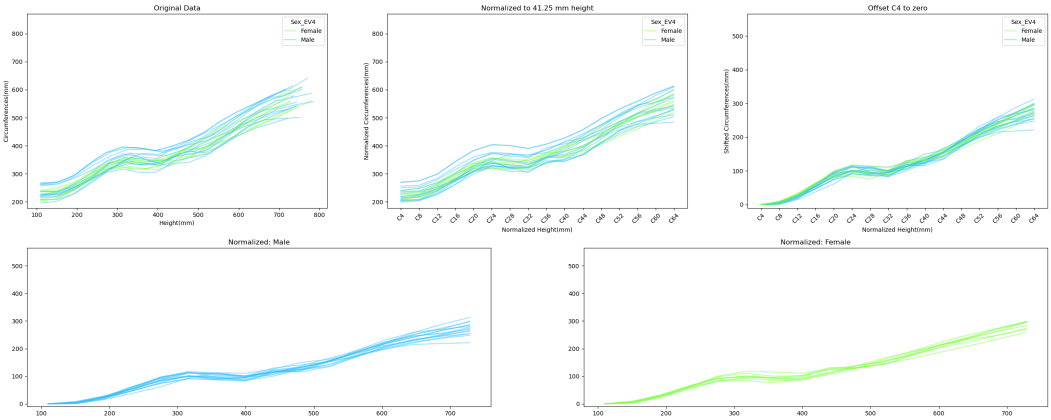


FIGURE 5.16: Evolution 4, illustrated in the three data forms, separated by Gender, with overlapping shapes between genders

In terms of sexual dimorphism, one interesting difference that we have found is the uneven growth of the lower leg region between C8 and C24, where women tend to have a straight evolution and men have a "s" shape evolution (concave-convex).

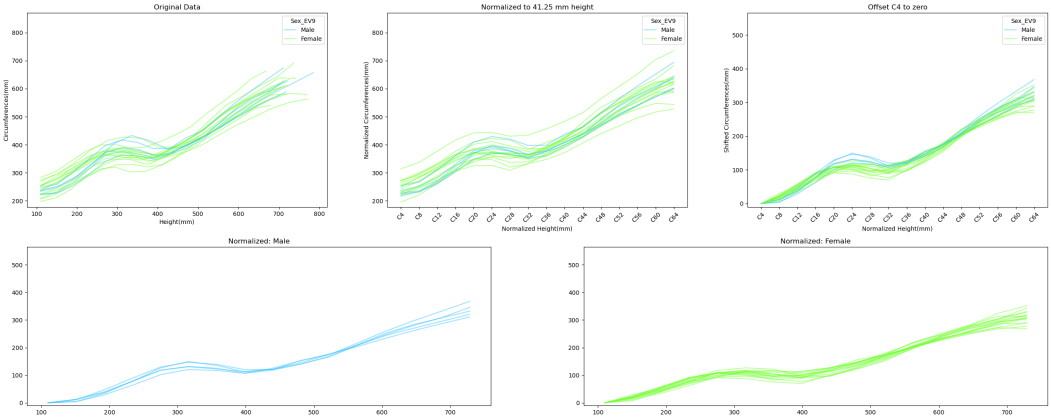


FIGURE 5.17: Evolution 9, illustrated in the three data forms, separated by Gender, with growth difference between male and female legs

This phenomenon is observed mostly in the case of Ankle group 2 and Ankle group 3, and not in the case of Ankle group 1, where men's data and female data overlap. These two cases are best illustrated with Figure 5.16,

where women have the same evolution as men, and Figure 5.17, where the two genders differ. This can be because men have a larger muscle mass than women (larger calf with minimal fat deposit); on the other hand, women tend to have more fat deposits than men.

The remaining factor that we needed to study was the three morphological groups and how these postural changes influence the identified evolutions. Figure 5.18 answers this question by highlighting the groups where we have found at least two of the three morphologies. The mean shape has been calculated for each group, and the differences are mostly only visible in the position of the lower leg. This makes us conclude that the posture of the leg, even if it is linked to a skeletal deformation, does not influence the way the soft tissues develop around the bone. The three morphologies defined in Chapter 3 are not directly linked to any of the specific Evolutions, which led us to the conclusion that making the "normal" postured leg (Morphotype 2) adaptable to all the above described evolutions would be an acceptable solution for sizing table driven parametrization and having the three postures adaptable to any Evolutions would increase the ability of the proposed method in terms of personalization.

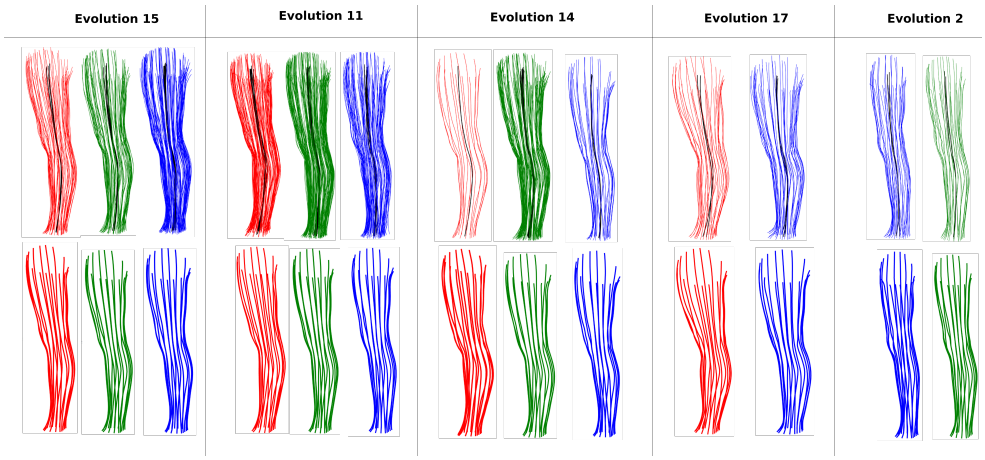


FIGURE 5.18: Visualization of a correct and wrong ground truth assignment

5.5 Conclusions

This chapter was dedicated to the identification of the current sizing system problem for medical compression stockings and the development of a more reliable and more inclusive sizing system. On the one hand, it has been proven that up to 21% of the subjects composing the studied database could not find a proper fit from the ready-to-wear range, proposed by Sigvaris. This is a rather large number of patients, who would be left with products that would not provide the correct therapeutic effect in the treatment of CVI. As a second objective, we have identified 18 circumferential evolutions that can cover the overall population (without counting the anomalous data), with the help of which we could construct new sizing systems that are more inclusive and more precise, with ranges stricter than that of the current sizing system. To facilitate the medical professionals and industrial partners to choose the correct size, we have designed a user interface that works as a recommendation tool, using a 3-step logic in identifying the proper size for a new patient.

The identified 18 subgroups describe highly detailed growth patterns, dividing the population into two different levels: based on the lower leg growth, where the precision is higher, and based on the thigh growth, where the precision decreases. Additionally, they are showing a linear growth pattern between sizes, which is an advance in comparison to the existing sizing system. We have found that the ankle is a driving parameter in growth, as most of the evolutions can be found in each ankle size category; therefore, this variable can be used as a key parameter in the creation of the adaptive model. We have also discovered that the BMI and gender are two factors that can influence the shape of circumferential evolution within the same group, but

they are not applicable as an absolute rule, as these observations do not repeat in all cases. It has been also noted that the three morphologies defined in Chapter 3 are not directly linked to any of the specific Evolutions, which led us to the conclusion that making the "normal" postured leg (Morphotype 2) adaptable to all the above described evolutions would be an acceptable solution for sizing table driven parametrization and having the three postures adaptable to any Evolutions would increase the ability of the proposed method in terms of personalization.

As in the industry, a large number of read-to-wear products proposed in a large number of sizes is very contraindicated because of fabrication constraints. We acknowledge that proposing 18 different evolutions in 6 sizes and 2 lengths each is unrealistic. Still, our approach represents a major step towards facilitating the personalization process of compression products, as we have identified a volumetric growth logic that allowed us the fully personalization of the parametric leg, which can be used directly in the 3D design of Compression products. In conclusion, this chapter summarizes preliminary results on a sizing system-based decision aid tool, usable in the healthcare and industrial sectors of MCS. An extended discussion of these findings will appear in forthcoming journal publications.

Chapter 6

Creation of adaptive morphotypes

6.1 Introduction

Parametric human models have been introduced with the purpose of simulating real body shape and measurements for virtual fashion in the context of evaluating the fit of garments or even virtual ergonomics [65] often with application in product sizing [174] or creation of adjustable physical mannequins [18]. A parametric human model can be defined as a model that is generated automatically with the help of parameters and measurements obtained from humans, by accounting for morphological or biomechanical properties of a target population [175]. Principal Component Analysis is a staple method used in shape analysis and parametric modeling [65], by learning linear regression between variables, and models created this way have to be able to simulate individual body shapes by using measures obtained in non-laboratory environments. Research shows that two-dimensional sizing techniques are not sufficient on their own to adequately describe the 3D body and parametrize it accordingly. For this, it is necessary to combine quantitative measurements with the corresponding 3D shapes [144]. The currently existing conflict between sizing systems and product development has not been sufficiently explored, which directly affects how the consumers may

experience the garment [19], especially when the garment should act as a second skin, in the case of medical compression stockings. Pattern development is limited to 2D drafting, which relies on proportional expectations, and transforming these products into 3D is rather difficult [19]; nevertheless, this type of pattern making is a time-consuming operation. More efficient pattern creation strategies are essential to incorporate the size and shape variation of a given population in the design process and to find the best connection between fit, size, and shape. Proper fit and sizing could enhance clothing comfort, as sensed by consumers and revolutionize the manufacturing industry [176] with possible evolvement in sustainable fabrication [18]. Through a 3D CAD system, product development could be sped up [21] by reducing manual workflow, and it could represent a potential option for custom-fit products, with the condition that the represented body shapes include diversity.

This Chapter is dedicated to the development of 3 parametric morphotypes that can be adapted to different circumferential evolutions defined in Chapter 5, with the help of which we could direct the development of compression garments to a personalization strategy. These adaptive morphotypes would encompass fit, size, shape, and functionality in one user interface, offering the option of fast product development for the industry, an easy recommendation tool for medical professionals, and most importantly, wearing comfort for patients.

6.2 Background and literature review

Serwatka et al. [177] have developed an adaptive female body morphotype for the ready-to-wear industry, which allows the automatic grading of garment patterns, created directly on the 3D mannequin in a CAD environment.

Garment patterns are generated according to a chosen size, facilitating instant manufacturing. The parametric morphotype model is a surface representation of a real person's scanned body, obtained by segmenting the body at anthropometrical heights and creating a wireframe-like structure that is controlled by different types of parameters. These parameters can be linked to limb length or height, to volume change, and distribution between anterior and posterior parts. To control the adaptive morphotype, two command variables are used: the stature (height) and the chest girth. The limbs also change size with the torso, and they have achieved these changes through linear and non-linear techniques, always dependent on the morphology of the mannequin. Their validation technique was to compare the original mannequin and the adapted mannequin after significant alterations of the stature and chest circumference, which in the end corresponded to the real shape of the scanned subject.

Hamad et al. [178] performed an unsupervised classification on a large set of 3D scans of female torsos (478 scans of French women) and extracted three morphotypes that represent the cluster populations. Similar to Serwatka et al. [177], they implemented an adaptive morphotyping approach, where the subject, representing the morphotype, was segmented in specific anthropometric zones to extract contours of the body shape and to create a symmetric torso wire-frame, driven by parameters and scaling axes. On this wireframe, the body's surface has been reconstructed to represent the parametric body. The adaptive mannequin can change volume and height based on dimensions taken from the sizing system developed at the classification stage. The mannequin is linked to a pre-calculated spreadsheet, through which the mannequin adapts to different sizes while maintaining its specific morphological type. The adaptive morphotype mannequin serves as a base for size systems and is a key component for virtual clothing try-on in the textile and

clothing sector.

An interesting example of user-specific adaptive modeling is presented in the works of Mosleh et al. [179], who studied the morphological deformation of subjects suffering from Scoliosis, which is an abnormal lateral curvature of the spine. First, they have created an adaptive 3D Vertebrae model that can adjust to a healthy subject as well as to a Scoliosis patient. They have completed the entire upper body skeleton, adding the thorax, clavicle, and scapulae. This 3D model follows the deformation of the spine and adjusts to the size and morphology of the patient. This parametric skeleton was placed in the interior of a healthy person and of a scoliosis patient, and a 3D adaptive garment was designed using the skeleton as a base with added ease allowances to fit the 3D bodies. Their experimental results show that by deforming the skeleton to a specific curvature of the spine, they can automatically adapt the 3D garment to fit the patient correctly, contributing to thermal comfort and overall well-being of the patient.

In the case of functional compression garments, such as medical compression garments, there have been advancements presented in the parameterization of the lower leg region to enhance the compression accuracy. This study was conducted by Xi et al. [14], who proved that relying purely on anthropometric parameters is not sufficient in the case of this product and that the real shape of the calf's curve is necessary. Their methodology involved the study of the circumference profile of the lower leg (between the lateral malleolus and the knee) of a population of 225 subjects suffering from CVI. Through PCA, they have identified that with only the first PC, which accounted for 96% of the total variations, they could create a parametric model using linear regression. The variance through the first PC that they have described has three components:

- straight or bent anterior tibia
- thick or thin gastrocnemius muscle (calf muscle)
- bulging or flat tibialis anterior muscle

Their model allows the reconstruction of the calf shape of an individual based on a sizing factor (according to the study, this factor is situated at 60% height between the lateral malleolus and the knee of the individual) and a corresponding ratio, which represents the deviation of the individual's calf shape from the average calf shape. To validate their approach, they have compared the reconstructed calf to a randomly chosen individual's real calf shape. The statistical analysis showed an average similarity of 0.8527, pointing out that the errors have occurred in the ankle and knee region. The proposed model was used to customize the size design of MCSs and evaluate the pressure mapping of MCSs.

6.3 Methodology

One of the main objectives of this thesis is to develop adaptive leg morphotypes to optimize the size and fit of medical compression stockings. In this section, we will present the methodology used to create such a parametric model that is directly linked to a sizing system.

6.3.1 Visible Human Project and bone center identification

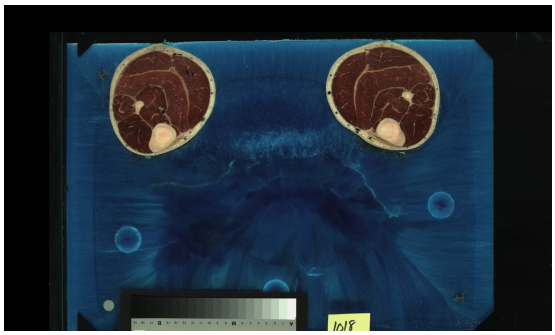
We hypothesize that the volumetric growth of the soft tissue in the leg happens around the leg bones (tibia and femur), and especially in the case of the tibia, which is situated in the anterior compartment of the lower leg, this volumetric growth is not centralized. The majority of the muscles are developing behind the tibia, and there is less soft tissue in front than behind (Figure

6.1a). When we want to apply volumetric growth to a leg cross-section, the center of the bone will be a guiding point, instead of the overall barycenter of the leg contour. For this, it is necessary to identify the bone center of all the leg contours in the 17 heights, already presented in Chapter 3. For this, the Visible Human Project is an ideal source as it includes digitized photographic images from cryosectioning, digital images derived from computerized tomography, and digital magnetic resonance images of a male and a female cadaver [180], usable for the study of human anatomy, and it is a common public-domain data. One of the main steps of this task is to identify the corresponding 17 anatomical levels in the Visible Humans. The "Visible male" has a height of 1,871 m, and the images of the anatomical cross sections are taken at each 1 mm, while the "Visible female" has a height of 1.71 m and has an image taken in every 0.33 mm. This way, they are composed of 1871 and 5189 cross-sectional images. The two landmarks, denoting the leg length, the lateral malleolus, and the crotch point, are also easily identifiable in the case of the anatomical sections. This way, we were able to extract the two images from both subjects and calculate the number of images contained between two heights. This way, we can know the length of the leg and the segment height (leg length/16) for both subjects:

- **Visible male**: leg length = 768; segment height = 48; each 48^{th} image between the lateral malleolus and the crotch has been extracted
- **Visible female**: leg length = 640; segment height = 40; each 120^{th} image between the two landmarks has been extracted

Figure 6.1a and 6.1b show the male and female calf anatomic cross-section, where we can observe that the male has more muscle mass, with limited fatty tissues and well-developed calf muscle, and the female has a larger subcutaneous fat ratio. This observation can be made along the entire set of cross

sections of both legs. We can also observe that the images of the male subject are taken with the leg in an "A" position, while the images of the female subject are taken with the legs placed next to each other. This is the reason why we have opted for the use of the male subject, as it corresponds to the scanning "A" position of the morphotypes.



(A) Anatomical cross section of the male calf



(B) Anatomical cross section of the female calf

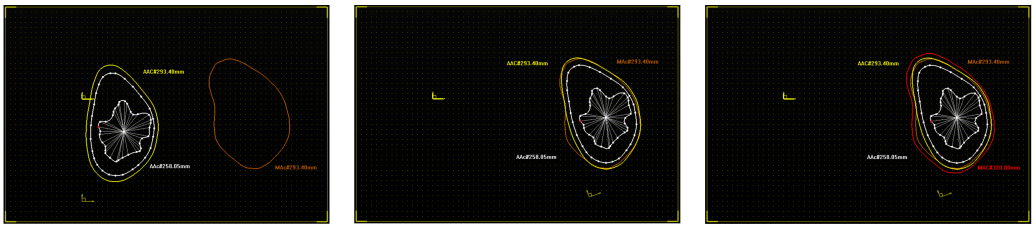
FIGURE 6.1: Cryosectioning of the human leg at the level of the calf [181]

To identify the bone centers, each anatomical section has been imported in the form of a bitmap in Design Concept V4 from Lectra. As the pixel dimensions of the images have been given by the source, the importation was calculated as follows:

- **Height** = 1216 pixels * 0.33 mm/pixel = 401.28 mm
- **Width** = 2048 pixels * 0.33 mm/pixel = 675.84 mm

This operation was particularly important because this way the size of the images corresponded to the size of the real leg cross-section. After importation, the outer contour of the leg as well as the outer contour of the bone, has been traced with a spline curve. This operation allowed the calculation of the bone barycenter, which served as a fixed point in the upcoming point-based uniform scaling. To match the two different morphologies (the Visible male

and the morphotype), both circumferences have been measured, and the Visible male's circumference has been matched to the morphotype's value, with the above-mentioned point-based uniform scaling, to ease the matching procedure, illustrated in Figure 6.2a. With three-level transformation (rotation Z+, translation X+, translation Y+), the above-described contours of the VH have been duplicated with the center point to the same level (same plane), and the transformation values have been modified until the two subjects' contours superposed, illustrated in Figure 6.2b. This operation defined the fixed point for the morphotype, which allowed the volumetric growth in the following steps, illustrated in Figure 6.2c.



(A) Visible human cross section with new value of circumference (right) and morphotype cross section (left) both at the Lateral Malleolus level.

(B) Tranformation of the visible human cross section, until it matches the morphotype's position

(C) New point based scale of the morphotype cross section (red)

FIGURE 6.2: Methodology used for the identification of bone centers, illustrated with an example at the ankle

6.3.2 Length adjustment

After finding the fixed reference point in the previous step, the next approach is to create a logic that allows the parametric modification of the leg length. For this, we have used a method that has already been proven to be effective in the works of Serwatka et al. [177], who duplicated body cross sections to the floor and back with a value derived from body height. In the case of the leg cross sections, three values were necessary:

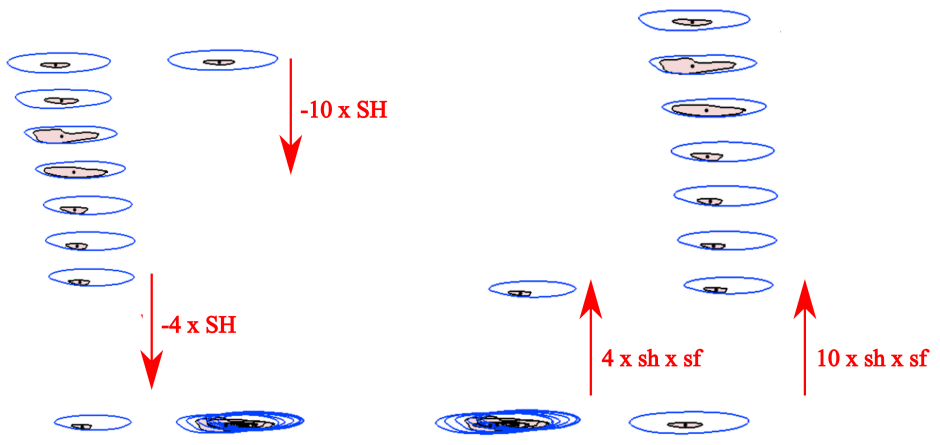
- The original Segment Height (SH) of the morphotype leg, which is equal to the distance between the crotch and lateral malleolus divided

by 16, also described in Chapter 3.

- The mean evolution's segment height (sh), equal to 41.25 mm, resulting from the normalization process also in Chapter 3.
- A size-defining segment height (nsh), which will define whether the leg would be long or short, its value varying between 36.25 mm and 46.75 mm, respectively.

Based on the last two parameters, we can define a scaling factor (sf) that is used to change the height of the new leg, and it is defined as follows:

$$sf = nsh/sh \tag{6.1}$$



(A) Translating to the floor with the original Segment Height (SH)

(B) Translating to back with a new segment height (sh) and a scaling factor (sf)

FIGURE 6.3: Methodology used to adjust the leg length

As a first step, each cross-section is translated to the floor with a multiplied value of SH. The example in Figure 6.3a. illustrates the cross sections of the leg between C16 and C40, where C16 is translated in Y^- direction with a value of $4 \cdot SH$, while C40 with a value of $10 \cdot SH$. On the contrary, when this duplication happens, it will be translated in the opposite Y^+ direction and

with the new sh value, multiplied with the scaling factor, also illustrated in Figure 6.3b.

6.3.3 Volume and size adjustment

A new set of circumferential values has been introduced for each of the levels from C4 to C64, serving as a placeholder for the 18 mean circumferential evolutions identified in Chapter 6. These parameters have been entitled as $C4_n, C8_n, C12_n, \ldots, C64_n$, and they are linked to an excel sheet, that allows the importation of the 16 values simultaneously. As the sizing tables are defined for a set of sizes ranging from XS to XXL, the adaptive morphotype has to include a solution that allows the user to interchange between these sizes. As presented in Chapter 5, Sigvaris defines sizes mostly based on the size of the ankle, with the ranges and means presented in Table 6.1.

Size	Range	Mean
XS	170 – 190	180
S	190 – 220	205
M	220 – 240	230
L	240 – 260	250
XL	260 – 290	275
XXL	290 – 320	305

TABLE 6.1: Ankle size ranges for Sigvaris products

With this logic, it is possible to use the 18 average curves (that are normalized to a leg length = 660 mm, sh = 41.25 mm), computed from the cluster analysis in Chapter 5, and offset the ankle from 0 to any of the above presented mean ankle values, as follows:

$$(x, y) \longrightarrow (x, y + Mean)$$

Table 6.2 presents the offset values of the first circumferential evolution for a size XS. These are the values that a user can introduce through the Excel sheet as the $C4_n, C8_n, C12_n, \ldots, C64_n$ values.

TABLE 6.2: Example values of Evolution 1 along the leg expressed in cm, as extracted from clustering and offset to an XS ankle size

C4_n	C8_n	C12_n	C16_n	C20_n	C24_n	C28_n	C32_n	C36_n	C40_n	C44_n	C48_n	C52_n	C56_n	C60_n	C64_n
18.0	18.5	20.2	23.4	26.9	29.2	29.3	28.1	28.9	31.4	34.4	38.8	42.5	45.5	47.8	50.6

To be able to interchange between sizes, without the need for constant importation, a new *Size* parameter has been defined, with the help of which we can define a scaling factor, which is specific for the circumferential growth:

$$csf = Size/C4_n$$

Where:

$Size$: the required mean ankle size

$C4_n$: the ankle value of the imported evolution

The formula used for fixed point transformation, presented in Chapter 3, where the volumetric line plots with x and y coordinates have been scaled, using the ankle point as an anchor, is the following:

$$x' = x_f + (x - x_f) \cdot s, \quad y' = y_f + (y - y_f) \cdot s$$

We can use this formula and calculate a new set of parameters, entitled $C4_p, C8_p, C12_p, \ldots, C64_p$, where $C4_p$, considered as the anchor point is an exception, because it is the circumference that will newer change position, it will always remain on the floor, therefore the scaling factor used for the height, will not be applied:

$$C4_p = C4_n \cdot csf$$

The remaining values will be calculated following the same logic:

$$
\begin{aligned}
C8_p &= C4_p + \left(C8_n \cdot csf - C4_p\right) \cdot sf, \\
C12_p &= C4_p + \left(C12_n \cdot csf - C4_p\right) \cdot sf, \\
C16_p &= C4_p + \left(C16_n \cdot csf - C4_p\right) \cdot sf, \\
&\dots \\
C64_p &= C4_p + \left(C64_n \cdot csf - C4_p\right) \cdot sf.
\end{aligned}
$$

The new circumferential values are calculated based on specific evolution rules and scaling rules, which makes it possible to scale the 2D cross sections at every level using the bone center as an anchor point, presented in Figure 6.2c., with the following scaling factor:

$$S_{factor} = Cn/Cn_p$$

Where:

- $Cn, \quad n \in \{4, 8, 12, \dots, 64\}$, - correspond to original morphotype circumference
- $Cn_p, \quad n \in \{4, 8, 12, \dots, 64\}$, - correspond to the new, parametrized and scaled circumference

Figure 6.4 shows the size shift from a tall XS leg to a tall XXL leg as well as the shift between the tall and short XXL and XS legs. This figure perfectly illustrates the correct way of scaling that we have achieved with our method, whereas the difference in circumferential size can be seen between the tall XXL and the short XXL. The taller the leg, the larger the circumference, and vice versa.

To achieve this shift between the sizes, the correct way to proceed is the following:

- **Step 1:** Import evolution via excel
- **Step 2:** Modify "sf" to 41.25 mm
- **Step 3:** Modify parameter "*Size*" to the required value from Table 6.1
- **Step 4:** Modify "*nsh*" to either 36.25 mm for short leg, or 46.75 mm for tall leg.

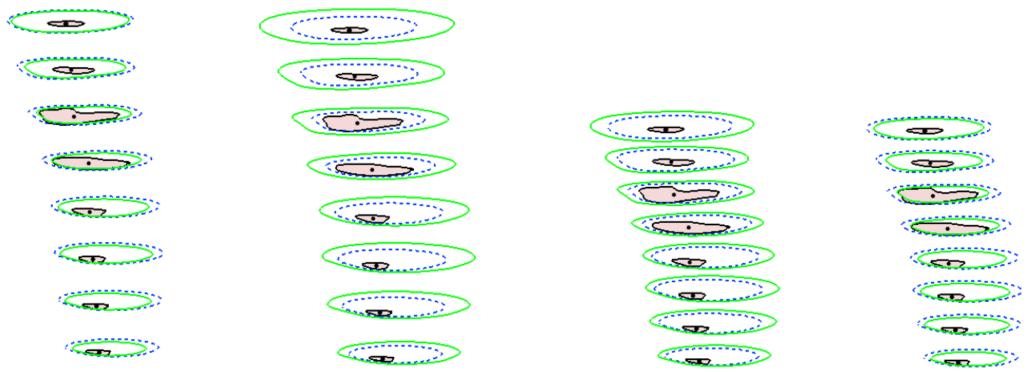


FIGURE 6.4: Scaling example of Tall XS to Tall XXL and Short XXL to Short XS

6.3.4 Circumferential evolution adjustment

The recommendation system developed in Chapter 5 will determine to which of the 18 circumferential evolutions a new subject belongs, and the length that the adaptive model should be set. Following the same methodology as described above, the parameters $C4_n, C8_n, C12_n, \ldots, C64_n$ can be changed to any required evolution. Figure 6.5 illustrates different evolutions all set to the same size.

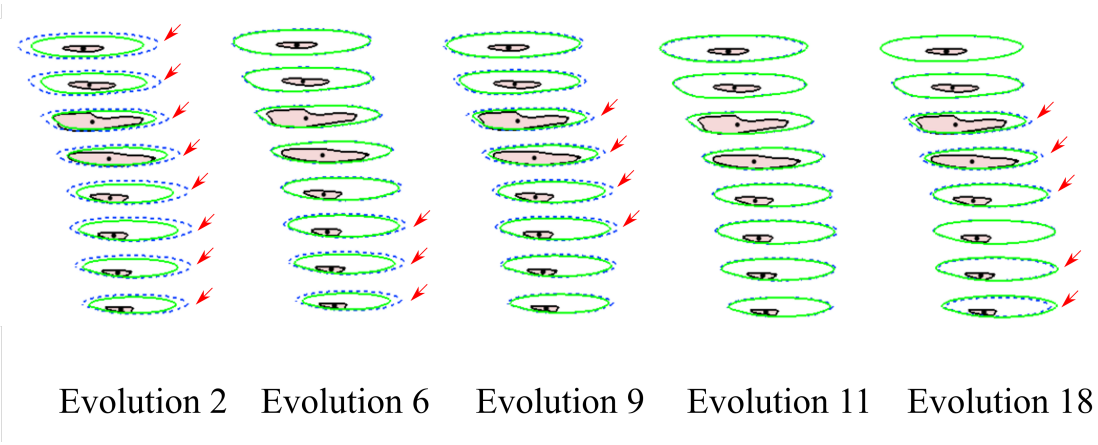


FIGURE 6.5: Evolution change for the same leg size. Dashed blue contours belong to the mean leg shape, green contours belong to the imported evolution type, and red arrows highlight the zones where the mean shape and the evolution differ.

6.3.5 Surface creation

The volumetric and lengthwise parametrization allows the creation of a surface that can represent the reconstructed leg. The applied method involves the creation of 16 equidistant points on each circumference, this distance being defined as $Cn_p/16$ starting from the medial silhouette. Connecting the corresponding points from each circumference creates a longitudinal wireframe structure of the leg, similar to the projection lines, obtained in Chapter 3. This process is illustrated in Figure 6.6, which also shows the shape shift between Evolution 18 and Evolution 11 (matching the mean morphotype).

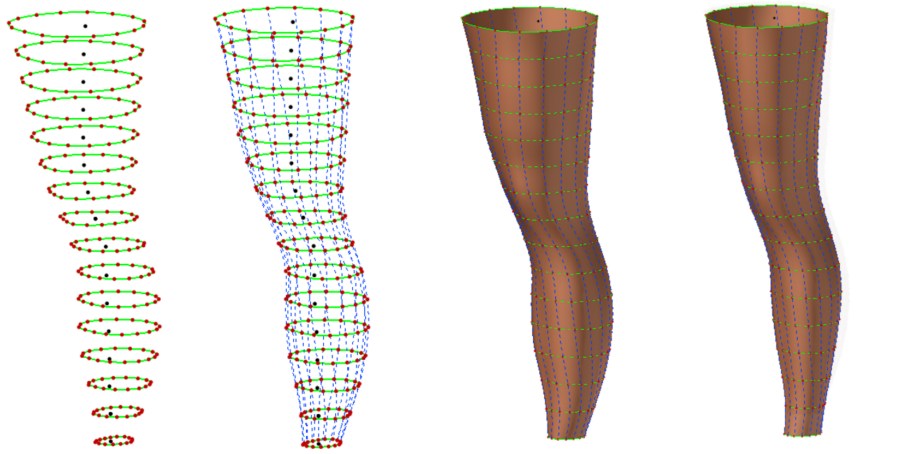
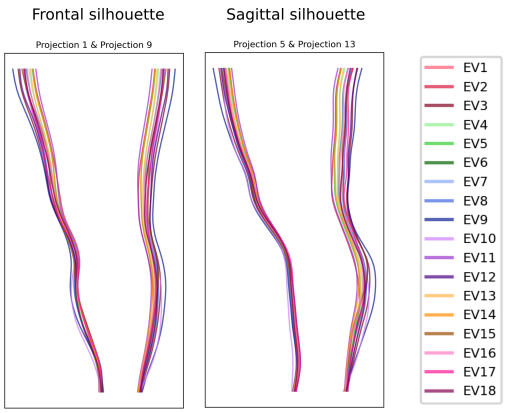


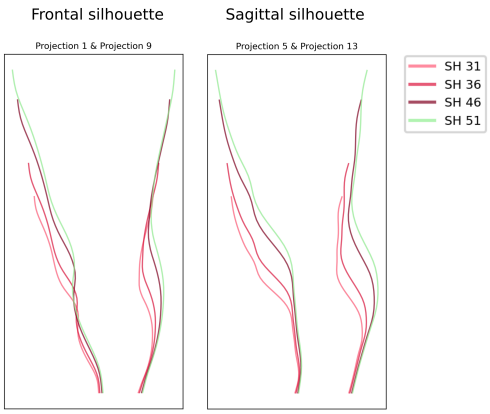
FIGURE 6.6: Patchwork surface creation using the wire-frame, constructed on the parametric cross-sections

6.4 Results

To address the research objectives highlighted above, we have experimented with the three adaptive morphotypes identified in Chapter 3, changing some parametric aspects and verifying the resulting geometric shapes. One of the main variables that we could experiment with was the circumferential evolution that the morphotype should follow. Based on the findings in Chapter 5, we have tested the parametric leg by adapting its $C4_n, C8_n, C12_n, \ldots, C64_n$ values to the 18 different circumferential evolutions. Figure 6.7a presents the geometric differences compared between the 18 identified circumferential evolutions, described with the help of 8 pair projection lines. The ankle size of the morphotype corresponds to an "M" size, equal to 230 mm, while the rest of the circumferential height reveals the variation between the evolutions.



(A) 18 identified circumferential evolutions



(B) Length difference of Size "M" of Evolution 9

FIGURE 6.7: Geometric differences between the generated parametric legs, illustrated with the lateral and sagittal silhouette projections

Figure 6.8 represents the 18 evolutions of the size "M" Morphotype 2 from a frontal and side view, where we can visualize the versatility in shape that the parametric model can achieve, with only a simple importation command.

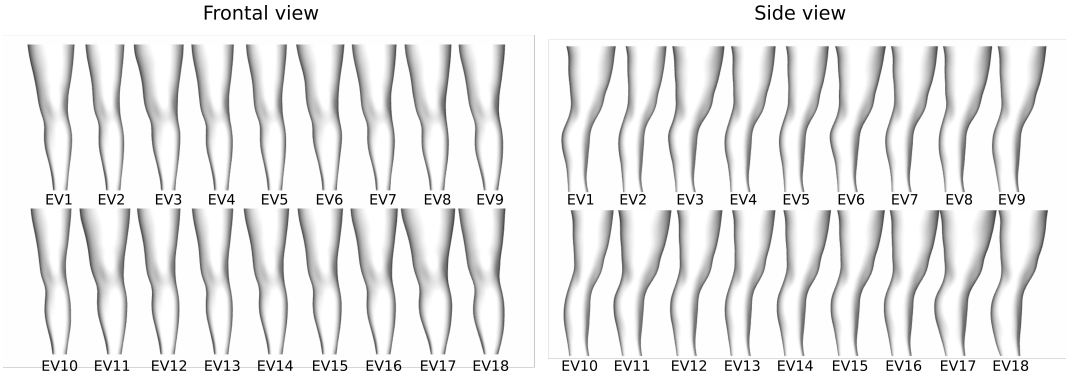


FIGURE 6.8: Geometric differences between the 18 identified circumferential evolutions, illustrated with the 3D surface model of the parametric leg

The second parameter is the leg length, as in general, the sizing of the length is available in less dimensions as the volume related measures, generally in two lengths, we have tested the accuracy of the model in terms of length adaptation for four segment heights: SH1 = 31 mm, SH2 = 36 mm, SH3 = 46 mm, SH4 = 51 mm, where SH1 and SH4 are min and max values of

leg length in our database and SH2 and SH3 are the two sizes determined for "short leg" and "long leg". As can be seen in Figure 6.7b, the volume of the leg changes according to the height; shorter legs will have smaller circumferences than the longer versions. It can also be observed that the geometry does not suffer from any form of distortion; it maintains the original shape of the leg evolution. This length change can also be visualized in Figure 6.7b, where we have illustrated the resulting leg shapes.

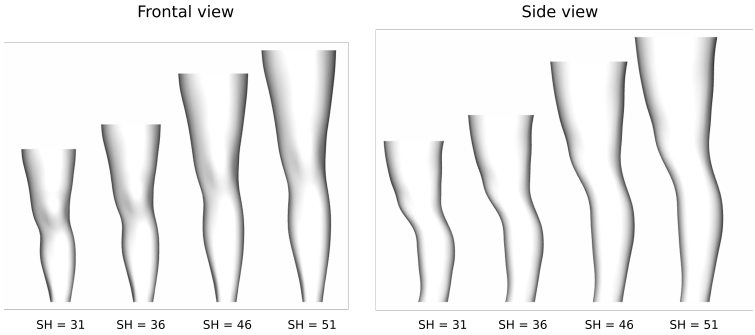
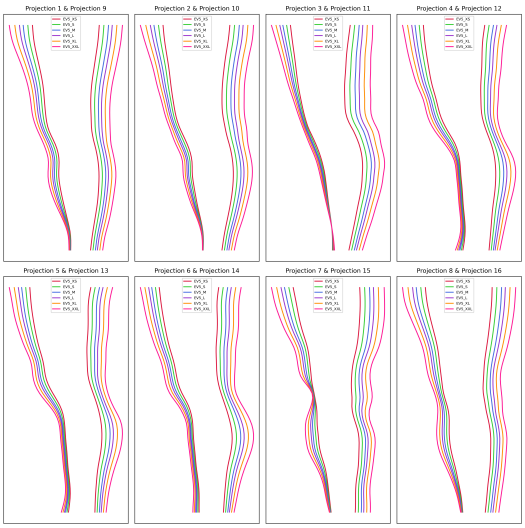


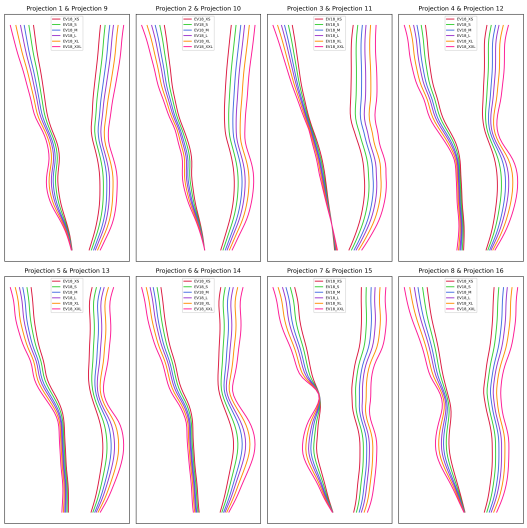
FIGURE 6.9: Change of the length parameter, illustrated in four stages of segment height

The third parameter that we have tested was the size of the ankle, based on which the adaptive leg is graded. After the importation of the required circumferential evolution, a "Size" parameter can be defined, described in 6.3.3. The results can be illustrated for two different Evolution types: Evolution 5 and Evolution 18, in Figure 6.10, where the 8 pairs of projection plots reveal the two different shape evolutions and the corresponding grading from size XS to size XXL. The main difference between these two types of evolutions can be observed in the mid thigh region, where the 18^{th} Evolution has a larger volume, as well as in the shape of the lower leg, with a completely different volumetric growth. In this Figure, we can also observe the effect of using the bone center as a guide for volume growth, as the volume is growing differently in certain zones. For example, Projections 3,4,5, and 6 reveal that indeed the model does not place much volume in front of the tibia bone

in the anterior compartment of the lower leg. Another fixed point is visible on Projection 7 (Subplot 7, right), which is a concave segment of the anterior-lateral part of the knee, creating a visible inner bump in that region.



(A) Geometric differences between the sizes of Evolution 5 (XS, S, M, L, XL, XXL)



(B) Geometric differences between the sizes of Evolution 18 (XS,S,M,L,XL,XXL)

FIGURE 6.10: Comparison of size growth between two different circumferential evolutions

The resulting sizes of Evolution 5 are presented in Figure 6.11 in a frontal and sagittal view, showing that even though we are manipulating the geometry by scaling around a fixed bone barycenter, the resulting form perfectly resembles a real, possible leg shape.

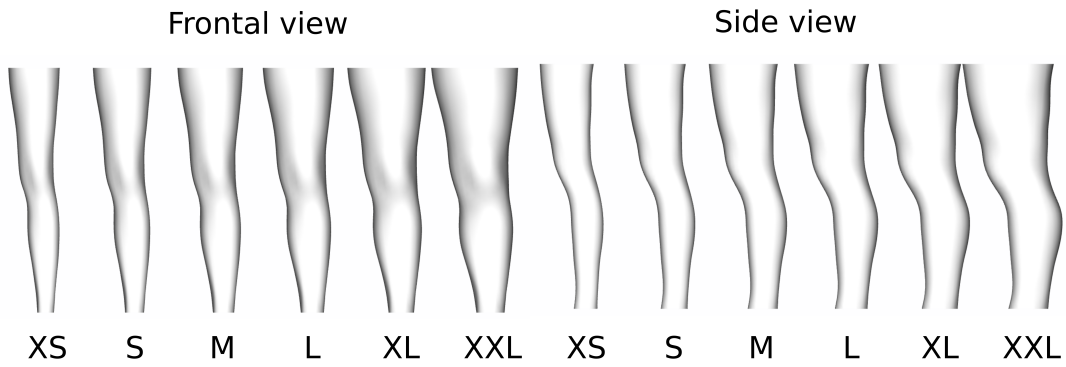


FIGURE 6.11: Size growth of the parametric leg, adapted for Evolution 5

To test the validity of the proposed model, three subjects have been chosen from the existing leg database based on the following criteria: they should have the same ankle and calf size, and they should be in different morphological groups. With this choice, we wanted to demonstrate that even if someone has the same ankle and calf size, the rest of the circumferential values can be significantly different, proving that a three-point-based sizing system, currently used in the industry, is not the optimal choice. The circumferential values of the three selected subjects are presented in Table 6.3. These values are also represented in the form of a 2D volume plot in Figure 6.12, which shows the superposition of volume in the ankle and calf, but also reveals that the values in between and above differ.

TABLE 6.3: Real circumferential and Segment Height values of Subject 21, 80, and 118

Subject	C4	C8	C12	C16	C20	C24	C28	C32	C36	C40	C44	C48	C52	C56	C60	C64	SH
21	221	225	255	298	350	373	351	329	367	376	417	470	520	556	572	593	45.12
118	221	235	268	312	354	372	365	340	345	363	362	397	440	478	513	546	40.82
80	221	247	287	325	357	364	346	331	365	386	408	447	483	516	552	588	44.35

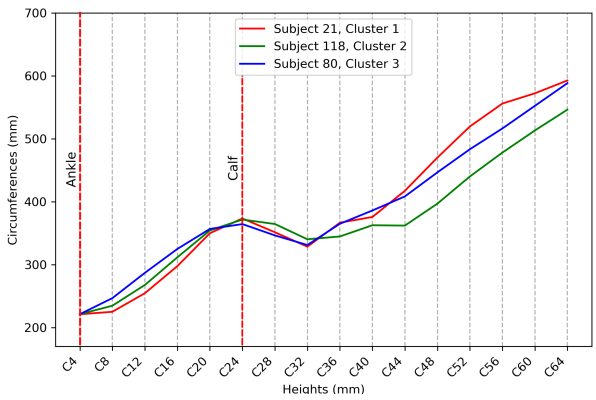


FIGURE 6.12: The three chosen subjects from different morphological groups, same ankle and calf sizes

The same observation can be made when the overall geometry is compared between these three subjects. The ankle and calf sizes might be very similar to each other, but there are major morphological alterations that are

illustrated in Figure 6.12. Having chosen these subjects from the three identified morphologies, the first observable difference is the posture of the leg, then other soft tissue changes can be observed, especially in the case of Subject 21, who is a muscly figure.

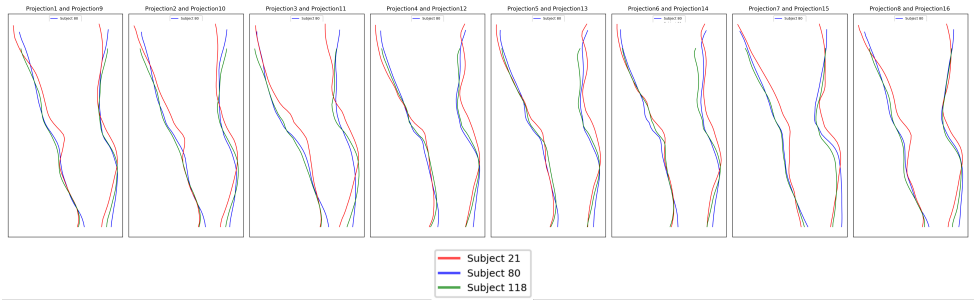


FIGURE 6.13: Geometric comparison of the selected 3 subjects

According to the recommendation system that we have presented in Chapter 5, Subject 21 corresponds to an Evolution 1, size M, long, Subject 118 to an Evolution 15, size S, short, and Subject 80 to an Evolution 9, size M, long leg (Table 6.4).

TABLE 6.4: Recommendation system results

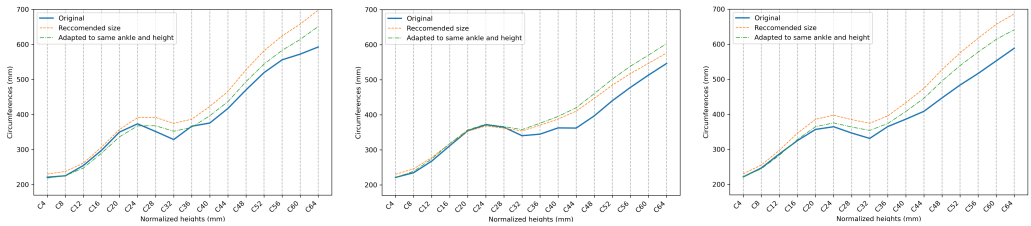
Subject	Size	Evolution	Length
21	M	Evolution 1	long
118	M	Evolution 12	short
80	M	Evolution 9	long

Based on the recommendations presented in Table 6.4, we have tested the volumetric outcome of the parametric leg in two conditions:

- **Case 1:** The parametric leg adapted to the recommended evolution, set for the recommended size and length
- **Case 2:** The parametric leg adapted to the recommended evolution, set for the real ankle size and segment height of the subject ("Semi-personalization")

The results of this experiment are illustrated in Figure 6.14, where the three volumes of each subject's leg are compared. It can be observed that in

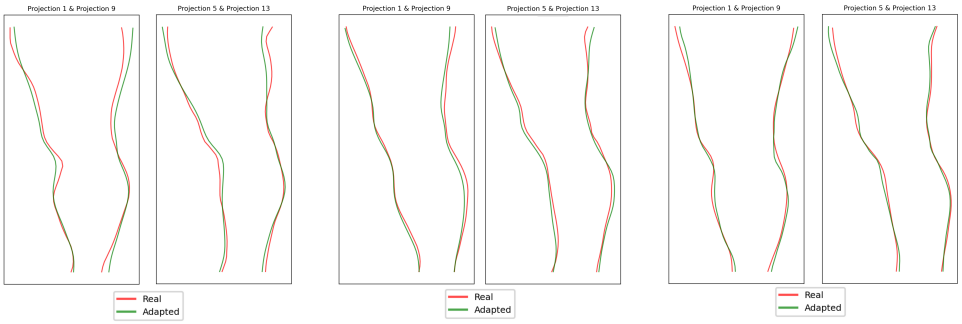
both cases, the region of the lower leg is very close to reality, a little closer in case two, when the ankle is personalized, but in the upper leg region, there is a larger difference. Even though the semi-personalization has produced closer values in the case of Subject 21 and Subject 80, in the case of Subject 118, it had a reverse effect. This can be explained by the relation between the short and long segment values and the real height of the leg. The closer the real segment height is to the mean value of short or long leg, the better the semi-personalization gets in comparison to the proposed size. For example, the real segment height of Subject 21 is equal to 45.12 mm, and the mean value of long legs is 46.75 mm. In this case, the semi-personalization result was better than the proposed size (Figure 6.14a.). On the other hand, in the case of Subject 118, these values are 40.82 mm and 36.25 mm, the real segment height being higher than the mean value, producing a larger leg size than the recommended one. If we see the overall results of the recommended size, we can conclude that in the lower leg region, the produced legs have a higher overlapping ratio, which is promising, as in the case of the compression stockings, this part needs to have a better fit, having a higher pressure gradient.



(A) Subject 21 (B) Subject 118 (C) Subject 80

FIGURE 6.14: Circumferential evolution and volume change between the original values and the adapted values in two conditions: one using the recommended evolution in corresponding size and length, the other, also using the recommended evolution, with the "Size" parameter set to original ankle size and the "NSH" parameter set to original segment height

The semi-personalized method has produced a rather unstable result in comparison to the recommended size; therefore, opting for a full personalization is a better approach, as introducing real values of the leg in the parametric model can reproduce a higher accuracy. This is what has been tested for the three morphological groups in the case of the three subjects. Figure 6.13 demonstrates the original geometry of each subject compared to the adaptive morphotype, set to the real circumferential values and real segment height of the person. The figure represents the frontal and side silhouette of each subject in question. Even though there is no perfect overlapping of the two geometries, the resulting leg shapes are still very similar, and they validate the postural differences between the three morphological groups as the posture of each subject overlaps with the posture of each morphotype. Appendix G shows the full geometric comparison of the 3 subjects.



(A) Subject 21, original geometry and the adapted version of Morphotype 1

(B) Subject 118, original geometry and the adapted version of Morphotype 2

(C) Subject 80, original geometry and the adapted version of Morphotype 3

FIGURE 6.15: Geometric comparison of the selected 3 subjects in original and adapted form

In terms of volume, that has been extracted directly from the CAD software, the following error calculation formulas have been used:

Let

- V_{ref} be the original volume of the leg;
- V_{test} be the adapted volume of the leg.

Absolute error

$$\Delta V = |V_{\text{test}} - V_{\text{ref}}|$$

Relative error

$$\varepsilon_r = \frac{\Delta V}{|V_{\text{ref}}|}$$

$$\varepsilon_r(\%) = \frac{\Delta V}{|V_{\text{ref}}|} \times 100$$

The results of the error calculations are presented in Table 6.5, where the relative error is the highest in the case of subject 21, with a value of 2.85%. It has already been mentioned that this subject has a muscular configuration, with a bow leg deformation, which makes its intrinsic shape particular, with muscles bulging in the thigh area and the knee pushed to the left. The morphotypes are computed as the mean shape of the cluster population. Therefore, they are smoothed in surface, losing personal features that are present in real legs. This is the reasoning for the increase in volume for this subject; a perfect overlap could not be reproduced (See Appendix G, Figure G.1). This volume increase in the case of the other two subjects is negligible, and the geometric overlapping between the original geometry and the adapted geometry is better.

TABLE 6.5: Volume error results

Volume	Subject 21	Subject 118	Subject 80
$Original(L)$	2.51	2.01	2.30
$Adapted(L)$	2.58	2.04	2.32
$\Delta V(L)$	0.07	0.03	0.02
$\varepsilon_r(\%)$	2.85	1.62	0.69

As an experiment, the 2D patterns of each of the 3 morphology representatives have been computed in Wecov3er CAD software to visualize the resulting patterns' shape. First, the 1-piece pattern has been computed with the cut placed in the back of the leg (= Projection 13), which has not revealed much difference between the morphologies. The second trial was

translated into a 2-piece 2D pattern with the cuts on the back and front of the leg along Projection 13 and Projection 5, revealing the difference of the first morphology but not the other two. The third trial translated the legs in a 4-piece pattern, with the same front and back cut, and additionally on the two sides along Projection 1 and Projection 9. This last experiment could correctly translate the 3D shape into a 2D state, also revealing the differences among all three morphologies. The results can be observed in Figure 6.16.

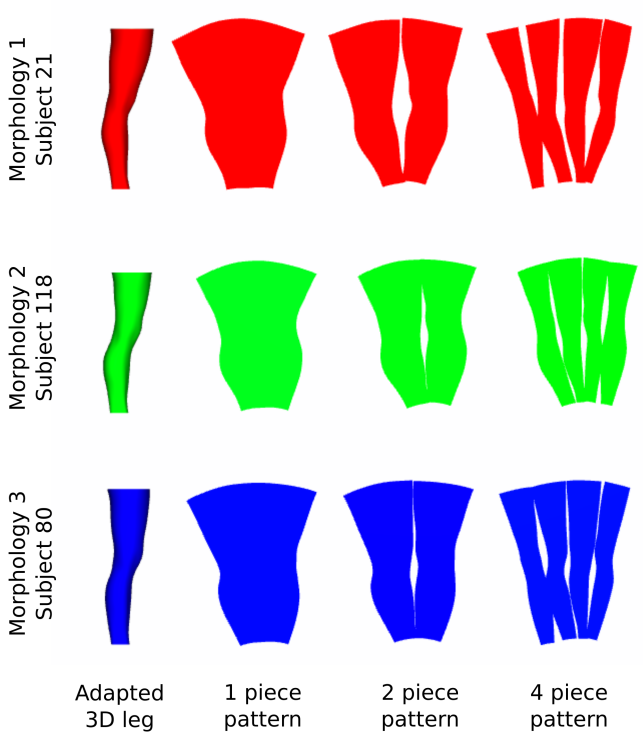


FIGURE 6.16: 2D patterns generated from the adapted geometry of the three morphology representatives in 3 different configurations: 1 piece, 2 piece and 4 piece models

6.5 Conclusions

In this chapter, we tried to answer our third research question, which was concentrated on the development of adaptive leg morphotypes that could be used to optimize the size and fit of medical compression stockings. For this,

we have leveraged the morphological and size-related findings in Chapter 3 and Chapter 5 respectively, and have created 3 parametric leg models that are adapting based on a systematic recommendation from a sizing table to a proper fit. For this, we have made a call to the Visible Human project to identify the necessary bone centers in 17 anthropometric heights along the leg, which served as guiding points for the volumetric growth.

The resulting adaptive leg morphotypes can be manipulated by changing three sets of parameters: the circumferential values of the identified evolution ($C4_n, C8_n, C12_n, \ldots, C64_n$), the new length (NSH = [36.25,46.75]), and the new ankle size (Size). Based on these three parameters, the model changes to a recommended size from a predefined sizing table. The experimental results show that the parametric model can reproduce very close volumes in the lower leg region and acceptable volumes in the thigh region, which is an achievement, as the medical compression stockings have to have a better fit in the lower leg, especially at the ankle and calf levels. The model has also been tested for semi- and fully-personalized modes, from which we have concluded that the semi-personalization could be more reliable than the size adaptation, and the fully-personalized version is the best way of producing this type of medical product, because it could achieve a volume match of 2.85% relative error, even in the case of a subject with differentiated morphology. The adaptive leg has demonstrated the possibility of the automatic development of medical products that can either create a fit using predefined sizes or by using personal data. The size of the compression stocking pattern can be calculated and modeled from the values of the parametric leg, automatically, so that it would respect the graduated compression rule that the product imposes, following the rigidity and mechanical properties of the knitted fabric. This represents a future direction and continuation of

the project that would ultimately revolutionize the way we design compression products. However, the methodology presented shows great potential in the personalization approach; there are also some drawbacks to this technology, as the industrialization process of such a large number of sizes and shapes is not yet possible due to time and production cost, and current knitting technology. The results discussed here form the basis of an article that is in preparation for submission to a peer-reviewed journal, which will detail the automatic creation of adaptive leg models, also integrating the upcoming research about the adaptive compression stockings.

Chapter 7

Conclusions

This thesis aimed to investigate the morphological variability of the human leg to reevaluate the current design of Medical Compression Stockings (MCS), to address the size and shape-related issues present in the ready-to-wear medical products, which slip, fall, and create discomfort for patients, who fall out of standard sizing, hence directly contributing to non-compliance and treatment failure. This thesis examines the power of unsupervised and deep learning methods in the identification of morphological groups and anomalous representatives extracted from different data forms: multidimensional shape descriptors, point-clouds, and triangular meshes, leveraging this information to create a workflow that not only automates the design process of Compression products, but also provides a decision tool for medical professionals in the form of a size recommendation tool. In addition to this, the deep learning model represents a novel approach to anomaly detection in medical data, offering the potential to identify leg geometries associated with chronic diseases.

In the following section, we provide a detailed overview of the research contributions that we have achieved during this study, providing an answer to the research questions. We finalize this document with a discussion of the

future perspectives, which provide a view of the directions that could potentially advance the field.

7.1 Overview of main findings

RQ1 How can AI techniques detect abnormal leg morphologies relevant to MCS treatment?

Classification algorithms are sensitive to outliers. Given the relatively small dataset size, with only 131 representatives, some of which can present early signs of lymphoedema, or other physiological markers that distinguish them from other subjects, with features that could potentially perturb the algorithm from identifying homogeneous morphological groups, it was necessary to study the dataset from the point of view of anomalies. To solve the issue of such data, we have investigated two novel anomaly detection methods along with a clustering method. By automatically learning latent features from the point cloud of the leg database through a novel Deep Convolutional Transform learning model, which optimally represents the 3D legs in a lower-dimensional space, we could cluster the data in four distinct groups using K-means clustering. Combining Deep Convolutional K-Means (DCKM) and Elliptic Envelope for anomaly detection has demonstrated its effectiveness in identifying morphological deviations, as 8 outliers have been correctly identified in an explainable manner. Each of the 7 outliers has demonstrated geometrical deviations from the overall dataset. While the DCTL framework extracts meaningful features using convolutional operations, the Elliptic Envelope method enhances the process by identifying potential outliers within the clusters, boosting anomaly detection accuracy and clustering performance.
The second anomaly detection method, called MeshDeepSVDD, has been

integrated into a Fully Convolutional Mesh Autoencoder structure and has been tested on three object categories (nut, piggy, and capsule) of the MultiSen-AD public dataset, successfully identifying the anomalous data with a mean score of 0.92 AUC-ROC. This result outperformed the traditional Support Vector Data Descriptors(SVDD), Kernel density estimation(KDE), and Isolation Forest(IF) methods, which performed significantly lower, not being able to distinguish anomalous data from normal data. Applying this method to the human leg database has successfully identified the top ten anomalous legs in the database of 131 subjects. These subjects have been identified as outliers for the following reasons: oversized or obese legs, knock-kneed or hyperextension of the knee, large and oddly shaped lower leg, especially in the case of two subjects with primary Lymphoedema, disproportionality between upper and lower soft tissue development, unique leg shape, and characteristics. The identification of such anomalies can significantly improve the outcome of data clustering and can even be used to detect chronic diseases like Lymphoedema.

Despite the algorithm's success in detecting anomalies, there are many possibilities for future research to be undertaken. In future works, we will address the "black-box" issue, which is currently the main limitation of the proposed method. This means that the lack of transparency in identifying anomalies and clustering the data into distinct groups has to be enhanced for better interpretability.

RQ2 What are the most effective combinations of unsupervised clustering and deep learning methods for classifying 3D leg morphologies and supporting adaptive design rules for medical compression stockings (MCSs)?

The staple method in the classification of 3D anthropometric data is PCA,

either applied to anthropometric measurements or normalized point clouds, obtained from 3D body scans. These methods, in case of the 1D measurements, are proven insufficient when the shape of the body has a high impact on the intended product, and in case of the 3D point clouds, are posture sensitive. Deep learning methods from non-Euclidean data are more and more widespread and have achieved success in classification tasks, detangling intrinsic and extrinsic shape on labeled data. With the lack of such labeling, the explainability of the achieved results is diminished, creating a "black-box" effect, which makes these models less trusted. To be able to include in our analysis the concept of shape, size, and posture, we have experimented with multiple forms and dimensions of human legs and their anthropometric measurements. The main classification algorithm that we have used was spectral clustering, which, based on the state of the art, is an excellent method when the data has a nonlinear structure. To feed this algorithm, first of all, we have studied the variation of the 1D shape descriptor extracted from the 3D legs by capturing the variability of 16 circumferences, measured at equally spaced intervals along the leg's length through PCA. This analysis made us focus on the eight most variable zones on the leg which were captured at $C_4, C_8, C_{12}, C_{16}, C_{20}, C_{24}, C_{36}, C_{48}$ and further proved that, simply clustering the first three principal components (overall size, lower-leg features, mid-leg features) does not correctly describe the shape of the leg, because it produced four groups that are dissimilar in size between groups but they also differ in shape within the groups. As a second achievement, we have successfully identified three morphological groups that are distinct in posture, two of which result from either hyperextension of the knee or flexion of the knee, which are both deformations of the skeletal system. This was achieved by leveraging the 3D shape descriptor that has been developed in CAD using projection lines to collect the simplified longitudinal intrinsic shape of each

leg in 16 anatomical sites. This simplified shape has been introduced in the spectral clustering algorithm on multiple levels:

- first, each projection has been clustered individually, following the recommended number of clusters and number of neighbors, and extracting the Laplacian matrix
- secondly, the Laplacian matrices have been summed to create a final partitioning.

The results indicate that the likelihood of these deformations occurring in a relatively young and healthy population is high, as the cluster sizes are similar. This leads us to conclude that, for this methodology to go beyond merely disentangling posture, a larger database for each posture would be required. Furthermore, in the case of the leg, this is not simply a matter of posture sensitivity - it must be recognized that the 'normal', relaxed posture of some subjects is itself altered. Even though the three morphotypes extracted from the three groups only differed in posture and the way the femur and tibia are connected, they still served as an optimal geometric base for the parametric legs.

The final sizing results have been extracted with the help of the 2D shape descriptor combined with the results of the PCA. The 2D shape descriptor is a normalized and superposed 2D graph of the 16 circumferences(y coordinates) and the corresponding heights (x coordinates). Based on the most variable zones of the leg, we could divide the classification of the 2D shape descriptor into three steps:

- By selecting only the coordinates of the most variable features in the lower-leg $C_4, C_8, C_{12}, C_{16}, C_{20}, C_{24}$ and partitioning data in 3 very well defined "Ankle" groups

- By selecting only the coordinates of the most variable features in the upper-leg $C_{36} and C_{48}$ and partitioning data into 8 "Thigh" groups
- By combining "Ankle" and "Thigh" labels, resulting in 18 evolution groups.

The identified 18 subgroups describe highly detailed growth patterns, dividing the population on two different levels: based on the lower leg growth, where the precision is higher, and based on the thigh growth, where the precision decreases. Additionally, they are showing a linear growth pattern between sizes, which is an advance in comparison to the existing sizing system. We have found that the ankle is a driving parameter in growth, as most of the evolutions can be found in each ankle size category (Sigvaris ankle size); therefore, this variable can be used as a key parameter in the creation of the adaptive model. We have also discovered that the BMI and gender are two factors that can influence the shape of circumferential evolution within the same group, but they are not applicable as an absolute rule, as these observations do not repeat in all cases. It has been also noted that the three morphologies are not directly linked to any of the specific Evolutions, which led us to the conclusion that making the "normal" postured leg (Morphotype 2) adaptable to all the 18 evolutions would be an acceptable solution for sizing table driven parametrization and having the three postures adaptable to any Evolutions would increase the ability of the proposed method in terms of personalization.

RQ3 How can morphological data be used to create a comprehensive system for automated sizing and fitting of medical compression stockings (MCSs), based on leg shape, pressure mapping, and fabric properties?

To answer this research question, we needed to identify the current sizing system problem for medical compression stockings to be able to develop a more reliable and more inclusive sizing system. On the first hand, it has been proven that up to 21% of the subjects composing the studied database (55 out of 258 subjects) could not find a proper fit from the ready-to-wear range, proposed by Sigvaris. This is a rather large number of patients, who would be left with products that would not provide the correct therapeutic effect in the treatment of CVI.

With the 18 new mean circumferential evolutions identified and presented in the previous point, we have created new ranges for 18 new sizing tables. To facilitate the medical professionals and industrial partners to choose the correct size, we have designed a user interface that works as a recommendation tool, using a 3-step logic in identifying the proper size for a new patient. Based on this recommendation, one of the three parametric legs can be adapted to a predefined size and evolution. To create a volumetric growth logic for the morphotypes, we have made a call to the Visible Human project to identify the necessary bone centers in 17 anthropometric heights along the leg, which served as guiding points for the volumetric growth.

The resulting adaptive leg morphotypes can be manipulated by changing three sets of parameters: the circumferential values of the identified evolution ($C4_n, C8_n, C12_n, \ldots, C64_n$), the new length (NSH = [36.25,46.75]), and the new ankle size (Size). Based on these three parameters, the model changes to a recommended size from a predefined sizing table.

The experimental results show that the parametric model can reproduce very close volumes in the lower leg region and acceptable volumes in the thigh region, which is an achievement, as the medical compression stockings have to have a better fit in the lower leg, especially at the ankle and calf levels. The model has also been tested for semi- and fully-personalized modes, from

which we have concluded that the semi-personalization could be more reliable than the size adaptation, and the fully-personalized version is the best way of producing this type of medical product, because it could achieve a volume match of 2.85% relative error, even in the case of a subject with differentiated morphology. The adaptive leg has demonstrated the possibility of the automatic development of medical products that can either create a fit using predefined sizes or by using personal data. The size of the compression stocking pattern can be calculated and modeled from the values of the parametric leg, in an automatic way, so that it would respect the graduated compression rule that the product imposes, following the rigidity and mechanical properties of the knitted fabric.

7.2 Limitations

While this study provides valuable insights into the morphological variability of the human leg, it is not without limitations, which open up discussion and may suggest paths for future investigation.

The 3D shape descriptor proved to be very useful in both the classification task and the explanation of the resulting cluster geometry. It is also usable for direct comparison between the original geometry and the reconstructed geometry. However, the collection of such a descriptor is a time-consuming, manual operation, which is not practical in the case of large datasets. To resolve this problem, which comes from the hand-crafted nature of the proposed 3D shape descriptor, an automated methodology could be developed, using topology-preserving mesh morphing, to obtain a triangular mesh similar to what we have presented in Chapter 4, and extract the projections as geodesic paths to obtain the intrinsic shape of the leg in different anatomical

zones. This would allow a faster exploitation of larger datasets, extending the possibility to deep-learn latent features in an unsupervised manner.

Like most deep learning approaches, our anomaly detection model (Mesh DeepSVDD) also suffers from the limitation of explainability. Despite the algorithm's success in detecting anomalies, there are many possibilities for future research to be undertaken. The "black-box" issue has to be addressed to ensure transparency and interpretability in identifying anomalies and clustering the data into distinct groups.

In the industry, a large number of read-to-wear products proposed in a large number of sizes is very contraindicated because of fabrication constraints. We acknowledge that proposing 18 different evolutions in 6 sizes and 2 lengths each is unrealistic. Still, our approach represents a major step towards facilitating the personalization process of compression products, as we have identified a volumetric growth logic (using the bone center as a guiding point for scaling) that allowed us to fully personalize the parametric leg, which can be used directly in the 3D design of Compression products.

The three morphological groups are correctly identified and describe real postural deformations of the studied population. In this research, we have found that these deformations do not influence the volumetric growth pattern of the legs, but geometrically speaking, they are distinct. It still needs to be proven whether the same compression stockings behave differently on the three morphotypes, and to evaluate if the comfort of wearing changes between subjects who are wearing the same product but have different postures of their leg. This step would be necessary for the implementation of postural-related compression design in the industry.

7.3 Future research perspectives

1. **Expanding the dataset to include Lymphoedema subjects** and other shape deformations linked to the lower limb. The current work has been conducted on a database composed of healthy subjects, with only a few representatives of early-stage Lymphoedema. It would represent a great advantage to compose a database focused on chronic diseases that alter the shape of the leg, as applying the same volumetric growth comparison and geometric comparison on lymphoedematous legs as presented in this dissertation would potentially reveal specific patterns, where the lymphatic fluid can build up. As lymphoedema often occurs in only one leg, leaving the other in a normal shape, it would also be interesting to compare the localized, anatomically specific projections of the normal and lymphoedematous leg, revealing where exactly and how exactly the lymphatic fluid alters the shape of the leg. We believe that this approach has great potential in the medical field.

2. **Deep learning, applied on the CT images of Lymphoedema patients**. Building on our approach of parametric modeling of the lower limb, where we used the bone center as the guiding point for scaling the volume of the leg, we hypothesized that the soft tissues develop less in front of the tibia than behind. In order to be able to apply a similar method to simulate the growth of a lymphoedematous leg, it would be necessary to study in depth the zones where the lymphatic fluid builds up. In the case of lymphoedema, we can not yet certainly determine whether the same logic could be applicable. If such a database could be acquired, it would not only answer this question but also contribute to the development of digital twins of the inner soft tissues used in finite element modeling.

3. **Integration of Explainable AI in the FCMA model**. Despite the proposed algorithm's success in detecting anomalies, there are many possibilities for future research to be undertaken. In future works, we will address the "black-box" issue, which is currently the main limitation of the proposed method. This means that the lack of transparency in identifying anomalies and clustering the data into distinct groups has to be enhanced for better interpretability.

4. **Integration of the mechanical properties of the knitted fabrics and the graduate compression rules of medical compression stockings in the adaptive model**The size of compression stocking pattern can be calculated and modeled from the values of the parametric leg, in an automatic way so that it would respect the graduate compression rule, that the product imposes, following the rigidity and mechanical properties of the knitted fabric. This represents a future direction and continuation of the project that would ultimately revolutionize the way we design compression products. However, the methodology presented here shows great potential in the personalization approach; there are also some drawbacks to this technology, as the industrialization process of such a large number of sizes and shapes is not yet possible due to time and production cost, and current knitting technology.

5. **Development of a 3D knitting pattern, suitable for knitting seamlessly on flat knitting machines**. There are multiple ways of knitting compression products, which can vary in function depending on the treated disease. For example, for CVI, they use circular knitting machines, and for lymphoedema, flat knitting machines are used. Some advancements have already been made in the direction of generating knitting patterns directly from 3D meshes; therefore, there is great potential in the use

of a 3D mesh in the form of a compression stocking, where the graded pressure and fabric rigidity have already been calculated. If the whole process of sizing can be automated, also conserving the shape of the leg, it would make the industrialization faster with more reliable medical products.

6. **Integration into Symphonies project**. This project aims to develop a digital solution to improve the care of patients with lymphoedema, affecting over 250000 people just in France. The developed digital tools will not only be useful for the patients and healthcare professionals to follow up on the development of the disease, but also for the industrial partners, who will be able to use these tools for better and more inclusive product design, and by this revolutionizing the medical textile market. For this digital tool, we have developed the adaptive morphotypes in a CAD software that is highly computational, license-dependent, and not yet included in the user interface. Our team has been working on a solution that would extract the adaptive morphotype from the CAD software and integrate the recommendation tool developed in this thesis into a web service that would send back the 3D mesh file, adjusted to the users' requirements. This 3D mesh could be further used by other members of the Symphonies project, directly, without the need for additional software. The architecture of the web service under development is illustrated in Figure 7.1.

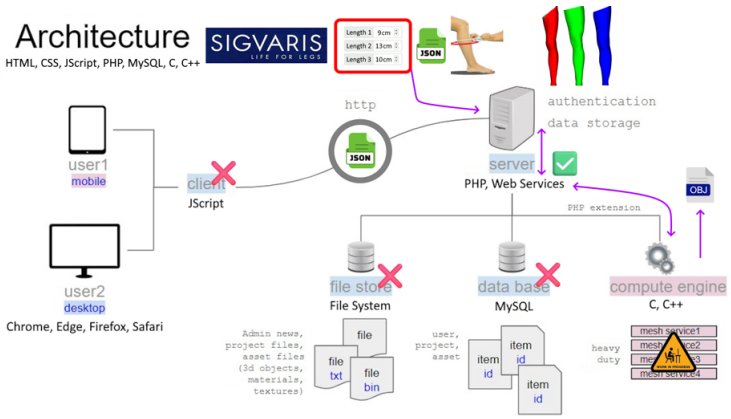


FIGURE 7.1: Architecture of Web service developed by We-Cov3r Studio

Appendix A

In this appendix, we are showing the four groups identified by the 2D shape descriptor in the first phase, presented in Chapter 3.

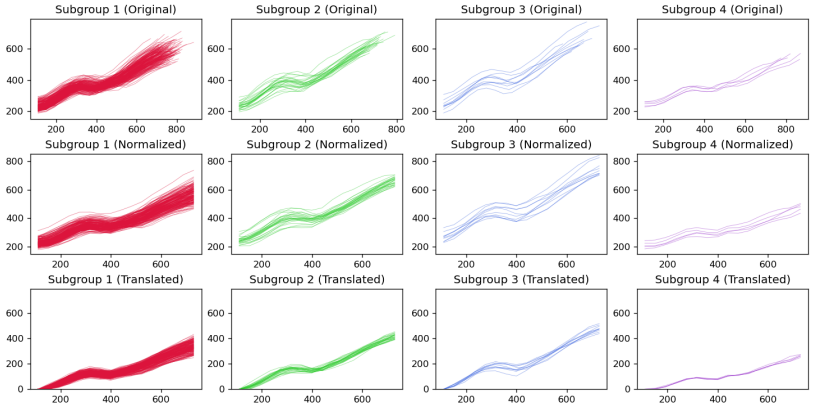


FIGURE A.1: Ankle size XS (170 - 200 mm), S (200 - 220 mm), M (220 - 240 mm), L (240 - 260 mm), XL (260 - 290 mm), XXL (290 - 320 mm) as taken from Sigvaris sizing table os medical compression stockings.

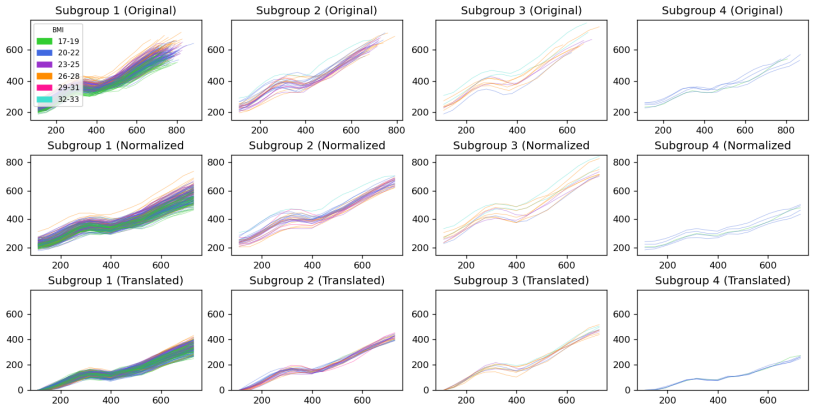


FIGURE A.2: Body Mass Index (BMI) divided in 6 ranges

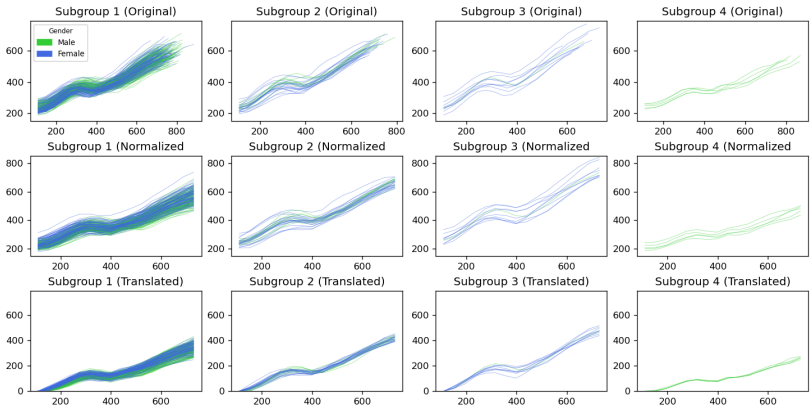


FIGURE A.3: Gender

Appendix B

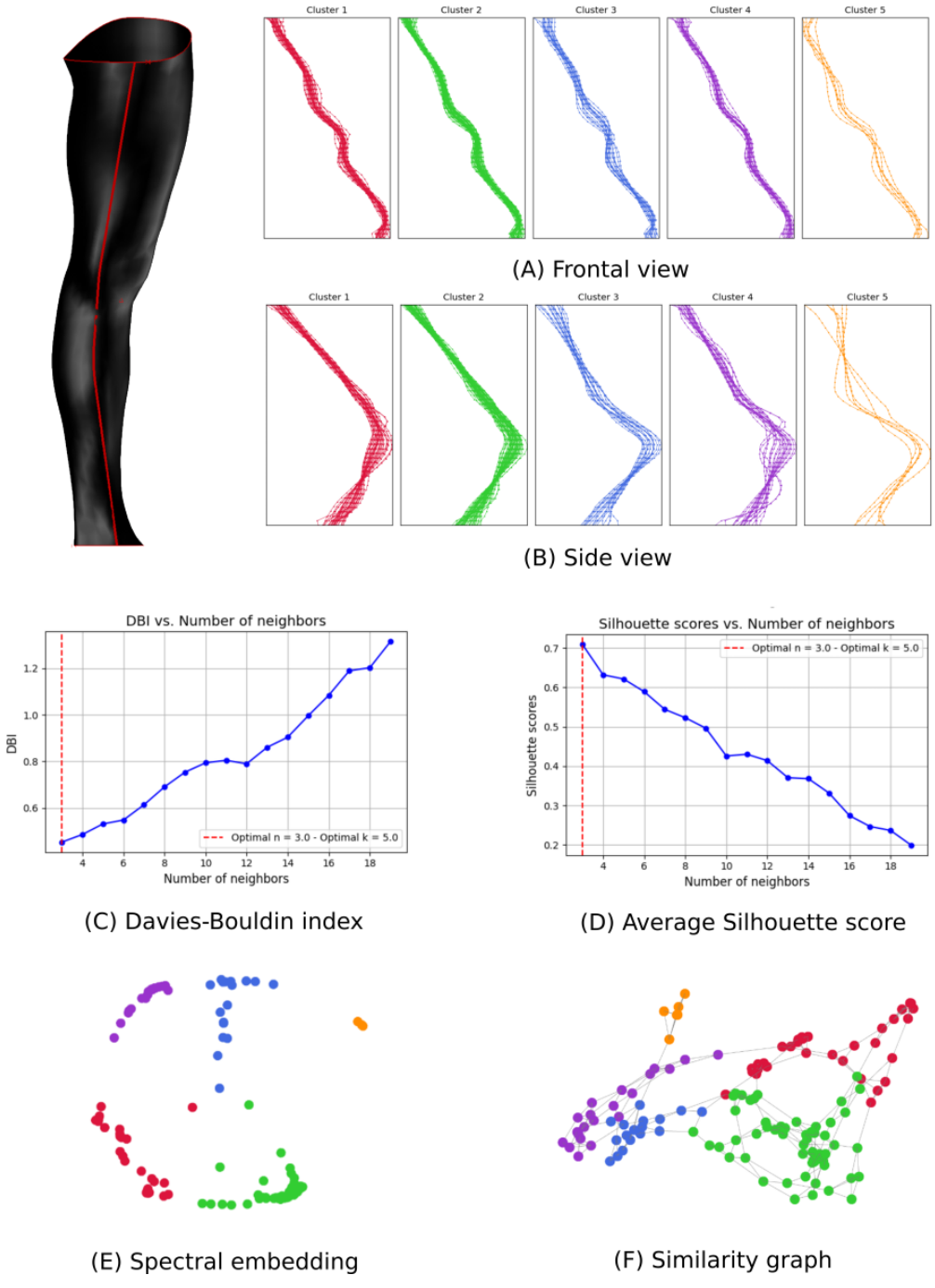


FIGURE B.1: Summary of data analysis of Projection line 1

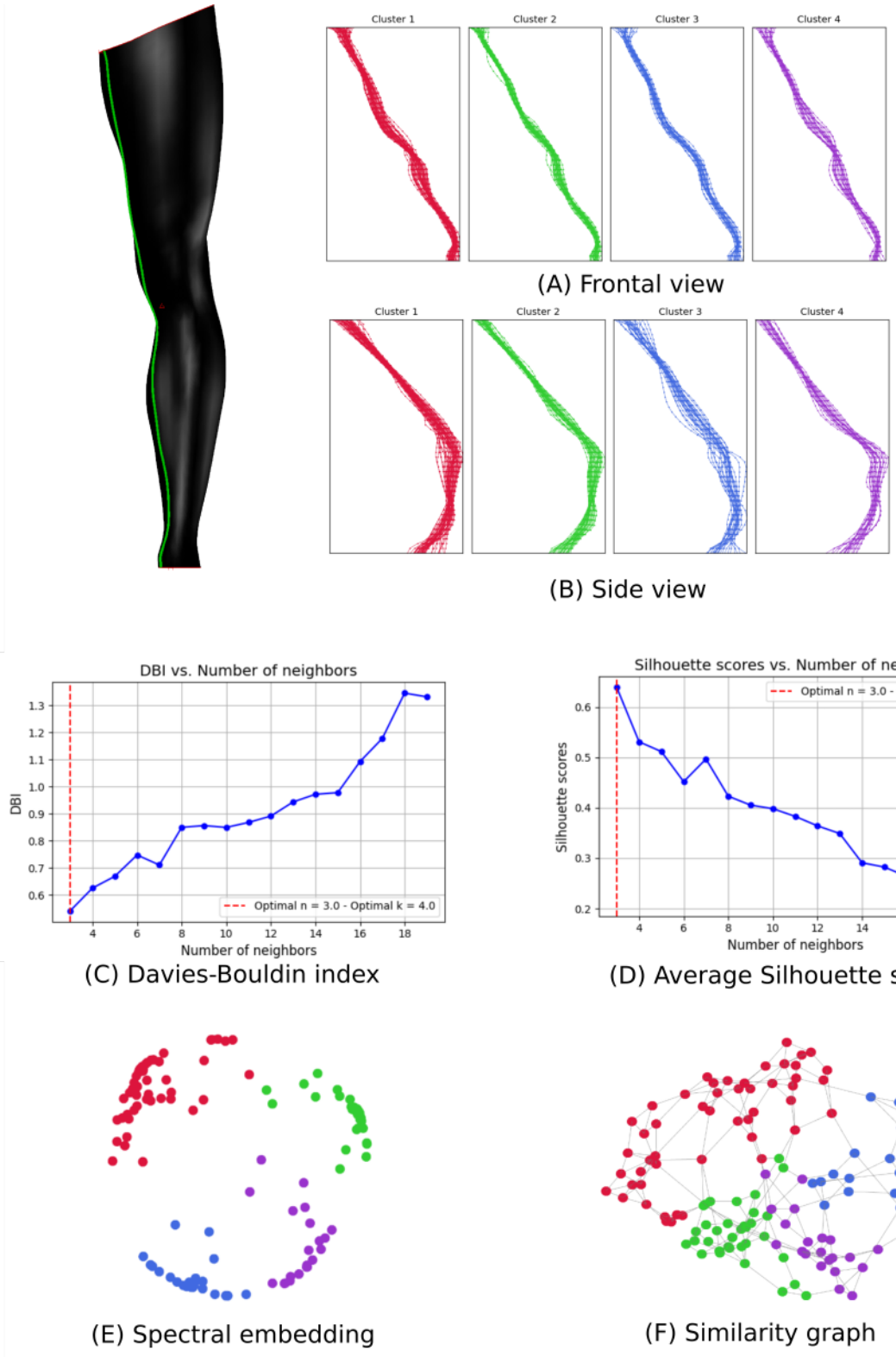


FIGURE B.2: Summary of data analysis of Projection line 2

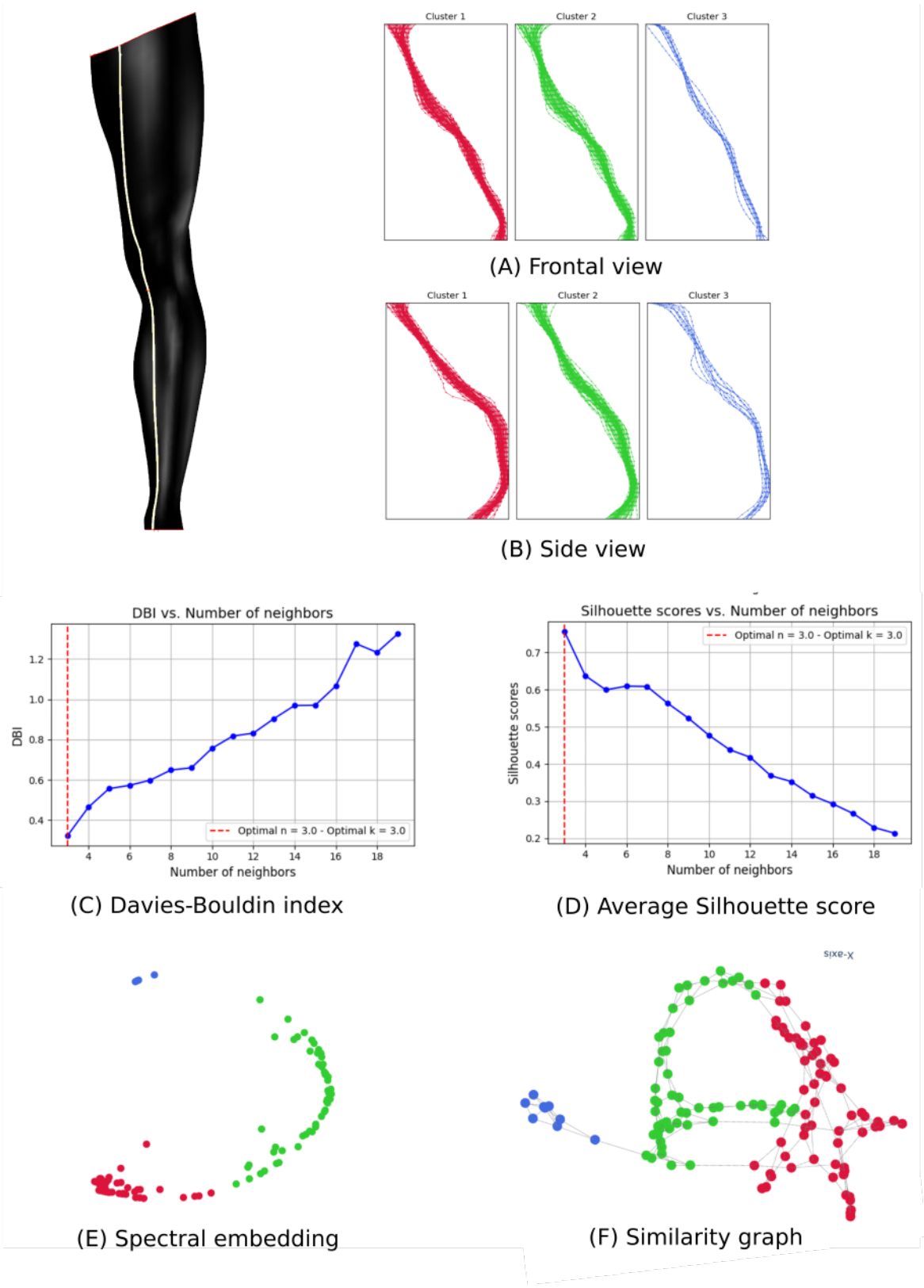


FIGURE B.3: Summary of data analysis of Projection line 3

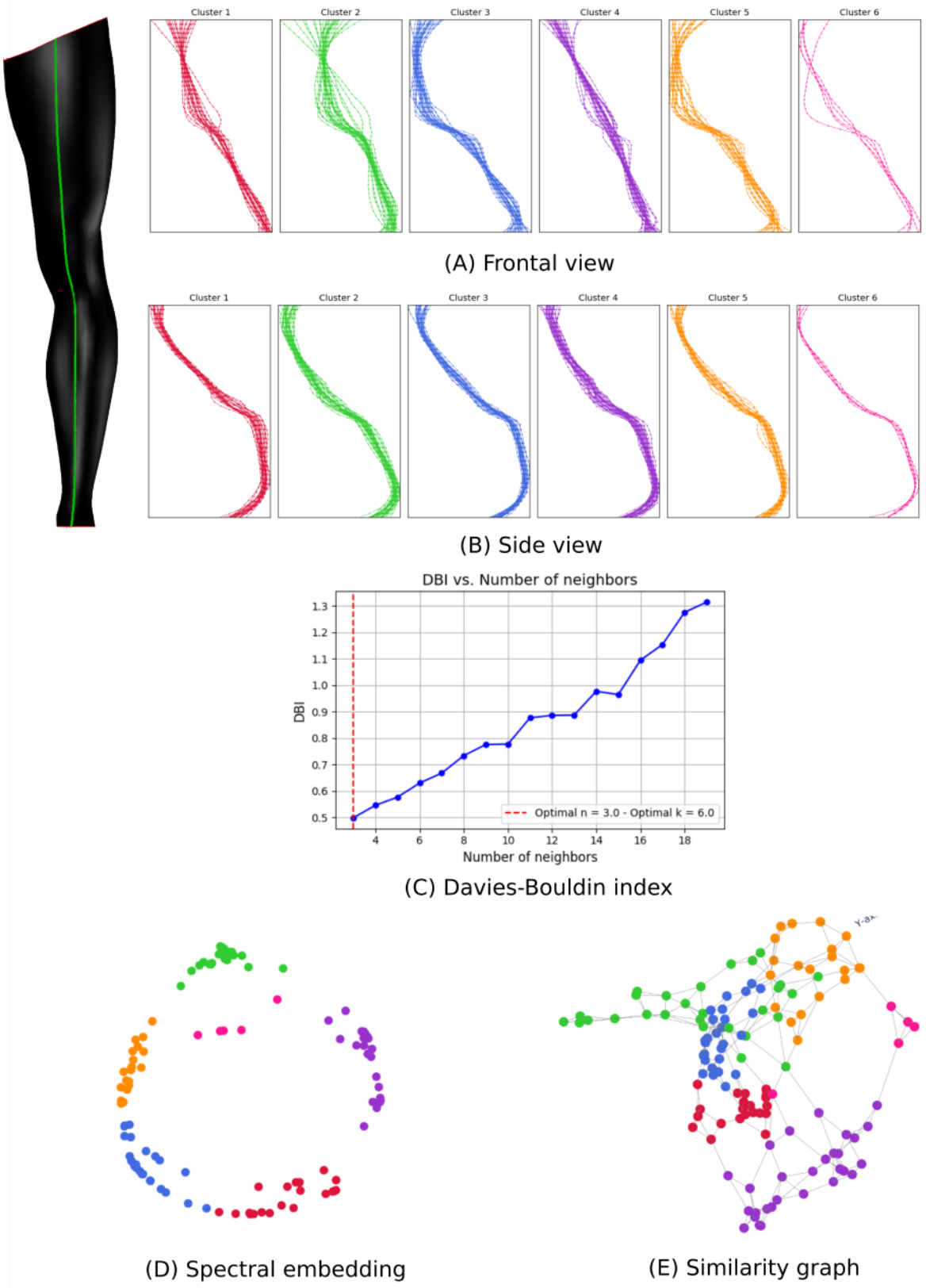
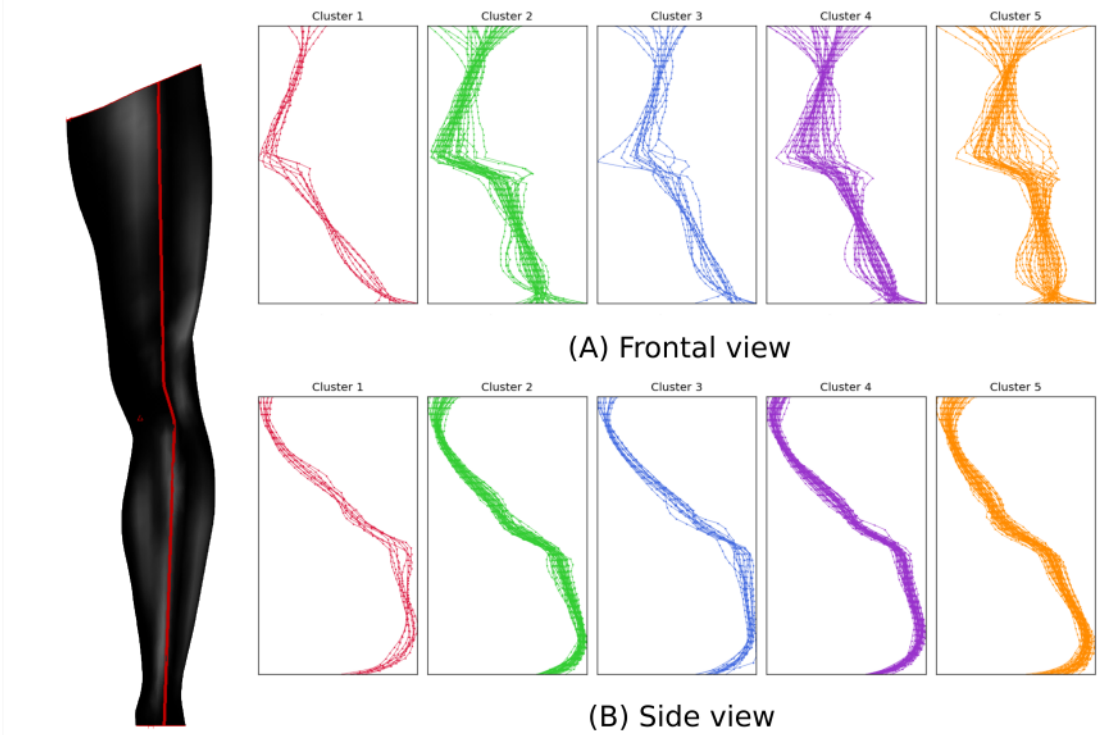
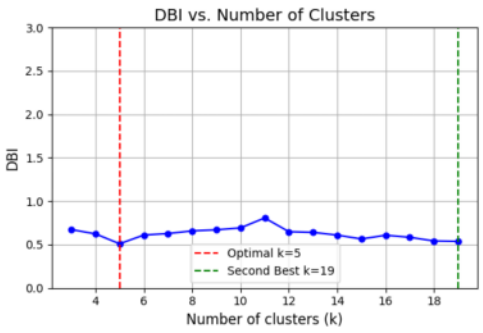
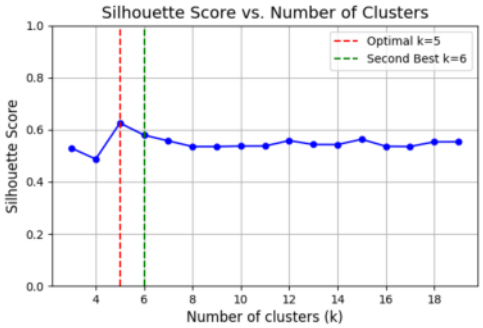


FIGURE B.4: Summary of data analysis of Projection line 4





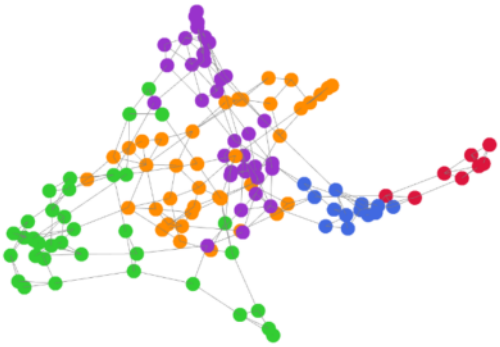
(C) Davies-Bouldin index



(D) Average Silhouette score



(E) Spectral embedding



(F) Similarity graph

FIGURE B.5: Summary of data analysis of Projection line 5

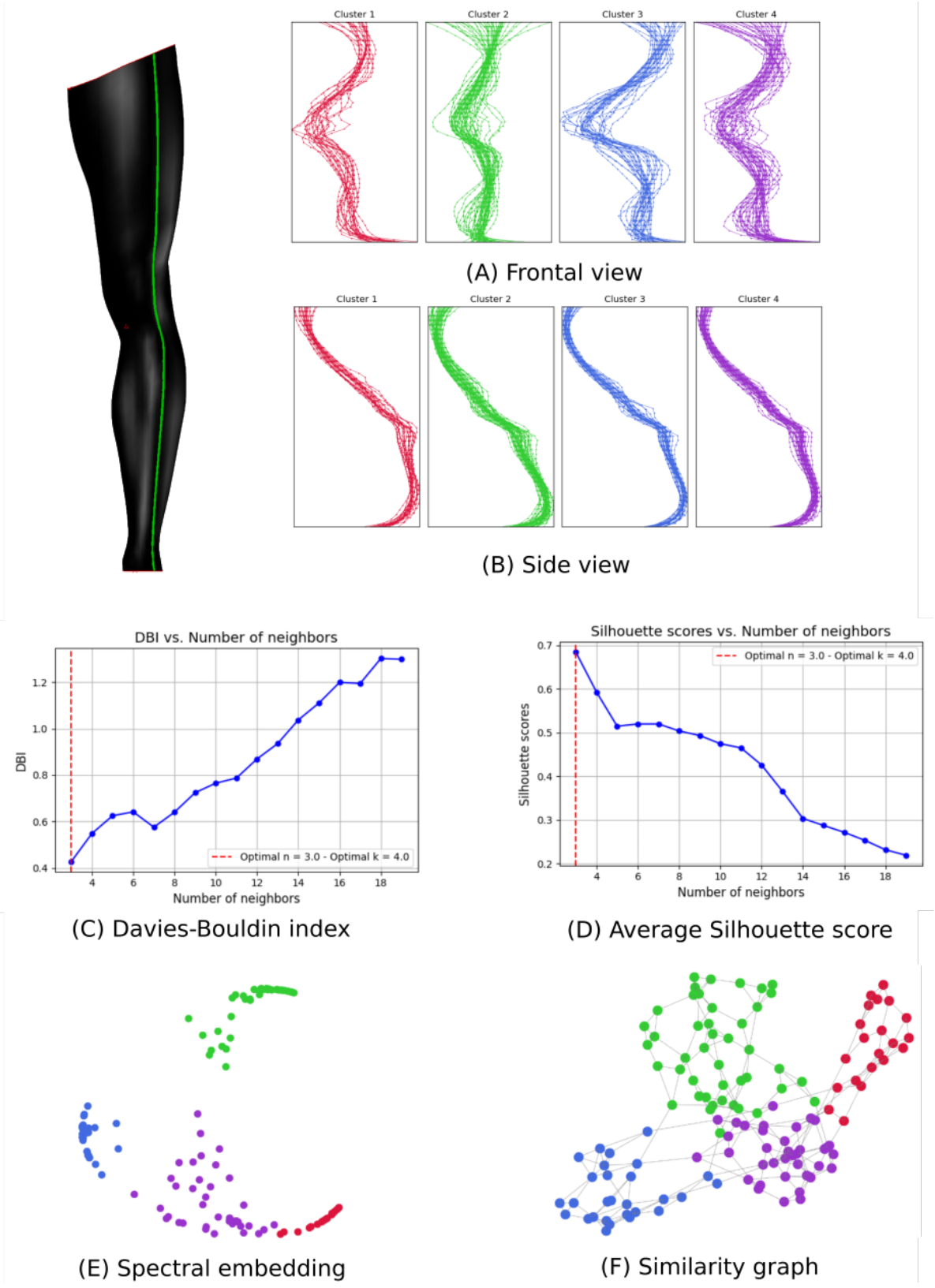


FIGURE B.6: Summary of data analysis of Projection line 6

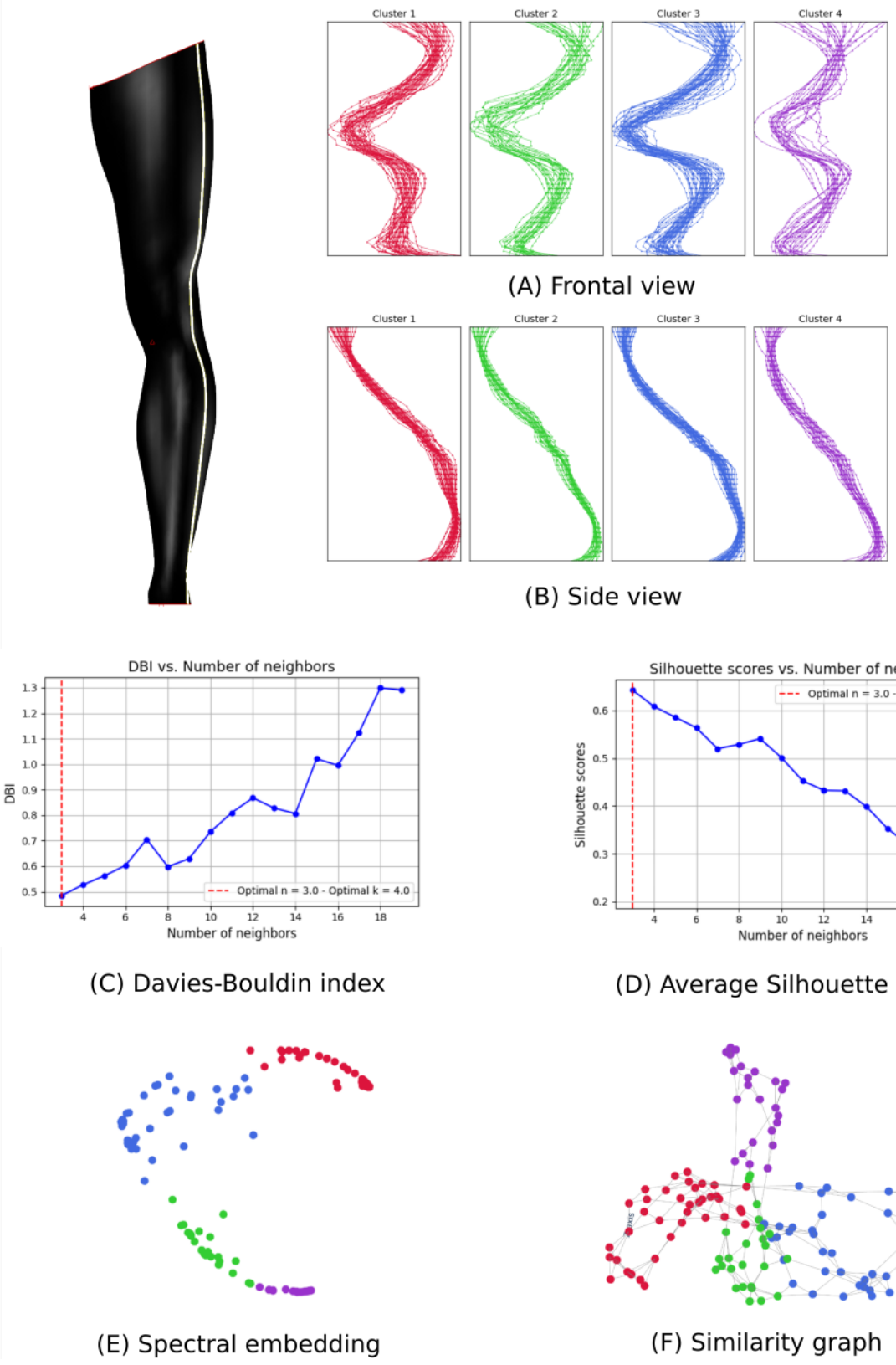


FIGURE B.7: Summary of data analysis of Projection line 7

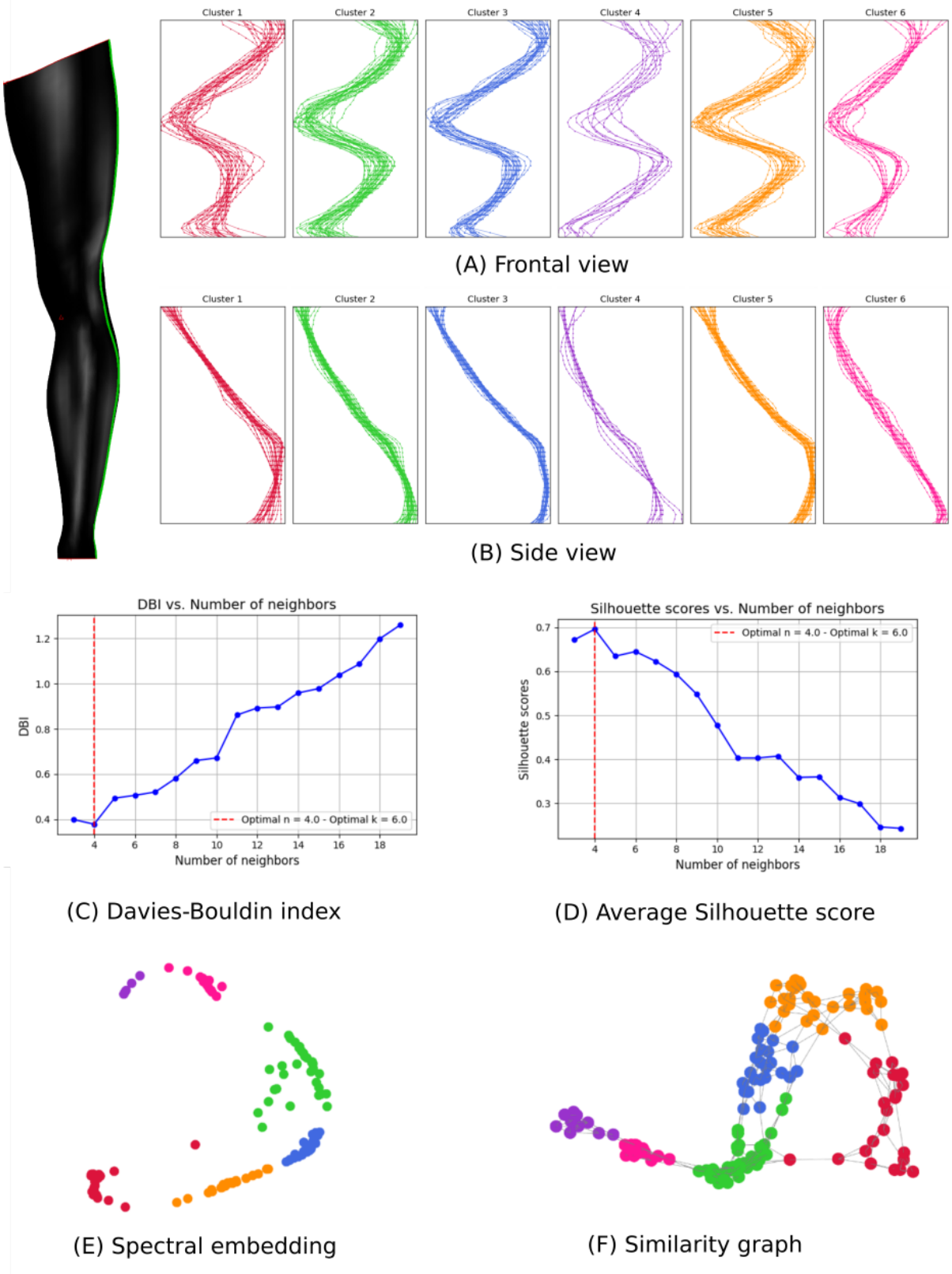


FIGURE B.8: Summary of data analysis of Projection line 8

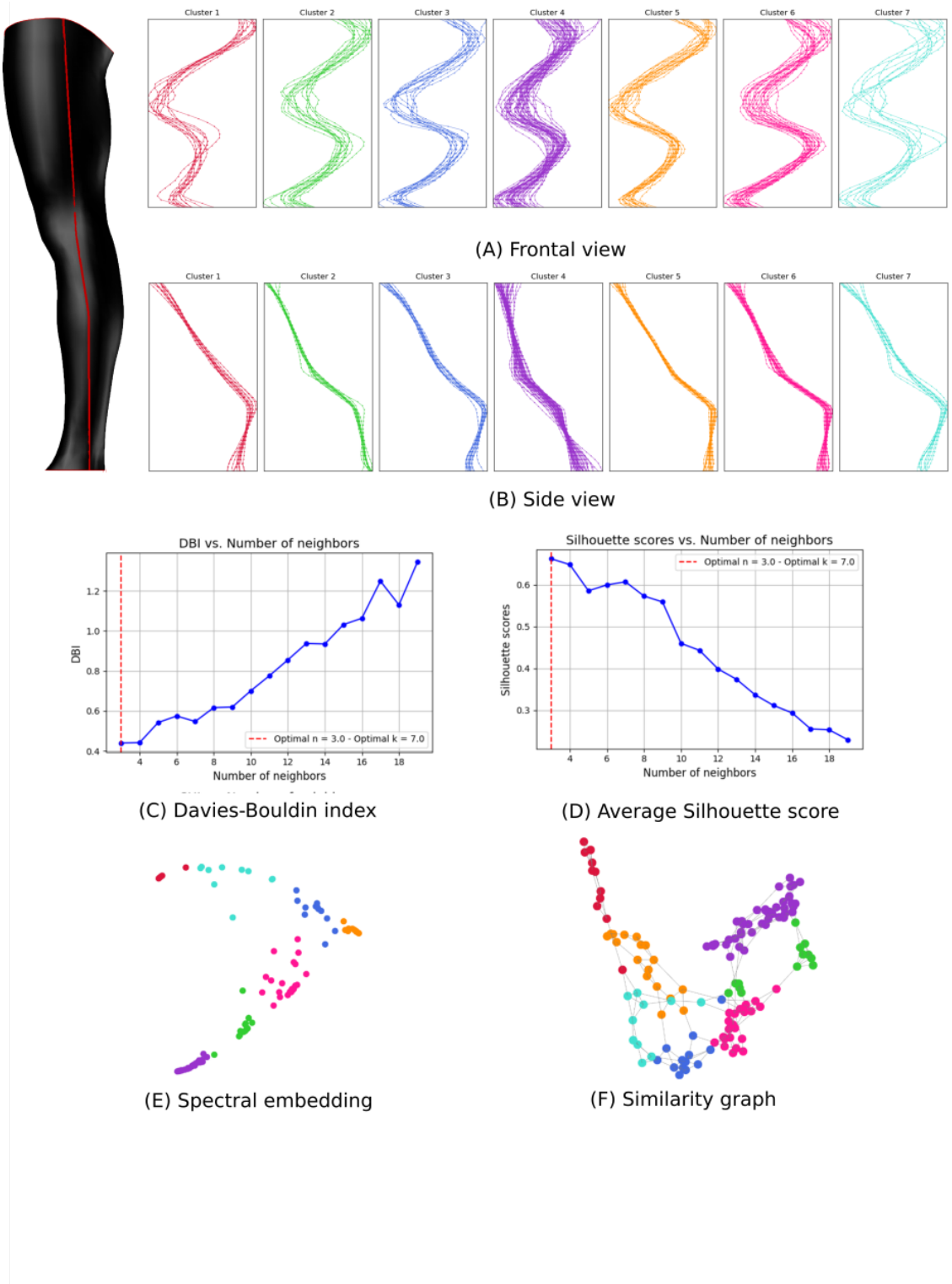


FIGURE B.9: Summary of data analysis of Projection line 9

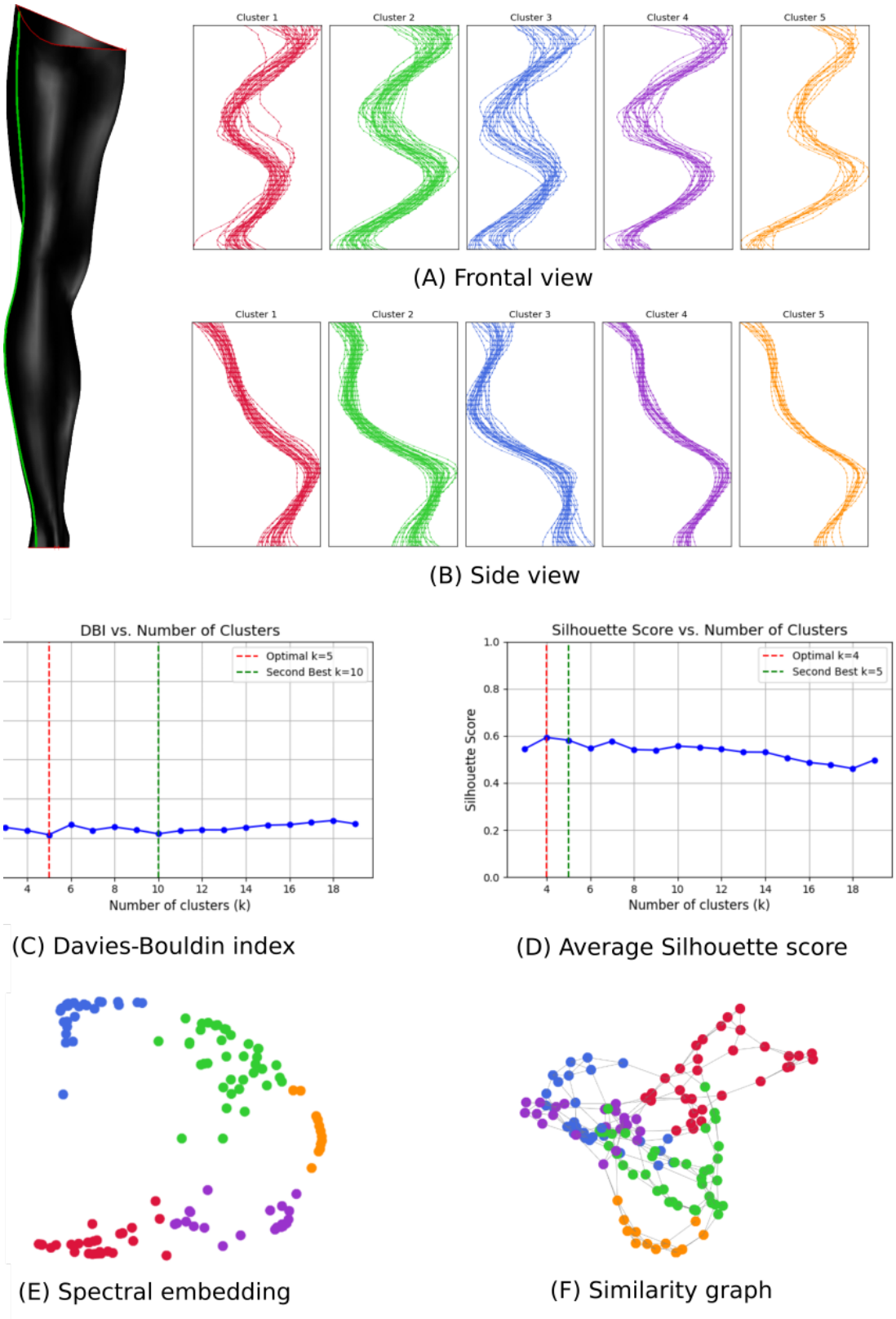


FIGURE B.10: Summary of data analysis of Projection line 10

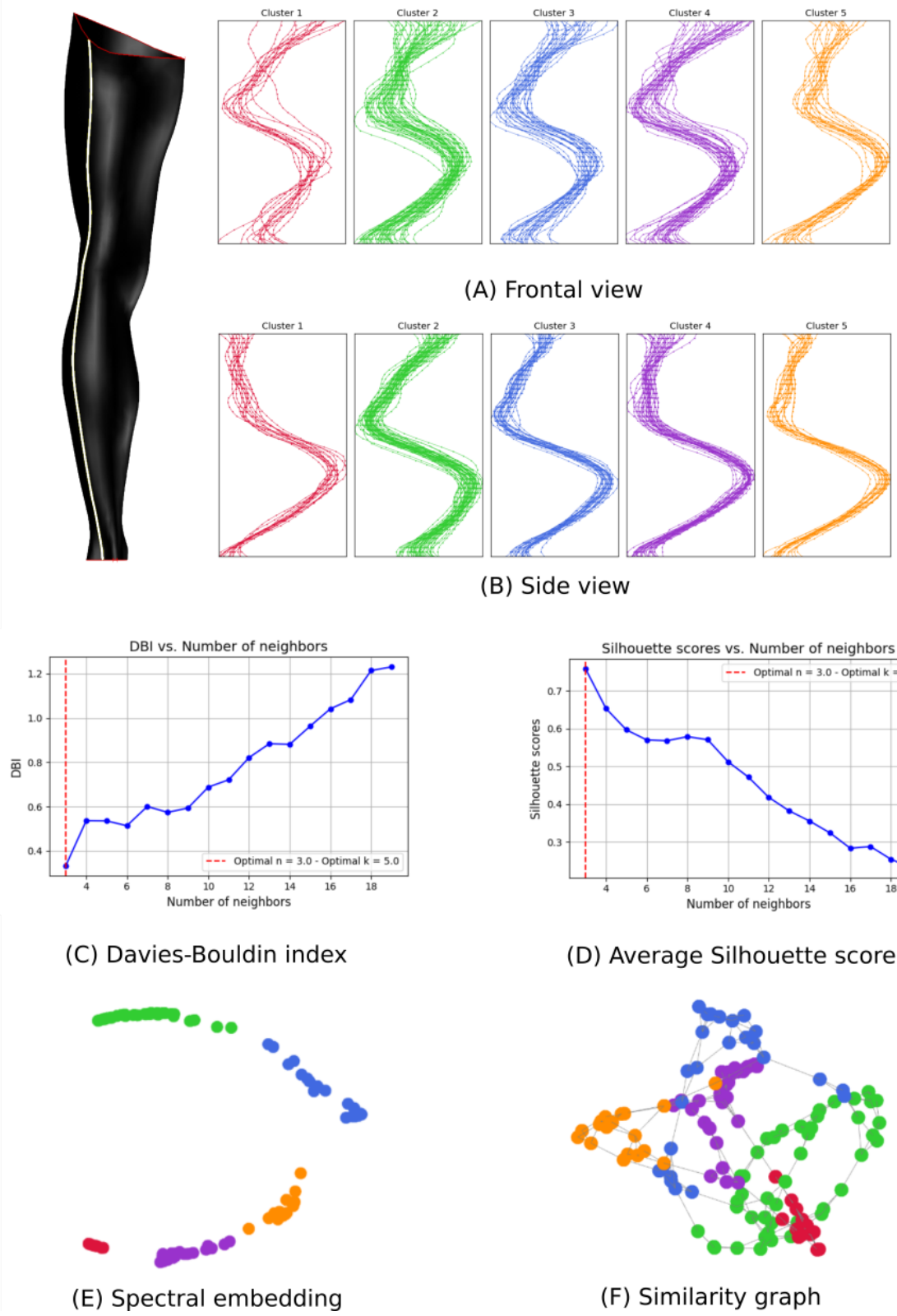


FIGURE B.11: Summary of data analysis of Projection line 11

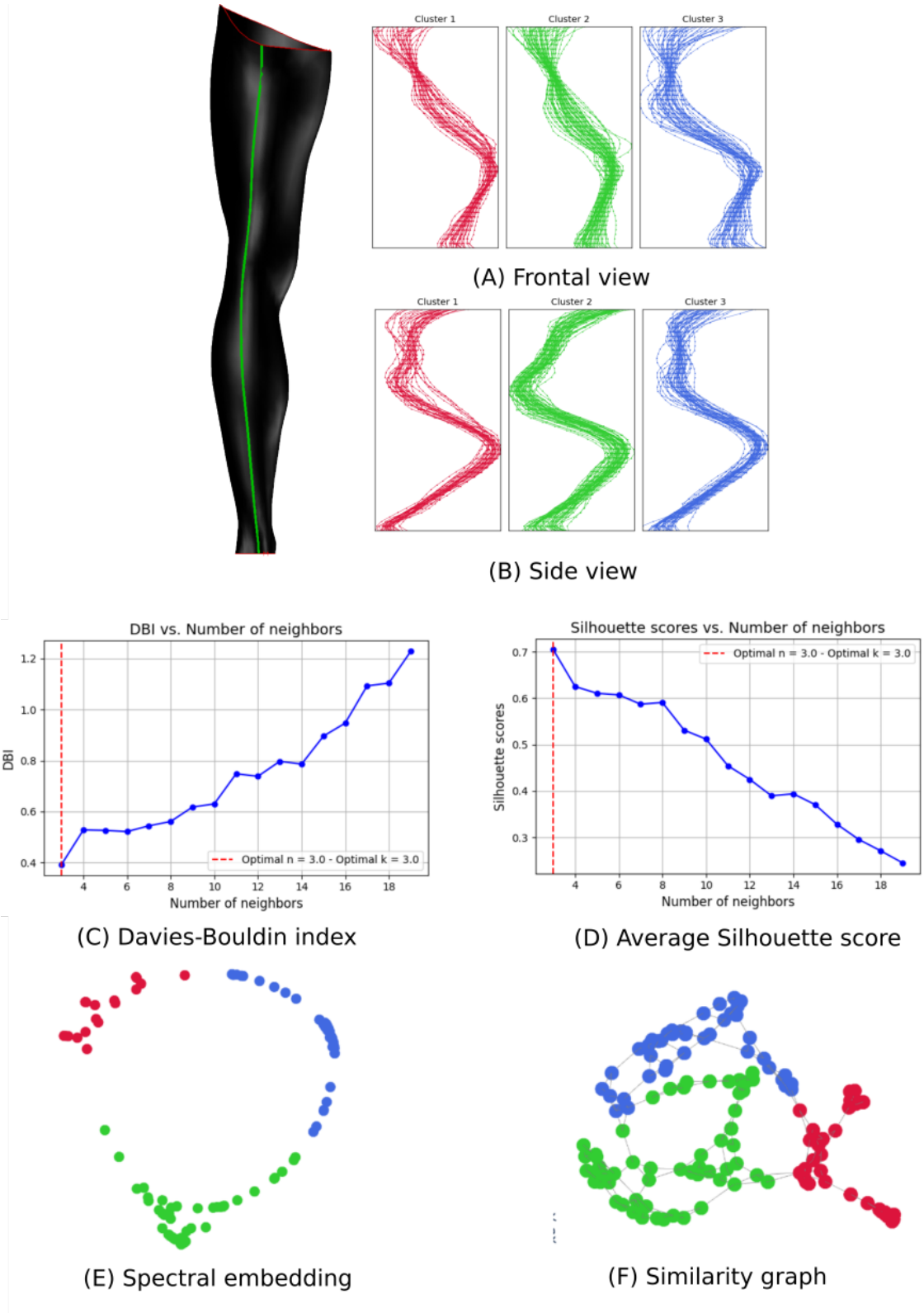


FIGURE B.12: Summary of data analysis of Projection line 12

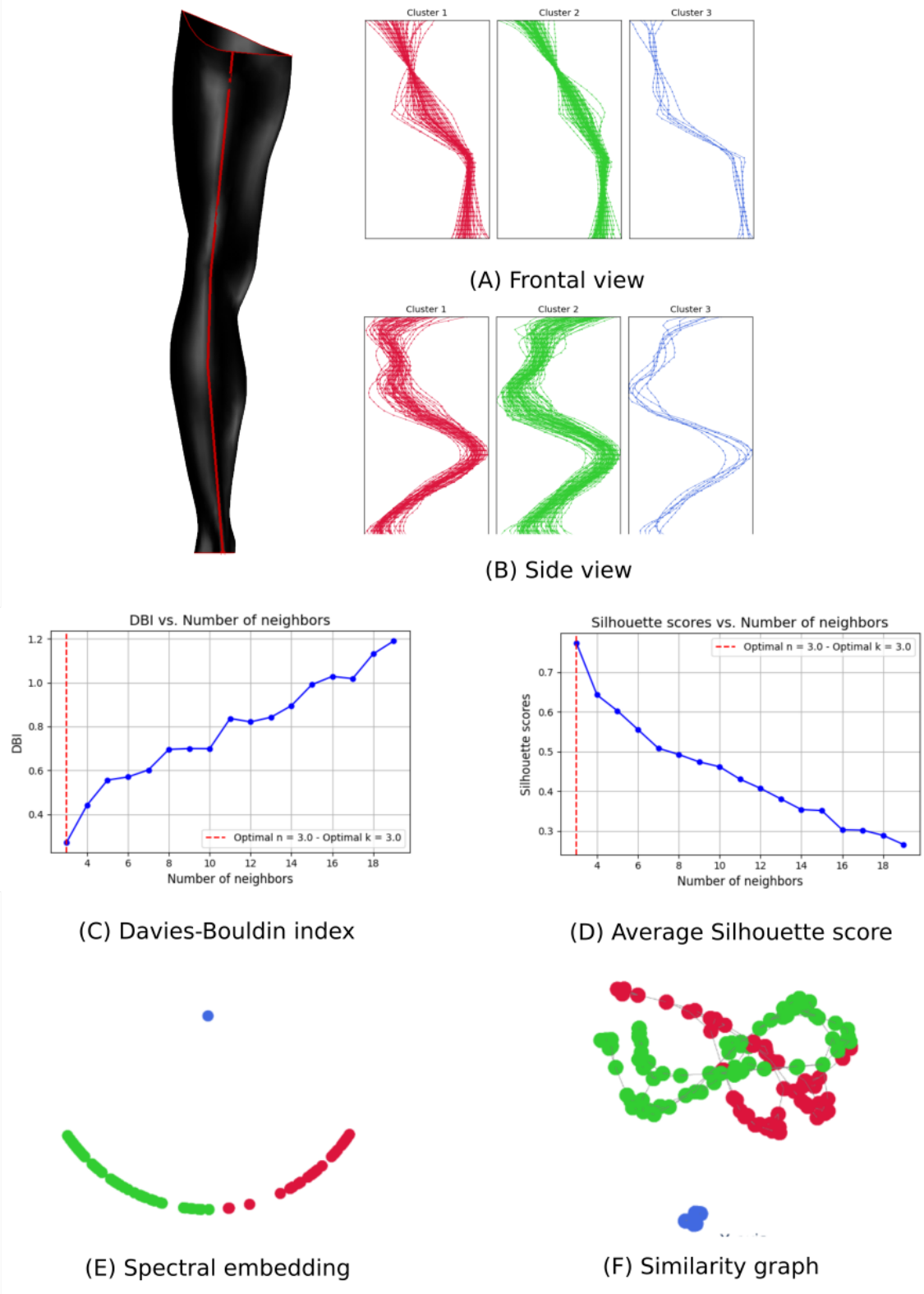


FIGURE B.13: Summary of data analysis of Projection line 13

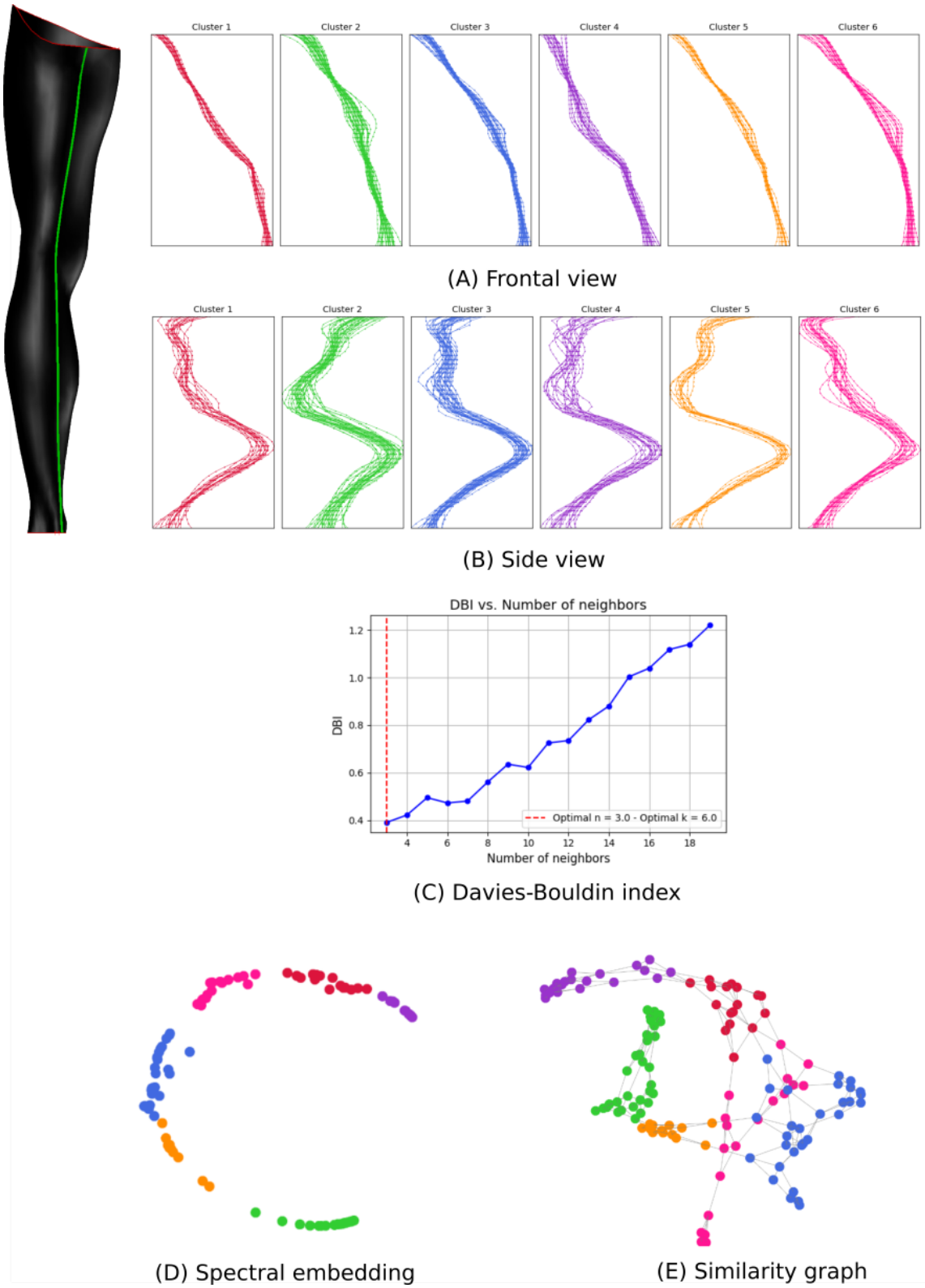


FIGURE B.14: Summary of data analysis of Projection line 14

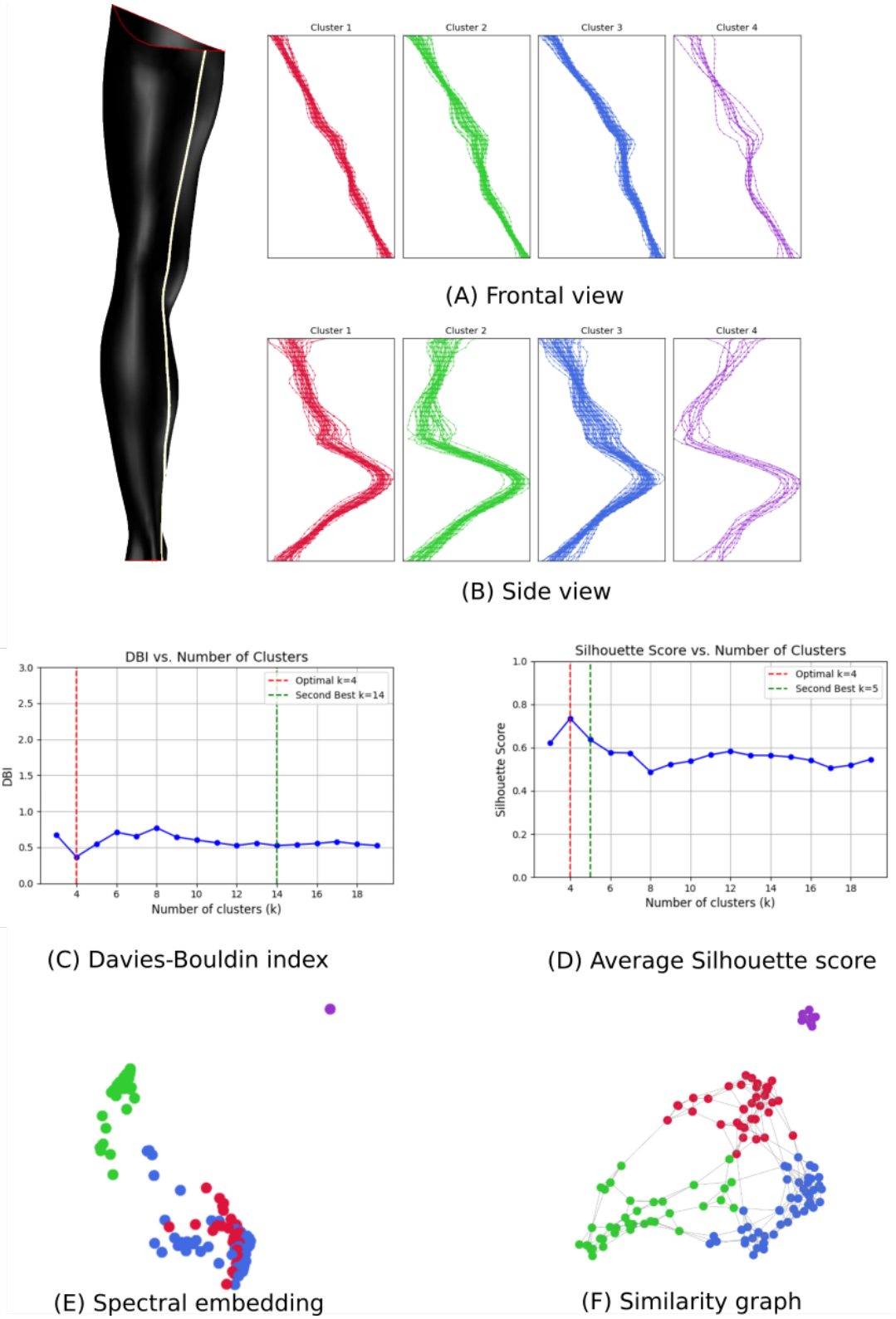


FIGURE B.15: Summary of data analysis of Projection line 15

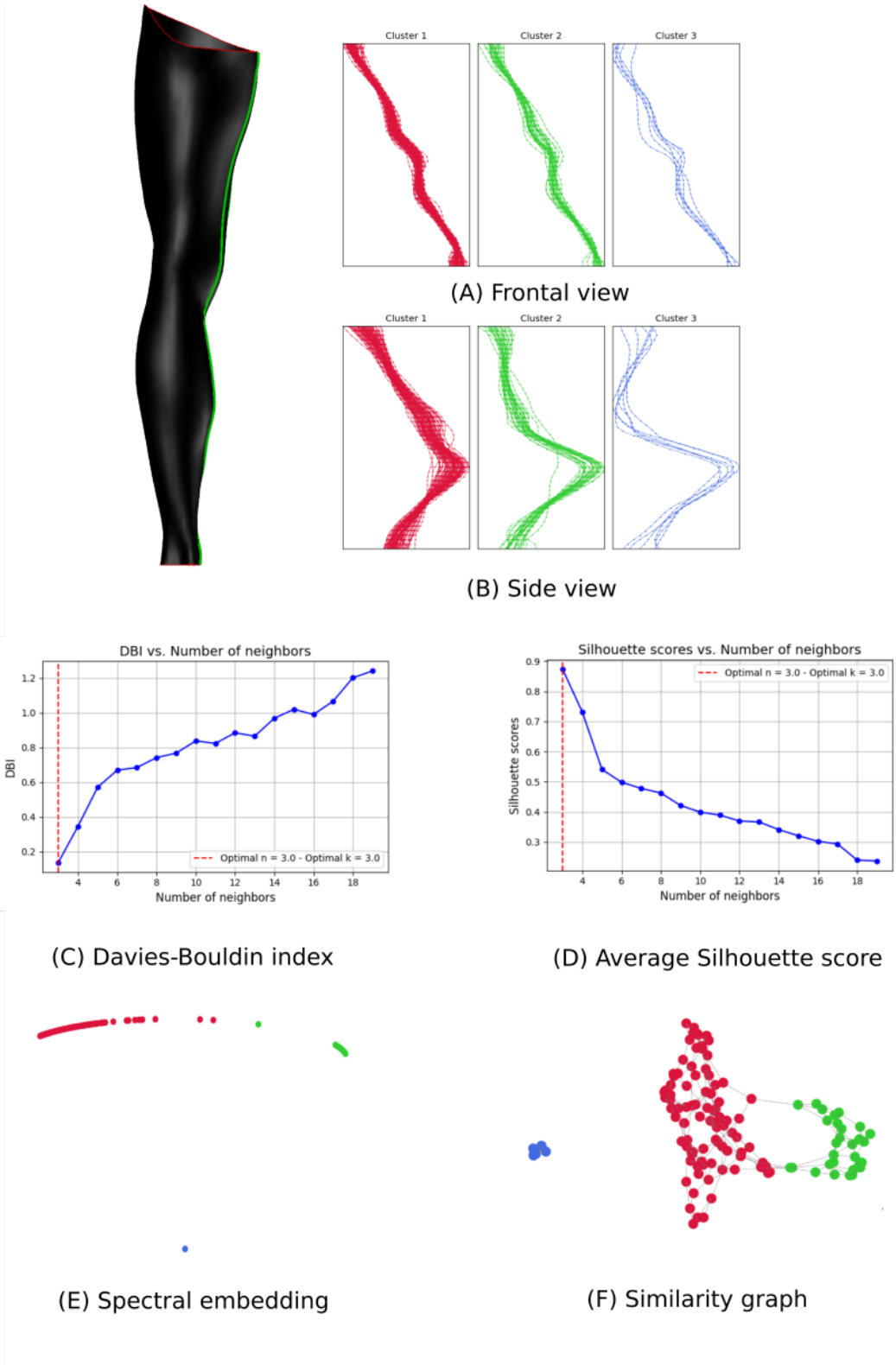


FIGURE B.16: Summary of data analysis of Projection line 16

Appendix C

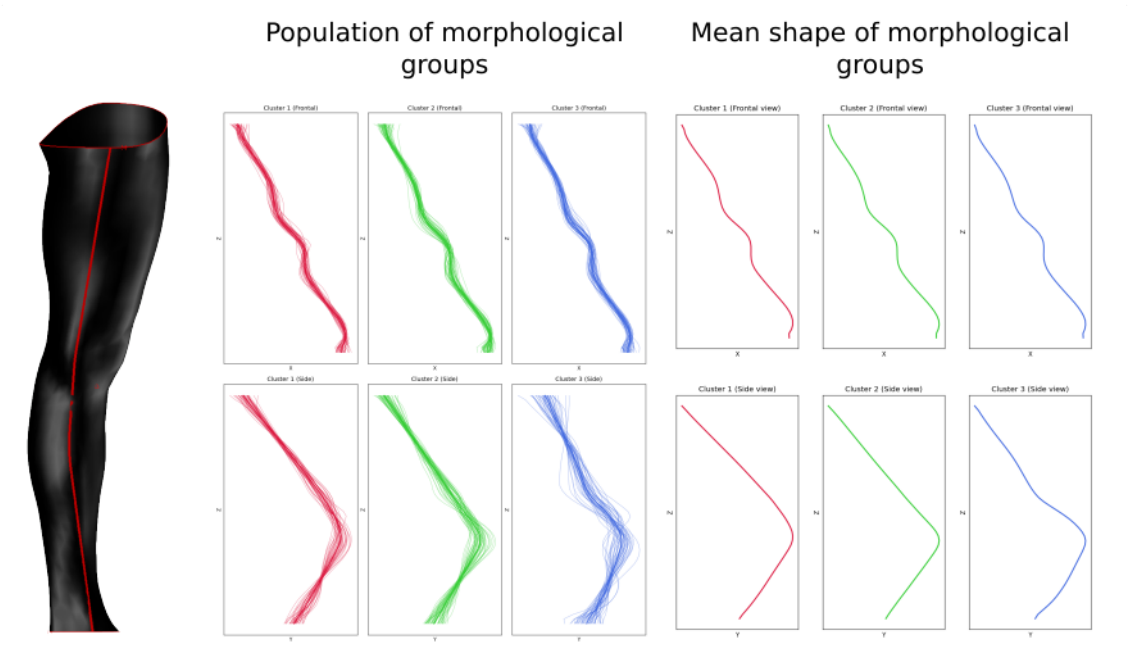


FIGURE C.1: Projection 1 - Population by cluster and mean shapes in two views Frontal view with x and z coordinates (top) and side view with y and z coordinates (bottom)

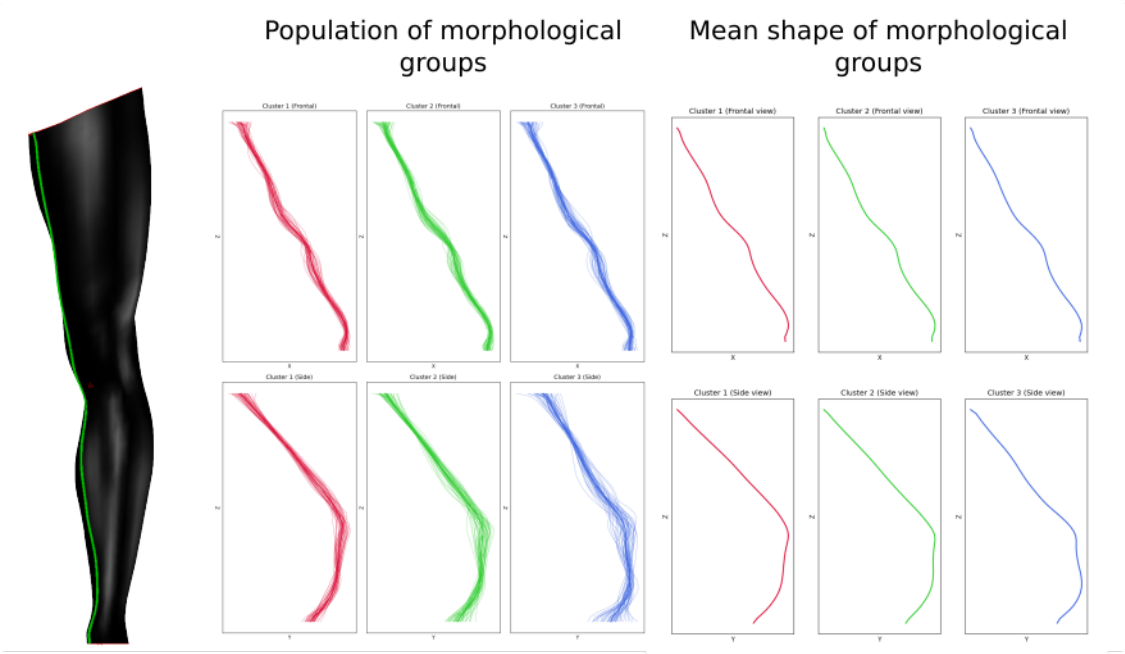


FIGURE C.2: Projection 2 - Population by cluster and mean shapes in two views Frontal view with x and z coordinates (top) and side view with y and z coordinates (bottom)

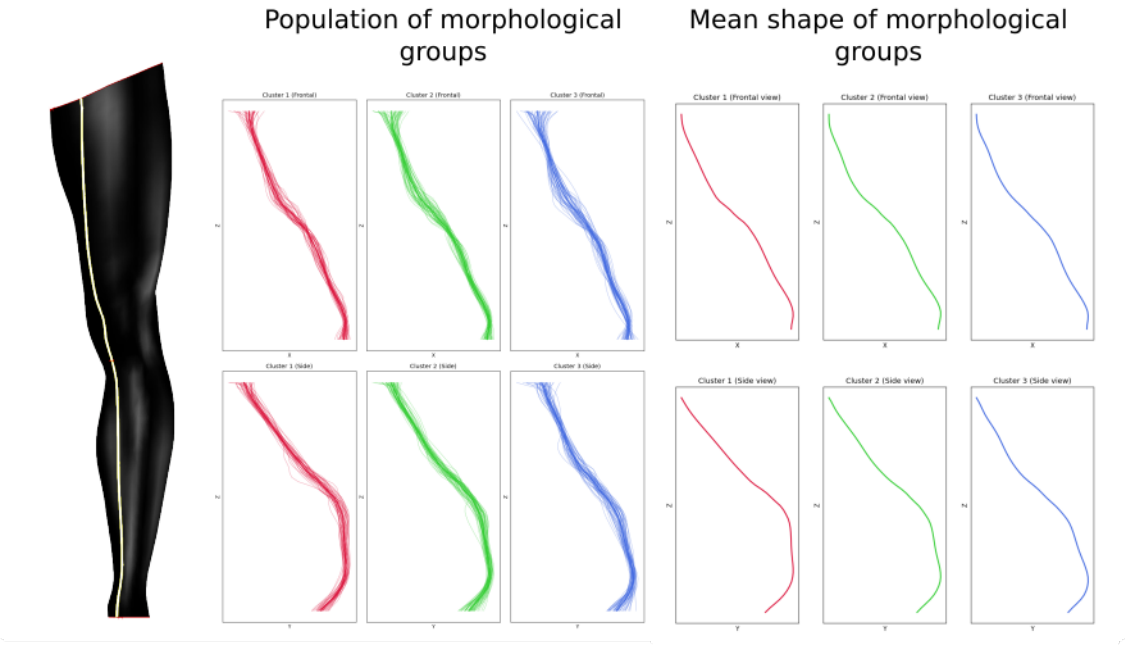


FIGURE C.3: Projection 3 - Population by cluster and mean shapes in two views Frontal view with x and z coordinates (top) and side view with y and z coordinates (bottom)

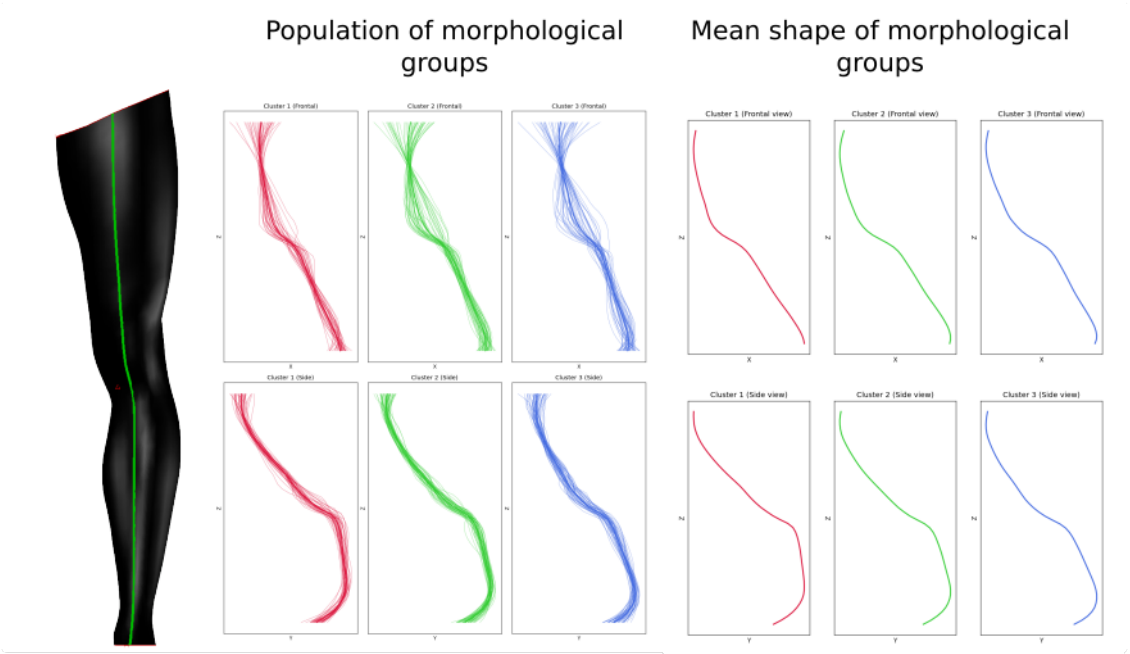


FIGURE C.4: Projection 4 - Population by cluster and mean shapes in two views Frontal view with x and z coordinates (top) and side view with y and z coordinates (bottom)

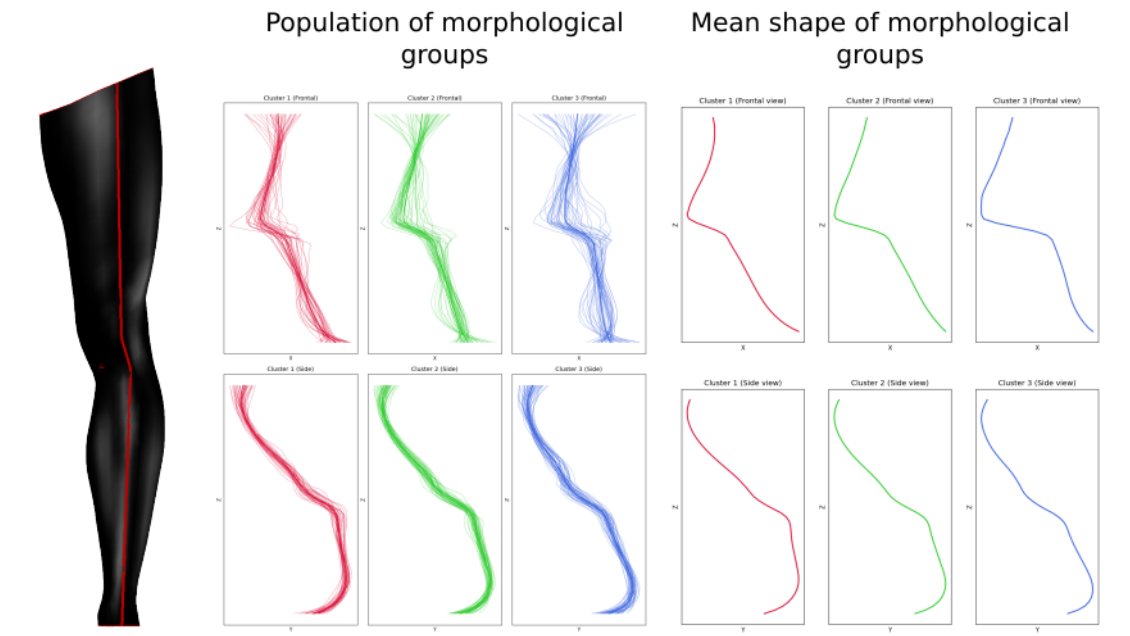


FIGURE C.5: Projection 5 - Population by cluster and mean shapes in two views Frontal view with x and z coordinates (top) and side view with y and z coordinates (bottom)

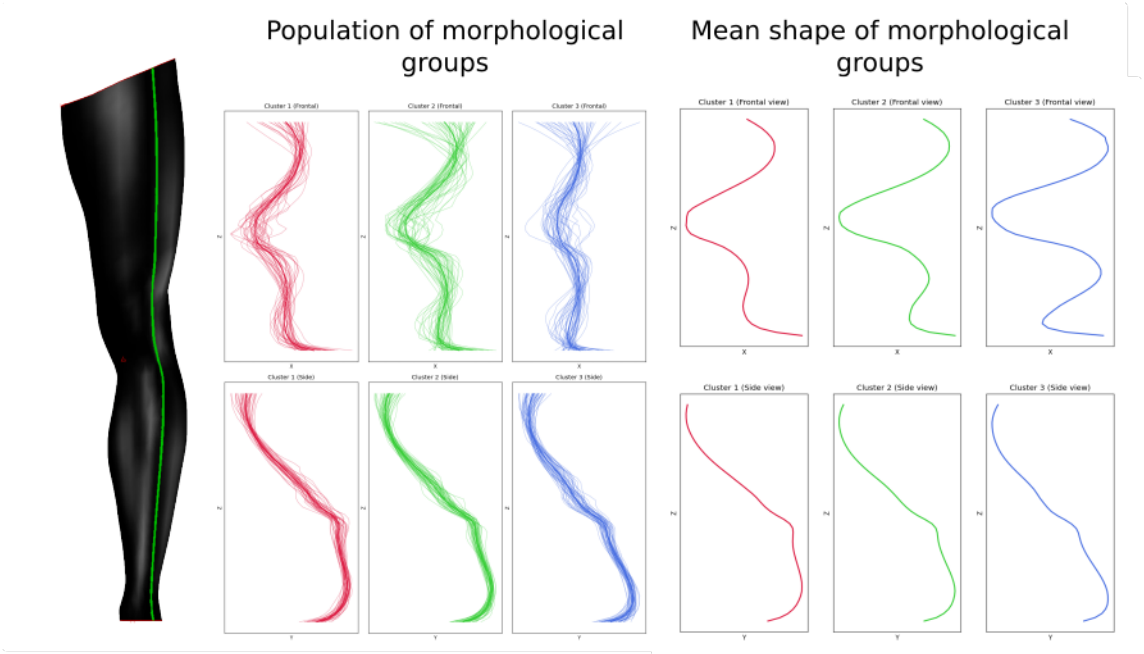


FIGURE C.6: Projection 6 - Population by cluster and mean shapes in two views Frontal view with x and z coordinates (top) and side view with y and z coordinates (bottom)

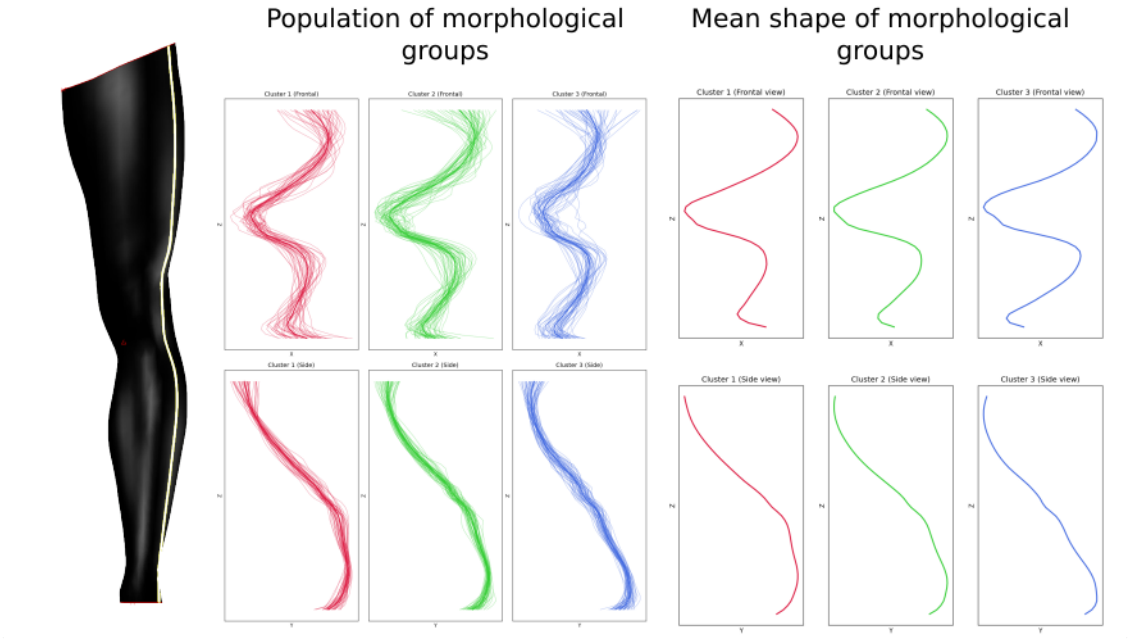


FIGURE C.7: Projection 7 - Population by cluster and mean shapes in two views Frontal view with x and z coordinates (top) and side view with y and z coordinates (bottom)

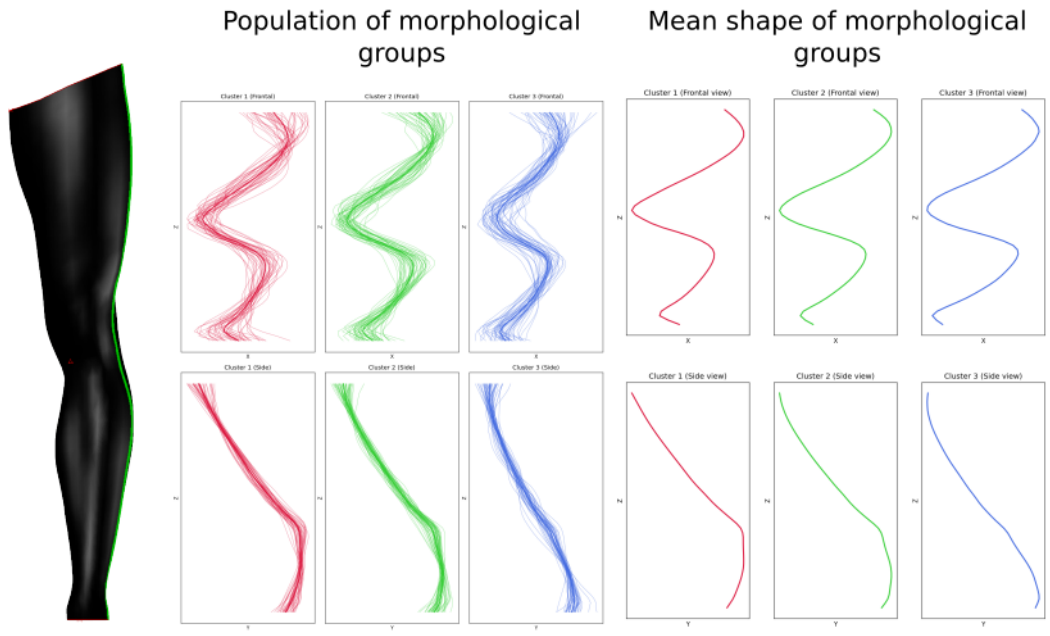


FIGURE C.8: Projection 8 - Population by cluster and mean shapes in two views Frontal view with x and z coordinates (top) and side view with y and z coordinates (bottom)

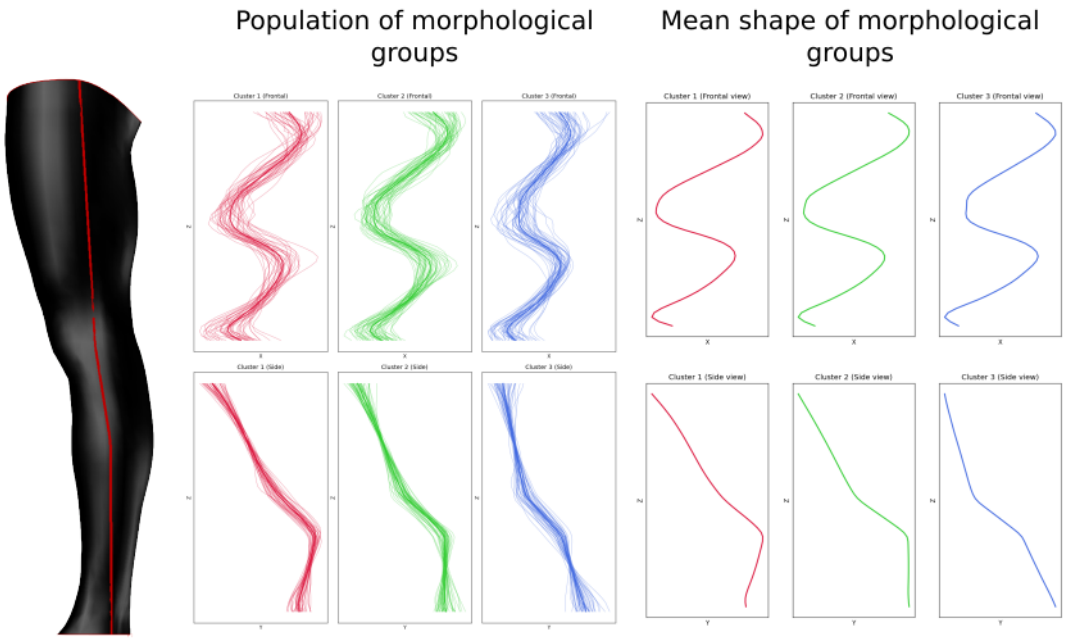


FIGURE C.9: Projection 9 - Population by cluster and mean shapes in two views Frontal view with x and z coordinates (top) and side view with y and z coordinates (bottom)

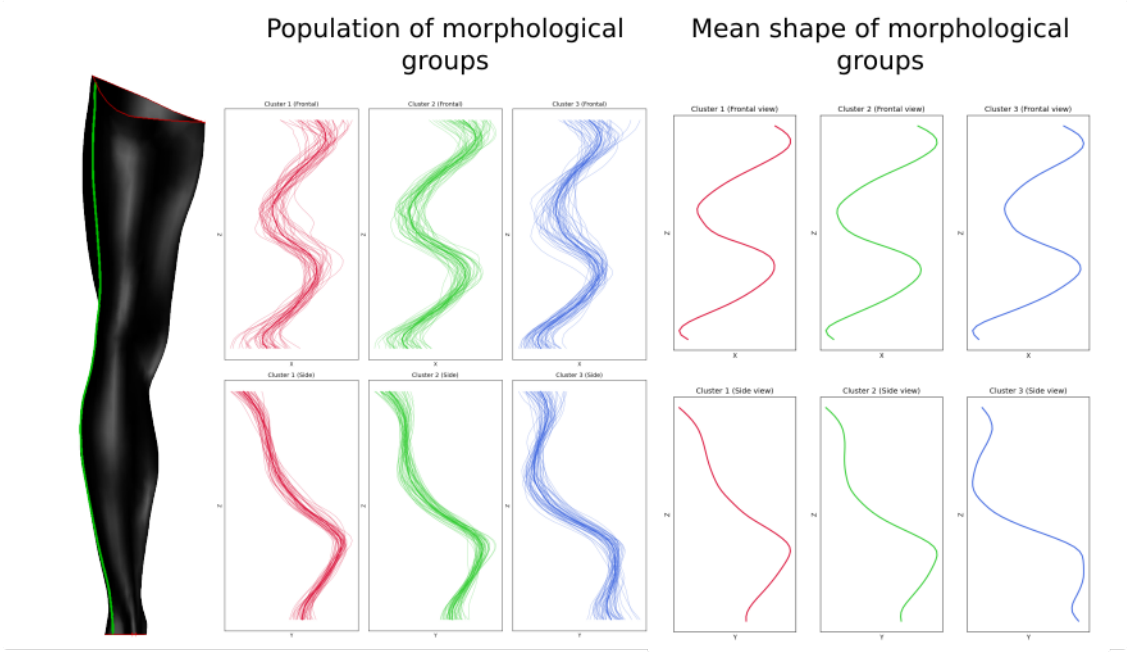


FIGURE C.10: Projection 10 - Population by cluster and mean shapes in two views Frontal view with x and z coordinates (top) and side view with y and z coordinates (bottom)

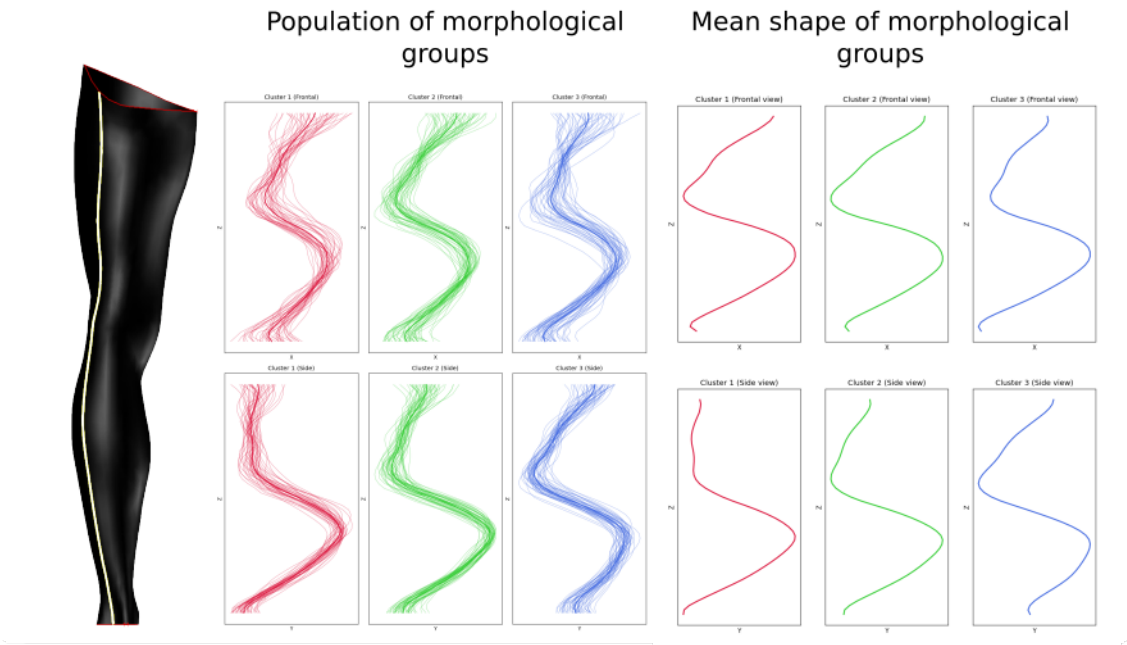


FIGURE C.11: Projection 11 - Population by cluster and mean shapes in two views Frontal view with x and z coordinates (top) and side view with y and z coordinates (bottom)

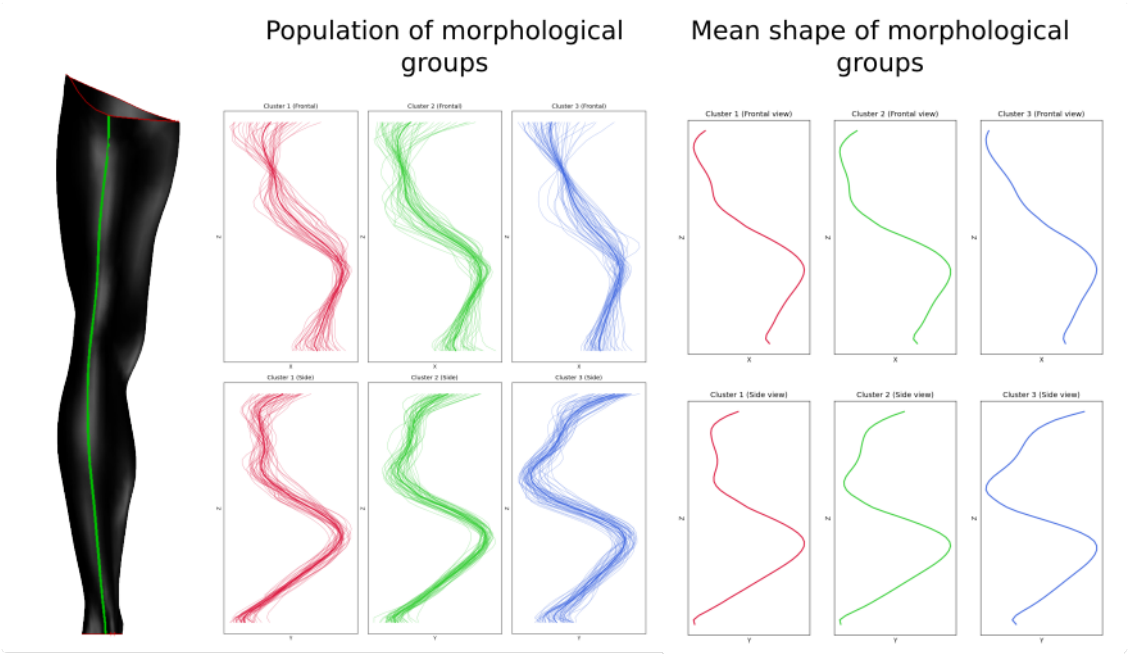


FIGURE C.12: Projection 12 - Population by cluster and mean shapes in two views Frontal view with x and z coordinates (top) and side view with y and z coordinates (bottom)

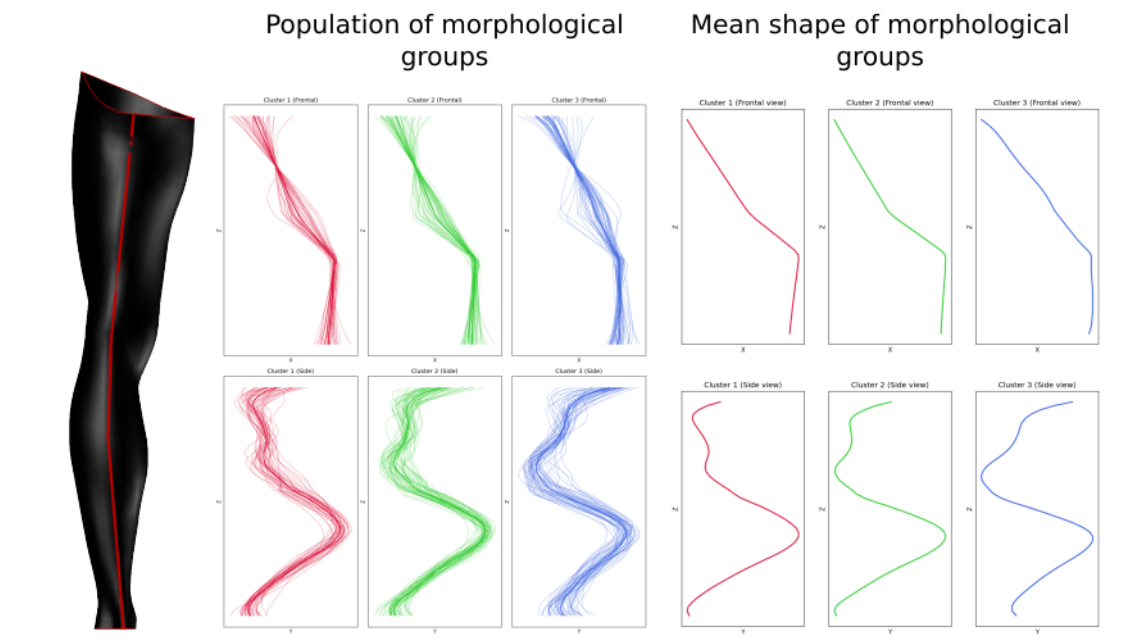


FIGURE C.13: Projection 13 - Population by cluster and mean shapes in two views Frontal view with x and z coordinates (top) and side view with y and z coordinates (bottom)

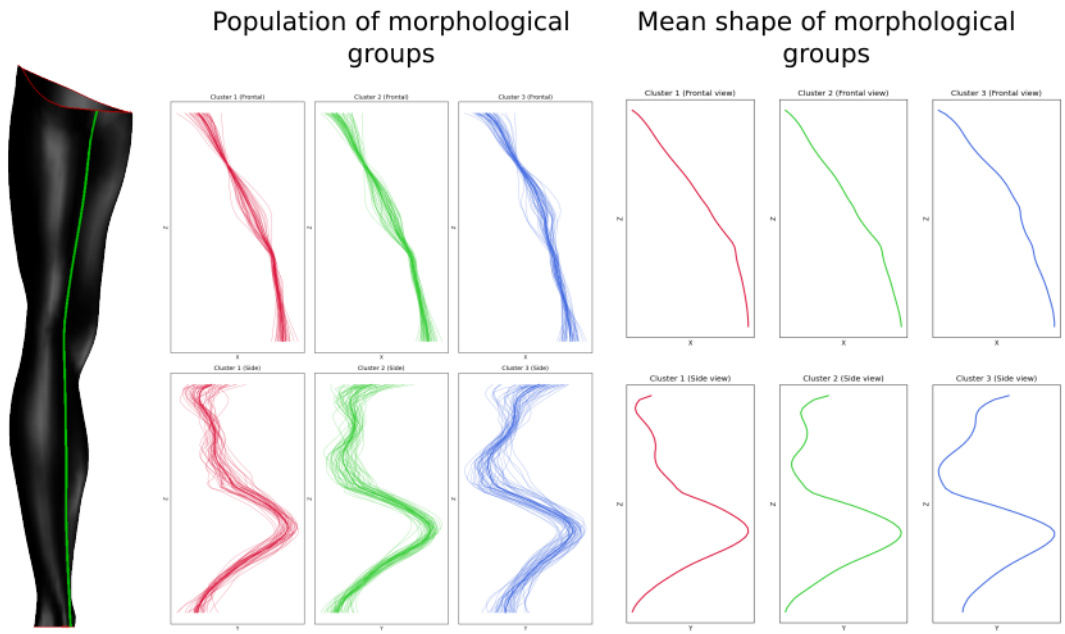


FIGURE C.14: Projection 14 - Population by cluster and mean shapes in two views Frontal view with x and z coordinates (top) and side view with y and z coordinates (bottom)

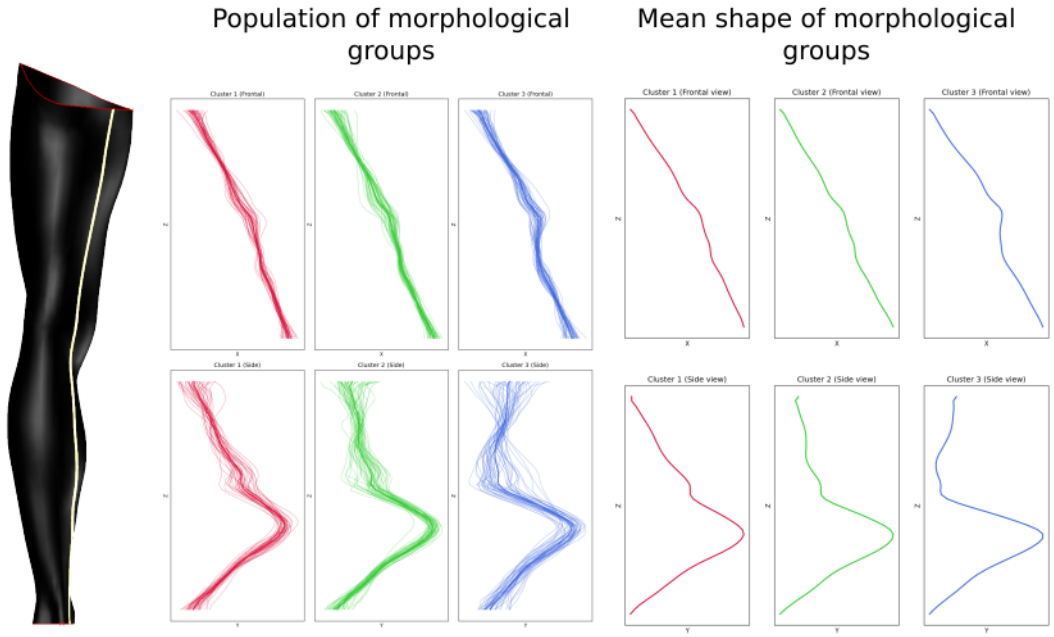


FIGURE C.15: Projection 15 - Population by cluster and mean shapes in two views Frontal view with x and z coordinates (top) and side view with y and z coordinates (bottom)

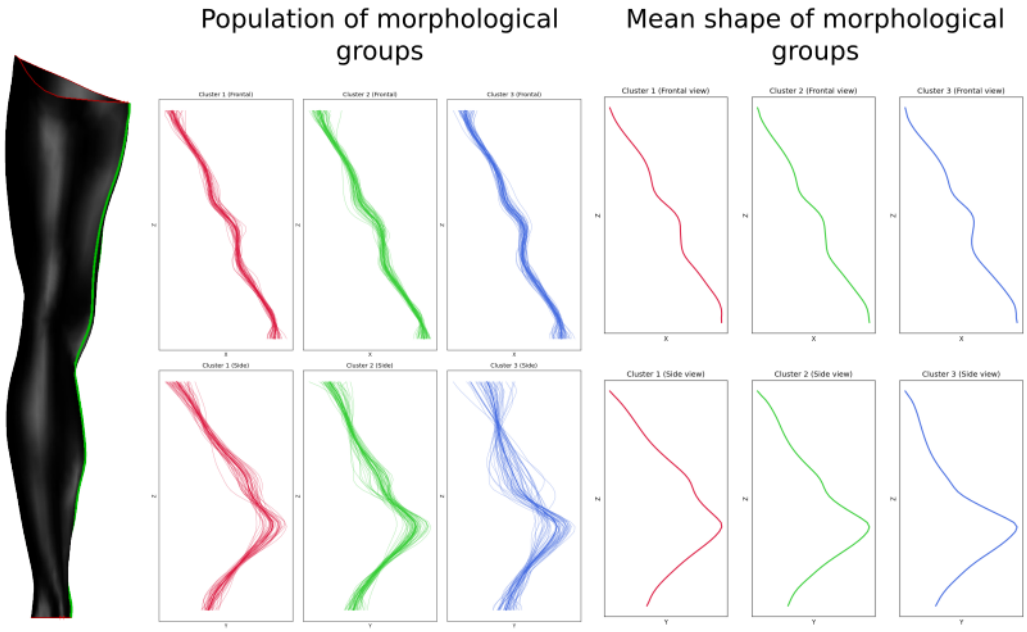


FIGURE C.16: Projection 16 - Population by cluster and mean shapes in two views Frontal view with x and z coordinates (top) and side view with y and z coordinates (bottom)

Appendix D

D.1 Outliers detected by MeshDeepSVDD

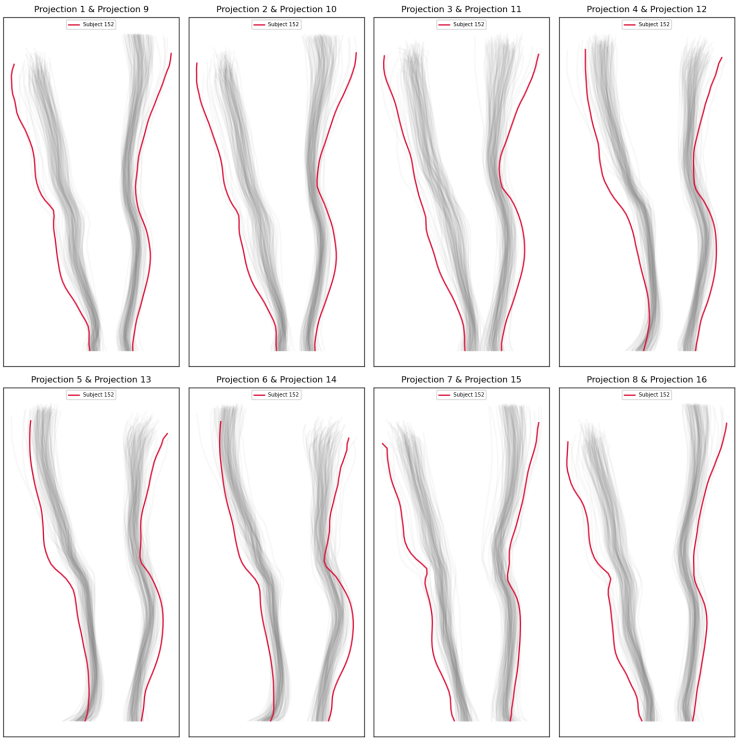


FIGURE D.1: Subject 152

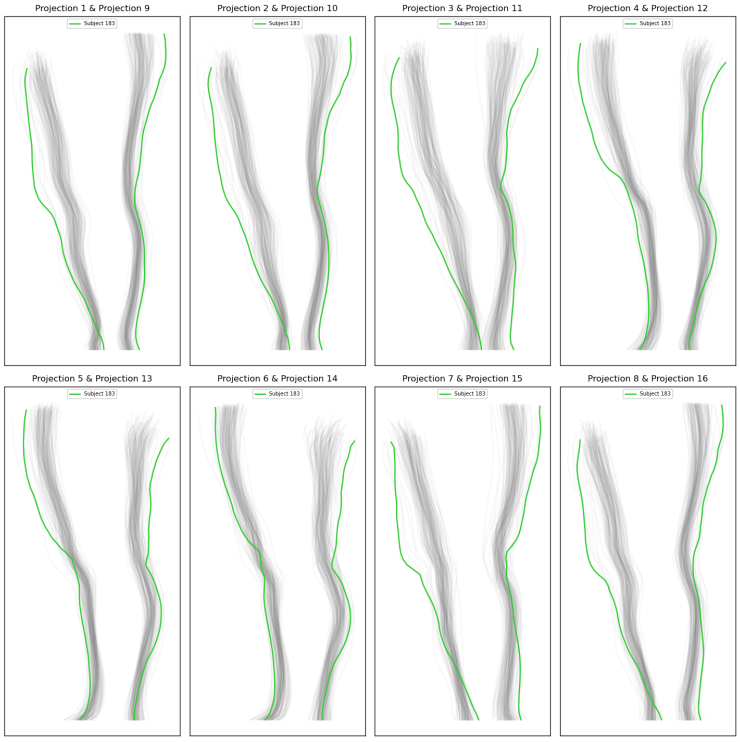


FIGURE D.2: Subject 183

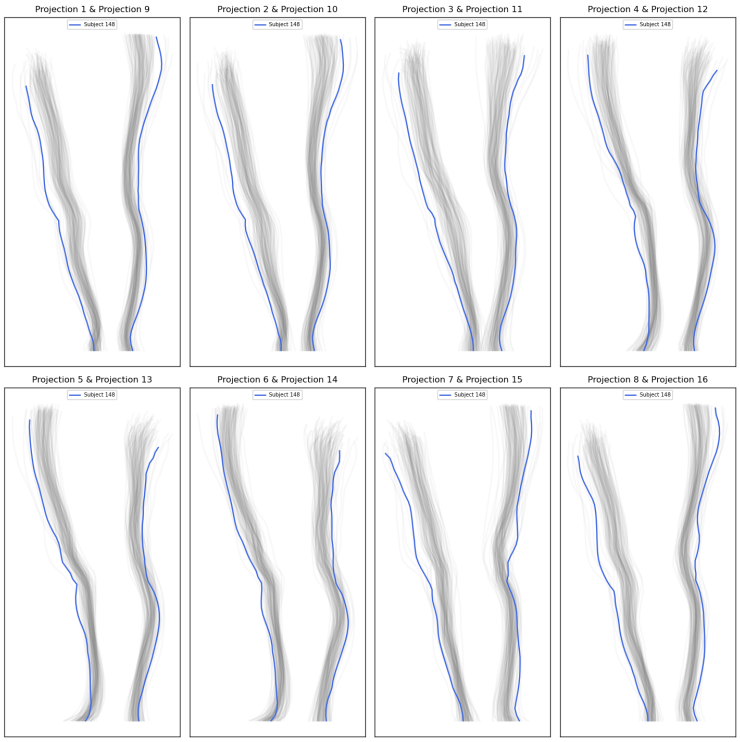


FIGURE D.3: Subject 148

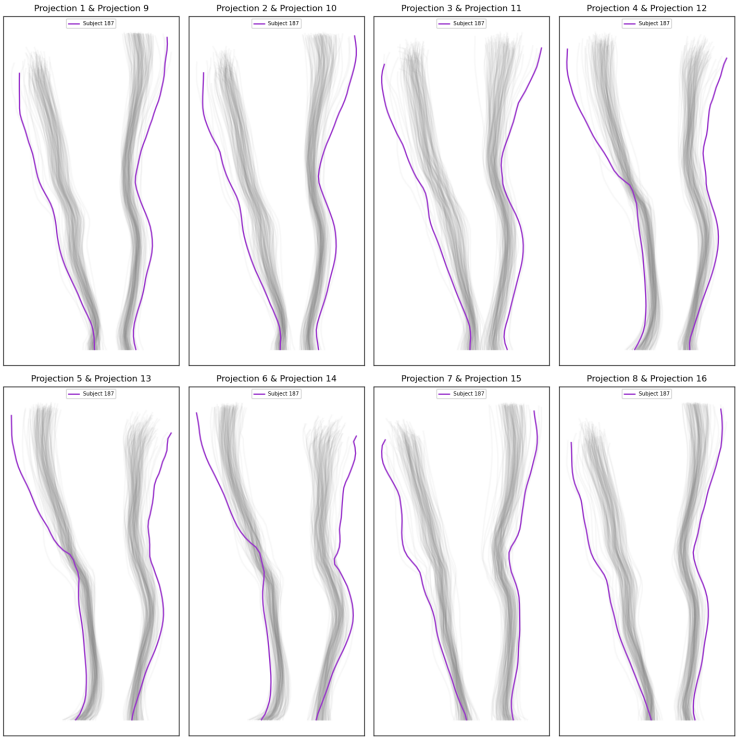


FIGURE D.4: Subject 187



FIGURE D.5: Subject 198

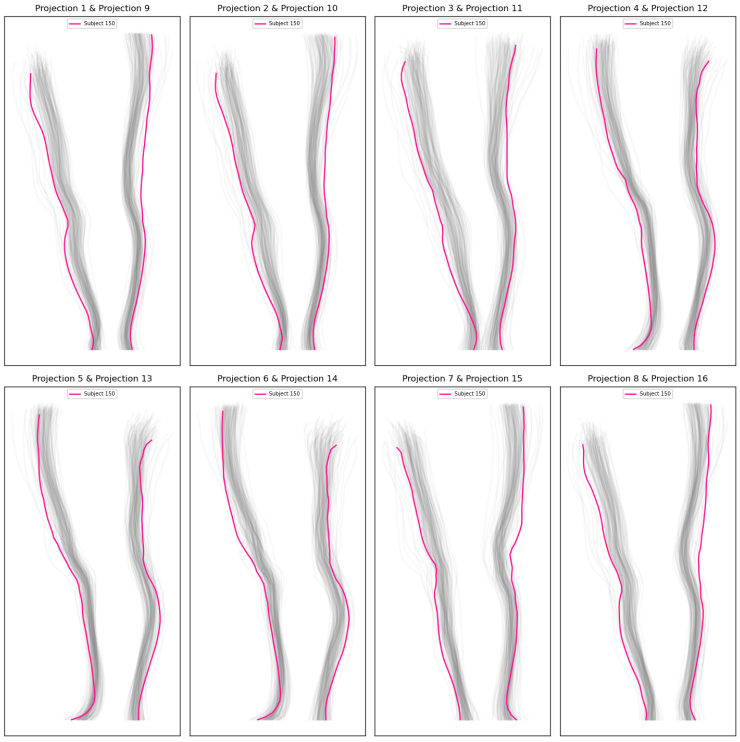


FIGURE D.6: Subject 150

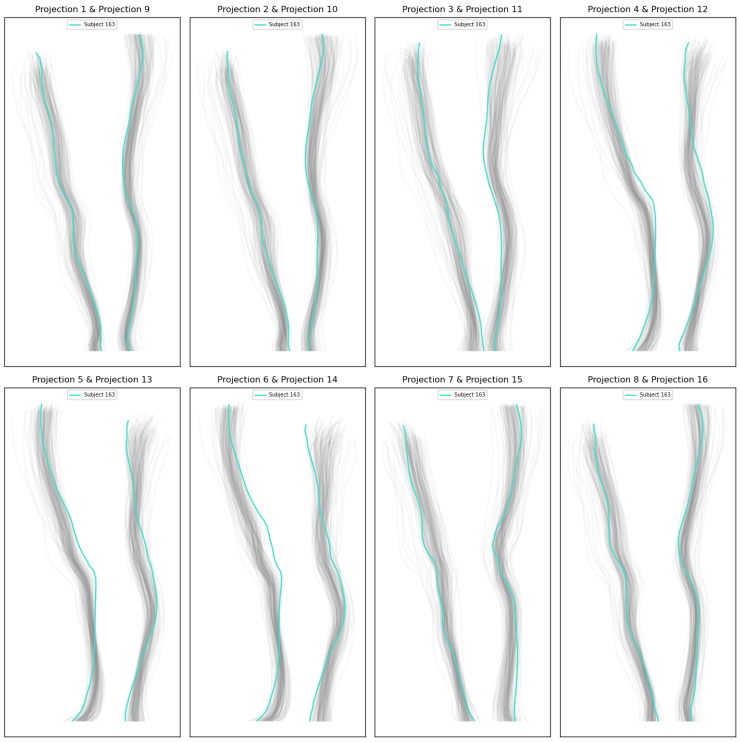


FIGURE D.7: Subject 163

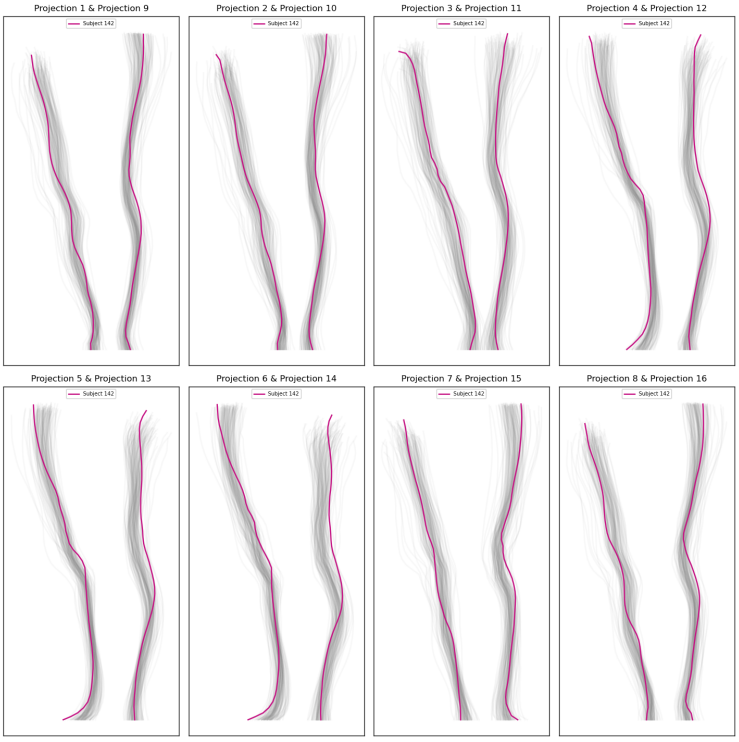


FIGURE D.8: Subject 142

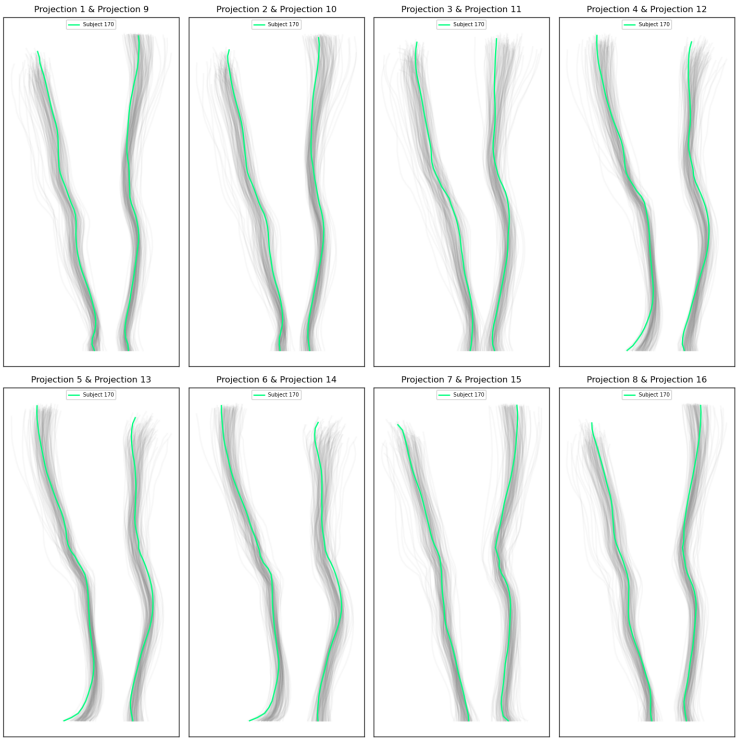


FIGURE D.9: Subject 170

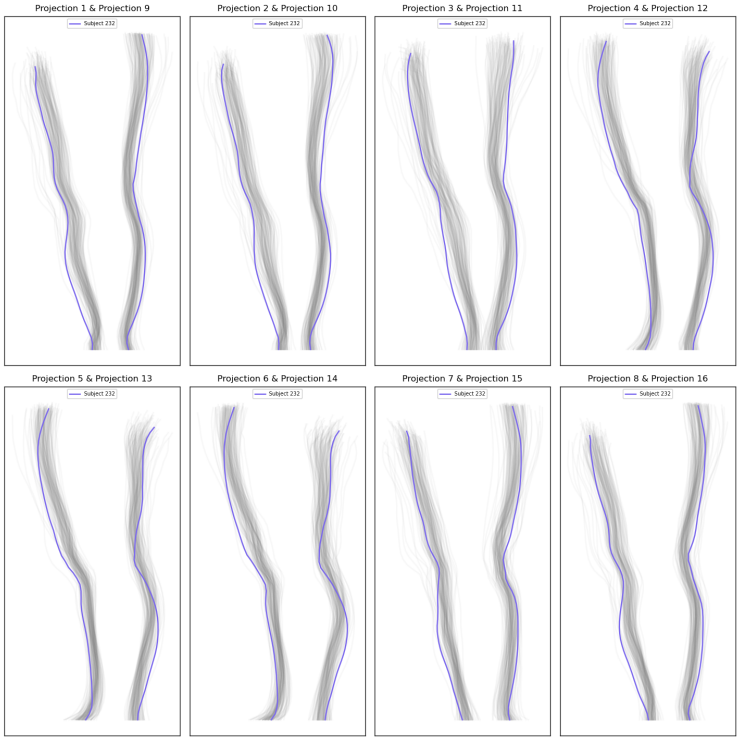


FIGURE D.10: Subject 232

Appendix E

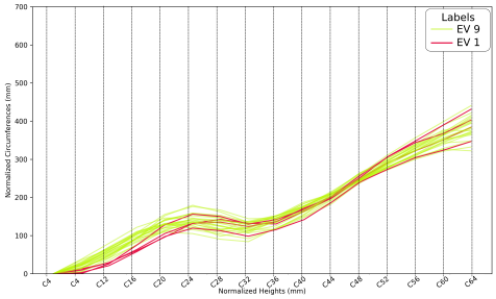


FIGURE E.1: Ankle group 1 and 2 with the same thigh group 1

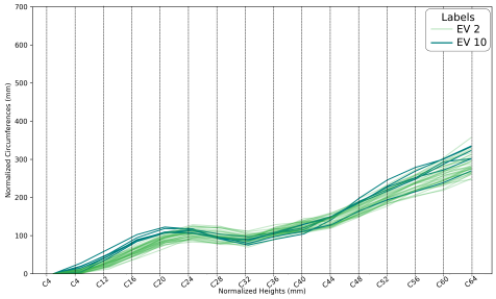


FIGURE E.2: Ankle group 1 and 2 with the same thigh group 2

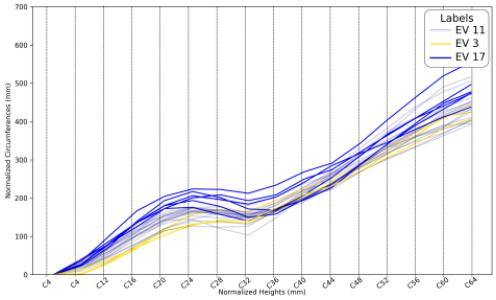


FIGURE E.3: Ankle group 1, 2, and 3 with the same thigh group 3

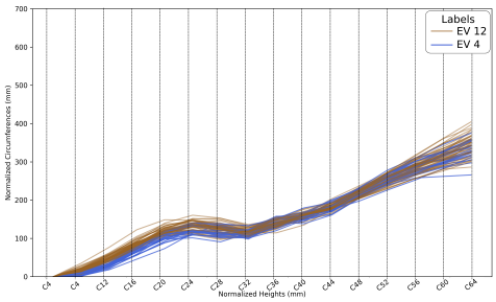


FIGURE E.4: Ankle group 1 and 2 with the same thigh group 4

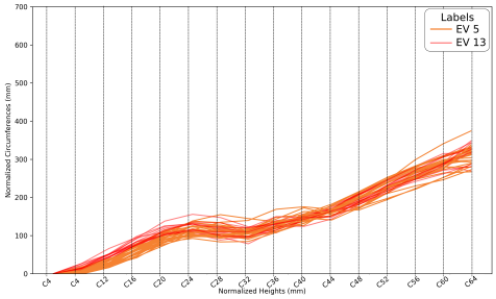


FIGURE E.5: Ankle group 1 and 2 with the same thigh group 5

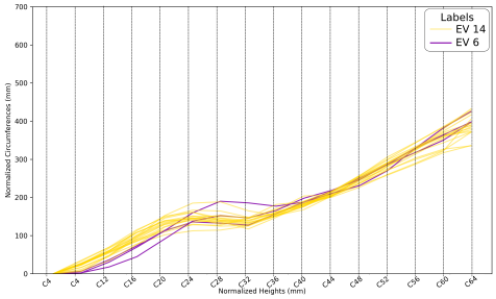


FIGURE E.6: Ankle group 1 and 2 with the same thigh group 6

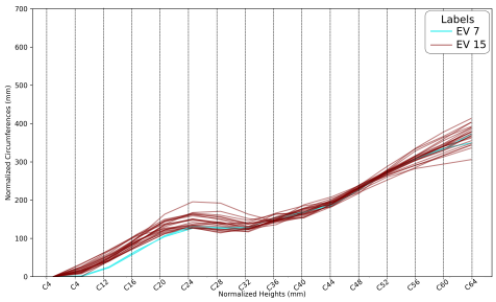


FIGURE E.7: Ankle group 1 and 2 with the same thigh group 7

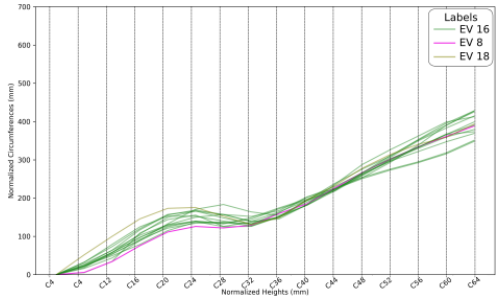


FIGURE E.8: Ankle group 1, 2, and 3 with the same thigh group 8

Appendix F

F.1 Geometrical separation of the 3 morphological groups defined by the 3D shape descriptor

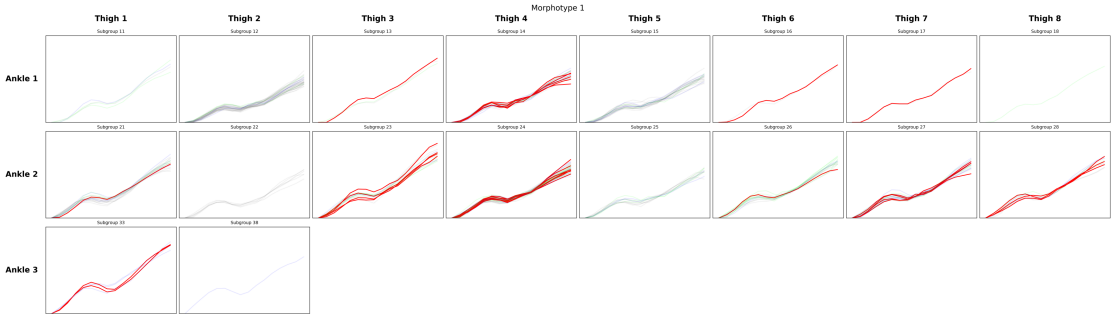


FIGURE F.1: 18 unique patterns and morphological group 1

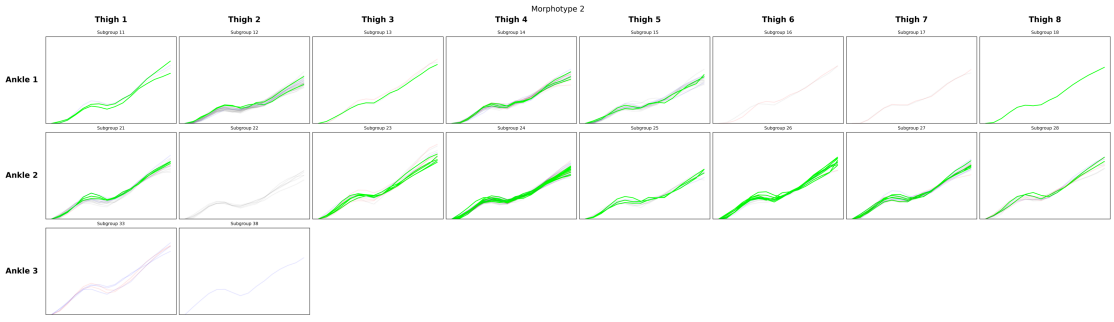


FIGURE F.2: 18 unique patterns and morphological group 2

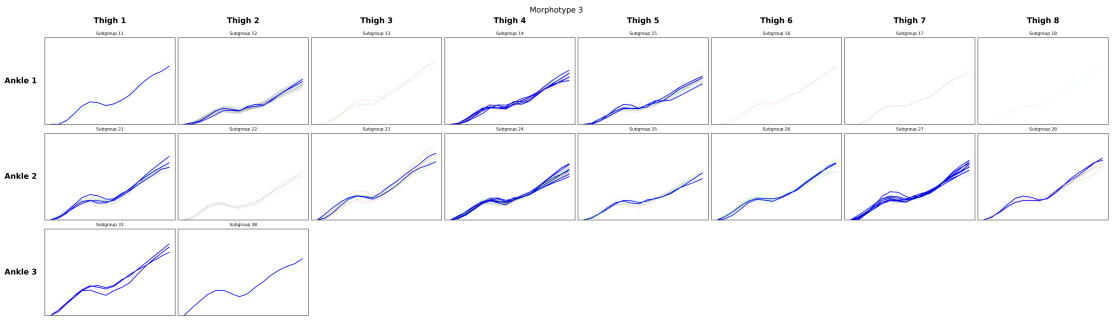


FIGURE F.3: 18 unique patterns and morphological group 3

F.2 Gender separation

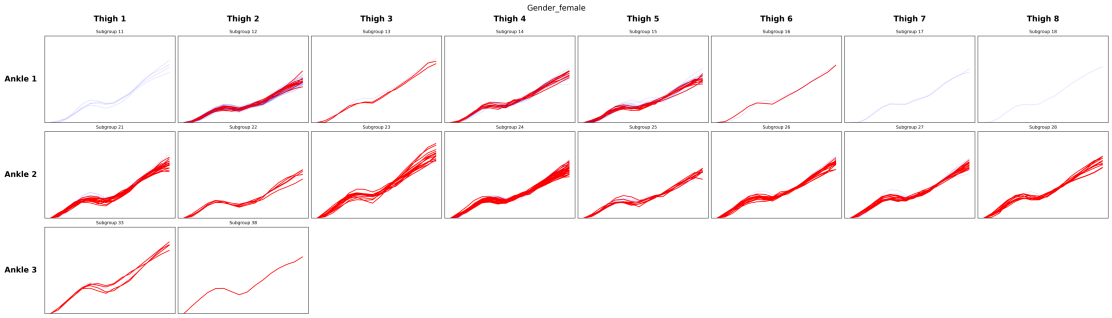


FIGURE F.4: 18 unique patterns of female subjects

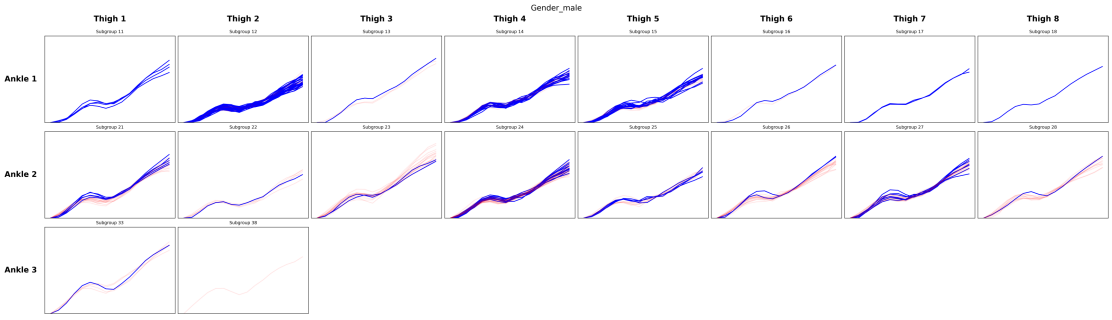


FIGURE F.5: 18 unique patterns of male subjects

F.3 Body mass index (BMI) separation

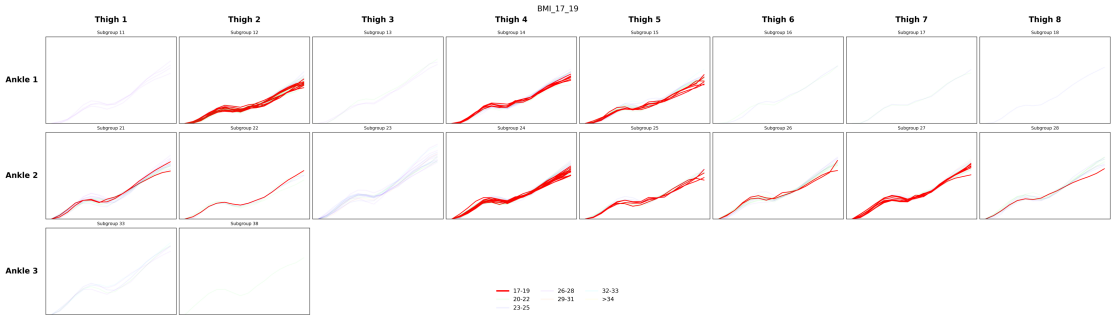


FIGURE F.6: 18 unique patterns of subjects with BMI 17 - 19

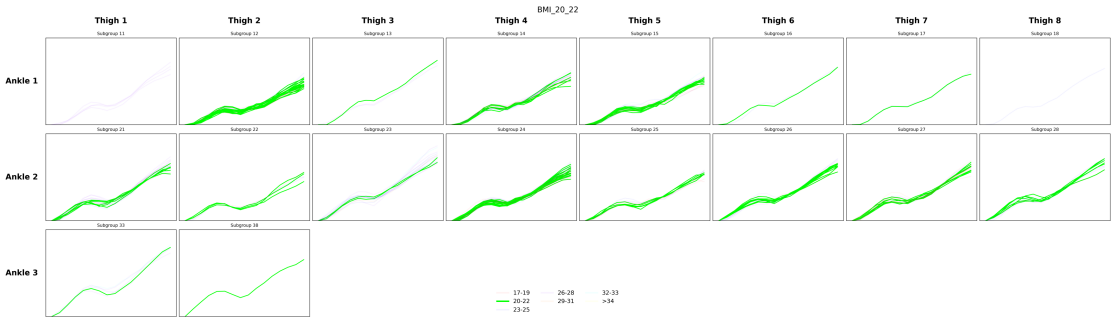


FIGURE F.7: 18 unique patterns of subjects with BMI 20 - 22

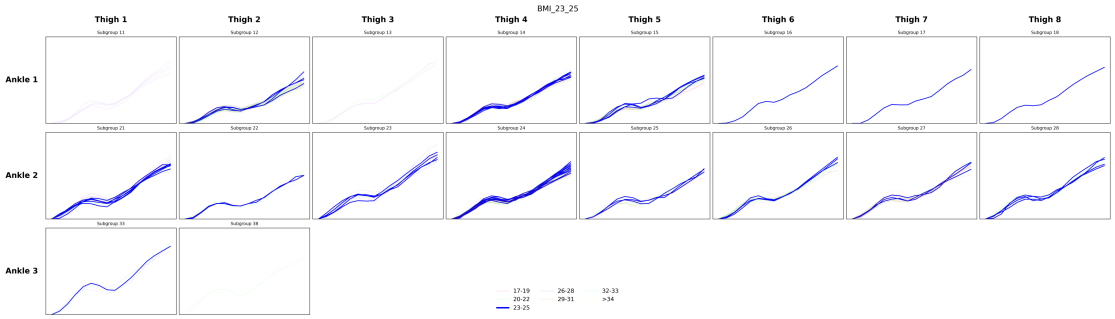


FIGURE F.8: 18 unique patterns of subjects with BMI 23 - 25

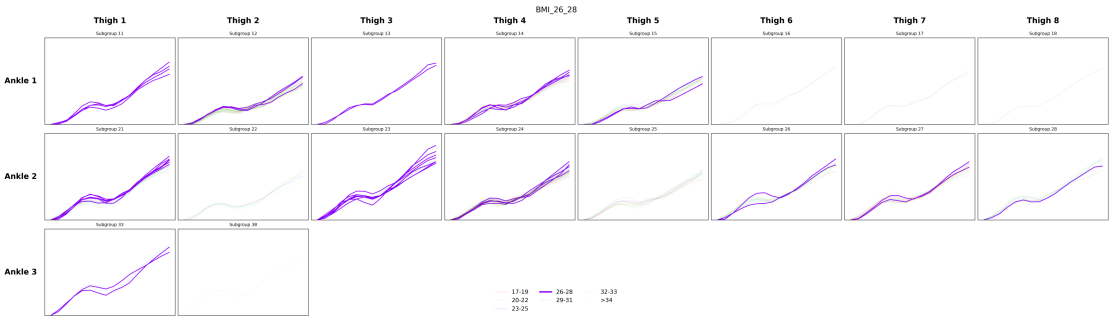


FIGURE F.9: 18 unique patterns of subjects with BMI 26 - 28

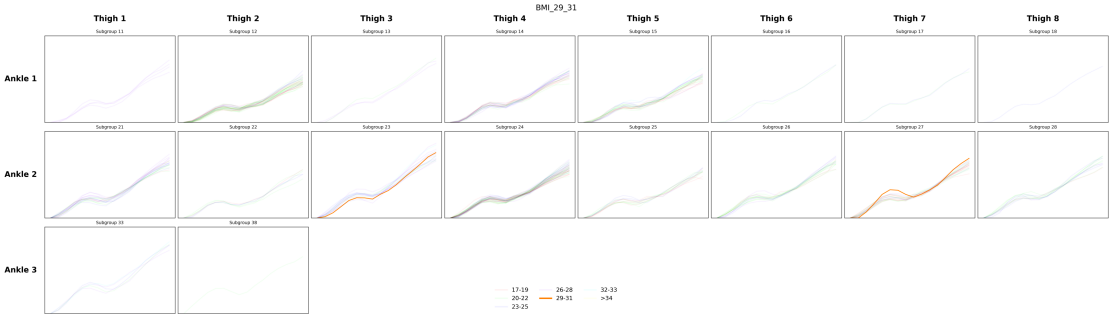


FIGURE F.10: 18 unique patterns of subjects with BMI 29 - 31

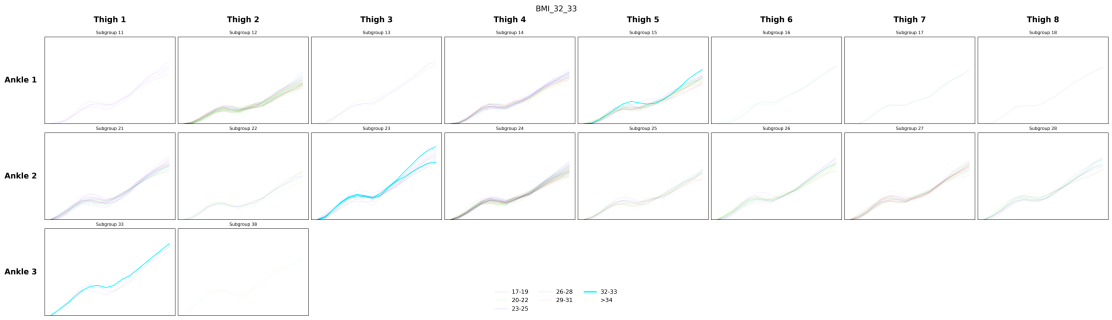


FIGURE F.11: 18 unique patterns of subjects with BMI 32 - 33

F.4 Sigvaris sizing separation

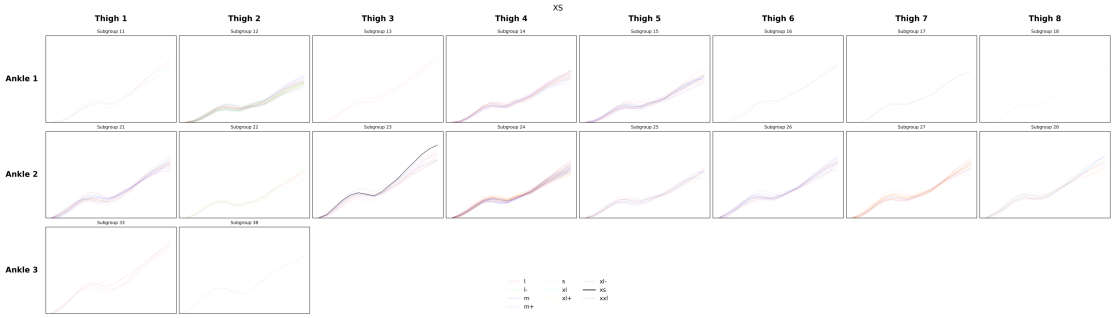


FIGURE F.12: 18 unique patterns of subjects with size XS

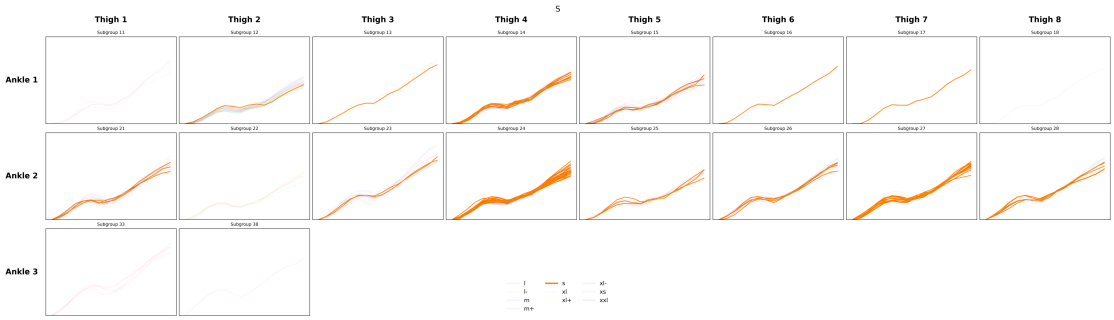


FIGURE F.13: 18 unique patterns of subjects with size S

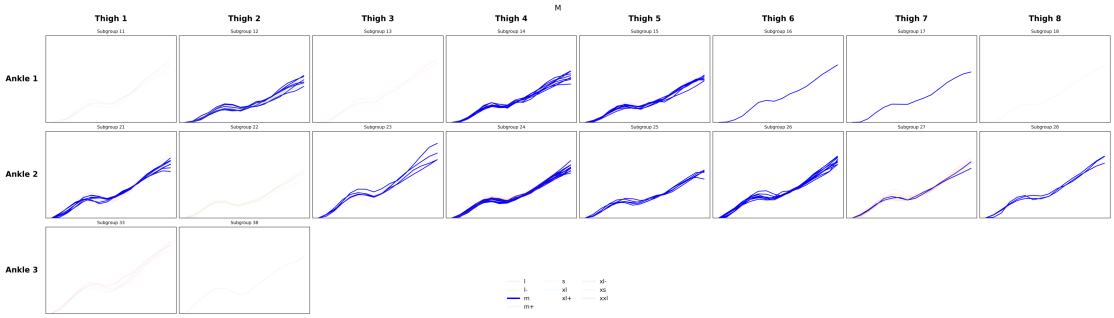


FIGURE F.14: 18 unique patterns of subjects with size M

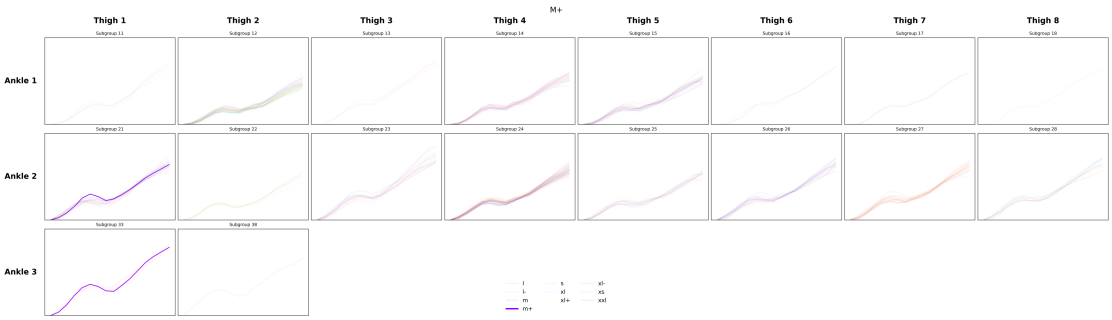


FIGURE F.15: 18 unique patterns of subjects with size M+

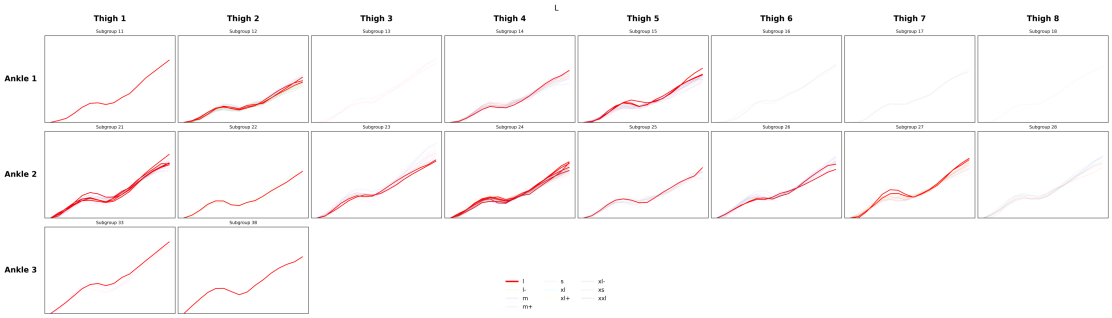


FIGURE F.16: 18 unique patterns of subjects with size L

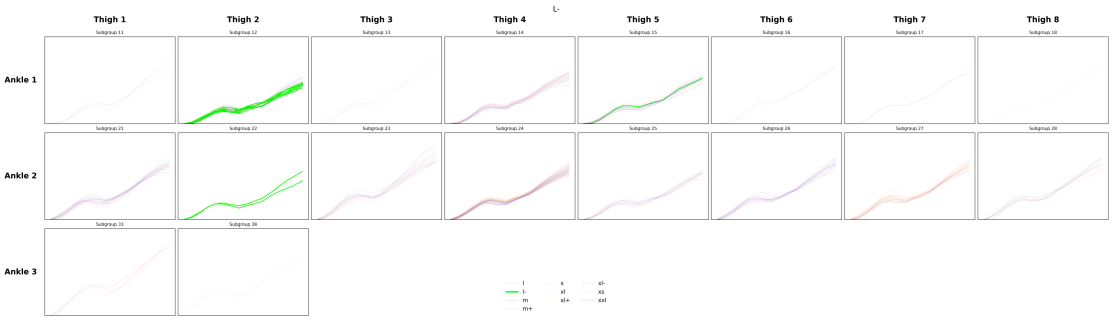


FIGURE F.17: 18 unique patterns of subjects with size L-

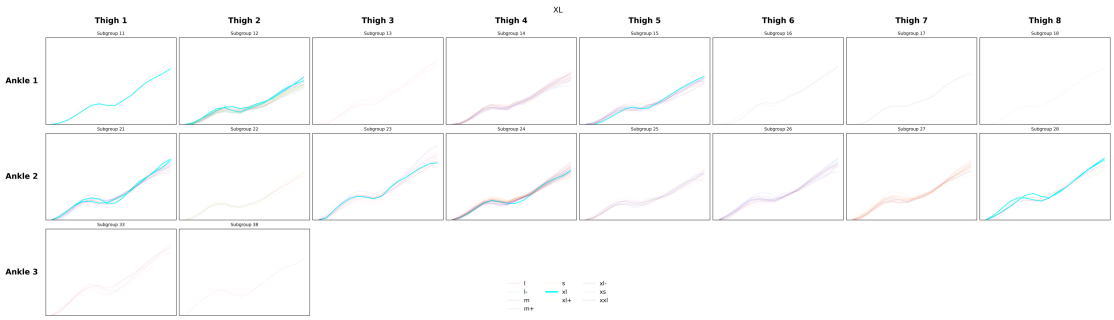


FIGURE F.18: 18 unique patterns of subjects with size XL

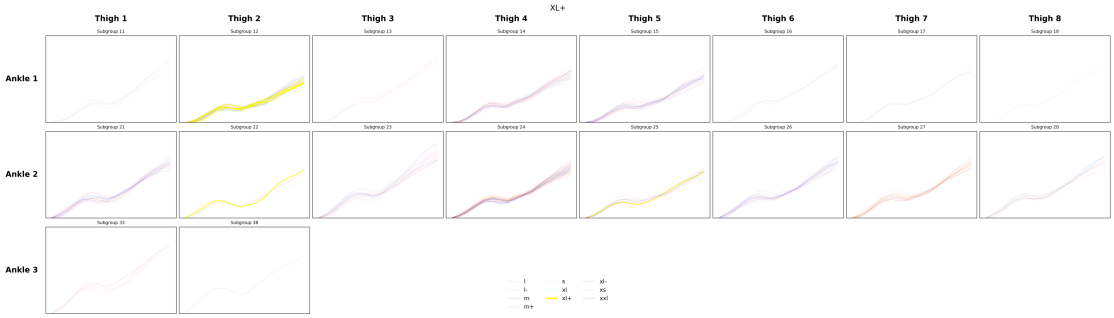


FIGURE F.19: 18 unique patterns of subjects with size XL+

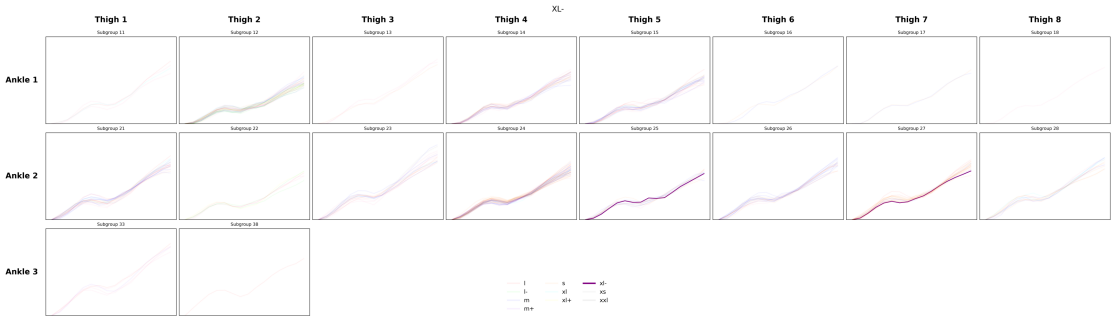


FIGURE F.20: 18 unique patterns of subjects with size XL-

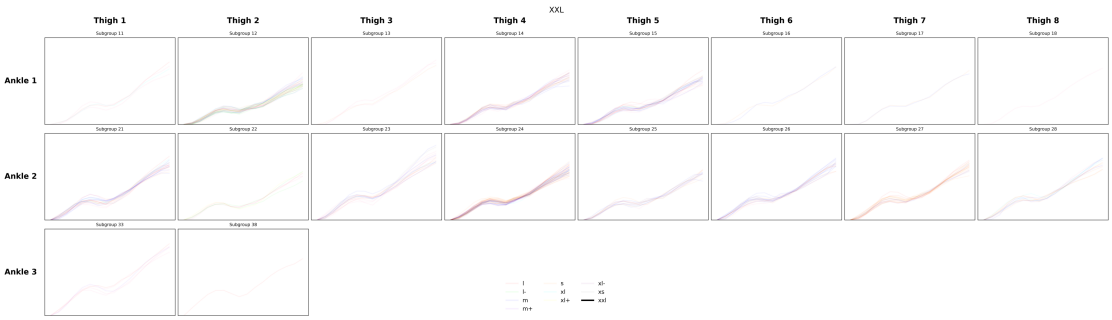


FIGURE F.21: 18 unique patterns of subjects with size XXL

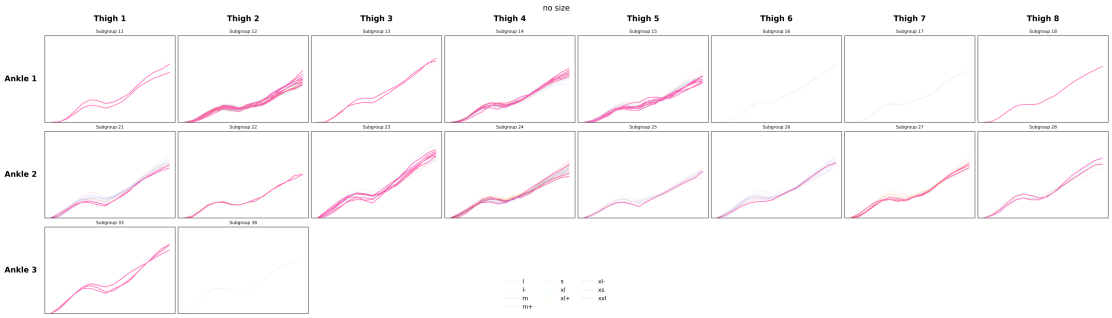


FIGURE F.22: 18 unique patterns of subjects with no matching size

Appendix G

G.1 Geometric comparison between original and adapted form of the legs

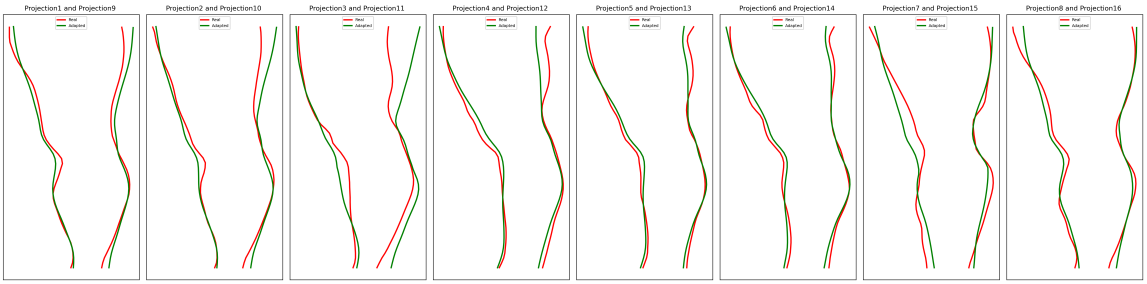


FIGURE G.1: Subject 21 - Original and adapted geometry, illustrated with 8 pair projection plots

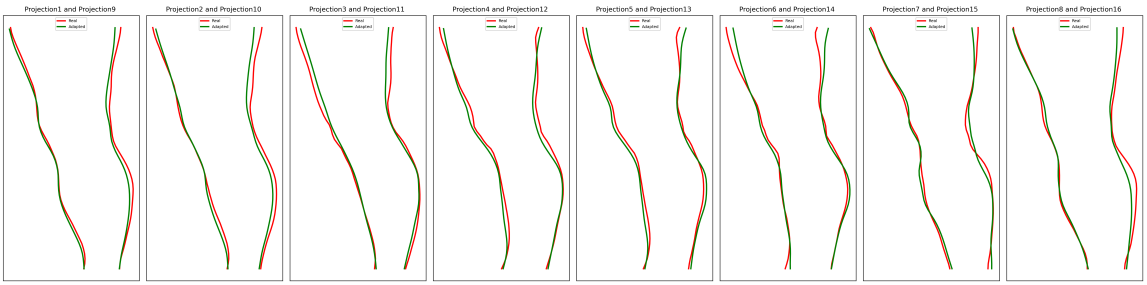


FIGURE G.2: Subject 118 - Original and adapted geometry, illustrated with 8 pair projection plots

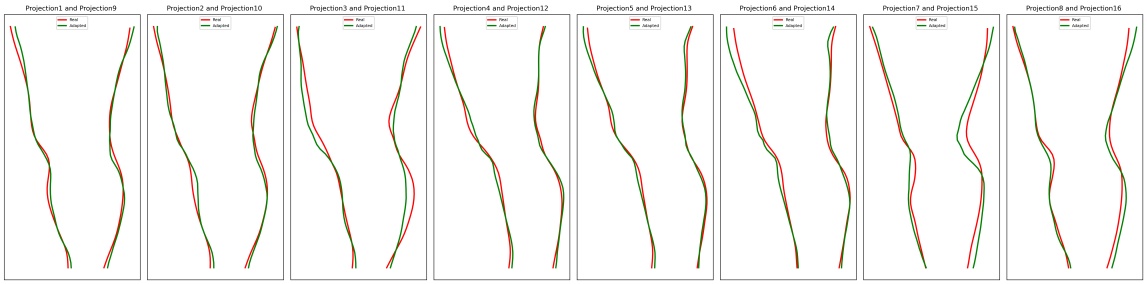


FIGURE G.3: Subject 80 - Original and adapted geometry, illustrated with 8 pair projection plots

References

[1] M. Tan, T. Urbanek, E. Rabe, *et al.*, "Compression therapy in the management of varicose veins," *Phlebology*, vol. 39, no. 4, pp. 276–279, 2024.

[2] S. Reich-Schupke, "Chronic venous insufficiency," *Phlebologie*, vol. 46, no. 01, pp. 34–36, 2017.

[3] J. M. Macdonald, N. Sims, and H. N. Mayrovitz, "Lymphedema, lipedema, and the open wound: The role of compression therapy," *Surgical Clinics*, vol. 83, no. 3, pp. 639–658, 2003.

[4] S. Kitayama, "Diagnosis and treatments of limb lymphedema," *Annals of Vascular Diseases*, vol. 17, no. 2, pp. 114–119, 2024.

[5] S. Palfreyman and J. Michaels, "A systematic review of compression hosiery for uncomplicated varicose veins," *Phlebology*, vol. 24, no. 1_suppl, pp. 13–33, 2009.

[6] N. Kankariya, "Material, structure, and design of textile-based compression devices for managing chronic edema," *Journal of Industrial Textiles*, vol. 52, p. 15 280 837 221 118 844, 2022.

[7] V. Kuzmichev and Z. Cheng, "Sizing and fit for pressure garments," in *Anthropometry, Apparel Sizing and Design*, Elsevier, 2020, pp. 331–370.

[8] R. Liu, T. T. Lao, T. J. Little, X. Wu, and X. Ke, "Can heterogeneous compression textile design reshape skin pressures? a fundamental study," *Textile Research Journal*, vol. 88, no. 17, pp. 1915–1930, 2018.

[9] M. Eagle, "Compression bandaging," *Nursing Standard (through 2013)*, vol. 15, no. 38, p. 47, 2001.

[10] A. K. Greene and J. A. Goss, "Diagnosis and staging of lymphedema," in *Seminars in plastic surgery*, Thieme Medical Publishers, vol. 32, 2018, pp. 012–016.

[11] P. JM, "Reporting standards in venous disease: An update," *J Vasc Surg*, vol. 21, pp. 635–645, 1995.

[12] K. Kowalski, M. Kłonowska, W. Sujka, I. Latańska, and T. M. Kowalski, "Computer-assisted modeling and design of compression garments with graded unit compression," *Autex Research Journal*, vol. 22, no. 1, pp. 80–88, 2022.

[13] Y. Shi, R. Liu, and C. Ye, "Personalized compression therapeutic textiles: Digital design, development, and biomechanical evaluation," *Frontiers in Bioengineering and Biotechnology*, vol. 12, p. 1 405 576, 2024.

[14] W. Xi, Y. Bao, L. Qiao, G. Xia, and T. Xiaoming, "Parametric modeling the human calves for evaluation and design of medical compression stockings," *Computer Methods and Programs in Biomedicine*, vol. 194, p. 105 515, 2020.

[15] P. Li, B. Corner, and S. Paquette, "Shape analysis of female torsos based on discrete cosine transform," *International Journal of Clothing Science and Technology*, vol. 27, no. 5, pp. 677–691, 2015.

[16] E. L. Scott, "The role of 3d measurement technology and anthropometric data for improved garment fit and sustainable manufacturing," in *Digital Manufacturing Technology for Sustainable Anthropometric Apparel*, Elsevier, 2022, pp. 23–48.

[17] N. Saaludin, A. Saad, and C. Mason, "Reliability and ethical issues in conducting anthropometric research using 3d scanner technology," in *Digital Manufacturing Technology for Sustainable Anthropometric Apparel*, Elsevier, 2022, pp. 71–95.

[18] C. C. Kooi, G. Wong, and Z. Qian, "3d anthropometric i. dummy for sustainable clothing design and fit," in *Digital Manufacturing Technology for Sustainable Anthropometric Apparel*, Elsevier, 2022, pp. 117–133.

[19] S. Gill, M. Januszkiewicz, and M. Ahmed, "Digital fashion technology: A review of online fit and sizing," *Digital Manufacturing Technology for Sustainable Anthropometric Apparel*, pp. 135–163, 2022.

[20] N. Zakaria, A. Vouyouka, and W. S. Ruznan, "Sustainable apparel technical and vocational education and training (tvet): Integrating technology for skills training," in *Digital Manufacturing Technology for Sustainable Anthropometric Apparel*, Elsevier, 2022, pp. 3–21.

[21] J. Pei, "The production system of mass customization using 3d body scanning technology," in *Digital manufacturing technology for sustainable anthropometric apparel*, Elsevier, 2022, pp. 185–209.

[22] Ministère de l'Économie, des Finances et de la Souveraineté industrielle et numérique, *France 2030*, https://www.economie.gouv.fr/france-2030, Accessed: 2025-05-14, 2023. [Online]. Available: https://www.economie.gouv.fr/france-2030.

[23] Bpifrance, *France 2030*, https://www.bpifrance.fr/nous-decouvrir/nos-partnaires/france-2030, Accessed: 2025-05-14, 2023. [Online]. Available: https://www.bpifrance.fr/nous-decouvrir/nos-partnaires/france-2030.

[24] Bpifrance, *Appel à projets générique n°3 « i-démo » – soutien aux projets structurants de r&d&i*, https://www.bpifrance.fr/nos-appels-a-projets-concours/appel-a-projets-generique-ndeg3-i-demo-soutien-aux-projets-structurants-de-rdi, Accessed: 2025-05-14, 2023. [Online]. Available: https://www.bpifrance.fr/nos-appels-a-projets-concours/appel-a-projets-generique-ndeg3-i-demo-soutien-aux-projets-structurants-de-rdi.

[25] MesInfos, *Sigvaris, chef de file d'un programme de recherche à 10 millions d'euros*, https://mesinfos.fr/42170-saint-just-saint-rambert/sigvaris-chef-de-file-dun-programme-de-recherche-a-10-millions-deuros-187948.html, Accessed: 2025-05-14, 2023. [Online]. Available: https://mesinfos.fr/42170-saint-just-saint-rambert/sigvaris-chef-de-file-dun-programme-de-recherche-a-10-millions-deuros-187948.html.

[26] SIGVARIS GROUP, *About sigvaris group*, Accessed: 2025-05-14, 2025. [Online]. Available: https://www.sigvaris.com/en-gb/company/about/about-sigvaris-group.

[27] P. Li and K. B. Mitchell, "A shape classification scheme for female torso," *Applied Ergonomics*, vol. 106, p. 103 904, 2023.

[28] Z. Ben Azouz, M. Rioux, C. Shu, and R. Lepage, "Characterizing human shape variation using 3d anthropometric data," *The visual computer*, vol. 22, pp. 302–314, 2006.

[29] T. Aumentado-Armstrong, S. Tsogkas, A. Jepson, and S. Dickinson, "Geometric disentanglement for generative latent shape models," in *Proceedings of the IEEE/CVF international conference on computer vision*, 2019, pp. 8181–8190.

[30] F.-G. Su, C.-S. Lin, and Y.-C. F. Wang, "Learning interpretable representation for 3d point clouds," in *2020 25th International conference on pattern recognition (ICPR)*, IEEE, 2021, pp. 7470–7477.

[31] A. Kascenas, P. Sanchez, P. Schrempf, *et al.*, "The role of noise in denoising models for anomaly detection in medical images," *Medical image analysis*, vol. 90, p. 102 963, 2023.

[32] S. Lu, W. Zhang, J. Guo, H. Liu, H. Li, and N. Wang, "Patchcl-ae: Anomaly detection for medical images using patch-wise contrastive learning-based auto-encoder," *Computerized Medical Imaging and Graphics*, vol. 114, p. 102 366, 2024.

[33] C. Huang, Y. Shi, B. Zhang, and K. Lyu, "Uncertainty-aware prototypical learning for anomaly detection in medical images," *Neural Networks*, vol. 175, p. 106 284, 2024.

[34] N. Kankariya, R. M. Laing, and C. A. Wilson, "Textile-based compression therapy in managing chronic oedema: Complex interactions," *Phlebology*, vol. 36, no. 2, pp. 100–113, 2021.

[35] Y. Teyeme, B. Malengier, T. Tesfaye, S. Vasile, W. Endalew, and L. Van Langenhove, "Predicting compression pressure of knitted fabric using a modified laplace's law," *Materials*, vol. 14, no. 16, p. 4461, 2021.

[36] D. Lawrence and V. Kakkar, "Graduated, static, external compression of the lower limb: A physiological assessment," *Journal of British Surgery*, vol. 67, no. 2, pp. 119–121, 1980.

[37] N. Brophy-Williams, M. W. Driller, C. M. Shing, J. W. Fell, and S. L. Halson, "Confounding compression: The effects of posture, sizing and garment type on measured interface pressure in sports compression clothing," *Journal of Sports Sciences*, vol. 33, no. 13, pp. 1403–1410, 2015.

[38] Wounds International, *Principles of compression in venous disease: A practitioner's guide to treatment and prevention of venous leg ulcers*, L. MacGregor, Ed., Available from: http://www.woundsinternational.com, 2013.

[39] C. Moffatt, "Variability of pressure provided by sustained compression," *International wound journal*, vol. 5, no. 2, pp. 259–265, 2008.

[40] A. Nicolaides, "Investigation of chronic venous insufficiency: A consensus statement," *Circulation*, vol. 102, no. 20, e126–e163, 2000.

[41] K. van der Wegen-Franken, *Medical elastic compression stockings*. 2009.

[42] G. Motykie, J. Caprini, J. Arcelus, J. Reyna, E. Overom, and D. Mokhtee, "Evaluation of therapeutic compression stockings in the treatment of chronic venous insufficiency," *Dermatologic surgery*, vol. 25, no. 2, pp. 116–120, 1999.

[43] M. Lozo, Ž. Penava, I. Lovričević, and Z. Vrljičak, "The structure and compression of medical compression stockings," *Materials*, vol. 15, no. 1, p. 353, 2022.

[44] A. Coull, M. Clark, S. Bale, *et al.*, "Best practice statement: Compression hosiery," *Wounds UK*, pp. 1–24, 2002, Last accessed 4 Mars 2025. [Online]. Available: http://www.wounds-uk.com/downloads/compression_hosiery_statement.pdf.

[45] S. Nørregaard, S. Bermark, and F. Gottrup, "Do ready-made compression stockings fit the anatomy of the venous leg ulcer patient?" *Journal of wound care*, vol. 23, no. 3, pp. 128–135, 2014.

[46] R. Granberry, J. Duvall, L. E. Dunne, and B. Holschuh, "An analysis of anthropometric geometric variability of the lower leg for the fit & function of advanced functional garments," in *Proceedings of the 2017 ACM international symposium on wearable computers*, 2017, pp. 10–17.

[47] C. Ruff, "Variation in human body size and shape," *Annual review of anthropology*, vol. 31, no. 1, pp. 211–232, 2002.

[48] D. Nikitovic, "Sexual dimorphism (humans)," *The international encyclopedia of biological anthropology*, pp. 1–4, 2018.

[49] T. W. Holliday and C. B. Ruff, "Relative variation in human proximal and distal limb segment lengths," *American Journal of Physical Anthropology: The Official Publication of the American Association of Physical Anthropologists*, vol. 116, no. 1, pp. 26–33, 2001.

[50] T. W. Holliday, "Brachial and crural indices of european late upper paleolithic and mesolithic humans," *Journal of human evolution*, vol. 36, no. 5, pp. 549–566, 1999.

[51] M. Pośnik, N. Zielinska, R. S. Tubbs, K. Ruzik, and Ł. Olewnik, "Morphological variability of the leg muscles: Potential pitfalls on ultrasound that await clinicians," *Folia Morphologica*, vol. 83, no. 2, pp. 275–293, 2024.

[52] A., *Tibialis anterior | Encyclopedia*, https://anatomy.app/encyclopedia/tibialis-anterior, Accessed: Jun. 18, 2024, 2024.

[53] A., *Gastrocnemius | Encyclopedia*, https://anatomy.app/encyclopedia/gastrocnemius, Accessed: Jun. 18, 2024, 2024.

[54] A., *Extensor Digitorum Longus | Encyclopedia*, https://anatomy.app/encyclopedia/extensor-digitorum-longus, Accessed: Nov. 7, 2024, 2024.

[55] J. C. Wells, "Sexual dimorphism of body composition," *Best practice & research Clinical endocrinology & metabolism*, vol. 21, no. 3, pp. 415–430, 2007.

[56] M. F. Mansour, C.-W. J. Chan, S. Laforest, A. Veilleux, and A. Tchernof, "Sex differences in body fat distribution," *Adipose Tissue Biology*, pp. 257–300, 2017.

[57] S. B. Heymsfield, R. Smith, M. Aulet, *et al.*, "Appendicular skeletal muscle mass: Measurement by dual-photon absorptiometry," *The American journal of clinical nutrition*, vol. 52, no. 2, pp. 214–218, 1990.

[58] B. C. Nindl, C. R. Scoville, K. M. Sheehan, C. D. Leone, and R. P. Mello, "Gender differences in regional body composition and somatotrophic influences of igf-i and leptin," *Journal of Applied Physiology*, vol. 92, no. 4, pp. 1611–1618, 2002.

[59] V. L. Winslow, *Classic Human Anatomy in Motion: The Artist's Guide to the Dynamics of Figure Drawing*. New York: Watson-Guptill, 2015, ISBN: 9780770434144.

[60] D. Boscaini, J. Masci, E. Rodolà, and M. Bronstein, "Learning shape correspondence with anisotropic convolutional neural networks," *Advances in neural information processing systems*, vol. 29, 2016.

[61] Y. Feng, Y. Feng, H. You, X. Zhao, and Y. Gao, "Meshnet: Mesh neural network for 3d shape representation," in *Proceedings of the AAAI conference on artificial intelligence*, vol. 33, 2019, pp. 8279–8286.

[62] M. Gao, N. Ruan, J. Shi, and W. Zhou, "Deep neural network for 3d shape classification based on mesh feature," *Sensors*, vol. 22, no. 18, p. 7040, 2022.

[63] E. Ahmed, A. Saint, A. Shabayek, *et al.*, "A survey on deep learning advances on different 3d data representations. arxiv 2018," *arXiv preprint arXiv:1808.01462*, 2019.

[64] T. Weyrich, M. Pauly, R. Keiser, S. Heinzle, S. Scandella, and M. Gross, "Post-processing of scanned 3d surface data," in *First Eurographics conference on Point-Based Graphics*, Eurographics Association, 2004.

[65] S. Alemany, A. Remon, A. Ballester, *et al.*, "Data management and processing of 3d body scans," in *Digital manufacturing technology for sustainable anthropometric apparel*, Elsevier, 2022, pp. 97–116.

[66] B. Hamad, "Contribution à l'optimisation de systèmes de tailles de vêtements par une approche morphologique orientée clients," 2020LILUI005, Ph.D. dissertation, 2020. [Online]. Available: http://www.theses.fr/2020LILUI005/document.

[67] R. Jin and J. Kim, "A method for 3d model identification using histogram normalization based on conformal factor," in *2016 IEEE International Conference on Electronic Information and Communication Technology (ICEICT)*, 2016, pp. 360–362. DOI: 10.1109/ICEICT.2016.7879717.

[68] M. Hamad, S. Thomassey, and P. Bruniaux, "A new sizing system based on 3d shape descriptor for morphology clustering," *Computers & Industrial Engineering*, vol. 113, pp. 683–692, 2017.

[69] B. Gärtner, "Fast and robust smallest enclosing balls," in *Algorithms - ESA' 99*, J. Nešetřil, Ed., Berlin, Heidelberg: Springer Berlin Heidelberg, 1999, pp. 325–338, ISBN: 978-3-540-48481-3.

[70] E. Welzl, "Smallest enclosing disks (balls and ellipsoids)," in *New Results and New Trends in Computer Science*, ser. Lecture Notes in Computer Science, H. Maurer, Ed., vol. 555, Springer, 1991, pp. 359–370. DOI: 10.1007/3-540-54945-7_121.

[71] A. Semechko, *Exact minimum bounding spheres and circles*, https://github.com/AntonSemechko/Bounding-Spheres-And-Circles, GitHub repository. Accessed: April 16, 2025, 2025.

[72] B. Gašparović, L. Morelato, K. Lenac, G. Mauša, A. Zhurov, and V. Katić, "Comparing direct measurements and three-dimensional (3d) scans for evaluating facial soft tissue," *Sensors*, vol. 23, no. 5, p. 2412, 2023.

[73] Y.-P. Xiao, Y.-K. Lai, F.-L. Zhang, C. Li, and L. Gao, "A survey on deep geometry learning: From a representation perspective," *Computational Visual Media*, vol. 6, pp. 113–133, 2020.

[74] A. J. Izenman, "Introduction to manifold learning," *WIREs Computational Statistics*, vol. 4, no. 5, pp. 439–446, 2012. DOI: https://doi.org/10.1002/wics.1222. eprint: https://wires.onlinelibrary.wiley.com/doi/pdf/10.1002/wics.1222. [Online]. Available: https://wires.onlinelibrary.wiley.com/doi/abs/10.1002/wics.1222.

[75] J. B. Tenenbaum, V. d. Silva, and J. C. Langford, "A global geometric framework for nonlinear dimensionality reduction," *science*, vol. 290, no. 5500, pp. 2319–2323, 2000.

[76] S. T. Roweis and L. K. Saul, "Nonlinear dimensionality reduction by locally linear embedding," *science*, vol. 290, no. 5500, pp. 2323–2326, 2000.

[77] M. Belkin and P. Niyogi, "Laplacian eigenmaps and spectral techniques for embedding and clustering," *Advances in neural information processing systems*, vol. 14, 2001.

[78] B. Nadler, S. Lafon, I. Kevrekidis, and R. Coifman, "Diffusion maps, spectral clustering and eigenfunctions of fokker-planck operators," in *Advances in Neural Information Processing Systems*, Y. Weiss, B. Schölkopf, and J. Platt, Eds., vol. 18, MIT Press, 2005. [Online]. Available: https://proceedings.neurips.cc/paper_files/paper/2005/file/2a0f97f81755e2878b264adf39cba68e-Paper.pdf.

[79] D. L. Bibissi, J. Yang, S. Quan, and Y. Zhang, "Dual spin-image: A bi-directional spin-image variant using multi-scale radii for 3d local shape description," *Computers & Graphics*, vol. 103, pp. 180–191, 2022.

[80] R. Rostami, F. S. Bashiri, B. Rostami, and Z. Yu, "A survey on data-driven 3d shape descriptors," in *Computer graphics forum*, Wiley Online Library, vol. 38, 2019, pp. 356–393.

[81] E. Ahmed, A. Saint, A. E. R. Shabayek, *et al.*, "A survey on deep learning advances on different 3d data representations," *arXiv preprint arXiv:1808.01462*, 2018.

[82] C. R. Qi, H. Su, K. Mo, and L. J. Guibas, "Pointnet: Deep learning on point sets for 3d classification and segmentation," in *Proceedings of the IEEE conference on computer vision and pattern recognition*, 2017, pp. 652–660.

[83] C. R. Qi, L. Yi, H. Su, and L. J. Guibas, "Pointnet++: Deep hierarchical feature learning on point sets in a metric space," *arXiv*, Jun. 2017, Accessed: Sep. 13, 2024. eprint: arXiv:1706.02413. [Online]. Available: http://arxiv.org/abs/1706.02413.

[84] S. Tiigimägi, *Introduction to 3D Polygon Mesh - 3D Studio — 3dstudio.co*, https://3dstudio.co/polygon-mesh/, [Accessed 11-07-2024], 2022.

[85] R. Hanocka, A. Hertz, N. Fish, R. Giryes, S. Fleishman, and D. Cohen-Or, "Meshcnn: A network with an edge," *ACM Transactions on Graphics (ToG)*, vol. 38, no. 4, pp. 1–12, 2019.

[86] Z. Wu, S. Song, A. Khosla, *et al.*, "3d shapenets: A deep representation for volumetric shapes," in *Proceedings of the IEEE conference on computer vision and pattern recognition*, 2015, pp. 1912–1920.

[87] S.-M. Hu, Z.-N. Liu, M.-H. Guo, *et al.*, "Subdivision-based mesh convolution networks," *ACM Transactions on Graphics (TOG)*, vol. 41, no. 3, pp. 1–16, 2022.

[88] K. He, X. Zhang, S. Ren, and J. Sun, "Deep residual learning for image recognition," in *Proceedings of the IEEE conference on computer vision and pattern recognition*, 2016, pp. 770–778.

[89] L.-C. Chen, G. Papandreou, I. Kokkinos, K. Murphy, and A. L. Yuille, "Deeplab: Semantic image segmentation with deep convolutional nets, atrous convolution, and fully connected crfs," *IEEE transactions on pattern analysis and machine intelligence*, vol. 40, no. 4, pp. 834–848, 2017.

[90] S. Alemany, J. Uriel, A. Ballester, and E. Parrilla, "Three-dimensional body shape modeling and posturography," in *DHM and Posturography*, Elsevier, 2019, pp. 441–457.

[91] B. Allen, B. Curless, and Z. Popović, "The space of human body shapes: Reconstruction and parameterization from range scans," *ACM transactions on graphics (TOG)*, vol. 22, no. 3, pp. 587–594, 2003.

[92] P. Xi, W.-S. Lee, and C. Shu, "A data-driven approach to human-body cloning using a segmented body database," in *15th Pacific Conference on Computer Graphics and Applications (PG'07)*, IEEE, 2007, pp. 139–147.

[93] P. Xi, W.-S. Lee, and C. Shu, "Analysis of segmented human body scans," in *Proceedings of graphics interface 2007*, 2007, pp. 19–26.

[94] O. Mendoza-Schrock, J. Patrick, G. Arnold, and M. Ferrara, "Applying manifold learning techniques to the caesar database," in *Evolutionary and Bio-Inspired Computation: Theory and Applications IV*, SPIE, vol. 7704, 2010, pp. 200–210.

[95] O. Mendoza-Schrock and M. L. Raymer, "Exploring the caesar database using dimensionality reduction techniques," in *Evolutionary and Bio-Inspired Computation: Theory and Applications VI*, SPIE, vol. 8402, 2012, pp. 170–179.

[96] A. Godil and S. Ressler, "Retrieval and clustering from a 3d human database based on body and head shape," *arXiv preprint arXiv:1105.2800*, 2011.

[97] E. U. Oti, M. O. Olusola, F. C. Eze, and S. U. Enogwe, "Comprehensive review of k-means clustering algorithms," *criterion*, vol. 12, pp. 22–23, 2021.

[98] A. M. Ikotun, A. E. Ezugwu, L. Abualigah, B. Abuhaija, and J. Heming, "K-means clustering algorithms: A comprehensive review, variants analysis, and advances in the era of big data," *Information Sciences*, vol. 622, pp. 178–210, 2023.

[99] A. Fahim, "K and starting means for k-means algorithm," *Journal of Computational Science*, vol. 55, p. 101 445, 2021.

[100] Pedregosa, F. and Varoquaux, G. and Gramfort, A. and Michel, V. and Thirion, B. and Grisel, O. and Blondel, M. and Prettenhofer, P. and Weiss, R. and Dubourg, V. and Vanderplas, J. and Passos, A. and Cournapeau, D. and Brucher, M. and Perrot, M. and Duchesnay, E., "Scikit-learn: Machine Learning in Python," *Journal of Machine Learning Research*, vol. 12, pp. 2825–2830, 2011.

[101] S. M. Miraftabzadeh, C. G. Colombo, M. Longo, and F. Foiadelli, "K-means and alternative clustering methods in modern power systems," *Ieee Access*, vol. 11, pp. 119 596–119 633, 2023.

[102] T. M. Ghazal, "Performances of k-means clustering algorithm with different distance metrics," *Intelligent Automation & Soft Computing*, vol. 30, no. 2, pp. 735–742, 2021.

[103] M. S. Al-Batah, E. R. Al-Kwaldeh, M. A. Wahed, M. Alzyoud, and N. Al-Shanableh, "Enhancement over dbscan satellite spatial data clustering," *Journal of Electrical and Computer Engineering*, vol. 2024, no. 1, p. 2 330 624, 2024.

[104] A. A. Bushra and G. Yi, "Comparative analysis review of pioneering dbscan and successive density-based clustering algorithms," *IEEE Access*, vol. 9, pp. 87 918–87 935, 2021.

[105] O. Kulkarni and A. Burhanpurwala, "A survey of advancements in dbscan clustering algorithms for big data," in *2024 3rd International conference on Power Electronics and IoT Applications in Renewable Energy and its Control (PARC)*, IEEE, 2024, pp. 106–111.

[106] H. V. Singh, A. Girdhar, and S. Dahiya, "A literature survey based on dbscan algorithms," in *2022 6th International Conference on Intelligent Computing and Control Systems (ICICCS)*, IEEE, 2022, pp. 751–758.

[107] L. Ding, C. Li, D. Jin, and S. Ding, "Survey of spectral clustering based on graph theory," *Pattern Recognition*, p. 110 366, 2024.

[108] U. Von Luxburg, "A tutorial on spectral clustering," *Statistics and computing*, vol. 17, pp. 395–416, 2007.

[109] U. von Luxburg, *A tutorial on spectral clustering*, Accessed: Mar. 08, 2023, Nov. 2007. [Online]. Available: http://arxiv.org/abs/0711.0189.

[110] U. von Luxburg, M. Belkin, and O. Bousquet, "Consistency of spectral clustering," *Annals of Statistics*, vol. 36, no. 2, 2008. DOI: 10.1214/009053607000000640.

[111] Y. Benkaouz, M. Erradi, and A.-M. Kermarrec, "Nearest neighbors graph construction: Peer sampling to the rescue," in *Networked Systems*, ser. Lecture Notes in Computer Science, P. A. Abdulla and C. Delporte-Gallet, Eds., vol. 9944, Cham: Springer International Publishing, 2016, pp. 48–62. DOI: 10.1007/978-3-319-46140-3_4.

[112] J. Shi and J. Malik, "Normalized cuts and image segmentation," *IEEE Transactions on Pattern Analysis and Machine Intelligence*, vol. 22, no. 8, 2000.

[113] S. White and P. Smyth, "A spectral clustering approach to finding communities in graphs," in *Proceedings of the 2005 SIAM international conference on data mining*, SIAM, 2005, pp. 274–285.

[114] P. J. Rousseeuw, "Silhouettes: A graphical aid to the interpretation and validation of cluster analysis," *Journal of Computational and Applied Mathematics*, vol. 20, pp. 53–65, Nov. 1987. DOI: 10.1016/0377-0427(87)90125-7.

[115] D. L. Davies and D. W. Bouldin, "A cluster separation measure," *IEEE Transactions on Pattern Analysis and Machine Intelligence*, vol. PAMI-1, no. 2, pp. 224–227, Apr. 1979. DOI: 10.1109/TPAMI.1979.4766909.

[116] T. Calinski and J. Harabasz, "A dendrite method for cluster analysis," *Communications in Statistics - Theory and Methods*, vol. 3, no. 1, pp. 1–27, 1974. DOI: 10.1080/03610927408827101.

[117] J. Han, M. Kamber, and J. Pei, *Data Mining: Concepts and Techniques* (Morgan Kaufmann Series in Data Management Systems), 3rd. Amsterdam Boston: Elsevier/Morgan Kaufmann, 2012.

[118] H. Li, X. Ye, A. Imakura, and T. Sakurai, "Ensemble learning for spectral clustering," in *2020 IEEE International Conference on Data Mining (ICDM)*, IEEE, 2020, pp. 1094–1099.

[119] M. R. Karim, O. Beyan, A. Zappa, *et al.*, "Deep learning-based clustering approaches for bioinformatics," *Briefings in Bioinformatics*, vol. 22, no. 1, pp. 393–415, 2021.

[120] X. Wei, Z. Zhang, H. Huang, and Y. Zhou, "An overview on deep clustering," *Neurocomputing*, p. 127 761, 2024.

[121] F. Xu, H. Uszkoreit, Y. Du, W. Fan, D. Zhao, and J. Zhu, "Explainable ai: A brief survey on history, research areas, approaches and challenges," in *Natural language processing and Chinese computing: 8th cCF international conference, NLPCC 2019, dunhuang, China, October 9–14, 2019, proceedings, part II 8*, Springer, 2019, pp. 563–574.

[122] F. K. Došilović, M. Brčić, and N. Hlupić, "Explainable artificial intelligence: A survey," in *2018 41st International convention on information and communication technology, electronics and microelectronics (MIPRO)*, IEEE, 2018, pp. 0210–0215.

[123] D. Gunning, E. Vorm, Y. Wang, and M. Turek, "Darpa's explainable ai (xai) program: A retrospective," *Authorea Preprints*, 2021.

[124] R. Ibrahim and M. O. Shafiq, "Explainable convolutional neural networks: A taxonomy, review, and future directions," *ACM Computing Surveys*, vol. 55, no. 10, pp. 1–37, 2023.

[125] Z. Zhang and X. Deng, "Anomaly detection using improved deep svdd model with data structure preservation," *Pattern Recognition Letters*, vol. 148, pp. 1–6, 2021.

[126] H. Zhang, N. Kumar, S. Wu, C. Wu, J. Wang, and P. Zhang, "Anomaly detection with memory-augmented adversarial autoencoder networks for industry 5.0," *IEEE Transactions on Consumer Electronics*, vol. 70, no. 1, pp. 1952–1962, 2023.

[127] J. Pang, X. Pu, and C. Li, "A hybrid algorithm incorporating vector quantization and one-class support vector machine for industrial anomaly detection," *IEEE Transactions on Industrial Informatics*, vol. 18, no. 12, pp. 8786–8796, 2022.

[128] J. Lesouple, C. Baudoin, M. Spigai, and J.-Y. Tourneret, "Generalized isolation forest for anomaly detection," *Pattern Recognition Letters*, vol. 149, pp. 109–119, 2021.

[129] V. Yepmo, G. Smits, M.-J. Lesot, and O. Pivert, "Leveraging an isolation forest to anomaly detection and data clustering," *Data & Knowledge Engineering*, vol. 151, p. 102 302, 2024.

[130] H. Xu, G. Pang, Y. Wang, and Y. Wang, "Deep isolation forest for anomaly detection," *IEEE Transactions on Knowledge and Data Engineering*, vol. 35, no. 12, pp. 12 591–12 604, 2023.

[131] Y. Zhou, X. Liang, W. Zhang, L. Zhang, and X. Song, "Vae-based deep svdd for anomaly detection," *Neurocomputing*, vol. 453, pp. 131–140, 2021.

[132] K. T. Mai, T. Davies, and L. D. Griffin, "Brittle features may help anomaly detection," *arXiv preprint arXiv:2104.10453*, 2021.

[133] B. Min, J. Yoo, S. Kim, D. Shin, and D. Shin, "Network anomaly detection using memory-augmented deep autoencoder," *IEEE Access*, vol. 9, pp. 104 695–104 706, 2021.

[134] K. Yang, S. Kpotufe, and N. Feamster, "An efficient one-class svm for anomaly detection in the internet of things," *arXiv preprint arXiv:2104.11146*, 2021.

[135] Y. Qiao, K. Wu, and P. Jin, "Efficient anomaly detection for high-dimensional sensing data with one-class support vector machine," *IEEE Transactions on Knowledge and Data Engineering*, vol. 35, no. 1, pp. 404–417, 2021.

[136] W. Li, X. Xu, Y. Gu, B. Zheng, S. Gao, and Y. Wu, "Towards scalable 3d anomaly detection and localization: A benchmark via 3d anomaly synthesis and a self-supervised learning network," in *Proceedings of the IEEE/CVF conference on computer vision and pattern recognition*, 2024, pp. 22 207–22 216.

[137] J. Liu, G. Xie, R. Chen, *et al.*, "Real3d-ad: A dataset of point cloud anomaly detection," *Advances in Neural Information Processing Systems*, vol. 36, pp. 30 402–30 415, 2023.

[138] E. Horwitz and Y. Hoshen, "Back to the feature: Classical 3d features are (almost) all you need for 3d anomaly detection," in *Proceedings*

of the IEEE/CVF Conference on Computer Vision and Pattern Recognition, 2023, pp. 2968–2977.

[139] J. Du, C. Tao, X. Cao, and F. Tsung, "3d vision-based anomaly detection in manufacturing: A survey," *Frontiers of Engineering Management*, pp. 1–18, 2025.

[140] R. Chen, G. Xie, J. Liu, *et al.*, "Easynet: An easy network for 3d industrial anomaly detection," in *Proceedings of the 31st ACM International Conference on Multimedia*, 2023, pp. 7038–7046.

[141] O. Habbal, "The science of anatomy: A historical timeline," *Sultan Qaboos University Medical Journal*, vol. 17, no. 1, e18, 2017.

[142] W. H. Sheldon, S. S. Stevens, and W. B. Tucker, "The varieties of human physique.," 1940.

[143] P. R. Jones and M. Rioux, "Three-dimensional surface anthropometry: Applications to the human body," *Optics and Lasers in Engineering*, vol. 28, no. 2, pp. 89–117, 1997.

[144] S. Ashdown, *Sizing in clothing*. Elsevier, 2007.

[145] Z. B. Azouz, M. Rioux, C. Shu, and R. Lepage, "Characterizing human shape variation using 3d anthropometric data," *Visual Comput*, vol. 22, no. 5, pp. 302–314, May 2006, See reference [5]. DOI: 10.1007/s00371-006-0006-6.

[146] R. Liu, X. Guo, Q. Peng, *et al.*, "Stratified body shape-driven sizing system via three-dimensional digital anthropometry for compression textiles of lower extremities," *Textile Research Journal*, vol. 88, no. 18, pp. 2055–2075, 2018.

[147] E. Tilburg Law Review, "Fundamental texts on european private law," *Tilburg Law Review*, vol. 11, no. 3, pp. 708–708,

[148] *Q angle*, Accessed: May 11, 2024. [Online]. Available: https://www.physio-pedia.com/Q_Angle.

[149] *2d transformations*, Online lecture notes, Minia University, No date. Accessed: 2025-06-24. [Online]. Available: https://courses.minia.edu.eg/Attach/907273004%202D_TRANSFORMATIONS.pdf.

[150] G. Strang, *Linear algebra and its applications*. 2000.

[151] *Wecov3r solutions*, https://www.wecov3r.com/?lang=EN, Accessed: 2025-12-03.

[152] C. Goodall, "Procrustes methods in the statistical analysis of shape," *Journal of the Royal Statistical Society: Series B (Methodological)*, vol. 53, no. 2, pp. 285–321, 1991.

[153] A. Ross, "Procrustes analysis," *Course report, Department of Computer Science and Engineering, University of South Carolina*, vol. 26, pp. 1–8, 2004.

[154] Q.-Y. Zhou, J. Park, and V. Koltun, "Open3d: A modern library for 3d data processing," *arXiv preprint arXiv:1801.09847*, 2018.

[155] I. Cohen, Y. Huang, J. Chen, *et al.*, "Pearson correlation coefficient," *Noise reduction in speech processing*, pp. 1–4, 2009.

[156] M. L. Waskom, "Seaborn: Statistical data visualization," *Journal of Open Source Software*, vol. 6, no. 60, p. 3021, 2021. DOI: 10.21105/joss.03021.

[157] I. T. Jolliffe, *Principal component analysis for special types of data*. Springer, 2002.

[158] A. Y. Ng, M. I. Jordan, and Y. Weiss, *On spectral clustering: Analysis and an algorithm*, 2000.

[159] M. E. Newman and M. Girvan, "Finding and evaluating community structure in networks," *Physical review E*, vol. 69, no. 2, p. 026 113, 2004.

[160] J. K. Loudon, H. L. Goist, and K. L. Loudon, "Genu recurvatum syndrome," *Journal of Orthopaedic & Sports Physical Therapy*, vol. 27, no. 5, pp. 361–367, 1998, PMID: 9580896. DOI: 10.2519/jospt.1998.27.5.361.

[161] J. Johnson, *The ins and outs of genu flexum*, Excerpt from *Postural Correction*, Retrieved July 2, 2025, from Human Kinetics blog, 2025. [Online]. Available: https://us.humankinetics.com/blogs/excerpt/the-ins-and-outs-of-genu-flexum?srsltid=AfmBOootLhCbveNYdbe_E8QmuwfBwOIcqdaq4UgMIMiRL6e3EhjLx9S2.

[162] J. Masci, D. Boscaini, M. M. Bronstein, and P. Vandergheynst, "Shapenet: Convolutional neural networks on non-euclidean manifolds," *CoRR, abs/1501.06297*, vol. 3, 2015.

[163] M. Mostapha, S. Kim, G. Wu, L. Zsembik, S. Pizer, and M. Styner, "Non-euclidean, convolutional learning on cortical brain surfaces," in *2018 IEEE 15th international symposium on biomedical imaging (ISBI 2018)*, IEEE, 2018, pp. 527–530.

[164] Y. Zhou, C. Wu, Z. Li, *et al.*, "Fully convolutional mesh autoencoder using efficient spatially varying kernels," *Advances in neural information processing systems*, vol. 33, pp. 9251–9262, 2020.

[165] F. Bogo, J. Romero, G. Pons-Moll, and M. J. Black, "Dynamic FAUST: Registering human bodies in motion," in *IEEE Conf. on Computer Vision and Pattern Recognition (CVPR)*, Jul. 2017.

[166] H.-J. Xing and P.-P. Zhang, "Contrastive deep support vector data description," *Pattern Recognition*, vol. 143, p. 109 820, 2023.

[167] W. Li, B. Zheng, X. Xu, *et al.*, *Multi-sensor object anomaly detection: Unifying appearance, geometry, and internal properties*, 2024. DOI: 10.48550/ARXIV.2412.14592. [Online]. Available: https://arxiv.org/abs/2412.14592.

[168] E. Rabe, H. Partsch, J. Hafner, *et al.*, "Indications for medical compression stockings in venous and lymphatic disorders: An evidence-based consensus statement," *Phlebology*, vol. 33, no. 3, pp. 163–184, 2018.

[169] H. K. Kankam, C. S. Lim, F. Fiorentino, A. H. Davies, and M. S. Gohel, "A summation analysis of compliance and complications of compression hosiery for patients with chronic venous disease or post-thrombotic syndrome," *European Journal of Vascular and Endovascular Surgery*, vol. 55, no. 3, pp. 406–416, 2018.

[170] D. Ziaja, P. Kocełak, J. Chudek, and K. Ziaja, "Compliance with compression stockings in patients with chronic venous disorders," *Phlebology*, vol. 26, no. 8, pp. 353–360, 2011.

[171] S. F. Tandler, "Challenges faced by healthcare professionals in the provision of compression hosiery to enhance compliance in the prevention of venous leg ulceration.," *EWMA Journal*, vol. 16, no. 1, 2016.

[172] R. Jindal, J.-F. Uhl, and J. Benigni, "Sizing of medical below-knee compression stockings in an indian population: A major risk factor for non-compliance," *Phlebology*, vol. 35, no. 2, pp. 110–114, 2020.

[173] A. Abdelhalim and I. Traore, "A new method for learning decision trees from rules," in *2009 International Conference on Machine Learning and Applications*, 2009, pp. 693–698. DOI: 10.1109/ICMLA.2009.25.

[174] M. Hamad, "Classification non-supervisée de morphologies 3d de corps humain pour la mise en œuvre de mannequins morphotypes adaptatifs | theses. fr," Ph.D. dissertation, Lille 1, 2015.

[175] J. Hu, "Parametric human modeling," in *Basic finite element method as applied to injury biomechanics*, Elsevier, 2018, pp. 417–445.

[176] S. M. Shariff, S. Japar, N. Shahlal, and A. A. Shariff, "Importance of sizing and fit using 3d technology," in *Digital Manufacturing Technology for Sustainable Anthropometric Apparel*, Elsevier, 2022, pp. 167–184.

[177] A. Serwatka, "Contribution à la modélisation et à la simulation de vêtements sur mannequin adaptatif," 2008LIL10029, Ph.D. dissertation, 2008. [Online]. Available: http://www.theses.fr/2008LIL10029/document.

[178] M. Hamad, "Classification non-supervisée de morphologies 3d de corps humain pour la mise en œuvre de mannequins morphotypes adaptatifs," 2015LIL10046, Ph.D. dissertation, 2015. [Online]. Available: http://www.theses.fr/2015LIL10046/document.

[179] S. Mosleh, "Processus de morphotype adaptatif pour un ajustement ergonomique optimal et une modélisation du confort thermique des vêtements pour les personnes souffrant d'un handicap rachidien," 2021LILUB005, Ph.D. dissertation, 2021. [Online]. Available: http://www.theses.fr/2021LILUB005/document.

[180] M. J. Ackerman, "The visible human project," *Proceedings of the IEEE*, vol. 86, no. 3, pp. 504–511, 2002.

[181] U.S. National Library of Medicine, *Visible Human Project*, https://www.nlm.nih.gov/research/visible/visible_human.html, No date. Accessed: 2025-07-09.